

## **INFORMATION TO USERS**

**This manuscript has been reproduced from the microfilm master. UMI films the text directly from the original or copy submitted. Thus, some thesis and dissertation copies are in typewriter face, while others may be from any type of computer printer.**

**The quality of this reproduction is dependent upon the quality of the copy submitted. Broken or indistinct print, colored or poor quality illustrations and photographs, print bleedthrough, substandard margins, and improper alignment can adversely affect reproduction.**

**In the unlikely event that the author did not send UMI a complete manuscript and there are missing pages, these will be noted. Also, if unauthorized copyright material had to be removed, a note will indicate the deletion.**

**Oversize materials (e.g., maps, drawings, charts) are reproduced by sectioning the original, beginning at the upper left-hand corner and continuing from left to right in equal sections with small overlaps.**

**ProQuest Information and Learning  
300 North Zeeb Road, Ann Arbor, MI 48106-1346 USA  
800-521-0600**

**UMI<sup>®</sup>**



**THE UNIVERSITY OF OKLAHOMA  
GRADUATE COLLEGE**

**HEAT TRANSFER AND FLUID FLOW IN  
ROTATING CYLINDERS WITH A POROUS SLEEVE**

**A THESIS  
SUBMITTED TO THE GRADUATE FACULTY**  
in partial fulfillment of the requirement for the  
Degree of  
**DOCTOR OF PHILOSOPHY**

**BY  
JIK CHANG LEONG**

Norman, Oklahoma

2002

**UMI Number: 3075333**

**UMI<sup>®</sup>**

---

**UMI Microform 3075333**

**Copyright 2003 by ProQuest Information and Learning Company.**

**All rights reserved. This microform edition is protected against  
unauthorized copying under Title 17, United States Code.**

---

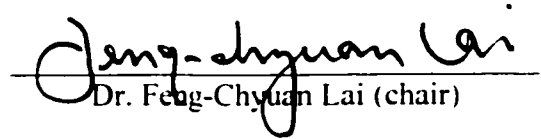
**ProQuest Information and Learning Company  
300 North Zeeb Road  
P.O. Box 1346  
Ann Arbor, MI 48106-1346**


**© Copyright by Jik Chang Leong 2002**  
**All rights reserved**

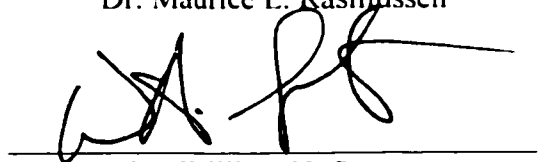
**HEAT TRANSFER AND FLUID FLOW IN  
ROTATING CYLINDERS WITH A POROUS SLEEVE**


**A DISSERTATION APPROVED FOR THE  
SCHOOL OF AEROSPACE AND MECHANICAL ENGINEERING**

BY

  
Dr. Feng-Chyuan Lai (chair)

  
Dr. Maurice L. Rasmussen

  
Dr. William H. Sutton

  
Dr. Luther W. White

  
Dr. Ramkumar Parthasarathy

## **ACKNOWLEDGEMENTS**

The author would like to express his appreciation and gratitude to Professor Feng-Chyuan Lai for being an excellent faculty advisor and the chairman of this dissertation committee. His suggestion of this exciting problem is highly appreciated. During his one-year sabbatical leave at UT Austin and UC Berkeley, contacts between us were difficult. However, his patience and guidance through emails have been very helpful. His understanding and support throughout these difficult years have been a key factor to the completion of this work.

The author also gratefully acknowledged the assistance and support from Professor Maurice L. Rasmussen, a Professor Emeritus of the School of Aerospace and Mechanical Engineering. Being a dedicated educator, Professor Rasmussen always promptly responded through emails to some questions that I encountered in part of the theoretical work in this dissertation, even if he was in vacation somewhere.

The author would also like to thank the members of this dissertation committee, Professor William H. Sutton, Professor Luther W. White and Professor Ramkumar Parthasarathy for their valuable time, tireless efforts and precious suggestions. Also, from their inspiring classes, the author learned a lot.

Financially, the author is indebted to Professor Feng-Chyuan Lai and Dr. Vince Wong (a senior scientist in the Center for Analysis and Prediction of Storms) for graduate research assistantships. In addition to the above faculties, the author must thank the directors of the School of Aerospace and Mechanical Engineering for graduate teaching assistantships. The teaching experience I gained here is always highly cherished.

Also, the research grant from the Graduate College to provide the support for flow-visualization experiment is greatly appreciated. Moreover, the sincere help, constructive suggestions and inspiring discussions from Ms. Shirley Chen and Ms. MeiRong Huang are greatly treasured. When building the experimental setup for flow visualization, the author would like to thank Mr. Billy Mays, Mr. Greg Williams, Mr. Adam Marshall, and Mr. Louis Edward Galleciez for their help in the design, fabrication and improvement of the experimental setup. Also, the discussions with Mr. Carlos Borrás and Mr. Noel Brown are also highly valued.

Lastly, this work is dedicated to the author's parents, Mr. and Mrs. Kwong Ying Leong. Without their love, understanding and support, this work would not have been accomplished. I also bow to Avalokiteshvara Bodhisattva (Kuan-Yin) for Her blessing, providing me inner peace to go through all difficult times, and showing me the great wisdom to solve the problems that I have never thought I would be capable of.



# TABLE OF CONTENTS

ACKNOWLEDGEMENTS .....	iv
TABLE OF CONTENTS .....	vi
LIST OF TABLES .....	ix
LIST OF FIGURES .....	x
NOMENCLATURE .....	xv
ABSTRACT .....	xviii
CHAPTER	
I. INTRODUCTION AND LITERATURE REVIEW	
1.1 Introduction .....	1
1.2 Literature Review .....	4
1.2.1 Development of Fundamental Theories .....	5
1.2.2 Beaver-Joseph Slip Velocity Model .....	12
1.2.3 Brinkman Model .....	14
1.2.4 Stability and Dynamic Characteristics of Porous Journal Bearings .....	15
1.2.5 Extension of Lubrication Theory to Turbulent Regime .....	17
1.2.6 Progress in Experimental Studies .....	18
1.2.7 Other Considerations .....	22
1.3 Scope of Present Study .....	29
II. FLOW AND TEMPERATURE FIELDS IN ROTATING CONCENTRIC AND ECCENTRIC CYLINDERS WITH A POROUS SLEEVE	
2.1 Introductory Remarks .....	33
2.2 Problem Statement .....	34
2.3 Annular Space without a Porous Sleeve .....	34
2.4 Annular Space with a Porous Sleeve .....	38
2.5 Analytical Solutions .....	43
2.5.1 Annular Space without a Porous Sleeve .....	43
2.5.2 Annular Space with a Porous Sleeve .....	43
2.6 Results and Discussion .....	48
2.7 Conclusions .....	75
III. NATURAL CONVECTION IN CONCENTRIC CYLINDERS WITH A POROUS SLEEVE	
3.1 Introductory Remarks .....	80

3.2	Problem Statement .....	81
3.3	Formulation .....	83
3.4	Perturbation Methods .....	85
3.5	Method of Solution .....	88
3.6	Results and Discussion .....	115
3.7	Conclusion .....	136
 IV. MIXED CONVECTION IN ROTATING CONCENTRIC CYLINDERS WITH A POROUS SLEEVE		
4.1	Introductory Remarks .....	138
4.2	Objective of the Present Study .....	139
4.3	Governing Equations .....	139
4.4	Boundary and Interface Conditions .....	143
4.5	Finite Difference Method .....	144
4.5.1	Source Terms .....	147
4.5.2	Diffusive Terms .....	147
4.5.3	Convective Terms .....	148
4.5.4	Finite Difference Equations .....	149
4.5.5	Discretization of Interface Equations .....	153
4.5.6	Convergence Criteria .....	153
4.5.7	Evaluation of Heat Transfer Performance .....	155
4.6	Results and Discussion .....	157
4.7	Conclusions .....	184
 V. FLOW VISUALIZATION USING A HELE-SHAW CELL		
5.1	Introductory Remarks .....	189
5.2	Hele-Shaw Analogy .....	191
5.3	Problem Statement .....	194
5.4	Theory of Hele-Shaw Analogy .....	194
5.5	Experimental Setup .....	197
5.5.1	The Cell Unit .....	200
5.5.2	The Reservoir Unit .....	203
5.5.3	The Rotor Unit .....	203
5.5.4	The Imaging Unit .....	204
5.6	Experimental Procedure .....	204
5.6.1	Model Assembly .....	204
5.6.2	Calibration of Rotational Speed .....	205
5.6.3	Adjustment of Camera Settings .....	207
5.6.4	Flow Visualization .....	207
5.7	Results and Discussion .....	209
5.8	Experimental Discrepancy .....	222
5.9	Conclusions .....	224
 VI. CONCLUSIONS		
6.1	Introductory Remarks .....	227
6.2	Effects of Various Parameters .....	228

6.3	Heat Transfer Performance .....	232
6.4	The Design of Porous Journal Bearings .....	233
6.5	Future Work .....	235
6.5.1	Bipolar Coordinate System .....	236
6.5.2	Governing Equations .....	241
6.5.3	Boundary and Interface Conditions .....	243
6.5.4	Method of Solution .....	243
REFERENCES .....		245
APPENDIX		
A.	DERIVATION OF PERTURBED BOUNDARY CONDITION .....	272
B.	MATHCAD CALCULATION FOR FORCED CONVECTION .....	274
C.	DERIVATION OF INTERFACE CONDITIONS .....	280
D.	FINITE FOURIER COSINE TRANSFORM FROM 0 TO $2\pi$ .....	288
E.	MATHCAD CALCULATION FOR NATURAL CONVECTION .....	290
F.	ADDITIONAL PLOTS OF FLOW AND TEMPERATURE FIELDS FOR MIXED CONVECTION .....	305

## **LIST OF TABLES**

### **Table**

4.1 Numerical parameters used for the comparison effort. ....	158
5.1 List of the components of the experimental apparatus and their specifications. ....	199
5.2 List of mechanical and thermal properties used in the experiment. ....	212
5.3 List of parameters and their corresponding values in experiment. ....	212

## LIST OF FIGURES

### Figure

2.1	An eccentric annulus subject to rotation and differential heating from the inner and outer walls ( $T_H > T_L$ ). .....	35
2.2	Flow fields in an eccentric annulus without a porous sleeve for $Da = 0.01$ , and $k_1/k_2 = 1$ . .....	49
2.3	Temperature fields in an eccentric annulus without a porous sleeve for $Da = 0.01$ , and $k_1/k_2 = 1$ ( $\Delta\theta = 0.2$ ). .....	50
2.4	Flow fields in an eccentric annulus with a porous sleeve for $Br = 1$ , $Da = 0.01$ , and $k_1/k_2 = 1$ . .....	52
2.5	Temperature fields in an eccentric annulus with a porous sleeve for $Br = 1$ , $Da = 0.01$ , and $k_1/k_2 = 1$ ( $\Delta\theta = 0.2$ ). .....	54
2.6	Flow fields of in an eccentric annulus with a porous sleeve for $b = 1.5$ , $\varepsilon = 0.1$ , and $k_1/k_2 = 1$ . .....	55
2.7	Temperature fields in an eccentric annulus with a porous sleeve for $b = 1.5$ , $\varepsilon = 0.1$ , and $k_1/k_2 = 1$ ( $\Delta\theta = 0.2$ ). .....	57
2.8	Flow fields in an eccentric annulus with a porous sleeve for $Br = 1$ , $Da = 0.01$ , and $\varepsilon = 0.1$ . .....	58
2.9	Temperature fields in an eccentric annulus with a porous sleeve for $Br = 1$ , $Da = 0.01$ , and $\varepsilon = 0.1$ ( $\Delta\theta = 0.2$ ). .....	60
2.10	Velocity profiles for various Darcy numbers in an eccentric annulus with a porous sleeve on the gap of $\theta = \pi/2$ ( $b = 1.50$ , $\varepsilon = 0.05$ , $Br = 0.1$ , and $k_1/k_2 = 1$ ). .....	62
2.11	Velocity profiles for various porous sleeve thickness in an eccentric annulus at the cross-section of $\theta = \pi/2$ ( $\varepsilon = 0.05$ , $Da = 0.01$ , $Br = 0.1$ , and $k_1/k_2 = 1$ ). .....	63
2.12	Temperature profiles for various Brinkman numbers in an eccentric annulus at the gap of $\theta = \pi/2$ ( $b = 1.50$ , $\varepsilon = 0.05$ , $Da = 0.01$ , and $k_1/k_2 = 1$ ). .....	65

2.13	Temperature profiles for various porous sleeve thickness in an eccentric annulus at the gap of $\theta = \pi/2$ ( $\varepsilon = 0.05$ , $Da = 0.01$ , $Br = 2.0$ , and $k_1/k_2 = 1$ ). .....	66
2.14	Temperature profiles for various Darcy numbers in an eccentric annulus at the gap of $\theta = \pi/2$ ( $b = 1.5$ , $\varepsilon = 0.05$ , $Br = 2.0$ , and $k_1/k_2 = 1$ ). .....	68
2.15	Temperature profiles for various effective thermal conductivity ratios in an eccentric annulus at the cross section of $\theta = \pi/2$ ( $b = 1.5$ , $\varepsilon = 0.05$ , $Br = 0.1$ , and $Da = 10^{-3}$ ). .....	69
2.16	Temperature profiles for various effective thermal conductivity ratios in an eccentric annulus at the cross-section of $\theta = \pi/2$ ( $b = 1.5$ , $\varepsilon = 0.05$ , $Br = 2.0$ , and $Da = 10^{-3}$ ). .....	71
2.17	Average Nusselt number on the inner cylinder of an eccentric annulus ( $\varepsilon = 0.1$ and $Br = 1$ ): (a) $b = 1.25$ , (b) $b = 1.50$ , (c) $b = 1.75$ . .....	72
2.18	Average Nusselt number on the outer cylinder of an eccentric annulus ( $\varepsilon = 0.1$ and $Br = 1$ ): (a) $b = 1.25$ , (b) $b = 1.50$ , (c) $b = 1.75$ . .....	74
2.19	Velocity profiles in an eccentric annulus with various eccentricity ratios ( $\varepsilon = 0.01$ and $0.05$ ) and at various gaps ( $\theta = 0$ , $\pi/2$ and $\pi$ ) ( $Da = 0.01$ , and $Br = 2$ ). .....	76
2.20	Temperature profiles in an eccentric annulus with various eccentricity ratios ( $\varepsilon = 0.01$ and $0.05$ ) and at various gap ( $\theta = 0$ , $\pi/2$ and $\pi$ ) ( $Da = 0.01$ , and $Br = 2$ ). .....	77
3.1	A concentric annulus with a porous sleeve subject to differential heating from the inner and outer wall ( $T_H > T_L$ ). .....	82
3.2	Flow fields in a concentric annulus with a porous sleeve for $b = 1.50$ , $Da = 10^{-4}$ , and $k_1/k_2 = 1.0$ ( $\Delta\Psi = 5.0 \times 10^{-6}$ ). .....	116
3.3	Temperature fields in a concentric annulus with a porous sleeve for $b = 1.50$ , $Da = 10^{-4}$ , and $k_1/k_2 = 1.0$ ( $\Delta\Theta = 0.2$ ). .....	118
3.4	Flow fields in a concentric annulus with a porous sleeve for $Da = 10^{-4}$ , $k_1/k_2 = 1.0$ , and $Pr = 20,000$ ( $\Delta\Psi = 2.0 \times 10^{-6}$ for $b = 1.25$ , $\Delta\Psi = 2.5 \times 10^{-6}$ for $b = 1.50$ , and $\Delta\Psi = 5.0 \times 10^{-6}$ for $b = 1.75$ ). .....	120
3.5	Temperature fields in a concentric annulus with a porous sleeve for $Da = 10^{-4}$ , $k_1/k_2 = 1.0$ , and $Pr = 20,000$ ( $\Delta\Theta = 0.2$ ). .....	122

3.6	Flow fields in a concentric annulus with a porous sleeve for $b = 1.50$ , $k_1/k_2 = 1.0$ , and $Pr = 20,000$ ( $\Delta\Psi = 5.0 \times 10^{-6}$ for $Da = 10^{-4}$ , and $\Delta\Psi = 2.5 \times 10^{-5}$ otherwise). .....	123
3.7	Temperature fields in a concentric annulus with a porous sleeve for $b = 1.50$ , $k_1/k_2 = 1.0$ , and $Pr = 20,000$ ( $\Delta\Theta = 0.2$ ). .....	125
3.8	Flow fields in a concentric annulus with a porous sleeve for $b = 1.50$ , $Da = 10^{-4}$ , and $Pr = 20,000$ ( $\Delta\Psi = 2.5 \times 10^{-6}$ for $Ra = 0.1$ , and $\Delta\Psi = 5.0 \times 10^{-6}$ otherwise). .....	126
3.9	Temperature fields in a concentric annulus with a porous sleeve for $b = 1.50$ , $Da = 10^{-4}$ , and $Pr = 20,000$ ( $\Delta\Theta = 0.2$ ). .....	127
3.10	Flow fields in a concentric annulus with a porous sleeve for $Da = 10^{-4}$ , $Pr = 20,000$ , and $Ra = 0.1$ ( $\Delta\Psi = 2.0 \times 10^{-6}$ ). .....	129
3.11	Temperature fields in a concentric annulus with a porous sleeve for $Da = 10^{-4}$ , $Pr = 20,000$ , and $Ra = 0.1$ ( $\Delta\Theta = 0.2$ ). .....	131
3.12	Flow fields in a concentric annulus with a porous sleeve for $b = 1.50$ , $Pr = 20,000$ , and $Ra = 0.1$ ( $\Delta\Psi = 2.5 \times 10^{-6}$ for $Da = 10^{-4}$ , and $\Delta\Psi = 5.0 \times 10^{-6}$ otherwise). .....	132
3.13	Temperature fields in a concentric annulus with a porous sleeve for $b = 1.50$ , $Pr = 20,000$ , and $Ra = 0.1$ ( $\Delta\Theta = 0.2$ ). .....	134
3.14	Average Nusselt numbers on the inner and outer cylinders for various values of $b$ and $k_1/k_2$ ( $Da = 10^{-4}$ and $Ra = 0.1$ ). .....	135
4.1	Concentric rotating cylinders with a porous sleeve. ....	140
4.2	Control volume for the node P. ....	145
4.3	Imaginary nodal points for the implementation of interface conditions. ....	154
4.4	Algorithm of the numerical approach. ....	156
4.5	Code validation: a comparison of solutions obtained using analytical (the previous chapter) and numerical approaches ( $\Delta\Psi = 5 \times 10^{-6}$ ). ....	159
4.6	Velocity field in the forms of streamlines and angular velocity profiles at various cross-sections ( $b = 1.5$ , $Da = 10^{-4}$ , $k_1/k_2 = 1$ , $Pr = 2 \times 10^4$ , $Ra = 10^5$ , and $Pe = 10$ ). .....	162

4.7	Angular velocity profiles at various cross-sections ( $b = 1.5$ , $Da = 10^{-4}$ , $k_1/k_2 = 1$ , $Pr = 2 \times 10^4$ , $Ra = 10^5$ , and $Pe = 10$ ). .....	164
4.8	Flow fields in concentric rotating cylinders with a porous sleeve for $b = 1.5$ , $Da = 10^{-4}$ , $k_1/k_2 = 1$ , and $Pr = 20,000$ ( $\Delta\Psi = 0.1$ for $Pe = 1$ and $Ra = 10^4$ , $\Delta\Psi = 1$ for $Pe = 1$ and $Ra = 10^5$ and $10^6$ , $\Delta\Psi = 10$ for $Pe = 10^3$ , and $\Delta\Psi = 2000$ for $Pe = 10^5$ ). .....	166
4.9	Temperature fields in concentric rotating cylinders with a porous sleeve for $b = 1.5$ , $Da = 10^{-4}$ , $k_1/k_2 = 1$ , and $Pr = 20,000$ ( $\Delta\Theta = 0.2$ ). .....	168
4.10	Flow fields in concentric rotating cylinders with a porous sleeve for $Da = 10^{-4}$ , $k_1/k_2 = 1$ , $Pe = 10$ , and $Pr = 20,000$ ( $\Delta\Psi = 0.5$ for $Ra = 10^4$ , $\Delta\Psi = 1$ for $Ra = 10^5$ , and $\Delta\Psi = 2$ for $Ra = 10^6$ ). .....	170
4.11	Temperature fields in concentric rotating cylinders with a porous sleeve for $Da = 10^{-4}$ , $k_1/k_2 = 1$ , $Pe = 10$ , and $Pr = 20,000$ ( $\Delta\Theta = 0.2$ ). .....	172
4.12	Flow fields in concentric rotating cylinders with a porous sleeve for $b = 1.5$ , $k_1/k_2 = 1$ , $Pe = 10$ , and $Pr = 20,000$ ( $\Delta\Psi = 1$ for $Ra = 10^4$ , $\Delta\Psi = 2$ for $Ra = 10^5$ , and $\Delta\Psi = 5$ for $Ra = 10^6$ ). .....	173
4.13	Temperature fields in concentric rotating cylinders with a porous sleeve for $b = 1.5$ , $k_1/k_2 = 1$ , $Pe = 10$ , and $Pr = 20,000$ ( $\Delta\Theta = 0.2$ ). .....	175
4.14	Flow fields in concentric rotating cylinders with a porous sleeve for $b = 1.5$ , $Da = 10^{-4}$ , $Pr = 20,000$ , and $Ra = 10^6$ ( $\Delta\Psi = 10$ for $Pe = 10^3$ , and $\Delta\Psi = 0.5$ otherwise). .....	177
4.15	Temperature fields in concentric rotating cylinders with a porous sleeve for $b = 1.5$ , $Da = 10^{-4}$ , $Pr = 20,000$ , and $Ra = 10^6$ ( $\Delta\Theta = 0.2$ ). .....	178
4.16	The dependence of average Nusselt number on Rayleigh and Peclet numbers for $b = 1.5$ , $Da = 10^{-4}$ , $k_1/k_2 = 1$ , and $Pr = 20,000$ . .....	180
4.17	The dependence of average Nusselt number on Rayleigh number and $b$ for $Da = 10^{-4}$ , $k_1/k_2 = 1$ , $Pe = 10$ , and $Pr = 20,000$ . .....	182
4.18	The dependence of average Nusselt number on Rayleigh and Darcy numbers for $b = 1.5$ , $k_1/k_2 = 1$ , $Pe = 10$ , and $Pr = 20,000$ . .....	183
4.19	The dependence of average Nusselt number on Rayleigh number and thermal conductivity ratio for $b = 1.5$ , $Da = 10^{-4}$ , $Pe = 10$ , and $Pr = 20,000$ . .....	185
5.1	Coordinate system used in the derivation of Hele-Shaw analogy. ....	196



5.2	Cross-section of the modified Hele-Shaw cell constructed for the current experiment. ....	196
5.3	Sketch of the experimental setup for flow visualization. ....	198
5.4	The dimensions of the Hele-Shaw cell and the shaft (in inches) (a) the bottom wall, (b) the bottom spacer, (c) the middle spacer, and (d) the top spacer. ....	201
5.4	continued. (e) the top wall, (f) the shaft, (g) the assembled cell, and (h) the extended cell. ....	202
5.5	Photograph of the modified Hele-Shaw cell. ....	206
5.6	Calibration curve of the rotational speed as a function of the electric current from the power supply. ....	208
5.7	Comparison of isothermal flow fields between (a) experimental observation at the rotational speed of $\varpi = 60 \text{ rpm}$ , and (b) numerical result at $Pe = 2.33 \times 10^5$ and $Ra = 0$ ( $\Delta\Psi = 5 \times 10^4$ ). ....	211
5.8	Comparison of non-isothermal flow fields between (a) experimental observation at the rotational speed of $\varpi = 39 \text{ rpm}$ , and (b) numerical result at $Pe = 10^3$ and $Ra = 10^6$ ( $\Delta\Psi = 20$ ). ....	213
5.9	Flow patterns in the modified Hele-Shaw cell at various shaft rotational speeds (a) $\varpi = 39 \text{ rpm}$ , (b) $\varpi = 100 \text{ rpm}$ , (c) $\varpi = 158 \text{ rpm}$ , and (d) $\varpi = 333 \text{ rpm}$ . ....	215
5.9	continued. ....	216
5.10	Various flow regions observed from the experimental study at high rotational speeds. ....	219
6.1	The coordinate systems for an eccentric porous journal bearing. ....	237
6.2	The computational domain for an eccentric porous journal bearing. ....	238
6.3	Three computational domains in the bipolar coordinate system. ....	240

## NOMENCLATURE

$a$	radius of the inner cylinder, [m]
$b$	inner radius of the porous sleeve, [m]
$c$	radius of the outer cylinder, [m]
$C_p$	heat capacity, [J/kg·K]
$Br$	Brinkman number, $Br = \nu U^2 / \alpha_l C_p (T_H - T_L)$
$Da$	Darcy number, $Da = K/b^2$
$e$	eccentricity, [m]
$g$	gravitational acceleration, [m/s <sup>2</sup> ]
$K$	permeability, [m <sup>2</sup> ]
$k$	effective thermal conductivity of porous medium, [W/m·K]
$Nu$	Nusselt number, $Nu = hL/k$
$\overline{Nu}$	average Nusselt number
$P$	pressure, [Pa]
$Pe$	Peclet number, $Pe = Re Pr$
$Pr$	Prandtl number, $Pr = \nu/\alpha_l$
$q$	variable for coordinate transformation
$R$	normalized radial distance in cylindrical coordinate system, $R = r/b$
$r$	radial distance in cylindrical coordinate system, [m]
$Ra$	Rayleigh number, $Ra = g\beta\Delta T b^3 / \nu\alpha_l$
$Re$	Reynolds number, $Re = Ub/\nu$
$T$	temperature, [K]

$T_H$	temperature on the inner cylinder, [K]
$T_L$	temperature on the outer cylinder, [K]
$U$	velocity on the inner cylinder, [m/s]
$u_r, u_\theta$	velocity components in cylindrical coordinate system, [m/s]
$x, y$	independent variables in Cartesian coordinate system, [m]

### **Greek Symbols**

$\alpha$	effective thermal diffusivity of porous medium, $\alpha = k / (\rho C_p)_f$ , [m <sup>2</sup> /s]
$\beta$	thermal expansion coefficient, $\beta = (-1/\rho)(\partial \rho / \partial T)_p$ , [K <sup>-1</sup> ]
$\Delta T$	temperature difference between the journal and housing, $\Delta T = T_H - T_L$ , [K]
$\phi$	attitude angle, [rad]
$\eta$	the first independent variable in the bipolar coordinate system
$\varphi$	the second independent variable in the bipolar coordinate system
$\mu$	dynamic viscosity of fluid, [kg/m·s]
$\tilde{\mu}$	effective viscosity in Brinkman model, [kg/m·s]
$\mu'$	ratio of effective viscosity to dynamic viscosity, $\mu' = \tilde{\mu} / \mu$
$\nu$	kinematic viscosity of fluid, [m <sup>2</sup> /s]
$\rho$	fluid density, [kg/m <sup>3</sup> ]
$\Theta$	normalized temperature, $\Theta = (T - T_L) / \Delta T$
$\theta$	azimuthal angle in cylindrical coordinate system
$\Omega$	dimensionless vorticity, $\Omega = \omega b^2 / \alpha_l$
$\omega$	vorticity, [s <sup>-1</sup> ]

- $\varpi$  angular velocity of the journal, [s<sup>-1</sup>]
- $\Psi$  normalized stream function.  $\Psi = \psi/\alpha_1$
- $\psi$  stream function, [m<sup>2</sup>/s]

### **Mathematical Symbols**

- $O(\delta)$  order of magnitude  $\delta$
- $\nabla$  gradient operator, [m<sup>-1</sup>]
- $\bar{\nabla}$  normalized gradient operator.  $\bar{\nabla} = h\nabla$
- $\bar{F}$  Finite Fourier Transform

### **Subscripts**

- i index of the layer
- 1 fluid
- 2 porous sleeve

## **ABSTRACT**

This work investigates the flow and temperature distributions in rotating cylinders with a porous sleeve resulting from a combined effect due to shearing and thermal buoyancy. Other secondary effects considered include the eccentricity of the inner cylinder, the permeability of the porous sleeve, its thickness and relative thermal conductivity with respect to the fluid layer. In general, this work consists of four major parts.

In the first part, the flow and temperature fields in rotating concentric or slightly eccentric cylinders with a porous sleeve were obtained using a perturbation method with the eccentricity ratio being the perturbation parameter. The flow and temperature fields were solved up to the second leading terms. Since the eccentricity ratio considered in this part is very small, the flow behaves like a polar Couette flow.

The second part deals with weak natural convection in a stationary concentric annulus with a porous sleeve. The inner cylinder is kept at a higher temperature than the outer cylinder. Once again, this study was performed using a perturbation method with the Rayleigh number being the perturbation parameter. The solutions for the momentum and energy equations were also obtained up to the second leading terms with the help of Fourier Integral Transform.

A finite-difference method was employed in the study of part three to obtain the flow and temperature fields in rotating cylinders with a porous sleeve. This configuration is identical to that in the second part, except that the inner cylinder rotates at a constant speed. The results obtained in this part cover all convection regimes: the forced, the

mixed, and the natural convection. Natural convection results obtained in this part agree very well with those from the part two.

In the last part, an experiment using a modified Hele-Shaw cell was performed to visualize the flow patterns in a concentric rotating cylinder with a porous sleeve. A custom-made stainless steel shaft was inserted through the Hele-Shaw cell that was filled with 50 cP silicone oil with suspended tracers. At a low rotational speed and nearly isothermal condition, the flow pattern observed closely resembled those of the numerical results presented in the part three.

Based on these studies, it is concluded that the buoyancy effect promotes convection, but shear effect enhances shear flow and demotes convective flow. The flow strength decreases with the porous sleeve thickness. Consequently, viscous dissipation becomes more important and generates more heat. The permeability of the porous sleeve has the opposite effect of the sleeve thickness. The effect of thermal-conductivity ratio depends on the Rayleigh number. As the annulus becomes eccentric, large velocity and temperature gradients will occur at the narrowest clearance. The overall heat-transfer performance of an annulus with a porous sleeve mainly depends on the Rayleigh and Peclet numbers. The rotation of the inner cylinder delays the onset of natural convection.

Based on this investigation, the operation and performance of a sintered journal bearing is better understood. The presence of a porous sleeve in a journal bearing causes a greater velocity gradient on the shaft and thus consumes more power than a conventional journal bearing. For a bearing that is very poorly conductive, the lubricant will be greatly heated up by friction.

# **CHAPTER ONE**

## **INTRODUCTION AND LITERATURE REVIEW**

### **1.1 Introduction**

“Tribology” is a subject related to the study of friction, wear, and lubrication. Its main concern is, by means of lubrication, to reduce wear of moving mechanical parts due to friction. In the history of mankind, tribology has taken part in many important historical events and scientific discoveries. Perhaps, one of the most famous tribological applications recorded is related to the building of the pyramids. During the construction of the pyramids, heavy stone blocks were placed on top of timbers and were transported by rolling the timbers. A contemporary application is the bearing in a hard disk drive assembly. In the assembly, a high-performance bearing can be found between the rotor and the pack of recording media. To capture a larger share of the market, hard disk drive manufacturers have spent a large amount of money and effort to make their products more competitive. One desirable feature is a reduced access time of the hard disk drive. To achieve this goal, manufacturers have increased the disk drive rotational speed. This eventually leads to a smaller design tolerance and higher lubrication performance for bearings.

In the past century, solid bearings were invented. However, it was later discovered that it was not the ultimate solution for all engineering applications because the lubricant oil might be lost after long hours of operation due to bearing side leakage, oxidation, and evaporation. As a result, solid journal bearings are always connected to an

external oil reservoir. During operation, oil is continuously fed into the bearing from the reservoir to prevent oil starvation. Otherwise, oil starvation will cause severe surface wear of machinery parts and thermal seizure. This drawback has made solid bearings less favorable in some applications because an external oil supply is simply impermissible owing to cost and other operational constraints. As a result, extensive research and development efforts have been made to seek alternatives that could either improve or replace the solid bearings.

In the early last century, with the advancement of powder metallurgy, sintered materials were introduced in the fabrication of journal bearings. Since then, bearings made of sintered materials have found progressively wider applications in industry. The porous structure of sintered materials allows the lubricant oil to be stored in the bearing, thus eliminating the need for an external oil reservoir. For this main reason, these relatively inexpensive sintered (porous) bearings have become so increasingly popular that they have left behind the conventional solid bearings in the race of engineering applications.

The sintered bearings operate under hydrodynamic lubrication conditions in the initial stages of their lives when the pores are saturated with lubricating oil. This is because the oil stored in the pores of the bearing matrix is readily available for hydrodynamic support of the journal carrying an external load. Only after frequent start-stop operations or significant oil loss following a long period of operation, they would operate under mixed or boundary lubrication conditions.

The alternative path of the oil flow provided by the pores in the sintered material considerably reduces cavitation, which is detrimental for oil and bearing life. Because of



the capillary action of the pores, oil is kept in the bearing. As a consequence, replenishment of oil is not necessary in short intervals. This mechanism makes these sintered bearings require less maintenance. Also, there is less danger of oil dripping (as in the case of solid bearings) which could be a source of contamination in the textile and food processing industries.

In hydrostatic (externally pressurized) solid bearings, the hydrodynamic pressure is not immediately developed within the recess after the lubricant oil is admitted into the bearing clearance, resulting in an uneven pressure distribution in the oil film. By means of porous materials, the oil can flow through the pores, yielding a more even pressure distribution along the journal surface. In terms of performance, the pores spread the supply pressure over the clearance space more effectively and allow a higher load capacity as compared with solid bearings with the same oil flow rate. Owing to the presence of a permeable surface adjacent to the clearance space, these bearings exhibit better damping characteristics than solid bearings. Zhang et al. (1992) found that sintered journal bearings are excellent dampers. Not only are these theories about porous bearings useful in engineering fields, but also provide insights for research in biomechanics (Linn, 1969; Tandon et al., 1983).

Despite the advantages discussed above, a sintered bearing does have its limitations. Its permeability decreases with its service life. Low-viscosity fluids can flow easily through the porous bush, but the impurities in the lubricant must be avoided or at least maintained to a minimum level. This is because the pores of a sintered bush may become clogged by impurities present in the lubricant. If the lubrication of a porous bearing is poor, the journal will eventually be in contact with the sintered bush and will

cause more pore obstructions by local deformation. Nevertheless, the clogged or deformed porous bushes can be easily replaced at regular intervals for better performance.

Since a complete description of lubrication theory and operational mechanisms of bearings can be readily found (Fuller, 1984; Williams, 1994; Szeri, 1998; Burton, 2000; Khonsari and Booser, 2001), it will not be attempted here to discuss them in detail. Instead, the following literature review will focus mainly on oil-lubricated porous journal bearings. Other bearings and lubrication effects, such as porous thrust bearings, porous slider bearings, and porous squeeze film effect, are not discussed here for brevity. In addition, porous gas bearings are excluded from the presentation because air as a lubricant behaves differently from oils and thus its solution involves a different form of Reynolds equation.

## **1.2 Literature Review**

Unlike solid bearings, extensive reviews about sintered bearings are not readily available in the literature. Only Morgan (1966) has presented a rather complete discussion about the fundamentals of sintered metal bearings. Although his work has underlain most of the basic theories and important issues about sintered bearings, the materials he presented may seem somewhat obsolete from today's technology point of view. Several years later, Kumar (1980a) reviewed the development of porous metal bearings. He commended on the types of hydrodynamic operation and discussed some potential research areas for further studies. Again, his review can no longer provide the

most up-to-date information on the development of porous bearings since a lot of research work has been carried out for the past twenty years.

The literature reviews in the following sections are intended to supplement Kumar's earlier review (1980a) and update the development of lubrication theory of porous journal bearings for the past two decades. Sections 1.2.1 to 1.2.3 present the evaluation of the lubrication theory from the early Reynolds equation for solid bearings to its latest form with the inclusion of Brinkman model. In sections 1.2.4 and 1.2.5, work related to the topics of stability, dynamics, and turbulence is surveyed. In the section that follows, section 1.2.6 provides an overview of all experimental studies reported in the literature, and finally the last section 1.2.7, summarizes other research activities that apply the lubrication theory to sintered journal bearings.

### **1.2.1 Development of Fundamental Theories**

Based on the continuity and Navier-Stokes equations, Reynolds (1886) derived an equation for pressure distribution in an infinite solid journal bearing. Later, this equation was named Reynolds equation. In addition to this equation, Reynolds also put forward a set of boundary conditions that became the first phase of what was later referred to as the Reynolds conditions. This theoretical model was named the lubrication theory.

Although Reynolds had developed the lubrication theory that predicts the pressure distribution within a solid journal bearing, the basic mathematical model of a full journal bearing was not known until Sommerfeld (1904) successfully obtained a complete solution of the Reynolds equation.

Despite the fact that Reynolds put forward the premature Reynolds conditions, he did not attempt to apply them. Later, it was Gumbel who made a few modifications to the Reynolds conditions and finalized their forms. These conditions stated that  $p = 0$  at  $\theta = 0$  and  $\theta = \pi + \alpha$ , and  $\partial p / \partial \theta = 0$  between  $\theta = \pi + \alpha$  and  $\theta = 2\pi$ .

More than two decades later, Cameron and Wood (1949) discussed the solution of full journal bearings. They examined the validity of Reynolds conditions so as to improve other boundary conditions, such as the Sommerfeld's full and half conditions. The Sommerfeld's full condition states that  $\partial p / \partial \theta = 0$  at  $\theta = \pi + \alpha$  while the Sommerfeld's half conditions require that  $p = 0$  at  $\theta = 0$  and from  $\theta = \pi$  to  $2\pi$ . When compared with the results obtained using the Sommerfeld's conditions, the results associated with the Reynolds conditions were found in better agreement with the experimental data.

While many studies were performed to further understand the behavior of solid bearings, the technology in powder metallurgy had advanced tremendously. This had led to the invention of sintered metal bearings which were possible to meet the industrial needs. Within a short time, sintered metal bearings became more favorable in most engineering applications than the solid bearings.

The sintered metal bearing is one of the most widely used self-lubricated bearings. Generally, sintered bearings are made of bronze (Geotzel, 1950). Beside the bronze bearings, Storchheim and Witt (1962) claimed that, depending on the working environment and engineering requirements, sintered aluminum bearings were competitive with other bearings in terms of cost, corrosion resistance, operating temperature and operation life. Other not-so-common self-lubricated bearings include those made of

graphite, low-friction plastic and impregnated wood. Not only did engineers change the make of bearings, they also used solid lubricants to achieve their goals (Carson, 1964). For brevity, only oil-lubricated sintered bearings are discussed in this work.

Morgan and Cameron (1957) were the first to develop the theory for the operation of porous bearings. By assuming a certain form of pressure gradient in the porous bearing, they derived the theory using the Darcy model and a modified Reynolds equation under the Ocvirk narrow bearing approximation (DuBois et al., 1951; DuBois and Ocvirk, 1952, 1953; Ocvirk, 1952). They obtained the load capacity by assuming that the eccentricity ratio and attitude angle of porous journal bearings were the same as those of solid journal bearings. Not only did they address almost every important issue about a porous journal bearing, but also they described the differences between porous and solid journal bearings. In addition, they also explained the mechanism of lubrication in porous metal bearings.

In the same year, Morgan (1957) established a theoretical basis for the design of porous bearings. He grouped his design criteria into three main categories. The first category was associated with the factors related to the oil flow in the porous matrix and the choice of the bearing dimensions and material. The second and third were the considerations of the behavior of porous metals (elastic or plastic) and the selection of lubricating oil. Based on his study, he reported several factors that had significant effects on the performance of porous bearings.

Rouleau (1962) extended the study by Morgan and Cameron (1957) for completeness. He calculated the load component acting along the line of centers and determined the total load of narrow porous bearings ( $H/b \leq 0.1$ ). The relative load-

carrying capacity recalculated was larger than that determined by Morgan and Cameron (1957). Furthermore, he recalculated the coefficient of friction based on the total load, the actual eccentricity ratio and the attitude angle. Since the solution of this study was not entirely satisfactory, he reformulated the boundary conditions and examined the performance of thicker porous bearings ( $H/b = 0.2$  and  $0.4$  (Rouleau, 1963)). His solution satisfied the practical condition of zero pressure at the ends of the bearings. In addition to the design parameter that Morgan and Cameron (1957) previously introduced, he introduced another important parameter, the ratio of porous wall thickness to the bearing length ( $H/b$ ).

Morgan (1963, 1964) discussed the importance of the porosity of a hydrodynamic sintered journal bearing in the oil-film pressure development and the practical design of thin-walled narrow porous bearings through the measurement of the permeability and design curves. He demonstrated how changes in the running clearance and shaft diameter could influence the overall performance of a porous journal bearing.

Under the guidance of Joseph, Shir (1965) successfully performed a theoretical study of infinitely long porous journal bearings. In his study, Shir (1965) made use of the method of successive approximation and the method of truncation to obtain the pressure distributions in the bearings. Based on the known pressure distribution, more important information regarding the force and torque was obtained.

Joseph and Tao (1966) studied a flow induced by the rotation of an infinite cylinder in an eccentric cylindrical hole in a fluid-saturated porous medium. They formulated the problem by introducing the Lagrange's stream function in complex variable. Their formulation was a limiting case for lubrication in an infinitely thick

porous journal bearing. They showed that transverse gradients in the lubricant film were negligible and hence justified the use of Reynolds equation. In the same year, Shir and Joseph (1966) presented another limiting case, an infinite full porous bearing. They modified the Reynolds equation to accommodate the mass transfer between the fluid-saturated porous bearing and lubricant film.

Sneck (1967) proposed an analogy to predict the performance of a finite porous bearing (for  $Hh \leq 0.2$  and  $\varepsilon \leq 0.6$ ). It allowed one to predict the performance of a finite porous bearing over a wide range of operating conditions without additional analysis if the performance characteristics of a comparable solid bearing were known. Unfortunately, his analogy was only applicable for  $Hh \leq 0.2$  and  $\varepsilon \leq 0.6$ .

Morgan (1969a) discussed several most practical issues of porous journal bearings related to application, installation, performance characteristics and maintenance. In another paper (1969b), he provided a step-by-step guideline in the design of a sintered metal bearing to meet engineering requirements. He pointed out that the running temperature of a bearing was the most critical factor in the design because it governed the useful life of the lubricant oil and eventually the useful life of the bearing itself.

It was agreed among all participating scientists and researchers in a symposium, that the theory developed for porous bearings was accurate enough to predict the limit of hydrodynamic lubrication provided that sufficient oil was present (Morgan, 1970). This had led to a conclusion that the use of Sommerfeld parameter alone was unable to characterize porous bearings. This Sommerfeld number  $S$  is defined as

$$S = \frac{\mu N_s}{P_l} \left( \frac{R}{C} \right)^2. \quad (1.1)$$

where  $C$  is the radial clearance,  $R$  is the radial distance,  $\mu$  is the fluid viscosity,  $N_s$  is the shaft speed in *rev/s*, and  $P_L$  is the projected load (Khonsari and Booser, 2001). Also, it was agreed in the symposium that the porosity of a flooded porous bearing could be dealt with on the macro-scale. But it had to be considered on a micro-scale if the oil was reduced.

Cusano (1970) had performed a rather complete study of porous journal bearings. In his analytical work, he obtained solutions for infinite, short, and finite porous journal bearings. Two of the special cases he considered were a short porous journal bearing whose permeability varied with length, and an infinite porous journal bearing in which pore closure took place.

The fact that the model based on Ocvirk short bearing assumptions could produce unrealistic results motivated Capone (1970) to develop a new model for infinite porous journal bearings. The configuration that he considered was similar to that studied by Shir and Joseph (1966). Dealing with cylindrical coordinates, he presented an analytical solution for the pressure distribution in an infinite porous bearing using the Sommerfeld boundary conditions. Later, Prakash and Vij (1972) solved the same set of equations but subject to the Reynolds conditions. They noticed a significant difference between their solution and Capone's numerical solution.

Murti (1971a, 1973a and 1973b) repeated Rouleau's study of narrow porous bearings (1963) using the cylindrical coordinates. The pressure distribution from his study was lower than that reported by Rouleau (1963), which was based on the Cartesian coordinates. In addition, Murti also made use of the cylindrical coordinates to study the hydrodynamic lubrication of long, short and finite porous bearings using series solution



and the Galerkin method (1971b, 1972a, 1972b, and 1973c). It is noteworthy that he attempted the first three-dimensional model for hydrodynamic lubrication of short porous bearings (1972a) but was only successful in modeling the three-dimensional flow of lubricant in the porous matrix.

Before 1970, no researcher had taken into consideration the cavitation of lubricant film in porous journal bearings. Rouleau and Steiner (Steiner, 1970; Rouleau and Steiner, 1974) were the first to compare the results obtained from the Sommerfeld and Reynolds boundary conditions. Physically, Sommerfeld conditions produce a negative pressure field in the bearing. On the other hand, Reynolds condition forces the negative pressure field to be zero. Almost at the same time, Prakesh and Vij (1972) also took into account the cavitation in their study.

At the same year, Cusano (1972a) analyzed the performance of a finite porous journal bearing subject to Sommerfeld's half conditions. Physically, these conditions are less accurate than the Reynolds condition, but they are much easier to implement analytically and numerically. By using these conditions, some portion of the pressure distribution would become negative. Experience has indicated that the region with negative pressure is usually associated with oil film rupture and cavitation. Although this might not be perfectly correct, it surely provided an approximate solution.

Reason and Dyer (1973) presented a numerical solution for a hydrodynamic porous journal bearing using the Cartesian coordinate system. They compared their computational result with the published approximate solutions (Morgan and Cameron, 1957; Rouleau, 1963; Shir and Joseph, 1966) and found a great discrepancy among them because these approximate solutions suffered from the assumptions imposed.

In an extension to the work of Shir and Joseph (1966), Kumar (1983) presented an exact mathematical analysis on an infinite partial porous journal bearing. His mathematical model was quite general because it covered partial and full journal bearings. In his model, these bearings could be either porous or solid.

In the physical sense, the configuration of ball bearings and their retainers is very similar to that of journal bearings, except that the axis of rotation is now absent. Most calculations in journal bearings were performed using the Cartesian coordinate system. This is widely accepted because of the negligible curvature effects. Without any justification, Gohart and So (1981) performed a rather skeptical study on the ball bearing porous retainers using the Cartesian coordinate system.

### **1.2.2 Beavers-Joseph Slip Velocity Model**

The previous model of porous journal bearings is obviously not physically plausible because the governing equations for the fluid region and the porous matrix are of different orders. A discontinuity in the tangential velocity component at the interface is thus embedded in the model.

While Joseph and Tao (1966) argued the necessity to impose an additional requirement on the tangential velocity component at the interface, Rouleau (1967) reported the existence of a small shear-induced boundary layer in the permeable material based on his experiment. The thickness of this layer increased with the shear stress on the porous interface. Subsequently, Beavers and Joseph (1967) proposed a tangential velocity slip at the interface between a porous matrix and a fluid layer. They assumed

that this slip-velocity is proportional to the shear rate at the interface. Beavers et al. (1970 and 1974) later experimentally confirmed this condition.

Goldstein and Braun (1971) applied the slip-velocity condition to porous bearings and attempted to verify the importance of slip-velocity on the bearing performance of small, high-speed, low-load porous bearings. Unfortunately, their attempt was based on an incorrect implementation of the Beavers-Joseph slip velocity model. Similarly, Murti performed a series of analyses for short porous journal bearings using the Cartesian coordinate system (1972c, 1973d and 1973e) and the cylindrical coordinate system (1975). His results clearly showed that slip-condition was detrimental to the load carrying capacity of the bearings. At the mean time, Prakash and Vij (1974) performed a similar study of short porous journal bearings using the Cartesian coordinate system. Later, they extended this study for infinite porous journal bearings using the cylindrical coordinate system (1976). Being inspired by the work of Prakash and Vij, Srinivasan (1977) extended Prakash and Vij's study by including the cavitation effect. Malik et al. (1981a) continued this line of study and analytically examined the static and dynamic characteristics of centrally loaded partial porous bearings.

In response to Murti's paper (1975), Rouleau (1975) questioned the applicability of Beavers-Joseph model in porous bearings because this model had not been verified for multidimensional applications. Also, he believed that a slip velocity model was unnecessary. In reply, Murti (1976) reasoned the validity of the Beavers-Joseph model and pointed out the fact that the slip-velocity derived from the Darcy law was a special case of the Beavers-Joseph model.

Before the computer became a powerful research tool, most studies in the lubrication of bearings were accomplished through the use of a product solution. On that account, Rohde (1973) outlined the steps to obtain the pointwise bounds for the solution of Reynolds equation for certain smooth film profiles. With the help of computers, Reason and Siew (1985) improved the previous results reported by Reason and Dyer (1973) by taking into account the curvature of the bearing wall, the velocity-slip condition and Reynolds boundary conditions.

The lubrication model of porous journal bearings developed thus far was also extended to study the hydrostatic bearings. Chattopadhyay and Majumdar (1984a) investigated the steady state characteristics of hydrostatic porous journal bearings with the slip-velocity condition.

### **1.2.3 Brinkman Model**

As Neale and Nader (1974) pointed out that Darcy's law is valid everywhere except in the immediate vicinity of the permeable surface, Lin and Hwang (1993, 1994a, and 1996) thus replaced the use of Darcy's law and Beaver-Joseph slip velocity with the Brinkman-extended Darcy model (Brinkman, 1947a and 1947b) to investigate the boundary-layer effects within the porous sleeve. They obtained analytical solutions for the hydrodynamic lubrication of short, finite and flexible long porous journal bearings.

In addition, they theoretically predicted the effects of viscous shears on the static and dynamic characteristics of long and short porous journal bearings (1994b and 1995). They presented their linear stability analysis and showed that the stability limits of the system were not negligible. This finding eventually motivated their subsequent linear

stability analysis of short and finite porous journal bearings (1994c and 1994d). Later, this was further extended to the dynamic behavior of pure squeeze film in short porous journal bearings (Lin, 1995).

#### **1.2.4 Stability and Dynamic Characteristics of Porous Journal Bearings**

Capone and D'Angostino (1974) were among the first to study the unsteady conditions of journal bearings. They extended their previous study on solid bearings to porous bearings. Their goal was to correlate the whirl amplitude and frequency to operating parameters such as angular velocity, oil viscosity, and bearing dimensions.

Another pioneering work was conducted by Conry and Cusano. They first investigated the stability characteristics (Conry and Cusano, 1974) and then the transmissibility characteristics of porous journal bearings (Cusano and Conry, 1978) using short bearing approximation. Although slip-velocity condition had been reported, their studies did not take this condition into consideration. They concluded that, under the short bearing approximation, porous journal bearings were less stable than solid journal bearings.

Similarly, Singh and Sinhasan (1974) examined the dynamic behavior of porous journal bearings. Instead of solving the modified Reynolds equation, they solved the equation of motion to investigate the stability and relative stability of misaligned porous journal bearing systems.

Kumar (1976) revised the modified Reynolds equation for stability analysis by taking into account the slip-velocity condition, film curvature and unsteady motion of the

journal. He obtained analytical solutions for the elastic and damping properties of partial porous journal bearings subject to synchronous whirl (i.e., dynamic loading).

Similar to their elaborate work on externally pressurized gas bearings, Majumdar and Rao (1979) analytically investigated the performance of externally pressurized porous oil journal bearings for small eccentricity ratio.

Sinhasan and co-workers studied the static and dynamic performance characteristics of two-lobe (Sinhasan et al., 1980) and three-lobe (Malik et al., 1981b) porous hydrodynamic journal bearings. Later, they used the same approach to study the velocity-slip effects on the static and dynamic performance characteristics of an infinitely long porous journal bearing (Chandra et al., 1981), but they ignored the rotational effect of the journal center.

Chattopadhyay and Majumdar (1984b) theoretically investigated the dynamic characteristics of finite porous journal bearings. They obtained a solution for the modified transient Reynolds equation which included the effect of velocity slip using perturbation technique. Later, they analyzed the threshold of oil whirl for a rigid rotor in self-acting finite porous journal bearings with and without externally pressurized oil (1986, 1987). They considered vibrations in both translational and azimuthal directions. In addition, they set up a modified Reynolds equation that took into account the anisotropy of the porous matrix and unsteady motion of the journal. Guha (1986) carried out a similar analysis, but focused on hydrostatic porous journal bearings.

Zhang et al. (1992) made use of porous journal bearings as vibration dampers. These bearings were referred to as porous squeeze film damper (PSFD). They reported

that the presence of the porous matrix remarkably improved the squeeze film damping properties.

### **1.2.5 Extension of Lubrication Theory to Turbulent Regime**

Kumar studied the effects of turbulence and slip-velocity in a narrow porous bearing using the perturbation approach (1978) and infinite Fourier series (1980b). He then extended his study using perturbation approach to infinite and finite porous journal bearings (1981a and 1981b). He also attempted to derive a three-dimensional lubrication equation for the hydrodynamic pressure generated in a porous bearing operating in the fully developed turbulent regime (1979). He later included in his study the bearing arc span and arbitrary attitude angle (1987).

Kumar and Rao (1992, 1993) investigated the performance of hybrid (combined hydrostatic and hydrodynamic) journal bearings and hydrodynamic journal bearings in response to various factors such as turbulence, slenderness ratio, and isotropy of permeability. Later, Kumar and Kumar (1996) numerically investigated a hydrodynamic porous journal bearing with non-homogeneous permeability operating in the turbulent regime. The Reynolds number they considered was as high as 13,300.

Kumar and Rao (1994) theoretically examined the stability of a rigid rotor in turbulent hybrid porous journal bearings following Constantinescu's turbulent lubrication theory. As expected, their analysis showed that turbulence deteriorated the rotor stability. As a result, the bearing feeding parameter should always be kept as small as possible to maintain the stability of the rotor. In a recent publication, Kumar (1998) theoretically

investigated the stability of hybrid porous journal bearings in turbulent flow due to conical whirl.

### **1.2.6 Progress in Experimental Studies**

While the development of lubrication theory for porous bearings was carried out extensively, further understanding and verification of theories were sought through experimental means. Unlike the theoretical approach, the experimental observations reported in the literature were often inconsistent and sometimes even contradicted with each other. On top of the human factors that are involved in experiments, the nature of sintered bearings further complicates the study. This is because identical sintered bearings are impossible to be manufactured in the metallurgical process.

In conjunction with their proposed lubrication theory for porous journal bearings (1957), Cameron et al. (1962) supplemented their theory with experimental results. Their experimental findings compared favorably with analytical results after correcting the end leakage by applying a correction factor (same as that for a solid bearing) to account for the variation of  $L/D$  of a porous journal bearing. Although the approach seemed brilliant at first, but later in a response to McHugh's inquiry, Morgan (1965) admitted that the use of this factor might be invalid.

Moreover, Morgan (1964) presented his experimental proof of pore closure at the surface of porous metal bearings as a consequence of under design or an insufficient oil supply. He experimentally justified that hydrodynamic lubrication was impossible for porous journal bearings when the Sommerfeld number was below a critical value.



Experiments for various  $PV$  values (whose common unit is  $psi\ ft/min$ ) have been conducted. The value of  $P$  is given by the total load  $C$  divided by the product of the journal diameter  $D$  and the bearing length  $L$ , and the value of  $V$  equals to the product of the revolutions per minute  $N$  and  $\pi D$ . For a porous bearing whose service life is at least 10,000 hours,  $PV$  values of 20,000 to 25,000 are considered conservative. However, a higher  $PV$  value is possible with good cooling mechanism or shorter operating life (Carson, 1964).

Youssef and Eudier (1966) found that rapid bearing failure took place at a  $PV$  value of 15,000 because of a progressive elevation of the oil temperature beyond 95 - 100 °C or a sudden rupture of the oil film when the oil became too fluid or when there was too much oil loss. However, reducing the oil viscosity could provide a remedy for the overheating problem. On the other hand, Mitani and Yokota (1973) reported that the temperature increment could be as high as 40 °C for a bearing with a  $PV$  value of 2,500  $kg/cm^2\cdot m/s$ . Observations by Cusano and Phelan (1973) showed that a  $PV$  value of 50,000 was too high for hydrodynamic porous journal bearings, but a value of 33,000 worked fine.

Although Cusano spent a great effort on analytical study, he (1970) also performed some experimental studies using a testing machine he designed and built for porous bearings (1967). Based on his observations, he concluded that a  $PV$  value of 50,000 was too high for the bearing to operate unless periodic lubrication was provided. Almost all experimental runs reported in his study operated under hydrodynamic lubrication conditions. His temperature measurements indicated that the  $PV$  value was a good indicator of temperature rise of the bearing under boundary lubrication mode.

Yung and Cameron (1979) used optical interferometry to visualize the lubrication of porous bearings. They also went through an order of magnitude analysis. Surprisingly, all their evidences were against the existence of a continuous oil film in the bearing. Hence, it was claimed that the original postulate of Morgan and Cameron (1957) could not be satisfied under normal operation.

Braun's investigation (1982) exclusively concerned porous journal bearings of diameters between 2.5 and 5 *mm* and with relatively less viscous oil. He observed that, after a short time of operation, the porous matrix was partially filled by air. This caused the hydrodynamic lubrication to break down. The oil loss, which was dependent on the type of oil, shaft roughness and temperature gradient, was caused by creep and evaporation.

Mokhtar et al. (1984) and Shawki et al. (1984) performed an analytical and experimental study for the performance of both full and partial porous journal bearings operating under steady load conditions. The experiments conducted on partial bearings were to study the oil film behavior in the negative pressure region. Although they did not include the slip-velocity condition in their formulation, they claimed that their test results showed quite good agreement with the theoretical predictions.

Since the data reported by Yung and Cameron (1979) and Braun (1982) were insufficient to predict the extent of oil film formation in the circumferential direction, Kaneko and Obara (1990) attempted to visualize the mechanism of lubrication in porous journal bearings impregnated with fluorescent-dyed oil. They confirmed the existence of oil circulation through the porous matrix. Due to the nature of the oil rupture observed, the half-film condition (i.e., the Sommerfeld half condition) was not applicable to the

theoretical analysis for hydrodynamic lubrication unless the bearing oil was supplied continuously (Kaneko et al., 1994a and 1994b). They also studied the effect of oil-feed pressure on the static characteristics of porous bearing both theoretically and experimentally.

Kaneko and Hashimoto (1995) experimentally investigated the frictional characteristics of porous bronze bearings under hydrodynamic and mixed lubrication conditions. They proposed a frictional model assuming that both the load supported by the fluid and the friction coefficient were determined by the oil film extent. This model yielded frictional coefficients that agreed reasonably well with their experimental results.

Slightly different in the configuration of porous journal bearings are the ball bearings retainers. Bertrand et al. (1995) studied the oil exchange between solid ball bearings and their porous Cotton-Phenolic retainers. Later, they extended their study to porous polyimide bearing retainers (Bertrand and Carre, 1997).

Yankovich and Stevanovich (1996a, 1996b) performed experimental and theoretical study to investigate the coefficients of sliding friction and structural parameter for porous tin-bronze bearings. They presented a rather complete documentation about their experiment.

Kaneko et al. (1997) theoretically and experimentally investigated the pressure distribution in the oil film of a porous journal bearing under hydrodynamic lubrication conditions. Their results from both approaches confirmed the existence of a negative film pressure at the trailing edge of the oil-film region.

Raman and Chennabasavan (1998) performed the first experimental investigation of porous journal bearings under dynamic loads. In their experiment, a porous journal

bearing was subject to vertical sinusoidally fluctuating loads. The frictional force was measured under various fluctuating load/steady load ratios, journal frequencies and load frequencies. It was found that the mean coefficient of friction was proportional to the fluctuating load/steady load ratio, the journal rotational speed and the Sommerfeld number. However, this mean coefficient was independent of the load frequency.

### **1.2.7 Other Considerations**

Based on his observation in the laboratory, Heuberger (1961) discussed the effects of oil flow within the porous sleeve of sintered bearings. Later, Carson (1964) provided a very complete review of self-lubricated bearings. In addition, another review by Pratt (1969) discussed the production, properties, and performance of five classes of sintered bearings. Most importantly, he pointed out that low shaft speeds, oscillating conditions, and frequent start-stop operations do not favor the formation of a hydrodynamic film in porous bearings.

Throughout the years, various research topics, although not directly related to the development of lubrication theory for porous bearings, have been attempted. These topics have covered a broad aspect of porous journal bearings, from the basic design of the bearings to the performance of lubricating oils.

Rhodes and Rouleau (1965, 1966) analyzed the effect of seal ends of full and partial porous bearings of  $120^\circ$ ,  $150^\circ$ , and  $180^\circ$ . Later, Rouleau and Steiner studied the effect of cavitation by employing both Sommerfeld and Reynolds boundary conditions (Steiner, 1970; Rouleau and Steiner, 1974). The materials of seal had been conventionally solid metals. Kaneko foresaw the possibility of replacing these solid

metals with sintered material. Brilliantly, he carried out a numerical investigation to verify his idea (1989a). However, this idea was not further pursued until a recent study by Kaneko et al. (1999) on static characteristics of sealed-end sintered journal bearings at the start of operation.

Conventional sintered bearings sometimes suffered from some undesirable operating conditions. In operation, they might become dry in certain region. When air was admitted, it produced an air/oil emulsion. A similar situation was also reported by Heuberger (1961). To overcome this problem, Eudier and Margerand (1969) introduced an internal layer of very fine powder onto the surface of a conventional porous bearing. By doing so, it not only allowed a higher  $PI'$  value of 1,000,000, but also it could operate at a higher load capacity (10 – 20 times of the conventional ones), lower temperatures and lower frictional factors. In support of the above idea, Cusano's analytical results (1972b and 1972c) of short and infinitely long two-layer porous bearings agreed qualitatively well with the findings by Eudier and Margerand (1969). Along the same line, Verma (1983) carried out an analytical study of double-layer porous journal bearings using the short bearing approximation. Although multiple-layer porous bearings were found to be beneficial, most studies were still centered on single-layer porous bearings.

Manufacturers of sintered bearings fabricate bearings of different thickness and length, so that, these bearings can be selected to meet the specific requirements of an application. For this reason, Perumal and Raman (1985) conducted experiments on bronze sintered bearings to further understand the design freedom. They found that the coefficient of friction increased with the bearing wall thickness but decreased with the

bearing length. Almost at the same time, Quan et al. (1985) found that sintered bronze bearings could work under hydrodynamic lubrication conditions even under high speed and light load. Their results indicated that it was very important to select suitable oil for lubrication.

Chattopadhyay (1995) presented a theoretical study to examine the effect of porous sleeve thickness on the bearing performance. Taking into account the overall bearing performance and practical manufacturing process, he suggested an optimum value of 0.2 for the ratio of porous sleeve thickness to the journal radius.

Gururajan and Prakash (1999) applied Christensen's stochastic theory of hydrodynamic lubrication of rough surface to study the effect of surface roughness in infinitely long porous journal bearings under steady load condition. They concluded that its effect was considerably significant.

Another interesting topic was about nonisotropic porous bearings. Cusano (1973) was the first to obtain an analytical solution for the performance of a short porous bearing whose permeability varied in both radial and axial directions. He compared these results to those for an isotropic bearing having the same axial permeability. Later, Kulkarni and Kumar (1975) included the Beavers-Joseph slip velocity condition and obtained a set of equations for non-isotropic porous bearings.

Capone et al. (1980) performed the first experimental study on nonisotropic porous bearings. The permeability of journal bearings they studied consisted of high and low regions. It was found that these bearings had a better performance than the corresponding isotropic ones.

From their experimental observation of a new type of porous metal bearing whose local permeability varied along its circumference. Quan and Wang (1985) found that these porous journal bearings could work under a lower coefficient of friction and a higher load capacity than the ordinary porous journal bearings. Their analytical solution, including the effects of non-uniform permeability, bearing curvature, cavitation and velocity slip, supported their experimental observation. Unfortunately, their work was not conclusive enough because the pattern of permeability was too restrictive.

Kaneko and Doi (Kaneko, 1989b; Kaneko and Doi, 1989) theoretically studied the static and dynamic characteristics of oil-filled porous journal bearings with three non-uniform distributions of permeability. For the first type, the permeability of the inner sleeve was lower than the outer sleeve. For the second type, the permeability of the loaded section of the sleeve was lower than the unloaded section. For the third type, the permeability of the bearing ends was lower than that of the middle. The conclusions they drew from this study were consistent with an analytical investigation conducted by Cieslicki and Krzeminski (1995a).

Later, Bujurke and Patil (1992) performed a mathematical analysis of the effect of rotation and variable permeability of a short porous journal bearing on the lubrication characteristics. The distribution of permeability they considered was a variation of the third type that was considered by Kaneko and Doi (1989).

Cieslicki's theoretical and experimental results (1993) proved that the characteristic permeability of a bearing could be evaluated using either static or dynamic method. He even included the effect of air flowing through porous bearing sleeves (1994). Later, he worked with Krzeminski (Cieslicki and Krzeminski, 1995b) to

experimentally study the permeability distribution in porous bearing sleeves. In the following year, they conducted another experiment on the flow of air and oil through porous sleeve (1996) and found that the characteristic permeabilities for air and oil calculated from experiments and equations were comparable. This implied that the characteristic permeability for oil could be predicted if the characteristic permeability of air was known a priori.

Other than the bearing itself, some researchers were interested in the various load conditions to which the bearing is subject. Kumar (1973) modeled a hydrodynamic finite partial porous journal bearing with arbitrary load by taking into account the bearing curvature and slip velocity separately. Then, Kumar and Wadhwa (1984) presented an exact solution for the performance characteristic of short porous journal bearings. Their results for full porous bearings agreed excellently with Murti's results (1972a). They further reported the performance characteristics of  $180^\circ$  partial journal bearings.

While most of the research work focused on the bearings and their structure, some were centered on the effect of lubricating oil on the performance of the porous journal bearings. Scott (1963) presented a rather complete guide about the selection of lubricant for porous bearings. Braun and Groenhof (1975) found that silicone lubricant could work as well as any other commercial lubricant if additional oil is provided. Otherwise, full film lubrication could not be maintained even at low  $PI'$  values.

Oil starvation is apparently the most serious problem in lubrication. However, there was not much attention paid to this subject. So far, there were only one theoretical and one experimental work found in the literature. Cusano (1979) performed an analytical study and presented his data for starved finite porous journal bearings. The



experimental work was conducted by Raman and Vinod Babu (1984). The only oil-starvation related study was an experimental investigation by Gnanaraj and Raman (1992). Based on their experimental measurements, they reported that the oil loss was minimal if the clearance was approximately 0.19% of the journal diameter.

Analytical studies about the non-Newtonian lubricating oil were reported by Zaheeruddin (1980), Wada and co-workers (Wada et al., 1985; Wada and Kawakami, 1986) as well as Bujurke and Naduvnamani (1991). The different types of non-Newtonian oil considered were a micropolar lubricant, a Bingham solid (grease), and a couple stress fluid. A micropolar lubricant is a non-Newtonian fluid because it is a base lubricant in which macromolecules or suspended particles are present as additives. Another area of studies on the variation of the lubricants considered the lubricants either compressible or gas-lubricated.

Most previous studies assumed that the bearings did not deform under any circumstances. In fact, the flexibility of porous bearings was much greater than that of solid bearings. Hence, neglecting the effects of bearing deformation might lead to significant errors. Mak and Conway (1977a, 1977b and 1978) studied the effects of flexibility in both long and short porous journal bearings.

Without particular significance, Sowmyan and Raman (1977) analyzed the performance characteristics of spherical sintered bearings and found that their characteristics could be determined more easily than those of corresponding cylindrical bearings.

Zhilinskii and Zozulya (1977) pointed out that a great number of porous bearings were used in fractional-horsepower electric motors. To further understand these

bearings, they compared the performance of various porous bearings in terms of the bearing lives, frictional forces, and noise levels.

It was reported that a team from Cranfield University had invented porous ceramic bearings. These bearings were lubricated with water pumped in from outside. More information and discussion about this new invention were reported by Corbett et al. (1998).

Numerical work that studies the flow field in porous journal bearings was extremely rare. Most probably, this is because analytical studies are possible when the difficulty of this problem is reduced by assuming that the problem is two-dimensional and only solving for the pressure distribution in the fluid film and the porous matrix. Because of these simplifications, a closed form solution is often possible.

After decades of studies, the first three-dimensional model was developed for gas lubricated thrust pads. Tian (1998) used a finite element method to discretize the modified Reynolds equation and Darcy equation to arrive at a set of nonlinear equations. His approach was advantageous because two sets of nonlinear equation would have to be solved if a conventional approach were used.

Another three-dimensional model was reported by Meurisse and Giudicelli (1999). They took into account the Darcy law, the generalized Reynolds equation with an adoption of Elrod's model (1981), and the mass flow conservation. Although this model did not consider slip velocity and seemed rather crude, their success in revealing the three-dimensional characteristics of oil-lubricated hydrodynamic porous journal bearing was inspiring.

### **1.3 Scope of Present Study**

After almost half a century of research, it is now understood that the general behavior of porous journal bearings does follow certain rules. Similar to solid journal bearings, hydrodynamic lubrication is impossible for porous journal bearings to operate below a certain critical Sommerfeld number. One of the most important parameters for sintered journal bearings is the permeability parameter, which is proportional to the bearing radius and permeability, but inversely proportional to the radial clearance. When the permeability parameter increases, pressure, load capacity, and stability threshold speed decrease, but friction coefficient, eccentricity ratio, and the absolute of dynamic coefficient increase. For a given permeability parameter, there exists a load that corresponds to the minimum friction. Based on these rules, one can predict the behaviors of other sintered journal bearings, such as multiple-layered bearings, two-lobe bearings and bearings with non-conventional oil.

In terms of geometry, finite bearings yield a higher friction coefficient than the long and short bearings. In terms of modeling, slip-velocity condition was deleterious to the load capacity. However, the Brinkman model yields a higher pressure distribution and load capacity, but lower friction parameter and attitude angle.

According to the literature, it is more beneficial to use as short a bearing as possible within certain limits (Youssef and Eudier, 1966). Also, the couple stress fluid is a better lubricant than viscous fluids because it provides a significant load carrying capacity and a lower friction coefficient.

Although there are extensive studies reported in the literature, no investigation of coupled flow and temperature fields in a porous journal bearing has been conducted. It is

the objective of this study to examine the flow and temperature fields in porous journal bearings to bring out additional information that will aid the design of such bearings. As the first attempt, only a configuration similar to an infinite porous journal bearing is considered here. In terms of geometry, the configuration of an infinite porous journal bearing is a special case of an eccentric annular space with a porous sleeve. It is more tempting to investigate an annular space than an infinite journal bearing because not only does the former configuration offer greater generality, but also it magnifies individual phenomenon that influences the lubrication mechanism of the bearing.

For the two main reasons described above, this work focuses on the flow and temperature distributions in a partially porous annular space whose inner cylinder rotates at a prescribed constant speed. The main interest is to understand the resultant effect due to centrifugal force and thermal buoyancy on the flow and temperature fields. In addition to these effects, other secondary considerations include the eccentricity of the inner cylinder, the fluid viscosity, the permeability of the porous layer, the porous layer thickness, and the relative thermal conductivity between the fluid and the porous layers. These secondary factors are considered because they are some of the major design parameters for sintered journal bearings.

This work includes theoretical, numerical, and experimental studies. The theoretical and numerical studies examine a full range of heat convection regimes in an annular space with a porous sleeve. The experimental study is to confirm the theoretical and numerical results.

- (a) The theoretical work consists of two cases. The first case examines the forced convection regime while the second case investigates the natural convection

regime. These two cases will provide some basic understanding for the asymptotic heat convection regimes. They are described as follows.

- (i) The flow and temperature fields in a rotating concentric or slightly eccentric annular space with a porous sleeve will be obtained using the regular perturbation method with the eccentricity ratio being the perturbation parameter. Since the eccentricity ratio considered is a very small quantity, the flow in the annular space, in the absence of buoyancy effects, is expected to look like a Couette flow in the polar coordinates.
  - (ii) A weak natural convection in a pair of concentric cylinders with a porous sleeve will also be investigated using the regular perturbation method with the Rayleigh number being its perturbation parameter. The inner non-rotating cylinder is kept at a higher temperature than the outer cylinder.
- (b) Finite difference method will be employed in the numerical work to obtain the flow and temperature fields in concentric cylinders with a porous sleeve. For this configuration, equations in both fluid and porous layers are formulated in the cylindrical coordinate system. This work aims to supplement the analytical work by providing numerical results that cover the entire convection regime.
- (c) An experiment is performed to visualize the flow patterns in a concentric annulus with a porous sleeve. This is achieved by means of a modified Hele-Shaw cell. The experimental setup consists of a Hele-Shaw cell made of Plexiglas and a rotating shaft inserted through the cell. The cell is filled with

silicone oil with suspended particle tracers. An SLR camera is used to capture the trace of the fluid particles.

It is hoped that this study marks the first attempt to understand the mechanism of lubrication and performance of sintered journal bearings from the mechanical engineering aspect. This simplified yet comprehensive study will provide basic understanding to improve the design of sintered journal bearings and their applications in various engineering fields.

# **CHAPTER TWO**

## **FLOW AND TEMPERATURE FIELDS IN ROTATING CONCENTRIC AND ECCENTRIC CYLINDERS WITH A POROUS SLEEVE**

### **2.1 Introductory Remarks**

Although the focus of most previous studies in journal bearings has been on the pressure distribution and load capacity of bearings, it is recognized that the lubricant flow in a solid journal bearing is a special case of the Couette flow. The study of flow fields in a solid journal bearing has been extended to that in a concentric sintered journal bearings by Berman (1958). Following the work of Wood (1957) as well as Diprima and Stuart (1972a, 1972b), Meena and Kandaswamy (2001) included a thin porous lining in a solid journal bearing, thus allowing a velocity slip on the outer boundary. Using the bipolar coordinate system, they analytically obtained the flow distribution in the liquid film.

The present work investigates the flow and temperature fields in a pair of rotating concentric and slightly eccentric cylinders with a porous sleeve. Different from the study of Meena and Kandaswamy (2001) that considered only a thin porous lining, the present study considers a porous layer of finite thickness. Therefore, an additional set of governing equations must be prescribed for the porous layer and solved simultaneously with those of the fluid layer. Although not directly related, it is interesting to note that Malashetty et al. (2001) have performed a similar study for an inclined planar system.

## 2.2 Problem Statement

The physical configuration (Figure 2.1) of the present study consists of two infinitely long cylinders maintained at constant temperatures,  $T_H$  (on the inner cylinder) and  $T_L$  (on the outer cylinder), with  $T_H > T_L$ . The radii of the inner and outer cylinder are  $a$  and  $c$ , respectively. A porous sleeve of radius  $b$  is press-fit into the inner surface of the outer cylinder. The annular space between these two cylinders is filled with a fluid of constant properties. It is assumed that the porous sleeve is isotropic, homogeneous and impregnated with the same fluid in the annular space. Since the buoyancy effect is neglected in the present study, the flow in the annular space is induced simply by the shear effect of the rotating inner cylinder.

Under these conditions, the governing equations for the two-dimensional, steady, laminar flow in the annular space, along with the boundary and interface conditions are given below for two special cases considered.

## 2.3 Annular Space without a Porous Sleeve

In the absence of the porous sleeve, the problem is reduced to that of the classic Couette flow in the polar coordinates. However, different from the classical problem is that the present study also includes the case of eccentric cylinders.

$\theta$ -momentum equation:

$$\frac{d}{dr} \left( r \frac{du_\theta}{dr} \right) - \frac{u_\theta}{r} = 0, \quad (2.1)$$

Energy equation:



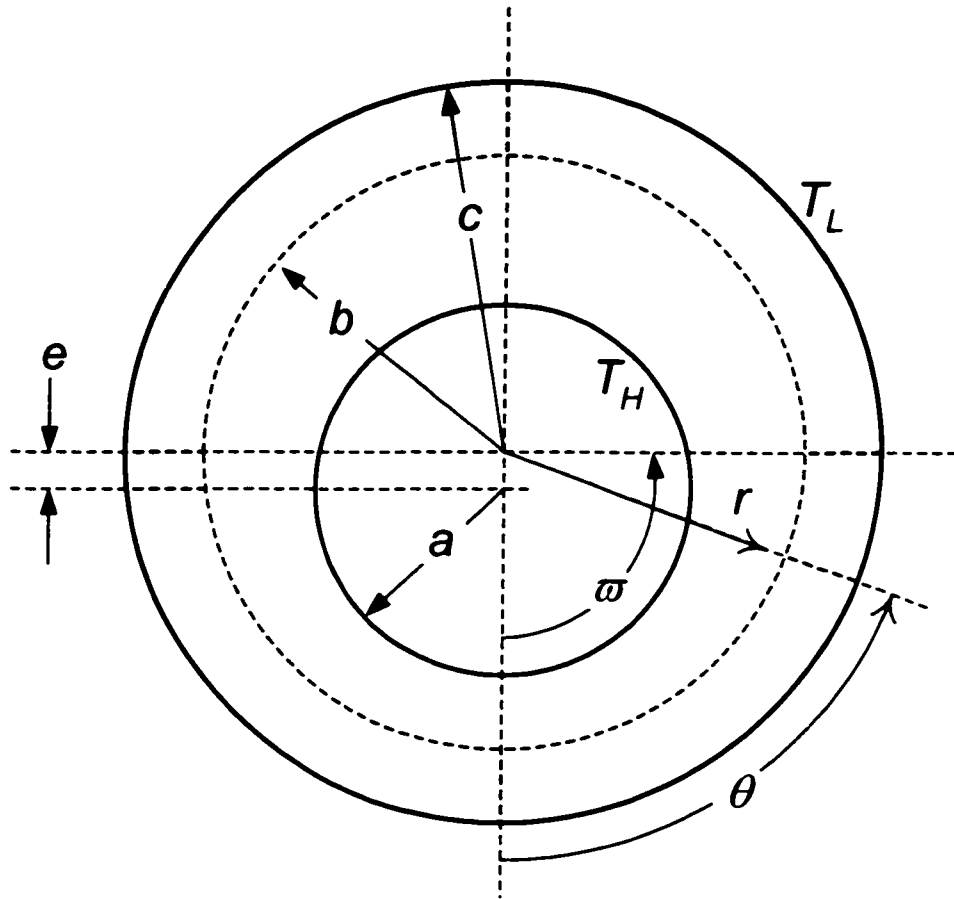


Figure 2.1 An eccentric annulus subject to rotation and differential heating from the inner and outer walls ( $T_H > T_L$ ).

$$\frac{\alpha}{r} \frac{d}{dr} \left( r \frac{dT}{dr} \right) + \frac{\nu}{C_p} \left( \frac{du_\theta}{dr} - \frac{u_\theta}{r} \right)^2 = 0, \quad (2.2)$$

which are subject to the following boundary conditions:

$$\text{At } r = a + e \cos \theta, \quad u_\theta = U, \quad \text{and} \quad T = T_H. \quad (2.3a)$$

$$\text{At } r = c, \quad u_\theta = 0, \quad \text{and} \quad T = T_L. \quad (2.3b)$$

Here,  $\theta$  is measured from the line of centers that corresponds to the minimum gap width and  $U$  is given by

$$U = \varpi a. \quad (2.4)$$

The above equations can be cast into dimensionless form by introducing proper scaling parameters, which read

$$R = \frac{r}{b}, \quad V = \frac{u_\theta}{U}, \quad \Theta = \frac{T - T_L}{T_H - T_L}, \quad \text{and} \quad \varepsilon = \frac{e}{b}. \quad (2.5)$$

Although  $b$  does not have any significance in the present case, the definitions of  $R$  and  $\varepsilon$  in the above equations are preferred for the sake of consistency in the formulation of the next case. The normalized governing equations and boundary conditions thus become,

$$\frac{d}{dR} \left( R \frac{dV}{dR} \right) - \frac{V}{R} = 0, \quad \text{and} \quad (2.6)$$

$$\frac{1}{R} \frac{d}{dR} \left( R \frac{d\Theta}{dR} \right) + Br \left( \frac{dV}{dR} - \frac{V}{R} \right)^2 = 0. \quad (2.7)$$

$$\text{At } R = (a/b) + \varepsilon \cos \theta, \quad V = 1, \quad \text{and} \quad \Theta = 1. \quad (2.8a)$$

$$\text{At } R = c/b, \quad V = 0, \quad \text{and} \quad \Theta = 0. \quad (2.8b)$$

Appearing in Eq. (2.7) is a dimensionless parameter called the Brinkman number, which is the product of the Prandtl and Eckert numbers and is given by

$$Br = \frac{\nu}{\alpha} \frac{U^2}{C_p(T_H - T_L)} \quad (2.9)$$

The physical significance of this number is that it represents the ratio of viscous dissipation to heat conduction. With an order of unity or greater, it means that the temperature rise due to dissipation is significant.

For this particular case, we are seeking solutions in the following forms,

$$V' = V'_0 + \varepsilon \cos \theta \ V'_1 + \dots \text{ and} \quad (2.10)$$

$$\Theta = \Theta_0 + \varepsilon \cos \theta \ \Theta_1 + \dots \quad (2.11)$$

The subscript in the above expression represents the order of the solution. Clearly, the zeroth order solutions correspond to the classic Couette flow in polar coordinates.

The boundary condition at  $R = a/b + \varepsilon \cos \theta$  can be expanded using Taylor series (see Appendix A) to yield

$$V'_0 + \varepsilon \cos \theta \ (V'_1 + V'_{10}) + \dots = 1, \text{ and} \quad (2.12)$$

$$\Theta_0 + \varepsilon \cos \theta \ (\Theta_1 + \Theta'_{10}) + \dots = 1. \quad (2.13)$$

Here, the primes denote the derivatives with respect to  $R$ . Substitute Eqs. (2.10) and (2.11) back to the governing equations (Eqs. (2.6) and (2.7)) as well as the boundary conditions (Eq. (2.8)). After collecting terms of the same power of  $\varepsilon \cos \theta$ , one obtains the governing equations and their corresponding boundary conditions at the various levels.

#### (a) Governing Equations and Boundary Conditions at the First Level

$$\underline{\mathcal{E}}^0: \quad \frac{d}{dR} \left( R \frac{dV'_0}{dR} \right) - \frac{V'_0}{R} = 0. \quad (2.14)$$

$$\frac{1}{R} \frac{d}{dR} \left( R \frac{d\Theta_0}{dR} \right) + Br \left( \frac{dV_0}{dR} - \frac{V_0}{R} \right)^2 = 0. \quad (2.15)$$

$$\text{At } R = a/b, \quad V_0 = 1, \quad \text{and} \quad \Theta_0 = 1. \quad (2.16a)$$

$$\text{At } R = c/b, \quad V_0 = 0, \quad \text{and} \quad \Theta_0 = 0. \quad (2.16b)$$

### (b) Governing Equations and Boundary Conditions at the Second Level

$$\underline{\varepsilon' \cos \theta}, \quad \frac{d}{dR} \left( R \frac{dV_1}{dR} \right) - \frac{V_1}{R} = 0, \quad (2.17)$$

$$\frac{1}{R} \frac{d}{dR} \left( R \frac{d\Theta_1}{dR} \right) + 2Br \left( \frac{dV_0}{dR} - \frac{V_0}{R} \right) \left( \frac{dV_1}{dR} - \frac{V_1}{R} \right) = 0. \quad (2.18)$$

$$\text{At } R = a/b, \quad V_1 = -V_0', \quad \text{and} \quad \Theta_1 = -\Theta_0'. \quad (2.19a)$$

$$\text{At } R = c/b, \quad V_1 = 0, \quad \text{and} \quad \Theta_1 = 0. \quad (2.19b)$$

## 2.4 Annular Space with a Porous Sleeve

With the presence of a porous sleeve, the complexity of the problem has increased considerably. Not only must more governing equations be solved simultaneously, but also an extra set of interface conditions must be satisfied. While the formulation for the fluid region is the same as that in the previous section, the formulation for the porous region is based on the Brinkman-extended Darcy model.

$\theta$ -momentum equations:

$$\text{fluid region:} \quad \frac{d}{dr} \left( r \frac{du_{\theta 1}}{dr} \right) - \frac{u_{\theta 1}}{r} = 0, \quad (2.20)$$

$$\text{porous region:} \quad \frac{\tilde{\mu}}{r} \frac{d}{dr} \left( r \frac{du_{\theta 2}}{dr} \right) - \frac{\mu}{K} u_{\theta 2} = 0, \quad (2.21)$$

Energy equations:

$$\text{fluid region:} \quad \frac{\alpha_1}{r} \frac{d}{dr} \left( r \frac{dT_1}{dr} \right) + \frac{\nu}{C_p} \left( \frac{du_{\theta 1}}{dr} - \frac{u_{\theta 1}}{r} \right)^2 = 0, \quad (2.22)$$

$$\text{porous region:} \quad \frac{\alpha_2}{r} \frac{d}{dr} \left( r \frac{dT_2}{dr} \right) + \frac{\nu}{C_p} \left( \frac{du_{\theta 2}}{dr} - \frac{u_{\theta 2}}{r} \right)^2 = 0. \quad (2.23)$$

The subscripts 1 and 2 represent the fluid region and porous layer, respectively. It should be noted that  $\tilde{\mu}$  in Eq. (2.21) is an empirical constant. Although it may play a role similar to that of the fluid viscosity, it is not exactly the same as fluid's viscosity and its value is usually determined experimentally (Nield and Bejan, 1999). Due to the lack of experimental data for  $\tilde{\mu}$ , it is customary to assume  $\tilde{\mu} = \mu$  in the literature. The above equations are subject to the following boundary and interface conditions:

$$\text{At } r = a + e \cos \theta, \quad u_{\theta 1} = U, \quad \text{and} \quad T_1 = T_H. \quad (2.24a)$$

$$\text{At } r = c, \quad u_{\theta 2} = 0, \quad \text{and} \quad T_2 = T_L. \quad (2.24b)$$

$$\text{At } r = b, \quad u_{\theta 1} = u_{\theta 2}, \quad \frac{du_{\theta 1}}{dr} = \frac{du_{\theta 2}}{dr}, \quad (2.25a)$$

$$T_1 = T_2, \quad \text{and} \quad k_1 \frac{dT_1}{dr} = k_2 \frac{dT_2}{dr}. \quad (2.25b)$$

The interface conditions imposed here satisfy the requirements of continuity in mass, stress, temperature and heat flux. Using the same set of scaling factors (Eq. (2.5)), the above governing equations, boundary and interface conditions are normalized to give.

$\theta$ -momentum equations:

$$\text{fluid region:} \quad \frac{d}{dR} \left( R \frac{dV_1}{dR} \right) - \frac{V_1}{R} = 0, \quad (2.26)$$

$$\text{porous region:} \quad \frac{d}{dR} \left( R \frac{dV_2}{dR} \right) - \frac{1}{Da} R V_2 = 0, \quad (2.27)$$

Energy equation:

$$\text{fluid region:} \quad \frac{1}{R} \frac{d}{dR} \left( R \frac{d\Theta_1}{dR} \right) + Br \left( \frac{dV_1}{dR} - \frac{V_1}{R} \right)^2 = 0, \quad (2.28)$$

$$\text{porous region:} \quad \frac{1}{R} \frac{d}{dR} \left( R \frac{d\Theta_2}{dR} \right) + Br \frac{k_1}{k_2} \left( \frac{dV_2}{dR} - \frac{V_2}{R} \right)^2 = 0. \quad (2.29)$$

$$\text{At } R = (a/b) + \varepsilon \cos \theta, \quad V = 1, \quad \text{and} \quad \Theta = 1. \quad (2.30a)$$

$$\text{At } R = c/b, \quad V = 0, \quad \text{and} \quad \Theta = 0. \quad (2.30b)$$

$$\text{At } R = l, \quad V_1 = V_2, \quad \frac{dV_1}{dR} = \frac{dV_2}{dR}. \quad (2.31a)$$

$$\Theta_1 = \Theta_2, \quad \text{and} \quad \frac{d\Theta_1}{dR} = \frac{k_2}{k_1} \frac{d\Theta_2}{dR}. \quad (2.31b)$$

An additional parameter that appears in Eq. (2.27) is the Darcy number. The Darcy number which is defined as

$$Da = \frac{K}{h^2}, \quad (2.32)$$

is a relative measure of the pore size of a porous medium.

Similar to the previous case, we seek solutions in the following forms.

$$V_1 = V_{10} + \varepsilon \cos \theta V_{11} + \dots, \quad (2.33)$$

$$V_2 = V_{20} + \varepsilon \cos \theta V_{21} + \dots, \quad (2.34)$$

$$\Theta_1 = \Theta_{10} + \varepsilon \cos \theta \Theta_{11} + \dots, \text{ and} \quad (2.35)$$

$$\Theta_2 = \Theta_{20} + \varepsilon \cos \theta \Theta_{21} + \dots \quad (2.36)$$

In the above expressions, the first index in the double subscripts represents the physical domain (1 for the fluid region and 2 for the porous layer as defined earlier) and the second index represents the order of the solution.

Similar to Eqs. (2.12) and (2.13), the boundary condition at  $R = (a/b) + \varepsilon \cos \theta$  is expressed in the following fashion.

$$V'_{10} + \varepsilon \cos \theta (V'_{11} + V'_{10}) + \dots = 1, \text{ and} \quad (2.37)$$

$$\Theta_{10} + \varepsilon \cos \theta (\Theta_{11} + \Theta'_{10}) + \dots = 1. \quad (2.38)$$

Again, by collecting the terms of the same power of  $\varepsilon \cos \theta$ , one obtains the governing equations as well as their corresponding boundary and interface conditions at different levels.

**(a) Governing Equations, Boundary Conditions, and Interface Conditions at the First Level**

$$\underline{\varepsilon^0}: \quad \frac{d}{dR} \left( R \frac{dV'_{10}}{dR} \right) - \frac{V'_{10}}{R} = 0, \quad (2.39)$$

$$\frac{d}{dR} \left( R \frac{dV'_{20}}{dR} \right) - \gamma^2 R V'_{20} = 0, \quad (2.40)$$

$$\frac{1}{R} \frac{d}{dR} \left( R \frac{d\Theta_{10}}{dR} \right) + Br \left( \frac{dV'_{10}}{dR} - \frac{V'_{10}}{R} \right)^2 = 0, \text{ and} \quad (2.41)$$

$$\frac{1}{R} \frac{d}{dR} \left( R \frac{d\Theta_{20}}{dR} \right) + Br \frac{k_1}{k_2} \left( \frac{dV'_{20}}{dR} - \frac{V'_{20}}{R} \right)^2 = 0. \quad (2.42)$$

$$\text{At } R = a/b, \quad V'_{10} = 1, \quad \text{and} \quad \Theta_{10} = 1. \quad (2.43a)$$

$$\text{At } R = c/b, \quad V_{20} = 0, \quad \text{and} \quad \Theta_{20} = 0. \quad (2.43b)$$

$$\text{At } R = l, \quad V_{10} = V_{20}, \quad \frac{dV_{10}}{dR} = \frac{dV_{20}}{dR}, \quad (2.44a)$$

$$\Theta_{10} = \Theta_{20}, \quad \text{and} \quad \frac{d\Theta_{10}}{dR} = \frac{k_2}{k_1} \frac{d\Theta_{20}}{dR}. \quad (2.44b)$$

**(b) Governing Equations, Boundary Conditions, and Interface Conditions at the Second Level**

$$\underline{\mathcal{E}' \cos \theta}, \quad \frac{d}{dR} \left( R \frac{dV_{11}}{dR} \right) - \frac{V_{11}}{R} = 0, \quad (2.45)$$

$$\frac{d}{dR} \left( R \frac{dV_{21}}{dR} \right) - \gamma^2 R V_{21} = 0. \quad (2.46)$$

$$\frac{1}{R} \frac{d}{dR} \left( R \frac{d\Theta_{11}}{dR} \right) + 2Br \left( \frac{dV_{10}}{dR} - \frac{V_{10}}{R} \right) \left( \frac{dV_{11}}{dR} - \frac{V_{11}}{R} \right) = 0, \text{ and} \quad (2.47)$$

$$\frac{1}{R} \frac{d}{dR} \left( R \frac{d\Theta_{21}}{dR} \right) + 2Br \frac{k_1}{k_2} \left( \frac{dV_{20}}{dR} - \frac{V_{20}}{R} \right) \left( \frac{dV_{21}}{dR} - \frac{V_{21}}{R} \right) = 0. \quad (2.48)$$

$$\text{At } R = a/b, \quad V_{11} = -V_{10}', \quad \text{and} \quad \Theta_{11} = -\Theta_{10}'. \quad (2.49a)$$

$$\text{At } R = c/b, \quad V_{21} = 0, \quad \text{and} \quad \Theta_{21} = 0. \quad (2.49b)$$

$$\text{At } R = l, \quad V_{11} = V_{21}, \quad \frac{dV_{11}}{dR} = \frac{dV_{21}}{dR}, \quad (2.50a)$$

$$\Theta_{11} = \Theta_{21}, \quad \text{and} \quad \frac{d\Theta_{11}}{dR} = \frac{k_2}{k_1} \frac{d\Theta_{21}}{dR}. \quad (2.50b)$$

For convenience, we have set  $\gamma^2 = Da^{-1}$  in the above equations.



## 2.5 Analytical Solutions

Analytical solutions up to the second leading terms are obtained for the perturbed governing equations presented in the previous section.

### 2.5.1 Annular Space without a Porous Sleeve

Solving Eqs. (2.14), (2.15), (2.17), and (2.18) subject to boundary conditions (2.16) and (2.19), the functions  $V_0$ ,  $V_1$ ,  $\Theta_0$ , and  $\Theta_1$  are determined to be

$$\underline{\varepsilon^0}: \quad V_0 = \frac{a}{b(a^2 - c^2)} \left( b^2 R - \frac{c^2}{R} \right), \quad (2.51)$$

$$\Theta_0 = Br \frac{c^2}{(a^2 - c^2)^2} \left[ -a^2 f(R; a) + c^2 f(R; c) - \frac{a^2 c^2}{b^2 R^2} \right] + f(R; c), \quad (2.52)$$

$$\underline{\varepsilon^1 \cos \theta}: \quad V_1 = -\frac{a^2 + c^2}{(a^2 - c^2)^2} \left( b^2 R - \frac{c^2}{R} \right), \text{ and} \quad (2.53)$$

$$\begin{aligned} \Theta_1 = & 2Br \frac{a(a^2 + c^2)}{b(a^2 - c^2)^3} \left[ \frac{c^4}{R^2} - b^2 c^2 \right] \\ & + \left\{ 2Br \frac{abc^2}{(a^2 - c^2)^2} - \frac{b[a^2 - c^2(1 + Br)]}{a(a^2 - c^2) \ln(a/c)} \right\} f(R; c). \end{aligned} \quad (2.54)$$

$$\text{where} \quad f(R; R^*) = \frac{\ln(R^*/b) - \ln(R)}{\ln(c/b) - \ln(a/b)}. \quad (2.55)$$

### 2.5.2 Annular Space with a Porous Sleeve

Solving Eqs. (2.39) to (2.42) and (2.45) to (2.48) subject to boundary conditions (2.43) to (2.44) and (2.49) to (2.50), the functions  $V_{10}$ ,  $V_{11}$ ,  $V_{20}$ ,  $V_{21}$ ,  $\Theta_{10}$ ,  $\Theta_{11}$ ,  $\Theta_{20}$ , and  $\Theta_{21}$  are determined to be

$$\underline{\mathcal{E}}^0: \quad V_{10} = \frac{ab}{f_3} \left[ (f_1 - f_2)R + \frac{f_1 + f_2}{R} \right]. \quad (2.56)$$

$$V_{20} = -2 \frac{ab}{f_3} \left[ K_0(\gamma c/b) I_0(\gamma R) - I_0(\gamma c/b) K_0(\gamma R) \right]. \quad (2.57)$$

$$\Theta_{10} = 1 - Br f_6 \left[ R^{-2} - (b/a)^2 + 1 \right] + F_1 \left[ \ln(R) - \ln(a/b) \right]. \quad (2.58)$$

$$\begin{aligned} \Theta_{20} = 1 + Br f_6 \left[ 2 \frac{k_1}{k_2} \ln(R) + (b/a)^2 - 1 \right] + F_1 \left[ \frac{k_1}{k_2} \ln(R) - \ln(a/b) \right] \\ - 4Br \frac{k_1}{k_2} \frac{a^2 b^2}{f_3^2} F(R). \end{aligned} \quad (2.59)$$

$$\underline{\mathcal{E}}^1 \cos \theta: \quad V_{11} = -f_4 \left[ (f_1 - f_2)R + \frac{f_1 + f_2}{R} \right]. \quad (2.60)$$

$$V_{21} = 2f_4 \left[ K_0(\gamma c/b) I_0(\gamma R) - I_0(\gamma c/b) K_0(\gamma R) \right]. \quad (2.61)$$

$$\Theta_{11} = -Br f_7 R^{-2} + F_2 \ln(R) + F_3, \text{ and} \quad (2.62)$$

$$\begin{aligned} \Theta_{21} = Br \left\{ -2 f_6 (b/a)^3 + f_7 \left[ (b/a)^2 + 2 \frac{k_1}{k_2} \ln(R) - 1 \right] \right\} - F_1 \frac{b}{a} \\ + F_2 \left[ \frac{k_1}{k_2} \ln(R) - \ln(a/b) \right] + 8Br \frac{k_1}{k_2} ab \frac{f_4}{f_3} F(R), \end{aligned} \quad (2.63)$$

where  $I$  and  $K$  are the modified Bessel functions of the first kind and second kind, respectively. Other constants and functions involved are given below.

$$f_1 = I_0(\gamma c/b) K_0(\gamma) - K_0(\gamma c/b) I_0(\gamma), \quad (2.64a)$$

$$f_2 = \gamma \left[ I_0(\gamma c/b) K_1(\gamma) + K_0(\gamma c/b) I_1(\gamma) \right], \quad (2.64b)$$

$$f_3 = (a^2 + b^2) f_1 - (a^2 - b^2) f_2, \quad (2.64c)$$

$$f_4 = \frac{ab^2}{f_3^2} [(a-b)f_1 - (a+b)f_2], \quad (2.64d)$$

$$f_5 = 2 \frac{k_1}{k_2} \ln(c/b) + (b/a)^2 - 1, \quad (2.64e)$$

$$f_6 = a^2 b^2 [(f_1 + f_2)/f_3]^2, \quad (2.64f)$$

$$f_7 = -2ab(f_1 + f_2)^2 f_4 / f_3, \quad (2.64g)$$

$$F_1 = - \frac{1 + Br f_6 f_5 - 4Br \frac{k_1}{k_2} \frac{a^2 b^2}{f_3^2} F(c/b)}{\frac{k_1}{k_2} \ln(c/b) - \ln(a/b)}, \quad (2.65a)$$

$$F_2 = - \frac{Br \left\{ -2 f_6 (b/a)^3 + f_7 f_9 \right\} - F_1 \frac{b}{a} + 8Br \frac{k_1}{k_2} ab \frac{f_4}{f_3} F(c/b)}{\frac{k_1}{k_2} \ln(c/b) - \ln(a/b)}, \quad (2.65b)$$

$$F_3 = Br \left[ -2 f_6 (b/a)^3 + f_7 (b/a)^2 \right] - F_1 \frac{b}{a} - F_2 \ln(a/b), \text{ and} \quad (2.65c)$$

$$\begin{aligned} F(R) = & \gamma^2 \ln(R) \int_1^R R \left[ K_0^2(\gamma c/b) I_1^2(\gamma R) + I_0^2(\gamma c/b) K_1^2(\gamma R) \right] dR \\ & - \gamma^2 \int_1^R R \ln(R) \left[ K_0^2(\gamma c/b) I_1^2(\gamma R) + I_0^2(\gamma c/b) K_1^2(\gamma R) \right] dR \\ & + \left[ K_0(\gamma c/b) I_0(\gamma) - I_0(\gamma c/b) K_0(\gamma) \right]^2 \ln(R) \\ & + \left[ \ln(R) - 1 \right] \int_1^R \frac{1}{R} \left[ K_0(\gamma c/b) I_0(\gamma R) - I_0(\gamma c/b) K_0(\gamma R) \right]^2 dR \\ & - \int_1^R \frac{\ln(R)}{R} \left[ K_0(\gamma c/b) I_0(\gamma R) - I_0(\gamma c/b) K_0(\gamma R) \right]^2 dR \end{aligned}$$

$$\begin{aligned}
& +2\gamma^2 I_0\left(\gamma \frac{c}{b}\right) K_0\left(\gamma \frac{c}{b}\right) \left\{ \ln(R) \int_1^R R [I_1(\gamma R) K_1(\gamma R)] dR \right. \\
& \left. - \int_1^R R \ln(R) [I_1(\gamma R) K_1(\gamma R)] dR \right\}. \tag{2.66}
\end{aligned}$$

Note that  $F(c/b)$  is a constant in the equations (2.65). It is evaluated as  $F(R)$  with  $R = c/b$ . Notice that the local Nusselt number, which signifies the relative importance between heat convection and heat conduction, is defined as

$$Nu = \frac{hb}{k}. \tag{2.67}$$

Equation (2.67) can be expressed in terms of the local temperature gradient (i.e., heat flux) and it reads

$$Nu = -\frac{\partial \Theta}{\partial R}. \tag{2.68}$$

For the present study, it is the average Nusselt number that provides the general heat transfer characteristics of a porous bearing. Integrating the local Nusselt number along the inner and outer surfaces, one obtains

$$\overline{Nu} = -\frac{1}{2\pi} \int_0^{2\pi} \frac{\partial \Theta}{\partial R} d\theta. \tag{2.69}$$

$$\overline{Nu} = -\frac{1}{2\pi} \int_0^{2\pi} \frac{\partial}{\partial R} (\Theta_{i0} + \varepsilon \cos \theta \Theta_{i1} + \dots) d\theta. \tag{2.70}$$

$$= -\frac{1}{2\pi} \left[ \int_0^{2\pi} \frac{\partial \Theta_{i0}}{\partial R} d\theta + \varepsilon \int_0^{2\pi} \cos \theta \frac{\partial \Theta_{i1}}{\partial R} d\theta + \dots \right]. \tag{2.71}$$

where  $i$  is the index of the physical domain as discussed. The average Nusselt numbers at the inner and outer cylinders are given, respectively, by

$$\overline{Nu}_{in} = -\frac{1}{2\pi} \left[ \int_0^{2\pi} \frac{\partial \Theta_{10}}{\partial R} \Big|_{R=a/b} d\theta + \varepsilon \int_0^{2\pi} \cos \theta \frac{\partial \Theta_{11}}{\partial R} \Big|_{R=a/b} d\theta \right] + \dots \text{ and} \quad (2.72)$$

$$\overline{Nu}_{out} = -\frac{1}{2\pi} \left[ \int_0^{2\pi} \frac{\partial \Theta_{20}}{\partial R} \Big|_{R=c/b} d\theta + \varepsilon \int_0^{2\pi} \cos \theta \frac{\partial \Theta_{21}}{\partial R} \Big|_{R=c/b} d\theta \right] + \dots \quad (2.73)$$

where

$$\frac{\partial \Theta_{10}}{\partial R} \Big|_{R=a/b} = 2Br f_6 \left( \frac{b}{a} \right)^3 + F_1 \frac{b}{a}, \quad (2.74a)$$

$$\frac{\partial \Theta_{11}}{\partial R} \Big|_{R=a/b} = 2Br f_7 \left( \frac{b}{a} \right)^3 + F_2 \frac{b}{a}, \quad (2.74b)$$

$$\frac{\partial \Theta_{20}}{\partial R} \Big|_{R=c/b} = (2Br f_6 + F_1) \frac{k_1}{k_2} \frac{b}{c} - 4Br \frac{k_1}{k_2} \frac{a^2 b^2}{f_3^2} G(c/b), \quad (2.74c)$$

$$\frac{\partial \Theta_{21}}{\partial R} \Big|_{R=c/b} = (2Br f_7 + F_2) \frac{k_1}{k_2} \frac{b}{c} + 8Br \frac{k_1}{k_2} ab \frac{f_4}{f_3} G(c/b), \text{ and} \quad (2.74d)$$

$$\begin{aligned} G(R) = & \frac{\gamma^2}{R} \int_1^R \left[ K_0^2(\gamma c/b) I_1^2(\gamma R) + I_0^2(\gamma c/b) K_1^2(\gamma R) \right] dR \\ & + 2 \frac{\gamma^2}{R} \int_1^R \left[ I_0(\gamma) K_0(\gamma c/b) I_1(\gamma R) K_1(\gamma R) \right] dR \\ & + \left[ I_0(\gamma) K_0(\gamma c/b) - I_0(\gamma c/b) K_0(\gamma) \right]^2 R \\ & - \left[ K_0(\gamma c/b) I_0(\gamma R) - I_0(\gamma c/b) K_0(\gamma R) \right]^2 R \end{aligned}$$

$$+ \frac{1}{R} \int_1^R \frac{1}{R} \left[ K_0(\gamma c/b) I_0(\gamma R) - I_0(\gamma c/b) K_0(\gamma R) \right]^2 dR. \quad (2.75)$$

## 2.6 Results and Discussion

Since the present solutions for the flow and temperature fields are obtained using the regular perturbation method, they are valid only for small eccentricities. For the discussion that follows, we limit our attention to a specific configuration of  $a = 1$ ,  $b = 1.5$ , and  $c = 2$ , unless specified otherwise.

Figure 2.2 shows the flow field in an eccentric annulus without porous sleeve for various Brinkman numbers and eccentricity ratios. The special case of concentric annulus ( $\varepsilon = 0$ ) is also included for comparison. In this study, we limit the eccentricity ratio to no more than  $0.1$ . The inner and outer circles represent the rotating inner cylinder and the stationary outer cylinder, respectively. The magnitude and directions of the flow velocity are visualized through vector representation. Due to the rotation of the inner cylinder, a shear-induced flow is observed throughout the entire fluid layer. Also observed is that the magnitude of the fluid velocity reduces to zero at the outer (stationary) cylinder. Since the buoyancy effect is neglected in the present analysis, the flow is initiated mainly due to the shearing action of the inner cylinder. As a result, the flow field is independent of Brinkman number. As the eccentricity ratio increases, the inner cylinder shifts downwards causing an increase in the flow velocity across the narrowest gap in the annulus as compared with other clearances.

Figure 2.3 presents the corresponding isotherms for the flow fields in Figure 2.2. When the annulus spaces are concentric, the isotherms are concentric as well. Similarly,

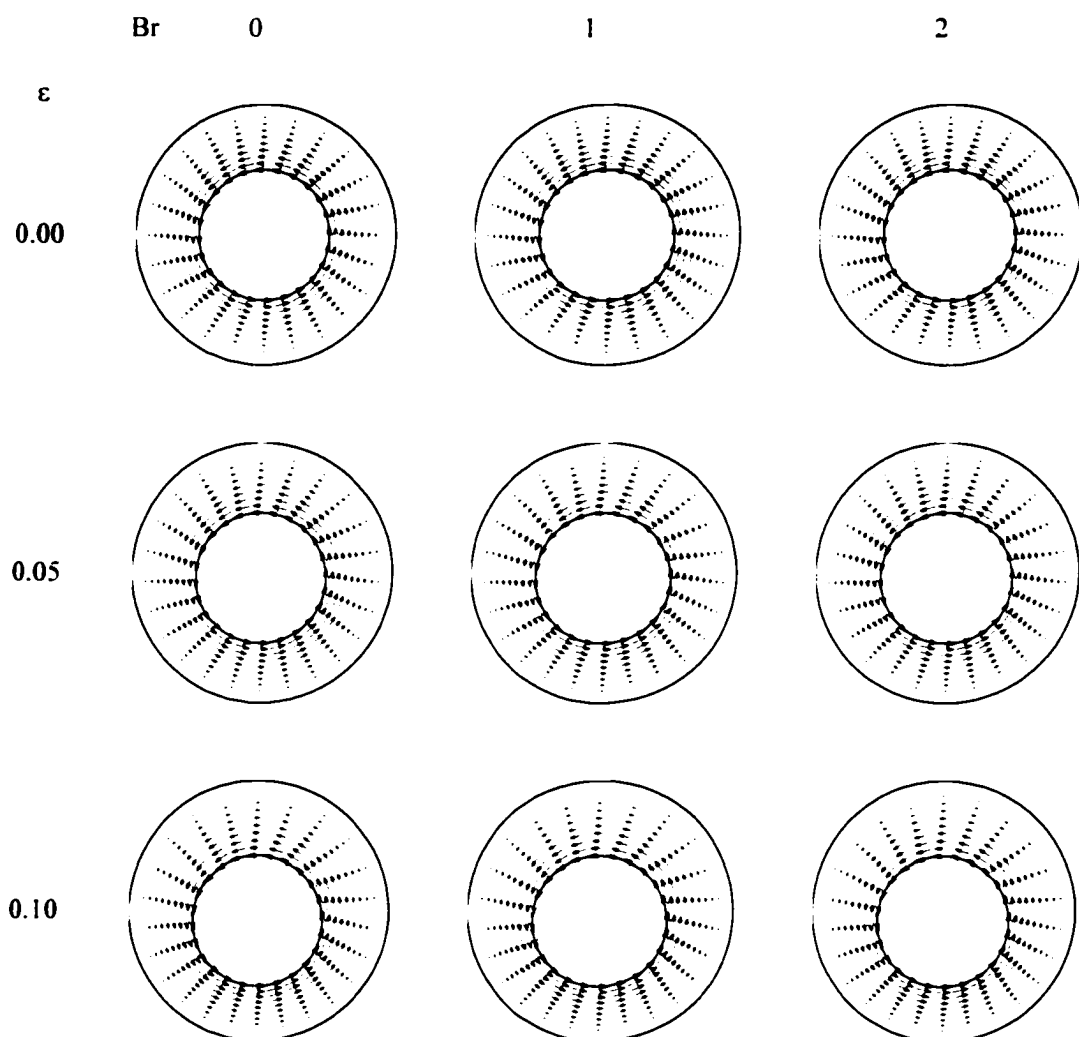


Figure 2.2 Flow fields in an eccentric annulus without a porous sleeve for  $Da = 0.01$ , and  $k_1/k_2 = 1$ .

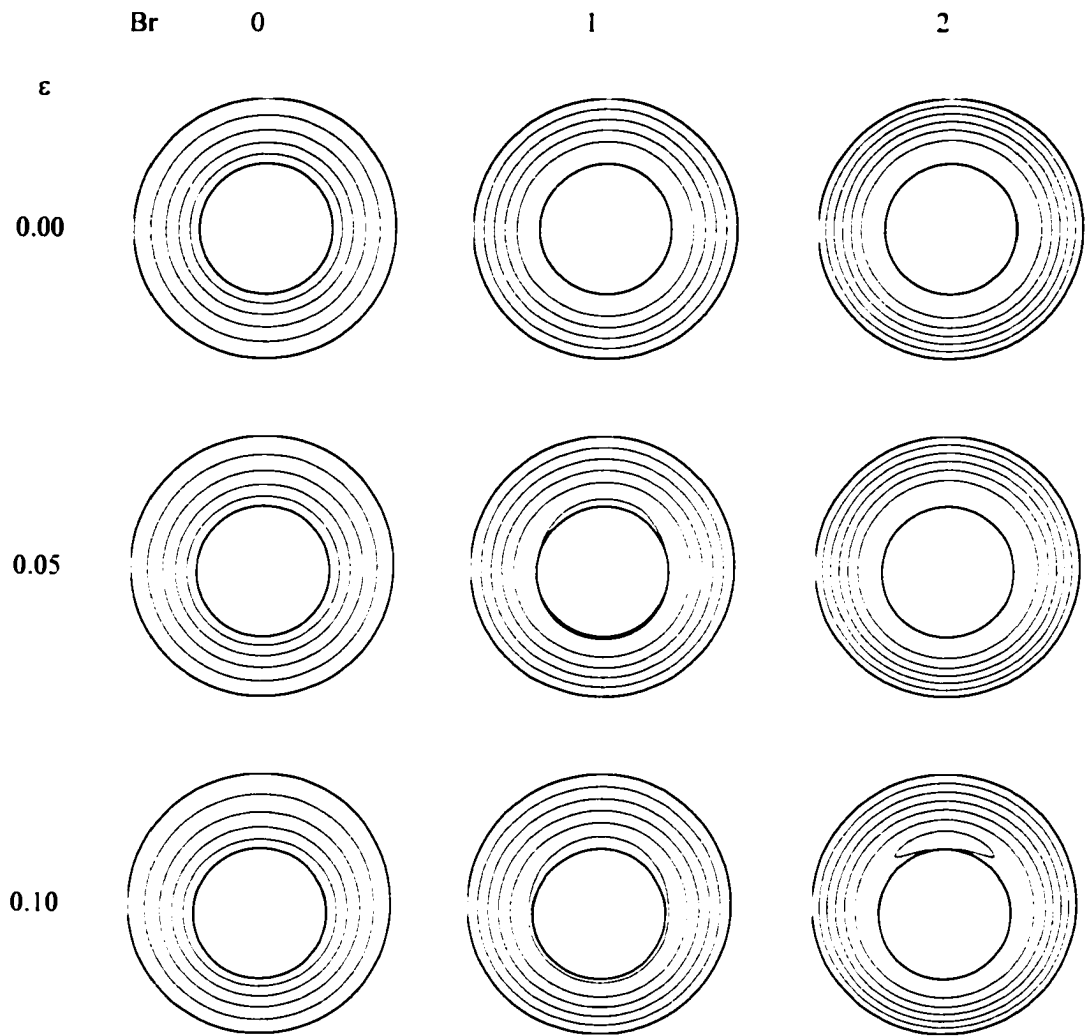


Figure 2.3 Temperature fields in an eccentric annulus without a porous sleeve for  $Da = 0.01$ , and  $k_1/k_2 = 1$  ( $\Delta\theta = 0.2$ ).



the isotherms become eccentric for an eccentric annulus. As observed, when  $Br = 0$ , heat transfer is dominated by conduction. As Brinkman number increases, the isotherms start moving radially outwards because fluid at the vicinity of the inner cylinder is heated up. At  $Br = 2$ , there are five or more isotherms within the inner and outer cylinders. This implies that the heat generation due to viscous dissipation is so great that the fluid temperature can exceed that of the inner cylinder. Again, it is observed that the inner cylinder shifts downwards when the eccentricity ratio increases, and the isotherms are compressed accordingly at the narrowest gap. For  $Br \geq 1$ , it is observed that heat generation due to viscous dissipation is more significant for an annulus with a large eccentricity ratio. This implies that the eccentricity ratio enhances the heat generation by viscous dissipation. As the eccentricity ratio increases to  $0.1$ , one observes that a ring of overheated fluid ( $\theta > 1$ ) completely surrounds the inner cylinder. As the Brinkman number increases, heat generation becomes even stronger. The dimensionless temperature of the fluid in the thermal plume on top of the inner cylinder becomes greater than  $1.2$ .

The effects of porous sleeve thickness on the development of flow field are shown in Figure 2.4. In these figures, a dashed line between the inner and outer cylinders indicates the interface between the fluid region and the porous sleeve. Due to shearing action in the fluid region, it is observed that there is a flow with finite velocities in the porous sleeve. This can be examined more closely in the velocity profiles shown in Figures 2.10 and 2.11. The thickness of porous sleeve examined here are  $b = 1.25$ ,  $1.50$ , and  $1.75$ . Among these three cases, the first column ( $b = 1.25$ ) corresponds to the thickest porous sleeve. Its velocity gradient in the fluid layer is the greatest and the

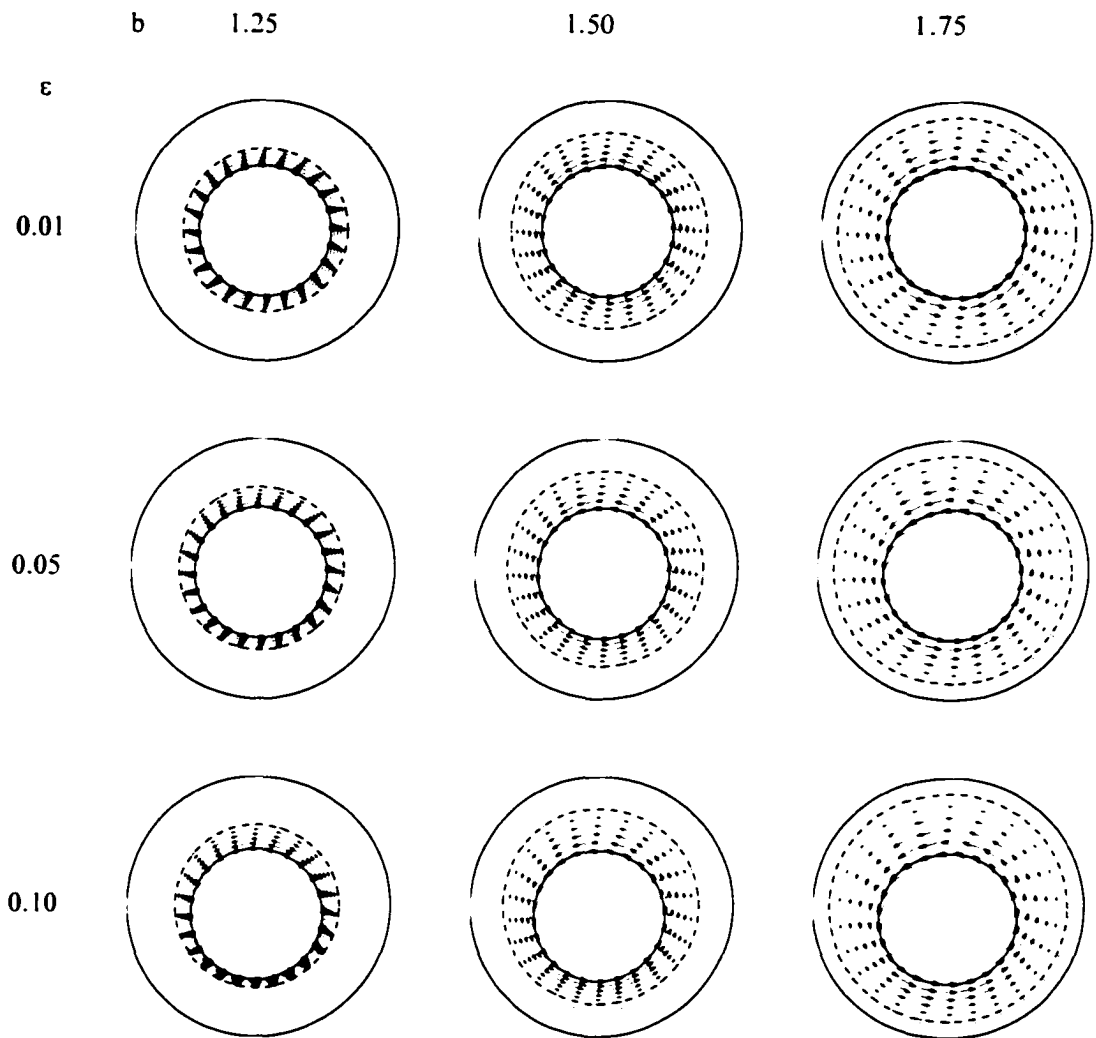


Figure 2.4 Flow fields in an eccentric annulus with a porous sleeve for  $Br = 1$ ,  $Da = 0.01$ , and  $k_1/k_2 = 1$ .

velocity components in the porous sleeve are the smallest because of the highest flow resistance. As  $b$  increases (the thickness of the porous sleeve reduces), the velocity gradient in the fluid layer decreases and the velocity components in the porous sleeve remain finite. Similar to Figure 2.2, one notices that the flow velocity increases at the narrowest gap when the eccentricity ratio increases. This phenomenon is the most apparent when the fluid layer is the thinnest (i.e.,  $b$  is the smallest).

The corresponding temperature fields are shown in Figure 2.5. Notice that for  $b = 1.25$  and  $1.50$ , there are at least five isotherms in the annulus. However, for  $b = 1.75$ , there are only four isotherms unless the eccentricity ratio is equal to  $0.10$ . This interesting finding implies that for a thick porous sleeve, with small eccentricity ratios, there exists a region of overheated fluid next to the inner rotating cylinder. Referring to Figure 2.4, one sees that the velocity gradient is the greatest for the smallest  $b$ . Since the heat generation due to viscous dissipation is directly proportional to velocity gradient, heat generation is also the greatest for the smallest  $b$ . As the porous sleeve thickness decreases, the region of overheated fluid diminishes. At  $\varepsilon = 0.10$ , a ring of overheated fluid is still observed. Although a large eccentricity ratio can enhance heat generation due to viscous dissipation, it is found that for an annulus with a reduced thickness of porous sleeve ( $b = 1.75$ ), the ring of overheated fluid reduces to a thermal plume arising from the top portion of the inner cylinder.

In Figures 2.6 and 2.7, one can examine the combined effects of Brinkman and Darcy numbers on the flow and temperature fields in an eccentric annulus. For a given Darcy number, one observes that the flow fields are identical. This is consistent with what observed in Figure 2.2 (i.e., the flow is independent of the Brinkman number

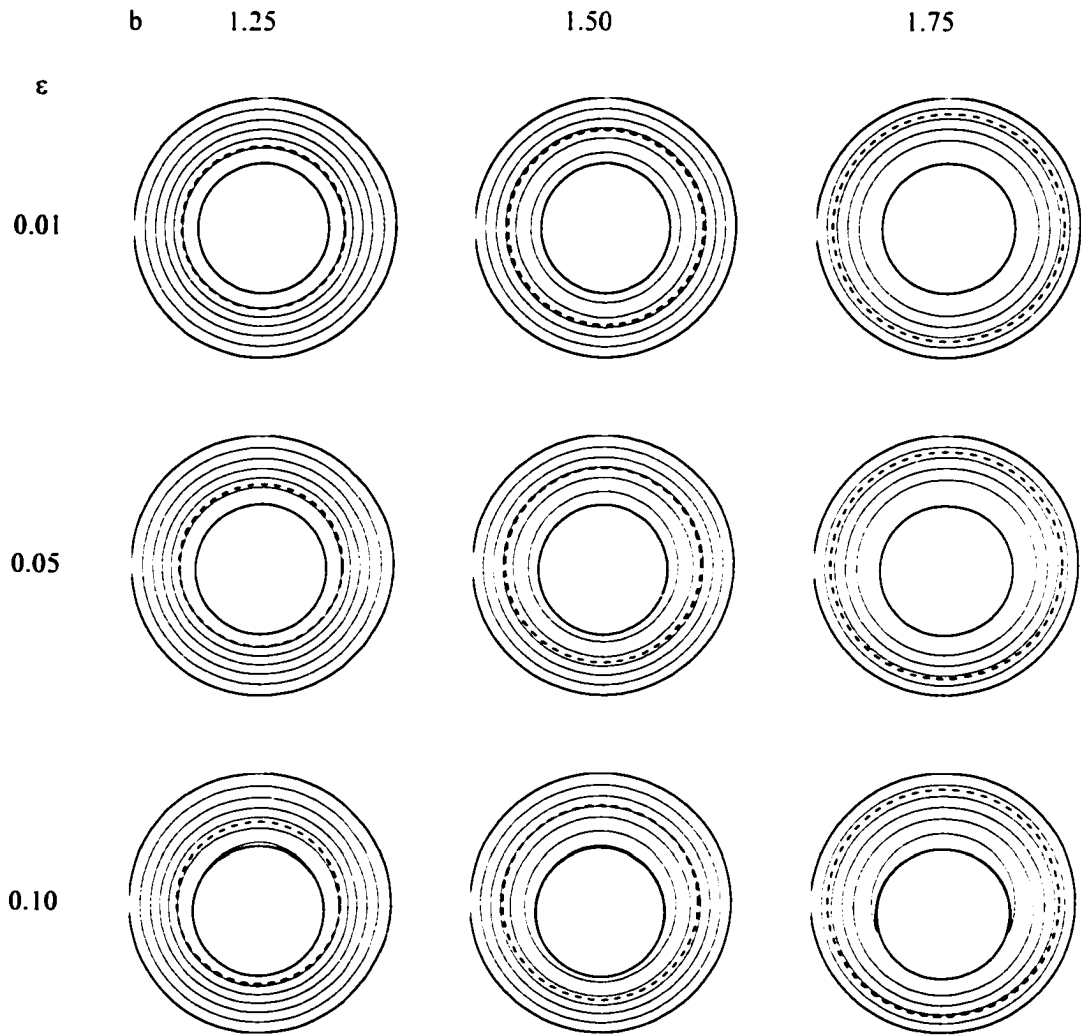


Figure 2.5 Temperature fields in an eccentric annulus with a porous sleeve for  $Br = 1$ ,  $Da = 0.01$ , and  $k_1/k_2 = 1$  ( $\Delta\theta = 0.2$ ).

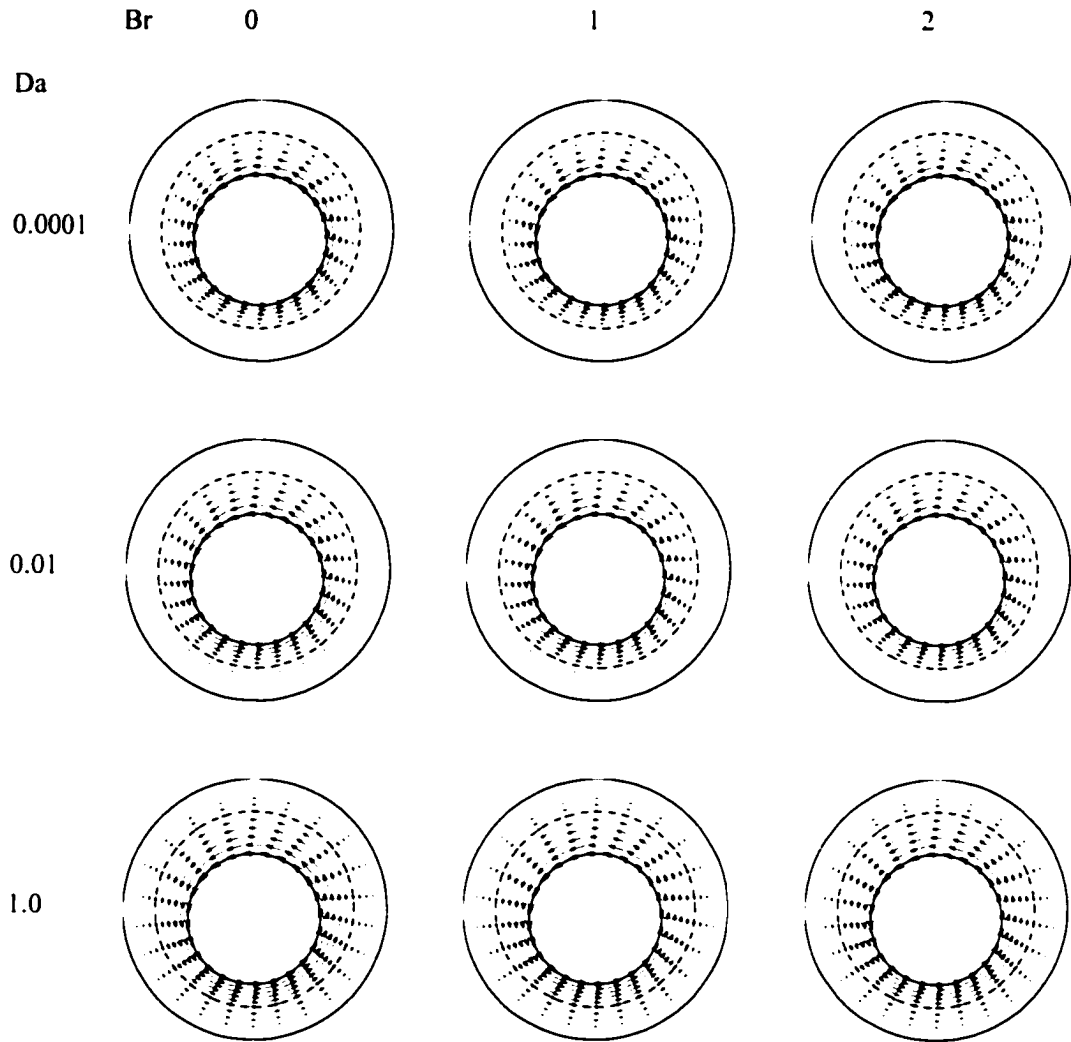


Figure 2.6 Flow fields of in an eccentric annulus with a porous sleeve for  $h = 1.5$ ,  $\varepsilon = 0.1$ , and  $k_1/k_2 = 1$ .

because buoyancy effect is neglected). As the Darcy number increases, the flow resistance in the porous sleeve decreases. As a result, the most remarkable difference among these plots is the flow in the porous sleeve. When  $Da = 10^{-4}$ , there is almost no flow in the porous sleeve. As the Darcy number increases, this velocity component in the porous sleeve becomes finite. This is particularly apparent when  $Da = 1.0$ .

Unlike the flow fields, the temperature fields behave very distinctively, as shown in Figure 2.7. At  $Br = 0$ , there are only 4 isotherms ( $\Delta\theta = 0.2$ ) appear between the inner and outer cylinders. This means that the maximum dimensionless temperature in the entire annular space is 1.0 and is located exactly on the inner cylinder. Also, it is observed that the temperature field is nearly independent of the Darcy number when  $Br = 0$ . This is because the flow in the porous layer is so insignificant when compared to that in the fluid layer, their effects on the temperature field are therefore very negligible. As the Brinkman number increases, additional isotherms appear. This indicates that heat generation becomes so great that the maximum fluid temperatures in the annulus exceed that of the inner cylinder and they are located near the inner cylinder. As the Darcy number increases, the region of overheated fluid shrinks. Thus, one can conclude that the Darcy number relieves the viscous dissipation because it reduces the velocity gradient by allowing more fluid flowing through the porous sleeve.

In the discussion above, it has been assumed that the effective thermal conductivities for the fluid and porous sleeve are the same. In reality, this may not always be the case. In Figure 2.8, one can examine the influence of porous sleeve thickness and thermal conductivity ratio on the flow field. Again, one observes that the flow fields only depend on the thickness of porous sleeve, but not the thermal

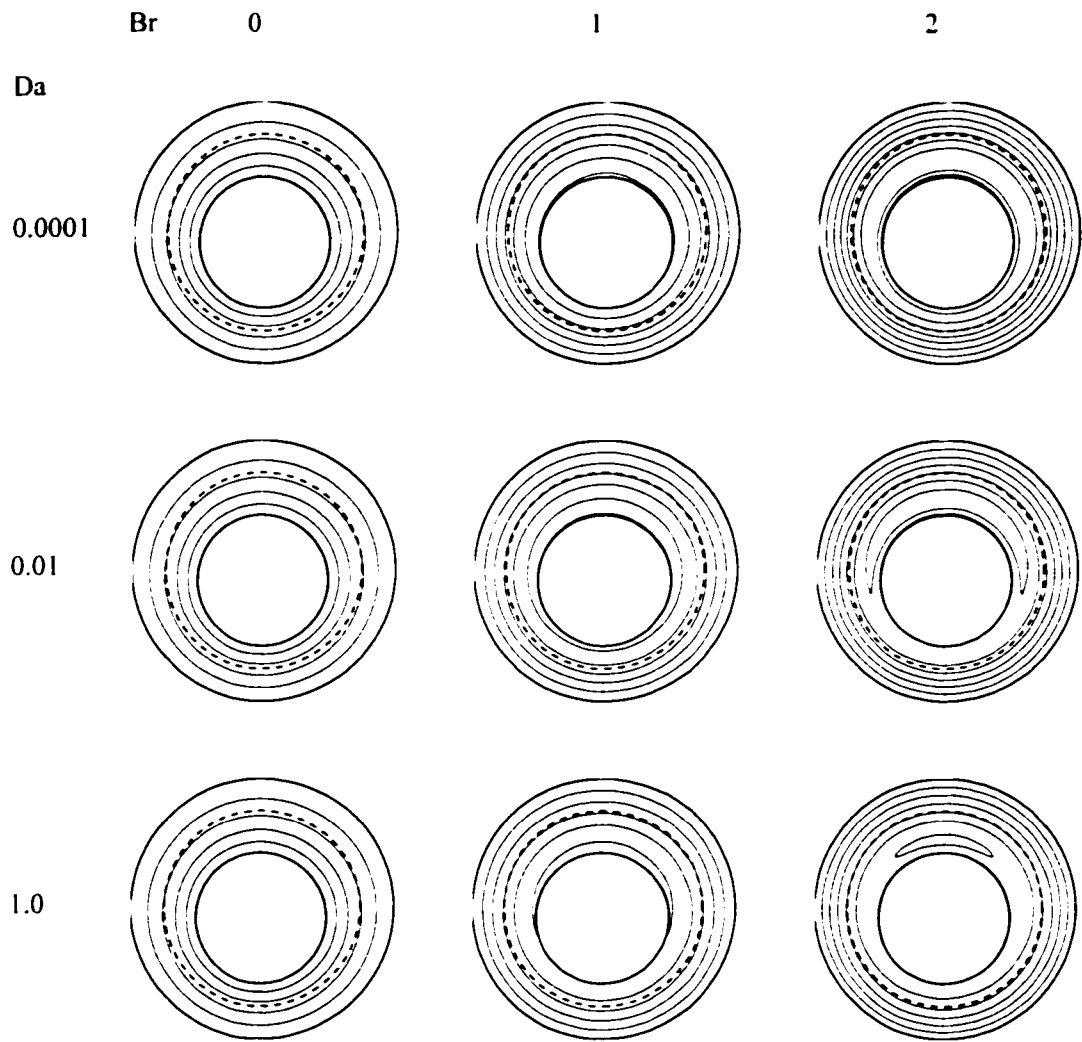


Figure 2.7 Temperature fields in an eccentric annulus with a porous sleeve for  $h = 1.5$ ,  $\varepsilon = 0.1$ , and  $k_1/k_2 = 1$  ( $\Delta\theta = 0.2$ ).

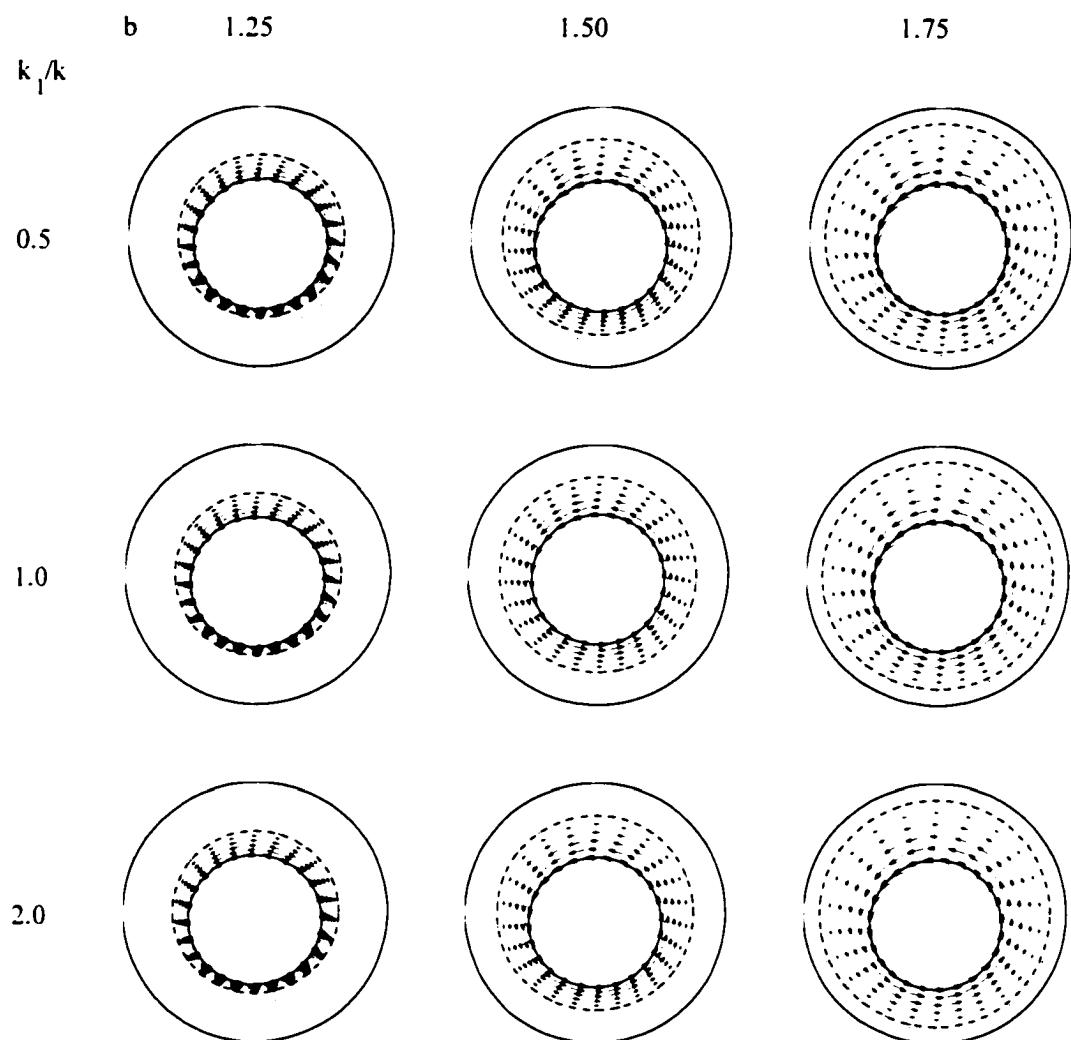


Figure 2.8 Flow fields in an eccentric annulus with a porous sleeve for  $Br = 1$ ,  $Da = 0.01$ , and  $\varepsilon = 0.1$ .



conductivity ratio. For the present study, the temperature field is not coupled with the flow field due to the assumption of negligible buoyancy effect. Since the thermal conductivity ratio, similar to Brinkman number, is a thermal property of the assembly, it has absolutely no effect on the velocity field.

As expected, their corresponding temperature fields, as shown in Figure 2.9, depend on both porous sleeve thickness and thermal conductivity ratio. Recall that heat generation increases with the porous sleeve thickness. This is especially clear for  $k_1/k_2 = 1.0$ . When  $k_1/k_2 < 1$ , it is found that there are fewer isotherms in the porous sleeve. This is because the thermal conductivity of the porous sleeve is high so that a smaller temperature gradient is required in the porous sleeve to transfer the same amount of heat. It is very interesting to note that there appears a reversed thermal plume for the case of  $b = 1.25$  and  $k_1/k_2 = 0.5$ . For  $k_1/k_2 = 0.5$ , the thermal conductivity of the fluid layer is only half of that of the porous sleeve. At this particular condition, viscous dissipation at the region on top of the inner cylinder can be effectively removed by heat conduction into the inner cylinder and through the porous sleeve into the outer cylinder. On the other hand, when the thermal conductivity of the fluid layer is double of that of the porous sleeve, there are more isotherms appear in the porous sleeve. It is worthwhile to point out that when  $k_1/k_2 = 2.0$  and  $b \leq 1.50$ , the dimensionless temperature of the entire fluid layer is greater than unity due to viscous dissipation. When the porous sleeve is thick ( $b = 1.25$ ), it is interesting to note that there are two isolated, overheated regions appeared on both sides of the fluid layer away from the inner cylinder. At this particular case, heat removal through the inner cylinder is very effective. For this reason, the heat generated by viscous dissipation right next to the inner cylinder is removed effectively. Only at the

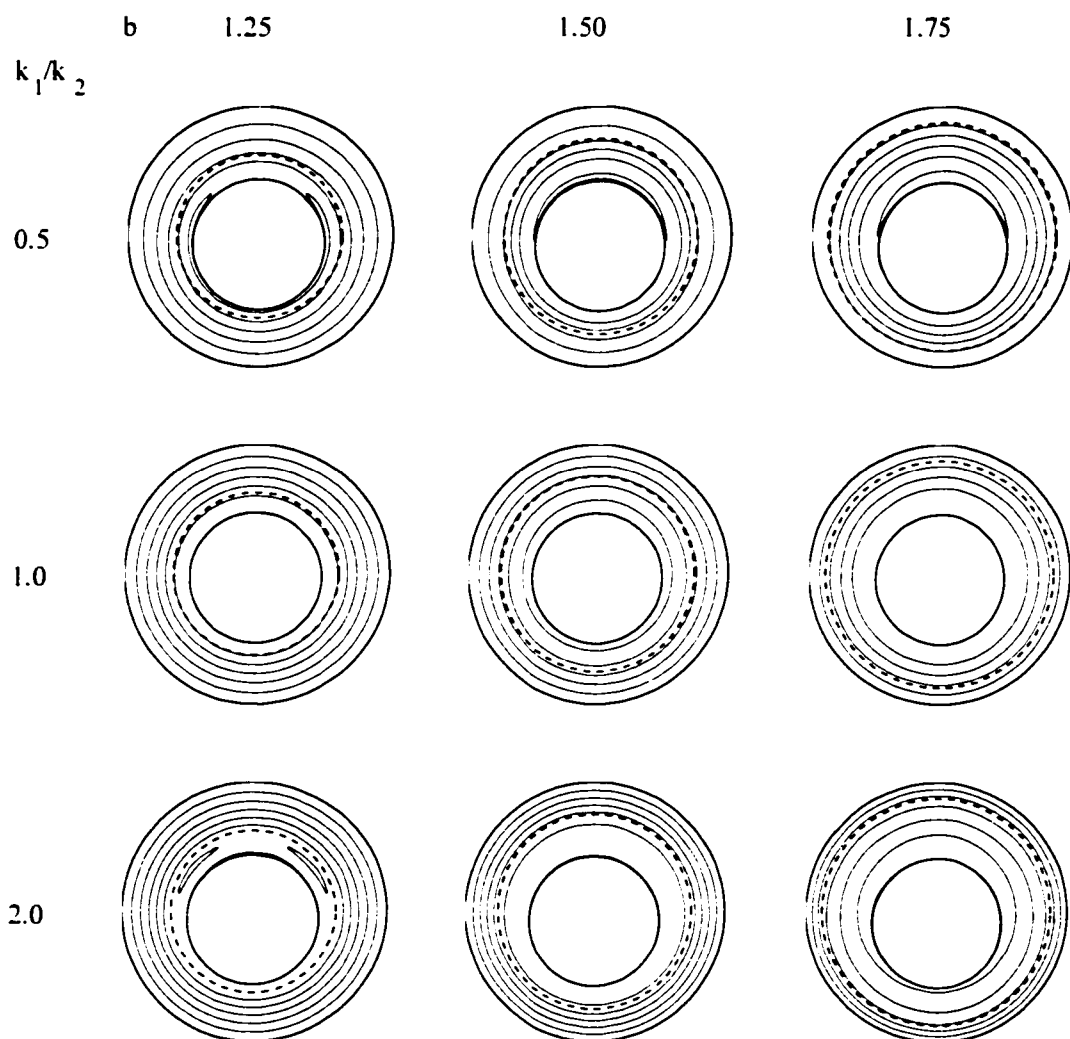


Figure 2.9 Temperature fields in an eccentric annulus with a porous sleeve for  $Br = 1$ ,  $Da = 0.01$ , and  $\varepsilon = 0.1$  ( $\Delta\theta = 0.2$ ).

region away from the inner cylinder, heat is removed not as effectively by conduction through the inner cylinder and porous sleeve.

For the ease of comparison, a normalized radial distance  $r^*$  is introduced, defined as  $r^* = (r - a) / (c - a)$ . By this definition,  $r^* = 0$  represents the surface of the inner cylinder while  $r^* = 1$  represents the surface of the outer cylinder. The interface is located at  $r^* = 0.5$  if  $b = 1.5$ . As shown in Figure 2.10, the change in velocity profiles is significant when the Darcy number is of the order between  $10^{-3}$  and  $10^0$ . For a small Darcy number, the flow resistance in the porous sleeve is very large, which results in a near-zero velocity profile in the porous layer. For a large Darcy number, the porous sleeve becomes more permeable. Hence, the velocity profile approaches that of the annulus without porous sleeve. As expected, the velocity profiles depend on the permeability of the porous sleeve. This dependence becomes more obvious as the Darcy number becomes greater than  $10^{-3}$ . For a sufficiently large Darcy number (e.g.,  $Da = 1$ ), the velocity profile approaches that of a single fluid layer and becomes independent of the properties of the porous sleeve. Since the fluid friction is proportional to the tangential velocity gradient, this implies that the insertion of a porous sleeve in a journal bearing increases the friction on the journal surface. More importantly, this frictional loss increases as the permeability of the porous sleeve decreases. For practical applications, a porous journal bearing usually consumes more power than a solid journal bearing.

To study the effect of various parameters on the velocity profiles, one can examine the results with the Darcy number varying in the range between  $10^{-3}$  and  $10^0$ . The effect of porous sleeve thickness on the velocity profiles is shown in Figure 2.11. In

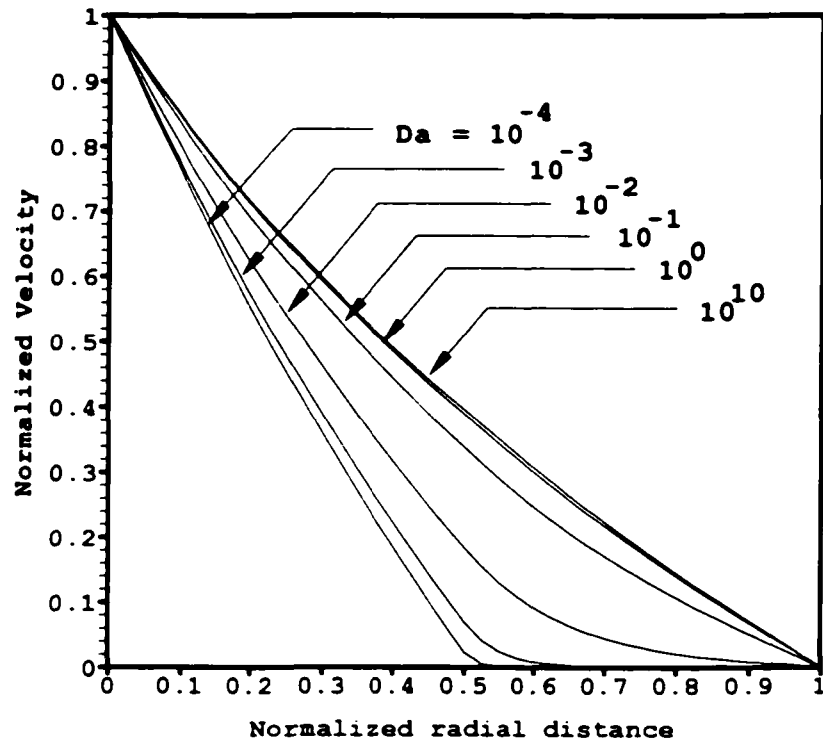


Figure 2.10 Velocity profiles for various Darcy numbers in an eccentric annulus with a porous sleeve on the gap of  $\theta = \pi/2$  ( $b = 1.50$ ,  $\varepsilon = 0.05$ ,  $Br = 0.1$ , and  $k_1/k_2 = 1$ ).

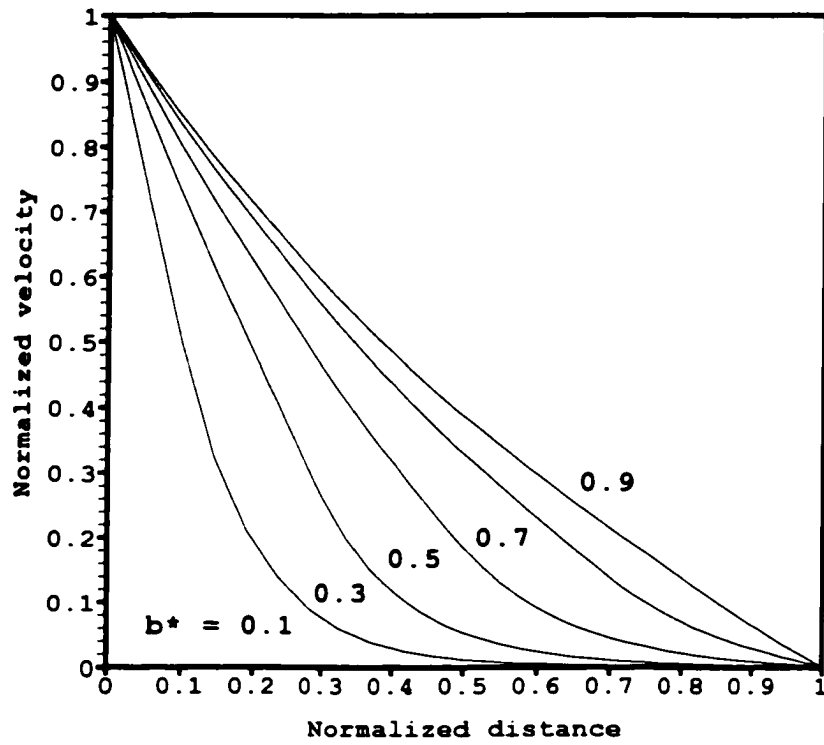


Figure 2.11 Velocity profiles for various porous sleeve thickness in an eccentric annulus at the cross-section of  $\theta = \pi/2$  ( $\varepsilon = 0.05$ ,  $Da = 0.01$ ,  $Br = 0.1$ , and  $k_1/k_2 = 1$ ).

this figure,  $b^*$  (defined as  $b^* = (b - a) / (c - a)$ ) indicates the location of the interface (or  $R = 1$ ). The values of  $b^* = 0.1, 0.3, 0.5, 0.7$ , and  $0.9$  represent  $b = 1.1, 1.3, 1.5, 1.7$ , and  $1.9$ , respectively. For a given journal bearing, the thicker the porous sleeve is, the thinner the fluid layer becomes. As shown by the figure, the flow velocity significantly decreases as the thickness of the porous sleeve increases. This eventually leads to a greater velocity gradient for a thicker porous sleeve. This also implies that a higher frictional loss is anticipated in a porous journal bearing with a thicker porous sleeve.

The temperature profiles in an eccentric annulus with a porous sleeve are shown in Figure 2.12 for various Brinkman numbers. Since it is assumed that the thermal conductivities of the fluid and the porous sleeve are the same for the case shown, there are no abrupt changes in the temperature profile across the interface. Recall that the Brinkman number signifies the importance of viscous dissipation as compared to heat conduction in the fluid. For  $Br \geq 1$ , the fluid is heated up by the viscous dissipation and this can be clearly observed from the figure. The maximum temperature rise is proportional to the Brinkman number and it occurs somewhere in the fluid layer ( $0.0 \leq r^* \leq 0.5$ ) but close to the inner cylinder. For  $Br < 1$ , the temperature profiles are weakly dependent on the Brinkman number and they decrease monotonously from the inner cylinder towards the outer cylinder. In this case, the maximum temperature occurs at the inner cylinder. Heat is removed from the inner cylinder to the outer cylinder mainly by diffusion. As a result, the temperature profiles are almost identical regardless of the porous sleeve thickness and Darcy number.

To further examine the effects of porous sleeve thickness on the temperature field, the temperature profiles are shown in Figure 2.13 for  $Br = 2$ . It is found that the

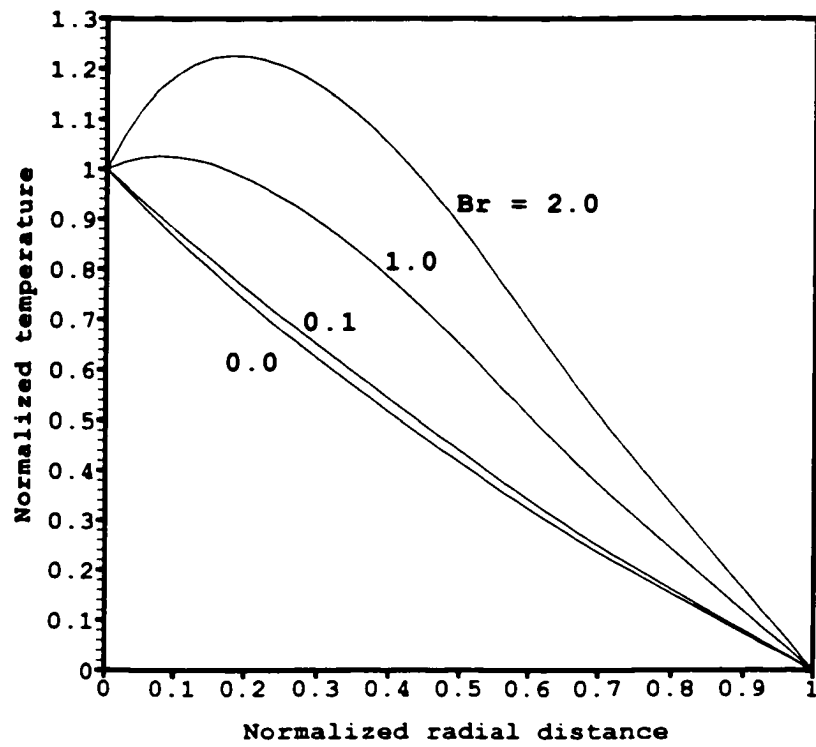


Figure 2.12 Temperature profiles for various Brinkman numbers in an eccentric annulus at the gap of  $\theta = \pi/2$  ( $b = 1.50$ ,  $\varepsilon = 0.05$ ,  $Da = 0.01$ , and  $k_1/k_2 = 1$ ).

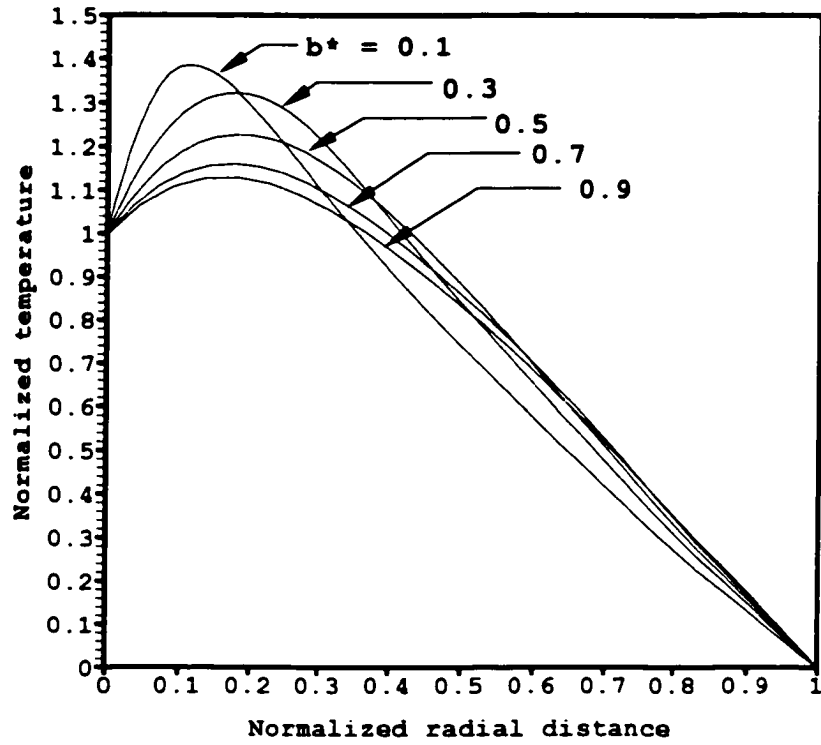


Figure 2.13 Temperature profiles for various porous sleeve thickness in an eccentric annulus at the gap of  $\theta = \pi/2$  ( $\varepsilon = 0.05$ ,  $Da = 0.01$ ,  $Br = 2.0$ , and  $k_1/k_2 = 1$ ).



maximum temperature rise is inversely proportional to the porous sleeve thickness. Recall from Figure 2.11 that the velocity gradient increases with the porous sleeve thickness. Since the viscous dissipation is directly related to the velocity gradient, the maximum fluid temperature thus increases with the porous sleeve thickness. Also noticed is that the location of the maximum fluid temperature moves away from the inner cylinder as the porous sleeve thickness decreases. For  $Br > 1$ , one can expect that the maximum temperature rise in fluid occurs along the narrow gap of an eccentric journal bearing.

The trend shown in Figure 2.13 suggests that the effect of viscous dissipation is more apparent when there is a large velocity gradient. Also shown in Figure 2.10, the velocity gradient is inversely proportional to the Darcy number. Hence, one can expect that the maximum fluid temperature is also inversely proportional to the Darcy number. This trend is clearly depicted in Figure 2.14. Note that there is no significant difference between the temperature profiles for  $Da \geq 1$ . In addition, it is observed that the temperature profiles approach another limiting case that corresponds to no flow in the porous layer when the porous sleeve permeability or the Darcy number is sufficiently small.

Figures 2.15 and 2.16 show the temperature profiles for various thermal conductivity ratios. For  $k_1/k_2 > 1$ , the thermal conductivity of the fluid is greater than that of the porous sleeve. For  $k_1/k_2 < 1$ , the effective thermal conductivity of the porous sleeve is greater than that of the fluid layer. When  $k_1/k_2 \neq 1$ , there is an abrupt change in temperature gradient across the interface. It is observed that the greater the thermal conductivity ratio, the higher the fluid temperature in the annulus. The value of  $k_1/k_2$

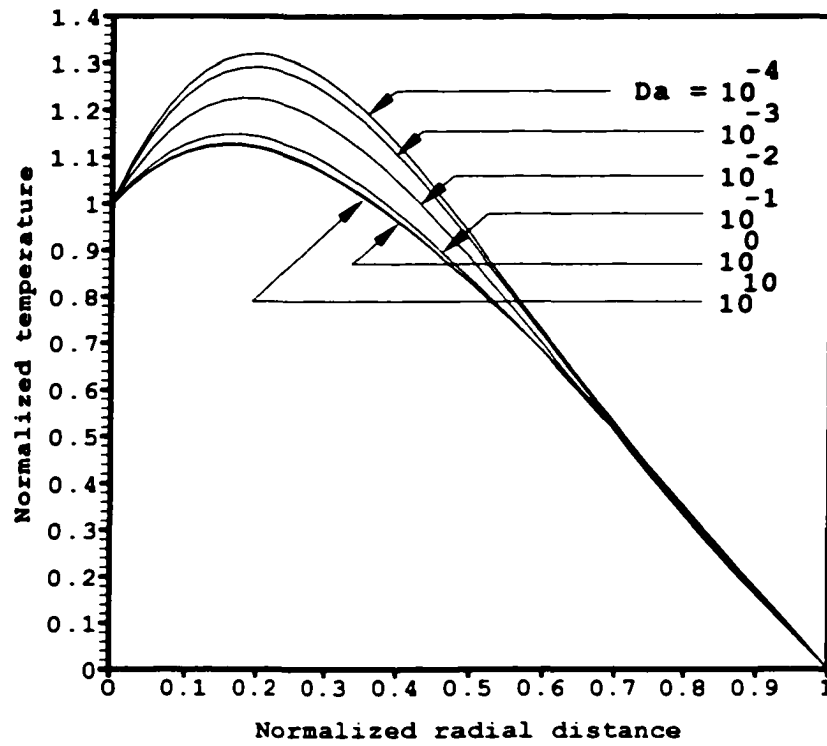


Figure 2.14 Temperature profiles for various Darcy numbers in an eccentric annulus at the gap of  $\theta = \pi/2$  ( $h = 1.5$ ,  $\varepsilon = 0.05$ ,  $Br = 2.0$ , and  $k_1/k_2 = 1$ ).

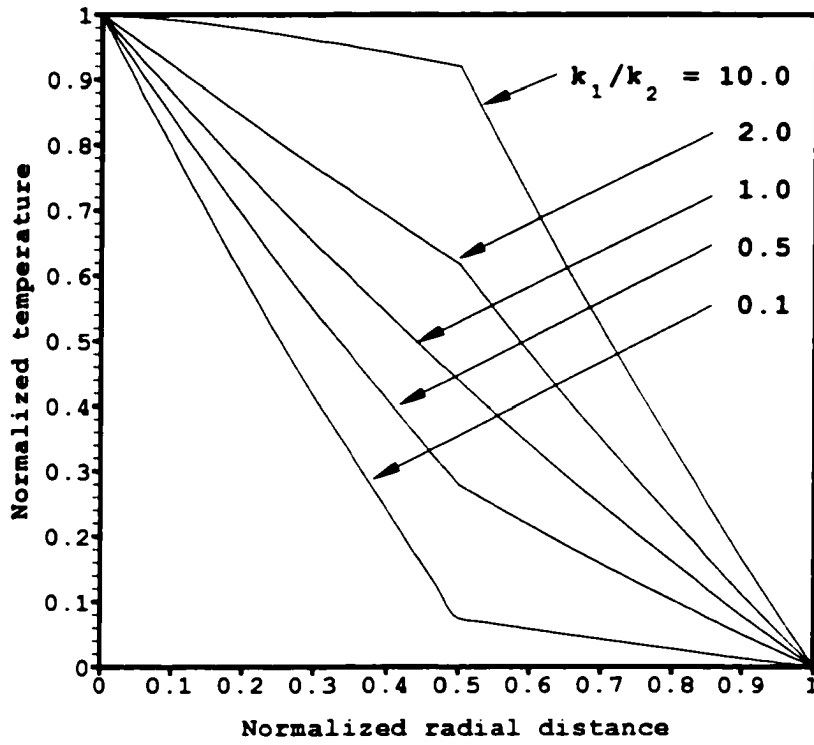


Figure 2.15 Temperature profiles for various effective thermal conductivity ratios in an eccentric annulus at the cross section of  $\theta = \pi/2$  ( $b = 1.5$ ,  $\varepsilon = 0.05$ ,  $Br = 0.1$ , and  $Da = 10^{-2}$ ).

actually represents the ratio of the temperature gradient in the porous sleeve to that in the fluid layer. When the thermal conductivity of the fluid layer is greater than that of the porous sleeve, heat energy is removed more efficiently in the fluid layer. As a result, the temperature gradient in the fluid layer next to the inner cylinder is small, and this causes the temperature at the interface to be accordingly higher.

As displayed in Figure 2.15, when  $Br < 1$ , the temperature profiles in the layers linearly decrease in the radial direction at different gradient. In contrast, as shown in Figure 2.16 where  $Br > 1$ , the temperature profiles in the fluid and porous layers behave in a different manner. In the fluid layer, it is found that the temperature profiles are nonlinear, while in the porous layer, the temperatures decay linearly with radial distance from the interface. This proves that the effect of viscous dissipation is more apparent in the fluid layer than in the porous sleeve. Depending on the effective thermal conductivity ratio, the temperature at the vicinity of the inner cylinder may increase with the radial distance.

Figure 2.17 shows the dependence of average Nusselt number on thermal conductivity ratio and porous sleeve thickness for the rotating inner cylinder. It is observed that the average Nusselt numbers are negative in general. The sign of Nusselt number signifies the direction of the heat flow. These negative Nusselt numbers imply that, instead of removing heat from the rotating inner cylinder, the fluid actually supplies heat to the inner cylinder due to viscous dissipation. As the Darcy number increases, they approach some asymptotic limits that heavily depend on the thermal conductivity ratios. Notice that the smaller the thermal conductivity ratio, the larger the average Nusselt number. At a small Darcy number, heat generation due to viscous dissipation is

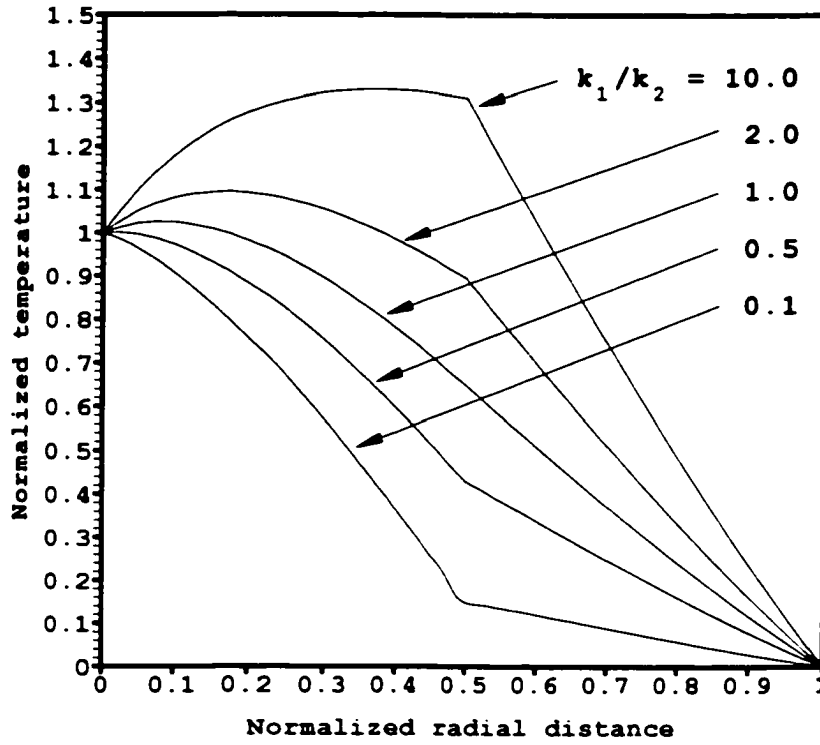


Figure 2.16 Temperature profiles for various effective thermal conductivity ratios in an eccentric annulus at the gap of  $\theta = \pi/2$  ( $b = 1.5$ ,  $\varepsilon = 0.05$ ,  $Br = 2.0$ , and  $Da = 10^{-2}$ ).

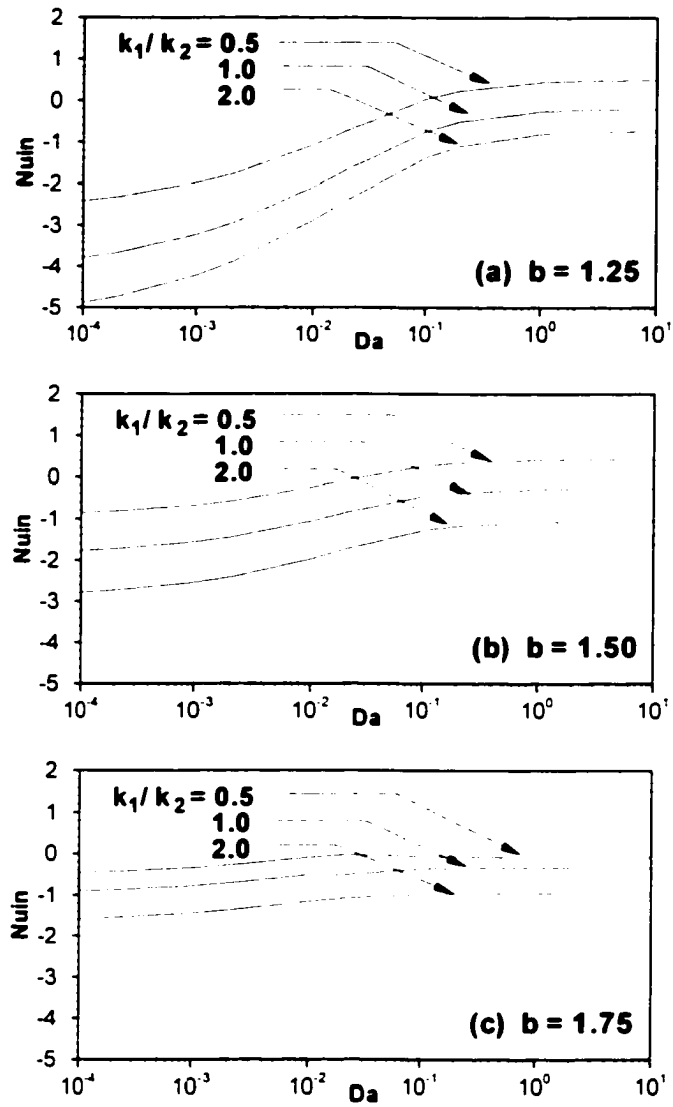


Figure 2.17 Average Nusselt number on the inner cylinder of an eccentric annulus ( $\varepsilon = 0.1$  and  $Br = 1$ ): (a)  $b = 1.25$ , (b)  $b = 1.50$ , (c)  $b = 1.75$ .

significant. The effect of viscous dissipation is more pronounced at a smaller value of  $b$ . As the Darcy number increases, the average Nusselt numbers increases. Since the viscous dissipation is reduced when the Darcy number increases, less heat is generated in the fluid layer. The overheating of fluid is relieved and less heat is transferred to the inner cylinder. In some cases, a further increase in the Darcy number will lead to a reversal of the heat flow direction and the average Nusselt number becomes positive. For example, in the case of  $b = 1.25$ ,  $k_1/k_2 = 0.5$ , and  $Da > 10^{-1}$ , the porous sleeve is thick and its effective thermal conductivity is greater than that of the fluid layer. Under these conditions, the relatively high permeability allows a finite flow in the porous sleeve and thus reduces the velocity gradient in the fluid layer and also the amount of heat generation. Since there is no overheating of fluid, all heat generated is transferred through the outer cylinder.

The average Nusselt numbers on the outer cylinder for various conditions are illustrated in Figure 2.18. Different from those presented in Figure 2.17, the Nusselt numbers on the outer cylinder are always greater than 1.0 and the largest average Nusselt numbers are always associated with  $k_1/k_2 = 2.0$ . Since the Nusselt numbers are always positive, the outer cylinder has served as an effective heat sink. For  $k_1/k_2 = 0.5$ , heat conduction is always the dominant heat transfer mode at small Darcy numbers. However, heat transfer is enhanced with the presence of convection and its enhancement increases with the thermal conductivity ratio. In general, the average Nusselt number is nearly independent of the Darcy number when the porous sleeve is not too thick ( $b > 1.25$ ). Notice that for  $k_1/k_2 > 1$ , the average Nusselt number reaches its minimum at  $Da \approx 10^{-1}$ . Also noticed is that the average Nusselt number increases with a reduction in the

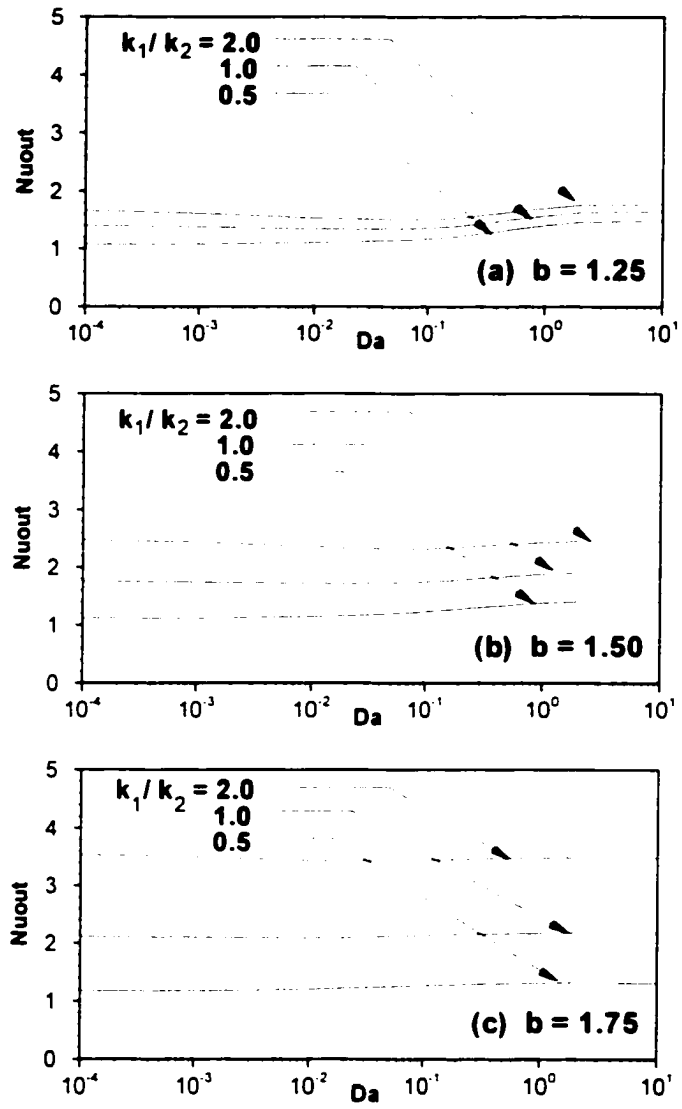


Figure 2.18 Average Nusselt number on the outer cylinder of an eccentric annulus ( $\varepsilon = 0.1$  and  $Br = 1$ ): (a)  $b = 1.25$ , (b)  $b = 1.50$ , (c)  $b = 1.75$ .



thickness of porous sleeve. This is expected because a thicker fluid layer provides more heat enhancement by convection.

The velocity and temperature profiles in an eccentric annulus with different eccentricity ratios and at various clearances are presented in Figures 2.19 and 2.20, respectively. For each eccentricity ratio, the profiles at three gaps ( $\theta = 0, \pi/2$ , and  $\pi$ ) are presented. From Figure 2.19, one notices that the perturbation solutions begin to fail as the eccentricity ratio increases. For example, the velocity profiles should satisfy the boundary condition that requires  $V = 1$  at the inner cylinder. As shown in Figure 2.19, as  $\varepsilon$  increases from 0.01 to 0.05, the discrepancy from the specified boundary condition at the inner cylinder becomes large. However, this deviation from the specified boundary condition is not observed for the temperature profiles (Figure 2.20). It is believed that the discrepancy in velocity at the inner cylinder is attributed to truncation error from both perturbation method and the Taylor expansion of the boundary condition at  $R = (a/b) + \varepsilon \cos\theta$ .

## 2.7 Conclusions

The present study has shown that a closed form solution is possible not only for the flow and temperature fields in a rotating concentric annulus, but also possible for those in a rotating eccentric annulus. The present study also shows that there are two limiting cases for the problem considered. For a sufficiently small Darcy number ( $Da < 10^{-4}$ ), the flow resistance in the porous sleeve becomes so large that there is essentially no flow in the porous sleeve. Hence, the porous sleeve behaves like a solid wall, which renders a porous bearing basically a solid bearing. The heat transfer mechanism in the

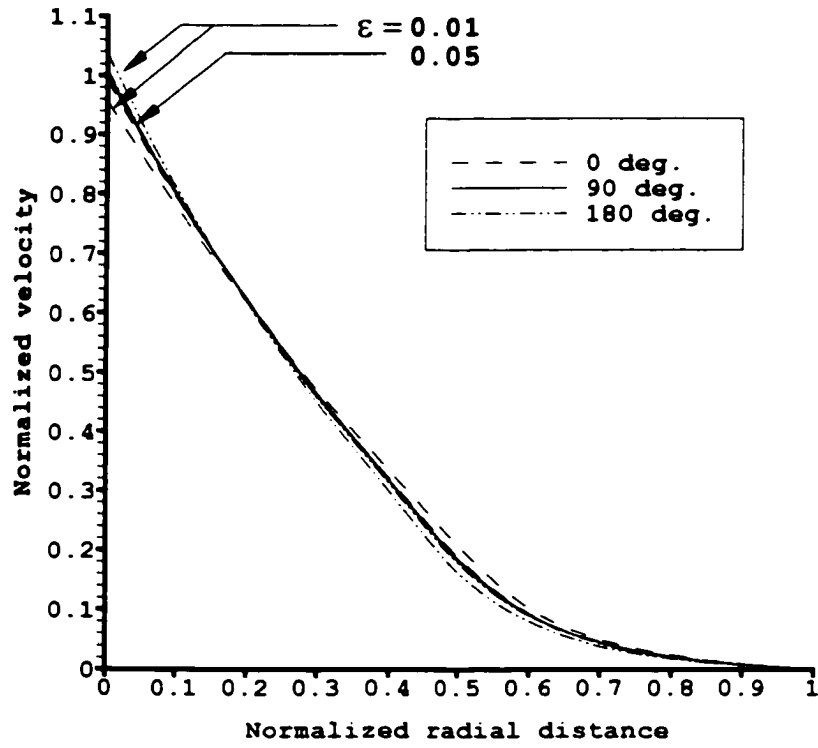


Figure 2.19 Velocity profiles in an eccentric annulus with various eccentricity ratios ( $\varepsilon = 0.01$  and  $0.05$ ) and at various gaps ( $\theta = 0, \pi/2$  and  $\pi$ ) ( $Da = 0.01$ , and  $Br = 2$ ).

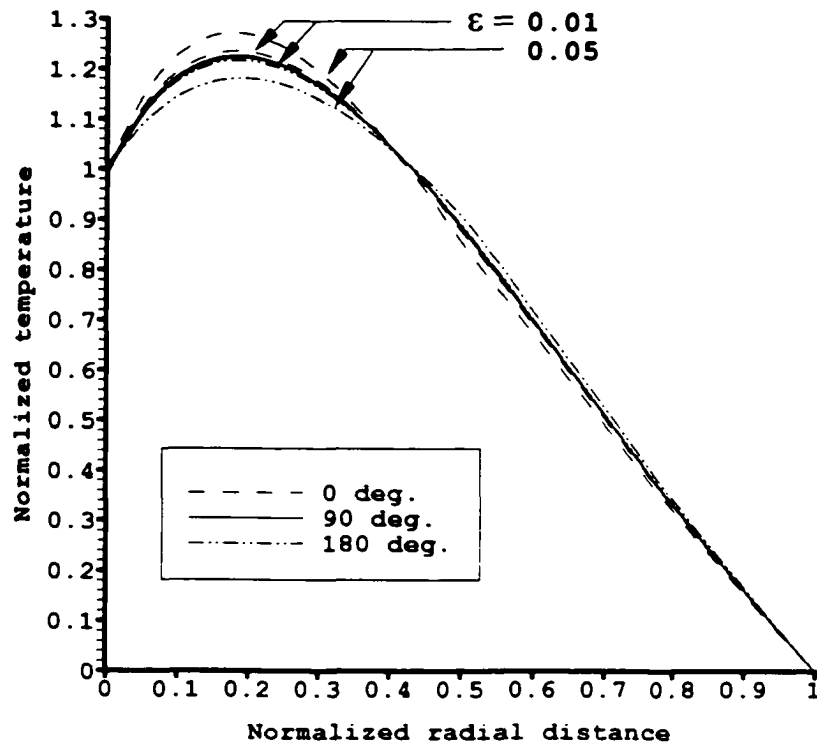


Figure 2.20 Temperature profiles in an eccentric annulus with various eccentricity ratios ( $\epsilon = 0.01$  and  $0.05$ ) and at various gap ( $\theta = 0, \pi/2$  and  $\pi$ ) ( $Da = 0.01$ , and  $Br = 2$ ).

porous sleeve for this case is purely conduction. On the other hand, for a sufficiently large Darcy number ( $Da \geq 1$ ), both velocity and temperature profiles approach those of a single liquid film. In this case, the presence of the porous sleeve has little effect on the flow and temperature distributions.

Since buoyancy effects are neglected in this study, the Brinkman number has effects only on the temperature distribution. For  $Br < 1$ , viscous dissipation in the fluid is insignificant and thus the temperature profile closely resembles that of  $Br = 0$ . For  $Br \geq 1$ , a maximum temperature occurs in the fluid region as a result of viscous dissipation. In some cases, this maximum temperature can exceed that of the inner cylinder.

The thickness of the porous sleeve also plays an important role in the distribution of flow and temperature profiles. When the fluid layer is much thinner than the porous sleeve, a high velocity gradient appears along the rotating inner cylinder producing high stresses and viscous dissipation, which in turn creates a region of overheated fluid. If the porous sleeve is thin, the shear flow in it becomes finite. This leads to a reduction in the velocity gradient and hence suppresses the heat generation by viscous dissipation.

Another important factor affecting the flow and temperature fields in an annular space is the eccentricity. It modifies the velocity and temperature distributions in each clearance. Across the narrowest clearance, the velocity and temperature gradients are larger than those at any other clearance. Across the widest gap, there is normally a thermal plume developing from the top portion of the rotating inner cylinder. For some cases, this thermal plume can grow all the way to completely encompass the inner cylinder and result in a ring of overheated fluid whose temperature is higher than that of the inner cylinder.

The average Nusselt number is found to increase with a reduced porous sleeve thickness. The average Nusselt number of the inner cylinder grows with the Darcy number and approaches some asymptotic values that depend on the effective thermal conductivity ratio. The smaller the effective thermal conductivity ratio, the greater the average Nusselt number on the inner cylinder. On the other hand, a larger average Nusselt number on the outer cylinder always corresponds to a larger effective thermal conductivity ratio. The dependency of Nusselt number on the Darcy number diminishes with a decrease in the porous sleeve thickness.

While the present study has provided useful insights on the flow and temperature distribution in a porous bearing, the solutions however are limited to the cases with a small eccentricity. For porous bearings with a moderate or large eccentricity, the solutions of flow and temperature fields must be obtained by numerical means.

# **CHAPTER THREE**

## **NATURAL CONVECTION IN CONCENTRIC CYLINDERS**

### **WITH A POROUS SLEEVE**

#### **3.1 Introductory Remarks**

In the previous chapter a special case was considered for flow and temperature fields in concentric and eccentric annuli with the inner cylinder rotating at finite angular velocities. This chapter focuses on a totally different scenario in which both cylinders remain stationary but subject to a differential heating between the two cylinders.

Natural convection in horizontal annuli has long been a subject of engineering interest. Earlier work includes several experimental studies with flow visualization by Bishop and Carley (1966) and Powe et al. (1969, 1971). Kuehn and Goldstein (1976, 1980) tackled this problem from both experimental and theoretical-numerical aspects. On the other hand, Charrier-Mojtabi et al. (1979) performed a numerical study on the same subject. Since then, many closely related studies have been reported. In addition, this problem has been extended to the field of porous media. Caltagirone (1976) studied natural convection in a saturated porous medium bounded by two horizontal concentric cylinders. Later, Bau (1984) studied the natural convection in eccentric porous annulus at low Rayleigh numbers using the perturbation method. Actually, the study of flow interaction between the fluid and porous layers can be dated back to the sixties. Ishizawa and Hori (1966) had obtained the normal velocity profiles of a viscous fluid through a porous wall into a narrow gap.

For applications, a horizontal annulus with a porous sleeve is of practical interest. For example, heat transfer in an annulus with scale or rust deposited on the inner surface of the outer cylinder is important for heat exchanger design. The present work examines the flow and temperature fields in a concentric annulus with a porous sleeve. Different from the studies published in the literature, the present study considers a fluid layer and a porous layer of finite thickness.

### 3.2 Problem Statement

The physical configuration of the present study (Figure 3.1) consists of two infinitely long cylinders of radii  $a$  and  $c$ . They are maintained at constant temperatures,  $T_H$  (on the inner cylinder) and  $T_L$  (on the outer cylinder) with  $T_H > T_L$ . In between, a porous sleeve of radius  $b$  is press-fit into the interior of the outer cylinder. Therefore, this configuration consists of an inner fluid region and an outer porous region. It is assumed that the porous matrix is homogeneous, isotropic and is saturated with the same fluid in the fluid region. The effects of temperature on the fluid and porous matrix properties are assumed negligible due to the small temperature difference. It is further assumed that the flow is steady and laminar.

Since both inner and outer cylinders are stationary, the fluid motion is induced by the thermal buoyancy resulting from the differential heating between the cylinders. This buoyancy induced flow and its corresponding temperature distribution are expected to depend on both the radial and azimuthal directions.

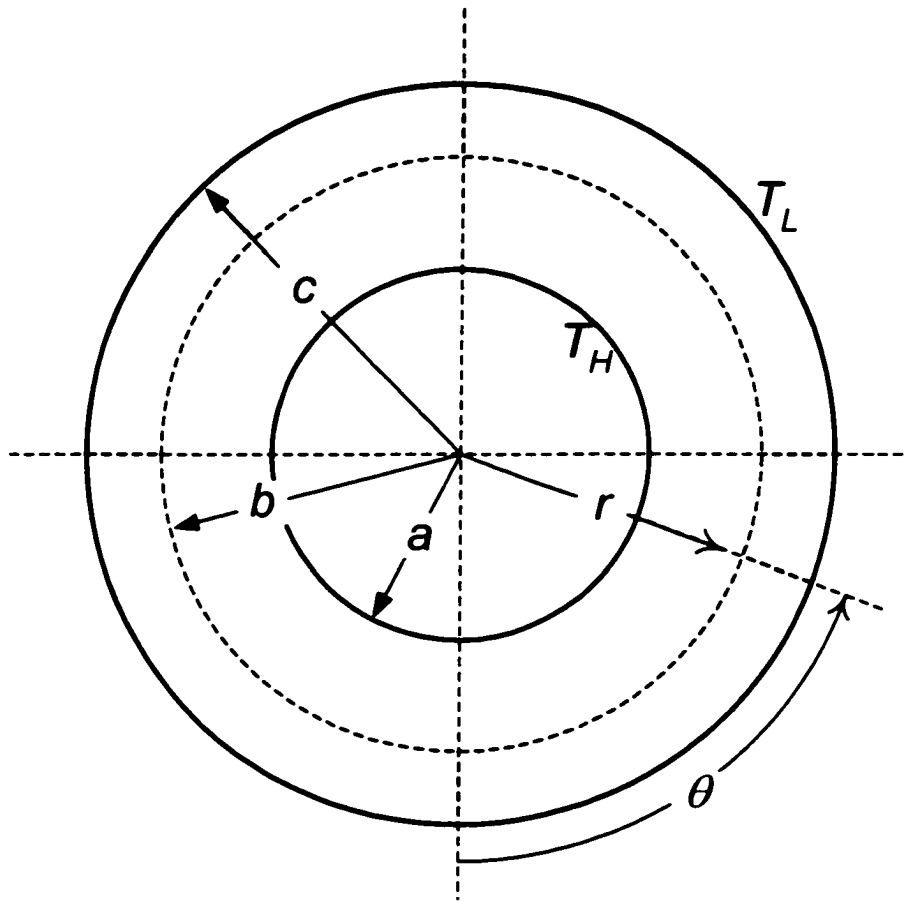


Figure 3.1 A concentric annulus with a porous sleeve subject to differential heating from the inner and outer wall ( $T_H > T_L$ ).



### 3.3 Formulation

Based on the above assumptions, the governing equations, boundary conditions, and interface conditions are now formulated. Unlike the previous chapter, the stream function is introduced in this chapter such that,

$$u_r = -\frac{1}{r} \frac{\partial \psi}{\partial \theta} \quad \text{and} \quad u_\theta = \frac{\partial \psi}{\partial r}. \quad (3.1a, b)$$

This leads to the definition of vorticity in the following form,

$$\nabla^2 \psi = \frac{1}{r} \frac{\partial}{\partial r} \left( r \frac{\partial \psi}{\partial r} \right) + \frac{1}{r^2} \frac{\partial^2 \psi}{\partial \theta^2} = \omega, \quad (3.2)$$

where the vorticity is originally defined as

$$\omega = \frac{1}{r} \frac{\partial}{\partial r} (r u_\theta) - \frac{1}{r} \frac{\partial u_r}{\partial \theta}. \quad (3.3)$$

Using the definitions from Eq. (3.1) for the stream function and employing Boussinesq approximation, the momentum equation for the liquid film is given by Yao (1980),

$$\frac{1}{r} \left( \frac{\partial \psi_1}{\partial r} \frac{\partial \nabla^2 \psi_1}{\partial \theta} - \frac{\partial \psi_1}{\partial \theta} \frac{\partial \nabla^2 \psi_1}{\partial r} \right) = g\beta \left( \sin \theta \frac{\partial T_1}{\partial r} + \frac{\cos \theta}{r} \frac{\partial T_1}{\partial \theta} \right) + \nu \nabla^4 \psi_1, \quad (3.4)$$

where the Laplacian operator is

$$\nabla^2 = \frac{\partial^2}{\partial r^2} + \frac{1}{r} \frac{\partial}{\partial r} + \frac{1}{r^2} \frac{\partial^2}{\partial \theta^2}. \quad (3.5)$$

The subscripts following the dependent variables  $\psi$  and  $T$  are the indices referring to the layers. Same as those in the previous chapter, the index 1 refers to the fluid layer and 2 refers to the porous sleeve. Introduce the following dimensionless parameters,

$$\psi_i = \frac{\psi_i}{\alpha_i}, \quad R = \frac{r}{b}, \quad \text{and} \quad \Theta_i = \frac{T_i - T_l}{\Delta T}. \quad (3.6a, b, c)$$

The Laplacian operator can be normalized to give

$$\bar{\nabla}^2 = \frac{\partial^2}{\partial R^2} + \frac{1}{R} \frac{\partial}{\partial R} + \frac{1}{R^2} \frac{\partial^2}{\partial \theta^2} = b^2 \nabla^2. \quad (3.7)$$

The bar on top of the Laplacian operator indicates that it is dimensionless. The momentum equation for the fluid layer then becomes

$$\frac{1}{Pr} \frac{1}{R} \left( \frac{\partial \Psi_1}{\partial R} \frac{\partial \bar{\nabla}^2 \Psi_1}{\partial \theta} - \frac{\partial \Psi_1}{\partial \theta} \frac{\partial \bar{\nabla}^2 \Psi_1}{\partial R} \right) = Ra \left( \sin \theta \frac{\partial \Theta_1}{\partial R} + \frac{\cos \theta}{R} \frac{\partial \Theta_1}{\partial \theta} \right) + \bar{\nabla}^4 \Psi_1. \quad (3.8)$$

where

$$Pr = \frac{\nu}{\alpha_1} \quad \text{and} \quad Ra = \frac{g \beta \Delta T h^3}{\nu \alpha_1}. \quad (3.9 - 3.10)$$

The dimensional momentum equation for the porous sleeve is given by

$$\frac{\rho}{r} \left( \frac{\partial \psi_2}{\partial r} \frac{\partial \nabla^2 \psi_2}{\partial \theta} - \frac{\partial \psi_2}{\partial \theta} \frac{\partial \nabla^2 \psi_2}{\partial r} \right) = \rho g \beta \left( \sin \theta \frac{\partial T_2}{\partial r} + \frac{\cos \theta}{r} \frac{\partial T_2}{\partial \theta} \right) - \frac{\mu}{K} \nabla^2 \psi_2 + \bar{\mu} \nabla^4 \psi_2. \quad (3.11)$$

Assuming  $\bar{\mu} = \mu$ , the above equation can be normalized to give

$$\begin{aligned} & \frac{1}{Pr} \frac{1}{R} \left( \frac{\partial \Psi_2}{\partial R} \frac{\partial \bar{\nabla}^2 \Psi_2}{\partial \theta} - \frac{\partial \Psi_2}{\partial \theta} \frac{\partial \bar{\nabla}^2 \Psi_2}{\partial R} \right) \\ &= Ra \left( \sin \theta \frac{\partial \Theta_2}{\partial R} + \frac{\cos \theta}{R} \frac{\partial \Theta_2}{\partial \theta} \right) - \frac{1}{Da} \bar{\nabla}^2 \Psi_2 + \bar{\nabla}^4 \Psi_2. \end{aligned} \quad (3.12)$$

where the Darcy number is defined as

$$Da = \frac{K}{h^2}. \quad (3.13)$$

Similar to Yao (1980), the dimensional energy equation takes the general form of

$$\frac{1}{r} \left( \frac{\partial \psi_i}{\partial r} \frac{\partial T_i}{\partial \theta} - \frac{\partial \psi_i}{\partial \theta} \frac{\partial T_i}{\partial r} \right) = \alpha_i \nabla^2 T_i. \quad (3.14)$$

Again, introducing the dimensionless parameters (Eqs. (3.6)), one can rewrite the energy equation for each layer as

$$\frac{1}{R} \left( \frac{\partial \Psi_1}{\partial R} \frac{\partial \Theta_1}{\partial \theta} - \frac{\partial \Psi_1}{\partial \theta} \frac{\partial \Theta_1}{\partial R} \right) = \bar{\nabla}^2 \Theta_1, \text{ and} \quad (3.15)$$

$$\frac{\alpha_1}{R} \left( \frac{\partial \Psi_2}{\partial R} \frac{\partial \Theta_2}{\partial \theta} - \frac{\partial \Psi_2}{\partial \theta} \frac{\partial \Theta_2}{\partial R} \right) = \alpha_2 \bar{\nabla}^2 \Theta_2. \quad (3.16)$$

The boundary and interface conditions are

$$\text{at } R = a b, \quad \frac{\partial \Psi_1}{\partial R} = \frac{\partial \Psi_1}{\partial \theta} = 0, \quad \Theta_1 = 1, \quad (3.17a, b, c)$$

$$\text{at } R = c h, \quad \frac{\partial \Psi_2}{\partial R} = \frac{\partial \Psi_2}{\partial \theta} = 0, \quad \Theta_2 = 0, \quad (3.17d, e, f)$$

$$\text{at } R = l, \quad \frac{\partial \Psi_1}{\partial R} = \frac{\partial \Psi_2}{\partial R}, \quad \frac{\partial \Psi_1}{\partial \theta} = \frac{\partial \Psi_2}{\partial \theta}, \quad (3.17g, h)$$

$$\bar{\nabla}^2 \Psi_1 = \bar{\nabla}^2 \Psi_2, \quad \frac{\partial \bar{\nabla}^2 \Psi_1}{\partial R} = \frac{\partial \bar{\nabla}^2 \Psi_2}{\partial R} - \frac{1}{Da} \frac{\partial \Psi_2}{\partial R}, \quad (3.17i, j)$$

$$\Theta_1 = \Theta_2, \quad \text{and} \quad k_1 \frac{\partial \Theta_1}{\partial R} = k_2 \frac{\partial \Theta_2}{\partial R}. \quad (3.17k, l)$$

The derivation of these interface conditions are explained in detail and presented in Appendix C.

### 3.4 Perturbation Methods

To solve the above system of equations, (3.8), (3.12), (3.15) and (3.16) the perturbation method is employed by assuming that the Rayleigh number is the small perturbed quantity. It is further assumed that the solutions take the following forms.

$$\Psi_1 = Ra \Psi_{11} + Ra^2 \Psi_{12} + \dots, \quad \Theta_1 = \Theta_{10} + Ra \Theta_{11} + \dots, \quad (3.18a, b)$$

$$\Psi_2 = Ra\Psi_{21} + Ra^2\Psi_{22} + \dots, \quad \text{and} \quad \Theta_2 = \Theta_{20} + Ra\Theta_{21} + \dots \quad (3.18c, d)$$

Substitute these solution forms into the governing equations, one yields

$$\begin{aligned} & \frac{1}{Pr} \frac{1}{R} \left[ \frac{\partial}{\partial R} (Ra\Psi_{11} + Ra^2\Psi_{12} + \dots) \frac{\partial \bar{\nabla}^2}{\partial \theta} (Ra\Psi_{11} + Ra^2\Psi_{12} + \dots) \right. \\ & \quad \left. - \frac{\partial}{\partial \theta} (Ra\Psi_{11} + Ra^2\Psi_{12} + \dots) \frac{\partial \bar{\nabla}^2}{\partial R} (Ra\Psi_{11} + Ra^2\Psi_{12} + \dots) \right] \\ & = Ra \left[ \sin \theta \frac{\partial}{\partial R} (\Theta_{10} + Ra\Theta_{11} + \dots) + \frac{\cos \theta}{R} \frac{\partial}{\partial \theta} (\Theta_{10} + Ra\Theta_{11} + \dots) \right] \\ & \quad + \bar{\nabla}^4 (Ra\Psi_{11} + Ra^2\Psi_{12} + \dots). \end{aligned} \quad (3.19)$$

$$\begin{aligned} & \frac{1}{Pr} \frac{1}{R} \left[ \frac{\partial}{\partial R} (Ra\Psi_{21} + Ra^2\Psi_{22} + \dots) \frac{\partial \bar{\nabla}^2}{\partial \theta} (Ra\Psi_{21} + Ra^2\Psi_{22} + \dots) \right. \\ & \quad \left. - \frac{\partial}{\partial \theta} (Ra\Psi_{21} + Ra^2\Psi_{22} + \dots) \frac{\partial \bar{\nabla}^2}{\partial R} (Ra\Psi_{21} + Ra^2\Psi_{22} + \dots) \right] \\ & = Ra \left[ \sin \theta \frac{\partial}{\partial R} (\Theta_{20} + Ra\Theta_{21} + \dots) + \frac{\cos \theta}{R} \frac{\partial}{\partial \theta} (\Theta_{20} + Ra\Theta_{21} + \dots) \right] \\ & \quad - \frac{1}{Da} \bar{\nabla}^2 (Ra\Psi_{21} + Ra^2\Psi_{22} + \dots) + \bar{\nabla}^4 (Ra\Psi_{21} + Ra^2\Psi_{22} + \dots). \end{aligned} \quad (3.20)$$

$$\begin{aligned} & \frac{1}{R} \left[ \frac{\partial}{\partial R} (Ra\Psi_{11} + Ra^2\Psi_{12} + \dots) \frac{\partial}{\partial \theta} (\Theta_{10} + Ra\Theta_{11} + \dots) \right. \\ & \quad \left. - \frac{\partial}{\partial \theta} (Ra\Psi_{11} + Ra^2\Psi_{12} + \dots) \frac{\partial}{\partial R} (\Theta_{10} + Ra\Theta_{11} + \dots) \right] \\ & = \bar{\nabla}^2 (\Theta_{10} + Ra\Theta_{11} + \dots), \text{ and} \end{aligned} \quad (3.21)$$

$$\frac{\alpha_1}{R} \left[ \frac{\partial}{\partial R} (Ra\Psi_{21} + Ra^2\Psi_{22} + \dots) \frac{\partial}{\partial \theta} (\Theta_{20} + Ra\Theta_{21} + \dots) \right.$$

$$\begin{aligned}
& -\frac{\partial}{\partial \theta} (Ra \Psi_{21} + Ra^2 \Psi_{22} + \dots) \frac{\partial}{\partial R} (\Theta_{20} + Ra \Theta_{21} + \dots) \Big] \\
& = \alpha_2 \bar{\nabla}^2 (\Theta_{20} + Ra \Theta_{21} + \dots). \tag{3.22}
\end{aligned}$$

The boundary and interface conditions (3.17) become

$$\text{at } R = a/b, \quad \frac{\partial}{\partial R} (Ra \Psi_{11} + Ra^2 \Psi_{12} + \dots) = \frac{\partial}{\partial \theta} (Ra \Psi_{11} + Ra^2 \Psi_{12} + \dots) = 0. \tag{3.23a, b}$$

$$\Theta_{10} + Ra \Theta_{11} + \dots = 1. \tag{3.23c}$$

$$\text{at } R = c/b, \quad \frac{\partial}{\partial R} (Ra \Psi_{21} + Ra^2 \Psi_{22} + \dots) = \frac{\partial}{\partial \theta} (Ra \Psi_{21} + Ra^2 \Psi_{22} + \dots) = 0. \tag{3.23d, e}$$

$$\Theta_{20} + Ra \Theta_{21} + \dots = 0. \tag{3.23f}$$

$$\text{at } R = 1, \quad \frac{\partial \Psi_1}{\partial R} (Ra \Psi_{11} + Ra^2 \Psi_{12} + \dots) = \frac{\partial}{\partial R} (Ra \Psi_{21} + Ra^2 \Psi_{22} + \dots). \tag{3.23g}$$

$$\frac{\partial}{\partial \theta} (Ra \Psi_{11} + Ra^2 \Psi_{12} + \dots) = \frac{\partial}{\partial \theta} (Ra \Psi_{21} + Ra^2 \Psi_{22} + \dots). \tag{3.23h}$$

$$\bar{\nabla}^2 (Ra \Psi_{11} + Ra^2 \Psi_{12} + \dots) = \bar{\nabla}^2 (Ra \Psi_{21} + Ra^2 \Psi_{22} + \dots). \tag{3.23i}$$

$$\frac{\partial \bar{\nabla}^2}{\partial R} (Ra \Psi_{11} + Ra^2 \Psi_{12} + \dots) = \frac{\partial \bar{\nabla}^2}{\partial R} (Ra \Psi_{21} + Ra^2 \Psi_{22} + \dots)$$

$$- \frac{1}{Da} \frac{\partial}{\partial R} (Ra \Psi_{21} + Ra^2 \Psi_{22} + \dots). \tag{3.23j}$$

$$\Theta_{10} + Ra \Theta_{11} + \dots = \Theta_{20} + Ra \Theta_{21} + \dots, \text{ and } \tag{3.23k}$$

$$k_1 \frac{\partial}{\partial R} (\Theta_{10} + Ra \Theta_{11} + \dots) = k_2 \frac{\partial}{\partial R} (\Theta_{20} + Ra \Theta_{21} + \dots). \tag{3.23l}$$

### 3.5 Method of Solution

Following very closely with the approach outlined in the previous chapter, one collects terms in Eqs. (3.19) to (3.23) with the same power of  $Ra$ . To facilitate the solution process, transformation is used so that the equations are further simplified.

#### (a) First Leading Terms in the Temperature Field ( $Ra^0$ )

Collecting terms of zero order of  $Ra$ , one obtains the following equations,

$$\bar{\nabla}^2 \Theta_{10} = 0, \quad \text{and} \quad \bar{\nabla}^2 \Theta_{20} = 0. \quad (3.24a, b)$$

$$\text{at } R = a/b, \quad \Theta_{10} = 1. \quad (3.25a)$$

$$\text{at } R = c/b, \quad \Theta_{20} = 0. \quad (3.25b)$$

$$\text{at } R = l, \quad \Theta_{10} = \Theta_{20}, \quad \text{and} \quad k_1 \frac{\partial \Theta_{10}}{\partial R} = k_2 \frac{\partial \Theta_{20}}{\partial R}. \quad (3.25c, d)$$

To solve the set of equations above, Finite Fourier Transform is used, in which the independent variable  $\theta$  is transformed to a parameter  $\sigma$ . Osizik (1968) has successfully demonstrated the use of this transform in classical heat conduction problems. In the present work, there is no prescribed boundary condition for the independent variable  $\theta$  except the requirement that the flow and temperature fields have to be continuous around the annulus with a period of  $2\pi$ . This transformation is performed as follows.

Fourier transform:

$$\bar{\Phi}(r, n, \sigma) = \bar{F}\{\Phi(r, \tilde{\sigma})\} = \int_0^{2\pi} \cos n(\sigma - \tilde{\sigma}) \cdot \Phi(r, \tilde{\sigma}) \cdot d\tilde{\sigma}, \text{ and} \quad (3.26a)$$

Inverse transform:

$$\Phi(r, \sigma) = \frac{1}{2\pi} \bar{\Phi}(r, 0, \sigma) + \frac{1}{\pi} \sum_{n=1}^{\infty} \bar{\Phi}(r, n, \sigma). \quad (3.26b)$$

The bar on top of the function  $\Phi$  implies that the function is in the transformed domain. Recognize that Eqs. (3.24) can be expressed as

$$\frac{\partial^2 \bar{\Theta}_{10}}{\partial R^2} + \frac{1}{R} \frac{\partial \bar{\Theta}_{10}}{\partial R} + \frac{1}{R^2} \frac{\partial^2 \bar{\Theta}_{10}}{\partial \theta^2} = 0, \quad \text{and} \quad \frac{\partial^2 \bar{\Theta}_{20}}{\partial R^2} + \frac{1}{R} \frac{\partial \bar{\Theta}_{20}}{\partial R} + \frac{1}{R^2} \frac{\partial^2 \bar{\Theta}_{20}}{\partial \theta^2} = 0. \quad (3.27a, b)$$

Apply the transform (3.26a) on Eq. (3.27), one yields

$$\frac{d^2 \bar{\Theta}_{10}}{dR^2} + \frac{1}{R} \frac{d \bar{\Theta}_{10}}{dR} - \frac{n^2}{R^2} \bar{\Theta}_{10} = 0, \quad \text{and} \quad (3.28a)$$

$$\frac{d^2 \bar{\Theta}_{20}}{dR^2} + \frac{1}{R} \frac{d \bar{\Theta}_{20}}{dR} - \frac{n^2}{R^2} \bar{\Theta}_{20} = 0, \quad (3.28b)$$

where

$$n = 0, 1, 2, 3, \dots \quad (3.29)$$

Clearly, the solution of Eq. (3.28) depends on the value of  $n$ . Recognize that the solutions can be classified into two categories.

For  $n = 0$ , the solutions are

$$\bar{\Theta}_{10} = C_{101}^0 + C_{102}^0 \ln(R), \quad \text{and} \quad \bar{\Theta}_{20} = C_{201}^0 + C_{202}^0 \ln(R). \quad (3.30a, b)$$

For  $n \neq 0$ , the solutions are

$$\bar{\Theta}_{10} = C_{101}^n R^n + C_{102}^n R^{-n}, \quad \text{and} \quad \bar{\Theta}_{20} = C_{201}^n R^n + C_{202}^n R^{-n}. \quad (3.31a, b)$$

These solutions are subject to the boundary and interface conditions (3.25). Also noticed is that the boundary condition (3.32a) also depends on the value of  $n$ . This is more clearly shown in Appendix D.

$$\text{At } R = a/b, \quad \bar{\Theta}_{10} = \begin{cases} 2\pi, & n = 0. \\ 0, & n \neq 0. \end{cases} \quad (3.32a)$$

$$\text{At } R = c/b, \quad \bar{\Theta}_{20} = 0. \quad (3.32b)$$

$$\text{At } R = l, \quad \bar{\Theta}_{10} = \bar{\Theta}_{20}, \quad \text{and} \quad \frac{\partial \bar{\Theta}_{10}}{\partial R} = \frac{k_2}{k_1} \frac{\partial \bar{\Theta}_{20}}{\partial R}. \quad (3.32c, d)$$

For  $n \neq 0$ , it is easy to prove that the solutions to Eq. (3.28) are trivial. For  $n = 0$ , however, the solutions are non-trivial and are given by

$$\Theta_{10} = \frac{(k_1/k_2)\ln(c/b) - \ln(R)}{(k_1/k_2)\ln(c/b) - \ln(a/b)}, \text{ and} \quad (3.33a)$$

$$\Theta_{20} = \frac{(k_1/k_2)\ln(c/b) - (k_1/k_2)\ln(R)}{(k_1/k_2)\ln(c/b) - \ln(a/b)}. \quad (3.33b)$$

Notice that the base solutions for the temperature field are merely dependent on the radial distance. This is consistent with the assumption made. Since the base solutions correspond to the case of  $Ra = 0$ , thermal convection is absent under this condition and heat conduction is the heat transfer mode. For this reason, the dependence of azimuthal angle is not required for the base solution. Notice that Eqs. (3.33a) and (3.33b) are identical if  $k_1 = k_2$ .

#### (b) First Leading Terms in the Velocity Field ( $Ra'$ )

Given the base solutions (3.33), one can proceed to solve the system of equations of the first order of  $Ra$ . Extracting terms corresponding to  $Ra$  in Eqs. (3.19) and (3.20), one obtains

$$\bar{\nabla}^4 \Psi_{11} = - \left( \sin \theta \frac{\partial \Theta_{10}}{\partial R} + \frac{\cos \theta}{R} \frac{\partial \Theta_{10}}{\partial \theta} \right), \text{ and} \quad (3.34)$$

$$\bar{\nabla}^4 \Psi_{21} - \frac{1}{Da} \bar{\nabla}^2 \Psi_{21} = - \left( \sin \theta \frac{\partial \Theta_{20}}{\partial R} + \frac{\cos \theta}{R} \frac{\partial \Theta_{20}}{\partial \theta} \right). \quad (3.35)$$

$$\text{at } R = a/b, \quad \frac{\partial \Psi_{11}}{\partial R} = \frac{\partial \Psi_{11}}{\partial \theta} = 0, \quad (3.36a, b)$$

$$\text{at } R = c/b, \quad \frac{\partial \Psi_{21}}{\partial R} = \frac{\partial \Psi_{21}}{\partial \theta} = 0, \quad (3.36c, d)$$

$$\text{at } R = 1, \quad \frac{\partial \Psi_{11}}{\partial R} = \frac{\partial \Psi_{21}}{\partial R}, \quad \frac{\partial \Psi_{11}}{\partial \theta} = \frac{\partial \Psi_{21}}{\partial \theta}, \quad (3.36e, f)$$



$$\bar{\nabla}^2 \Psi_{11} = \bar{\nabla}^2 \Psi_{21}, \quad \text{and} \quad \frac{\partial \bar{\nabla}^2 \Psi_{11}}{\partial R} = \frac{\partial \bar{\nabla}^2 \Psi_{21}}{\partial R} - \frac{1}{Da} \frac{\partial \Psi_{21}}{\partial R}. \quad (3.36g, h)$$

With the introduction of the dimensionless vorticity, the above equations can be split into two sets of equations of lower order. The dimensionless vorticities for the fluid and porous layers are defined as

$$\bar{\nabla}^2 \Psi_{11} = \Omega_{11} \quad \text{and} \quad \bar{\nabla}^2 \Psi_{21} = \Omega_{21}. \quad (3.37 - 38)$$

Based on the temperature profiles obtained for  $\Theta_{10}$  and  $\Theta_{20}$ , one can first conclude that

$$\frac{\partial \Theta_{10}}{\partial R} = -\frac{q}{R}, \quad \frac{\partial \Theta_{20}}{\partial R} = -\frac{k_1}{k_2} \frac{q}{R}. \quad (3.39 - 40)$$

$$\frac{\partial \Theta_{10}}{\partial \theta} = 0, \quad \text{and} \quad \frac{\partial \Theta_{20}}{\partial \theta} = 0. \quad (3.41 - 42)$$

where

$$q = \frac{1}{(k_1/k_2) \ln(c/b) - \ln(a/b)}. \quad (3.43)$$

Now, introduce the dimensionless vorticities (3.37) and (2.38) into the governing equations and then perform the Finite Fourier transform, one obtain the general equations below,

$$\frac{d^2 \bar{\Omega}_{11}}{dR^2} + \frac{1}{R} \frac{d\bar{\Omega}_{11}}{dR} - \frac{n^2}{R^2} \bar{\Omega}_{11} = -\frac{\partial \Theta_{10}}{\partial R} \bar{F} \{ \sin \theta \}, \quad \text{and} \quad (3.44)$$

$$\frac{d^2 \bar{\Omega}_{21}}{dX^2} + \frac{1}{X} \frac{d\bar{\Omega}_{21}}{dX} - \left( 1 + \frac{n^2}{X^2} \right) \bar{\Omega}_{21} = -Da \frac{\partial \Theta_{20}}{\partial R} \bar{F} \{ \sin \theta \}, \quad (3.45)$$

where

$$n = 0, 1, 2, 3, \dots, \quad X = \gamma R, \quad \text{and} \quad \gamma = \frac{1}{\sqrt{Da}}. \quad (3.46a, b, c)$$

The boundary and interface conditions (3.36) become

$$\text{at } R = a/b, \quad \frac{d\bar{\Psi}_{11}}{dR} = j n \bar{\Psi}_{11} = 0, \quad (3.47a, b)$$

$$\text{at } R = c/b, \quad \frac{d\bar{\Psi}_{21}}{dR} = j n \bar{\Psi}_{21} = 0, \quad (3.47c, d)$$

$$\text{at } R = 1, \quad \frac{d\bar{\Psi}_{11}}{dR} = \frac{d\bar{\Psi}_{21}}{dR}, \quad j n \bar{\Psi}_{11} = j n \bar{\Psi}_{21}, \quad (3.47e, f)$$

$$\bar{\Omega}_{11} = \bar{\Omega}_{21}, \quad \text{and} \quad \frac{d\bar{\Omega}_{11}}{dR} = \frac{d\bar{\Omega}_{21}}{dR} - \frac{1}{Da} \frac{d\bar{\Psi}_{21}}{dR}, \quad (3.47g, h)$$

where,  $j = \sqrt{-1}$ .

Before solving the equations, one can first evaluate the non-homogeneous terms in equations (3.44) and (3.45). According to the integral transform (3.26a).

$$\bar{F}\{\sin\theta\} = \int_0^{2\pi} \cos n(\sigma - \theta) \sin(\theta) d\theta. \quad (3.48a)$$

One yields,

$$\bar{F}\{\sin\theta\} = \begin{cases} \pi \sin\sigma, & n = 1, \\ 0, & \text{otherwise.} \end{cases} \quad (3.48b)$$

A more complete list of the Finite Fourier Transformation is compiled and provided in Appendix D. It is found that the transformed non-homogeneous terms are essentially zero unless  $n = 1$ . Since the set of equations now reduces to Laplace equations that subject to the boundary condition whose values and gradients are zero, this leads to trivial solutions. Therefore, only the formulation for  $n = 1$  will provide a nontrivial solution. The governing equations in terms of dimensionless vorticity are

$$\frac{d^2 \bar{\Omega}_{11}}{dR^2} + \frac{1}{R} \frac{d\bar{\Omega}_{11}}{dR} - \frac{1}{R^2} \bar{\Omega}_{11} = \frac{2\bar{F}_{11}}{R}, \quad (3.49)$$

$$\frac{d^2 \bar{\Omega}_{21,1}}{dX^2} + \frac{1}{X} \frac{d\bar{\Omega}_{21,1}}{dX} - \left(1 + \frac{1}{X^2}\right) \bar{\Omega}_{21,1} = -\frac{\gamma \bar{\Gamma}_{21}}{X}, \quad (3.50)$$

where, for convenience, the following shorthand notation have been introduced

$$\bar{\Gamma}_{11} = -\frac{q}{2} \pi \sin \sigma, \quad \text{and} \quad \bar{\Gamma}_{21} = \frac{k_1}{k_2} Da q \pi \sin \sigma, \quad (3.51a, b)$$

so that the solutions (3.52) and (3.53) will take a simpler form. Notice that  $\bar{\Gamma}_{11}$  and  $\bar{\Gamma}_{21}$  are only angular dependent. The bar on top of these parameters indicates that the parameters are defined in the transformed domain and therefore expressed in terms of the transformed angle  $\sigma$ . In equations (3.49) and (3.50), the subscript  $l$  after the comma indicates that the vorticity is for  $n = l$ . The general forms of solutions are given by

$$\bar{\Omega}_{11,1} = \bar{A}_{11,1} R + \bar{B}_{11,1} R^{-1} + \bar{\Gamma}_{11} R \ln(R), \quad \text{and} \quad (3.52)$$

$$\bar{\Omega}_{21,1} = \bar{A}_{21,1} I_1(\gamma R) + \bar{B}_{21,1} K_1(\gamma R) + \bar{\Gamma}_{21} R^{-1}, \quad (3.53)$$

where  $I_1(\gamma R)$  and  $K_1(\gamma R)$  are the *modified Bessel functions of the first order of the first and second kinds*, and  $\bar{A}_{11,1}$ ,  $\bar{B}_{11,1}$ ,  $\bar{A}_{21,1}$ , and  $\bar{B}_{21,1}$  are  $\sigma$ -dependent functions that behave like constants in the transformed domain. Here, the subscripts  $l$  after the comma in the functions mentioned above imply the same thing as those with the vorticity. According to the definitions (3.37) and (3.38), for  $n = l$ ,

$$\bar{\Omega}_{11,1} = \bar{\nabla}^2 \bar{\Psi}_{11,1} = \frac{d^2 \bar{\Psi}_{11,1}}{dR^2} + \frac{1}{R} \frac{d\bar{\Psi}_{11,1}}{dR} - \frac{1}{R^2} \bar{\Psi}_{11,1}, \quad \text{and} \quad (3.54)$$

$$\bar{\Omega}_{21,1} = \bar{\nabla}^2 \bar{\Psi}_{21,1} = \frac{d^2 \bar{\Psi}_{21,1}}{dR^2} + \frac{1}{R} \frac{d\bar{\Psi}_{21,1}}{dR} - \frac{1}{R^2} \bar{\Psi}_{21,1}. \quad (3.55)$$

Therefore, to obtain the stream functions, we need to solve

$$\frac{d^2 \bar{\Psi}_{11,1}}{dR^2} + \frac{1}{R} \frac{d\bar{\Psi}_{11,1}}{dR} - \frac{1}{R^2} \bar{\Psi}_{11,1} = \bar{A}_{11,1} R + \bar{B}_{11,1} R^{-1} + \bar{\Gamma}_{11} R \ln(R), \quad \text{and} \quad (3.56)$$

$$\frac{d^2 \bar{\Psi}_{21,1}}{dR^2} + \frac{1}{R} \frac{d \bar{\Psi}_{21,1}}{dR} - \frac{1}{R^2} \bar{\Psi}_{21,1} = \bar{A}_{21,1} I_1(\gamma R) + \bar{B}_{21,1} K_1(\gamma R) + \bar{F}_{21} R^{-1}. \quad (3.57)$$

The solutions for these equations are

$$\bar{\Psi}_{11,1} = \frac{\bar{A}_{11,1}}{8} R^3 + \frac{\bar{B}_{11,1}}{2} R \ln(R) + \bar{C}_{11,1} R + \bar{D}_{11,1} R^{-1} + \left( \frac{\ln(R)}{8} - \frac{3}{32} \right) \bar{F}_{11} R^3, \text{ and} \quad (3.58)$$

$$\bar{\Psi}_{21,1} = \frac{\bar{A}_{21,1}}{\gamma^2} I_1(\gamma R) + \frac{\bar{B}_{21,1}}{\gamma^2} K_1(\gamma R) + \bar{C}_{21,1} R + \bar{D}_{21,1} R^{-1} + \frac{\bar{F}_{21}}{2} R \ln(R), \quad (3.59)$$

where  $\bar{C}_{11,1}$ ,  $\bar{D}_{11,1}$ ,  $\bar{C}_{21,1}$ , and  $\bar{D}_{21,1}$  are four additional  $\sigma$ -dependent functions that behaves like constants in the transformed domain. Apply the boundary and interface conditions (3.47), one obtains

$$\bar{A}_{11,1} = -\bar{B}_{11,1} + I_1(\gamma) \bar{A}_{21,1} + K_1(\gamma) \bar{B}_{21,1} + \bar{F}_{21}, \quad (3.60a)$$

$$\begin{aligned} \bar{B}_{11,1} = & \left[ a_{r1} (b_{421} c_{821} - b_{821} c_{421}) + b_{r1} (a_{821} c_{421} - a_{421} c_{821}) \right. \\ & \left. + c_{r1} (a_{421} b_{821} - a_{821} b_{421}) \right] / d_1, \end{aligned} \quad (3.60b)$$

$$\bar{C}_{11,1} = -\frac{(a/b)^2}{4} \bar{A}_{11,1} - \left( \frac{\ln(a/b)}{2} + \frac{1}{4} \right) \bar{B}_{11,1} - (a/b)^2 \left( \frac{\ln(a/b)}{4} - \frac{1}{8} \right) \bar{F}_{11}, \quad (3.60c)$$

$$\bar{D}_{11,1} = \frac{(a/b)^4}{8} \bar{A}_{11,1} + \frac{(a/b)^2}{4} \bar{B}_{11,1} + (a/b)^4 \left( \frac{\ln(a/b)}{8} - \frac{1}{32} \right) \bar{F}_{11}, \quad (3.60d)$$

$$\begin{aligned} \bar{A}_{21,1} = & \left[ -a_{r1} (2b_{821} + b_{811} c_{821}) + b_{r1} (a_{811} c_{821} + 2a_{821}) \right. \\ & \left. + c_{r1} (a_{821} b_{811} - a_{811} b_{821}) \right] / d_1, \end{aligned} \quad (3.60e)$$

$$\begin{aligned} \bar{B}_{21,1} = & \left[ a_{r1} (b_{811} c_{421} - 2b_{421}) - b_{r1} (2a_{421} - a_{811} c_{421}) \right. \\ & \left. + c_{r1} (a_{811} b_{421} - a_{421} b_{811}) \right] / d_1, \end{aligned} \quad (3.60f)$$

$$\bar{C}_{21,1} = -\frac{I_0(\gamma c/b)}{2\gamma} \bar{A}_{21,1} + \frac{K_0(\gamma c/b)}{2\gamma} \bar{B}_{21,1} - \left( \frac{\ln(c/b)}{2} + \frac{1}{4} \right) \bar{F}_{21}, \text{ and} \quad (3.60g)$$

$$\begin{aligned}\bar{D}_{211} = & \left[ (c/b)^2 \frac{I_0(\gamma c/b)}{2\gamma} - (c/b) \frac{I_1(\gamma c/b)}{\gamma^2} \right] \bar{A}_{211} \\ & - \left[ (c/b)^2 \frac{K_0(\gamma c/b)}{2\gamma} + (c/b) \frac{K_1(\gamma c/b)}{\gamma^2} \right] \bar{B}_{211} + \frac{(c/b)^2}{4} \bar{F}_{21},\end{aligned}\quad (3.60h)$$

where

$$a_{H11} = -\frac{1}{8} - \frac{1}{2} \ln(a/b) + \frac{1}{8} (a/b)^4, \quad (3.61a)$$

$$\begin{aligned}a_{A21} = & -\frac{1}{\gamma} I_0(\gamma) + \left[ \frac{1}{\gamma^2} + \frac{3}{8} - \frac{1}{4} (a/b)^2 - \frac{1}{8} (a/b)^4 \right] I_1(\gamma) \\ & + \frac{1+(c/b)^2}{2\gamma} I_0(\gamma c/b) - \frac{c/b}{\gamma^2} I_1(\gamma c/b),\end{aligned}\quad (3.61b)$$

$$\begin{aligned}a_{H21} = & \frac{1}{\gamma} K_0(\gamma) + \left[ \frac{1}{\gamma^2} + \frac{3}{8} - \frac{1}{4} (a/b)^2 - \frac{1}{8} (a/b)^4 \right] K_1(\gamma) \\ & - \frac{1+(c/b)^2}{2\gamma} K_0(\gamma c/b) - \frac{c/b}{\gamma^2} K_1(\gamma c/b),\end{aligned}\quad (3.61c)$$

$$\begin{aligned}a_{F11} = & \left\{ \frac{(a/b)^4}{8} \left[ -\ln(a/b) + \frac{1}{4} \right] + \frac{(a/b)^2}{4} \left[ -\ln(a/b) + \frac{1}{2} \right] - \frac{5}{32} \right\} \bar{F}_{11} \\ & + \left[ \frac{1}{8} - \frac{(a/b)^2}{4} - \frac{(a/b)^4}{8} + \frac{1}{2} \ln(c/b) + \frac{(c/b)^2}{4} \right] \bar{F}_{21},\end{aligned}\quad (3.61d)$$

$$b_{H11} = -\frac{1}{2} \ln(a/b) - \frac{3}{8} + \frac{(a/b)^2}{2} - \frac{(a/b)^4}{8}, \quad (3.61e)$$

$$\begin{aligned}b_{A21} = & \frac{1-(c/b)^2}{2\gamma} I_0(\gamma c/b) + \left[ \frac{1}{8} - \frac{(a/b)^2}{4} + \frac{(a/b)^4}{8} - \frac{1}{\gamma^2} \right] I_1(\gamma) \\ & + \frac{c/b}{\gamma^2} I_1(\gamma c/b),\end{aligned}\quad (3.61f)$$

$$b_{B21} = -\frac{1-(c/b)^2}{2\gamma} K_0(\gamma c/b) + \left[ \frac{1}{8} - \frac{(a/b)^2}{4} + \frac{(a/b)^4}{8} - \frac{1}{\gamma^2} \right] K_1(\gamma) + \frac{c/b}{\gamma^2} K_1(\gamma c/b), \quad (3.61g)$$

$$b_{F1} = \left\{ \frac{(a/b)^4}{8} \left[ \ln(a/b) - \frac{1}{4} \right] - \frac{(a/b)^2}{4} \left[ \ln(a/b) - \frac{1}{2} \right] - \frac{3}{32} \right\} \bar{F}_{11} + \left[ \frac{3}{8} - \frac{(a/b)^2}{4} + \frac{(a/b)^4}{8} + \frac{1}{2} \ln(c/b) - \frac{(c/b)^2}{4} \right] \bar{F}_{21}, \quad (3.61h)$$

$$c_{A21} = \left( \frac{1}{\gamma Da} - \gamma \right) I_0(\gamma) - \frac{1+(c/b)^2}{2\gamma Da} I_0(\gamma c/b) + \left( 2 - \frac{1}{\gamma^2 Da} \right) I_1(\gamma) + \frac{c/b}{\gamma^2 Da} I_1(\gamma c/b), \quad (3.61i)$$

$$c_{B21} = \left( -\frac{1}{\gamma Da} + \gamma \right) K_0(\gamma) + \frac{1+(c/b)^2}{2\gamma Da} K_0(\gamma c/b) + \left( 2 - \frac{1}{\gamma^2 Da} \right) K_1(\gamma) + \frac{c/b}{\gamma^2 Da} K_1(\gamma c/b), \quad (3.61j)$$

$$c_{F1} = \bar{F}_{11} + \left( -\frac{\ln(c/b)}{2Da} + 2 + \frac{1-(c/b)^2}{4Da} \right) \bar{F}_{21}, \text{ and} \quad (3.61k)$$

$$d_1 = a_{B11} (b_{B21} c_{A21} - b_{A21} c_{B21}) + a_{A21} (b_{B11} c_{B21} + 2b_{B21}) - A_{B21} (2b_{A21} + b_{B11} c_{A21}). \quad (3.61l)$$

Generally, the inverse transform is given by

$$\psi_{11} = \frac{1}{2\pi} \bar{\psi}_{11,0} + \frac{1}{\pi} \sum_{n=1}^{\infty} \bar{\psi}_{11,n} \quad \text{and} \quad \psi_{21} = \frac{1}{2\pi} \bar{\psi}_{21,0} + \frac{1}{\pi} \sum_{n=1}^{\infty} \bar{\psi}_{21,n}. \quad (3.62 - 63)$$

Since only the solution associated with  $n = 1$  is non-trivial, one obtains

$$\Psi_{11} = \frac{A_{11}}{8} R^3 + \frac{B_{11}}{2} R \ln(R) + C_{11} R + D_{11} R^{-1} + \left( \frac{\ln(R)}{8} - \frac{3}{32} \right) \Gamma_{11} R^3, \text{ and} \quad (3.64)$$

$$\Psi_{21} = \frac{A_{21}}{\gamma^2} I_1(\gamma R) + \frac{B_{21}}{\gamma^2} K_1(\gamma R) + C_{21} R + D_{21} R^{-1} + \frac{\Gamma_{21}}{2} R \ln(R). \quad (3.65)$$

Notice that  $\Gamma_{11} \neq \bar{\Gamma}_{11}$  and  $\Gamma_{21} \neq \bar{\Gamma}_{21}$  because  $\bar{\Gamma}_{11}$  and  $\bar{\Gamma}_{21}$  are  $\sigma$ -dependent. whereas  $\Gamma_{11}$  and  $\Gamma_{21}$  are  $\theta$ -dependent. The latter functions are obtained from the inverse transform as

$$\Gamma_{11} = F^{-1}\{\bar{\Gamma}_{11}\} = -\frac{q}{2} \sin \theta, \quad \text{and} \quad \Gamma_{21} = F^{-1}\{\bar{\Gamma}_{21}\} = \frac{k_1}{k_2} Da q \sin \theta. \quad (3.66a, b)$$

Similarly,  $A_{11}$ ,  $B_{11}$ ,  $C_{11}$ ,  $D_{11}$ ,  $A_{21}$ ,  $B_{21}$ ,  $C_{21}$ , and  $D_{21}$  are  $\theta$ -dependent functions. Respectively, these functions can be derived directly from  $\bar{A}_{11,1}$ ,  $\bar{B}_{11,1}$ ,  $\bar{C}_{11,1}$ ,  $\bar{D}_{11,1}$ ,  $\bar{A}_{21,1}$ ,  $\bar{B}_{21,1}$ ,  $\bar{C}_{21,1}$ , and  $\bar{D}_{21,1}$  by replacing the function  $\pi \sin \sigma$  with the function  $\sin \theta$ .

### (c) Second Leading Terms in the Temperature Field ( $Ra'$ )

Recall that the energy equations are given by

$$\bar{\nabla}^2 \Theta_{11} = \frac{1}{R} \left( \frac{\partial \Psi_{11}}{\partial R} \frac{\partial \Theta_{10}}{\partial \theta} - \frac{\partial \Psi_{11}}{\partial \theta} \frac{\partial \Theta_{10}}{\partial R} \right), \text{ and} \quad (3.67)$$

$$\bar{\nabla}^2 \Theta_{21} = \frac{k_1}{k_2} \frac{1}{R} \left( \frac{\partial \Psi_{21}}{\partial R} \frac{\partial \Theta_{20}}{\partial \theta} - \frac{\partial \Psi_{21}}{\partial \theta} \frac{\partial \Theta_{20}}{\partial R} \right). \quad (3.68)$$

The corresponding boundary and interface conditions are given by

$$\text{at } R = a/b, \quad \Theta_{11} = 0, \quad (3.69a)$$

$$\text{at } R = c/b, \quad \Theta_{21} = 0, \quad (3.69b)$$

$$\text{at } R = 1, \quad \Theta_{11} = \Theta_{21}, \quad \text{and} \quad \frac{k_1}{k_2} \frac{\partial \Theta_{11}}{\partial R} = \frac{\partial \Theta_{21}}{\partial R}. \quad (3.69c, d)$$

Given the temperature profiles of  $\Theta_{10}$  and  $\Theta_{20}$ , the energy equations reduces to

$$\bar{\nabla}^2 \Theta_{11} = \frac{q}{R^2} \frac{\partial \Psi_{11}}{\partial \theta}, \quad \text{and} \quad \bar{\nabla}^2 \Theta_{21} = \left( \frac{k_1}{k_2} \right)^2 \frac{q}{R^2} \frac{\partial \Psi_{21}}{\partial \theta}. \quad (3.70 - 71)$$

Or,

$$\bar{\nabla}^2 \Theta_{11} = q \frac{\partial}{\partial \theta} \left[ \frac{A_{11}}{8} R + \frac{B_{11}}{2} \frac{\ln(R)}{R} + \frac{C_{11}}{R} + \frac{D_{11}}{R^3} + \left( \frac{\ln(R)}{8} - \frac{3}{32} \right) \Gamma_{11} R \right], \text{ and} \quad (3.72)$$

$$\bar{\nabla}^2 \Theta_{21} = q \left( \frac{k_1}{k_2} \right)^2 \frac{\partial}{\partial \theta} \left[ \frac{A_{21}}{\gamma^2} \frac{I_1(\gamma R)}{R^2} + \frac{B_{21}}{\gamma^2} \frac{K_1(\gamma R)}{R^2} + \frac{C_{21}}{R} + \frac{D_{21}}{R^3} + \frac{\Gamma_{21}}{2} \frac{\ln(R)}{R} \right]. \quad (3.73)$$

Using prime to denote the partial derivative with respect to the independent variable  $\theta$ , the above Eqs. (3.72) and (3.73) can be reduced to

$$\bar{\nabla}^2 \Theta_{11} = q \left[ \frac{A'_{11}}{8} R + \frac{B'_{11}}{2} \frac{\ln(R)}{R} + \frac{C'_{11}}{R} + \frac{D'_{11}}{R^3} + \left( \frac{\ln(R)}{8} - \frac{3}{32} \right) \Gamma'_{11} R \right], \text{ and} \quad (3.74)$$

$$\bar{\nabla}^2 \Theta_{21} = q \left( \frac{k_1}{k_2} \right)^2 \left[ \frac{A'_{21}}{\gamma^2} \frac{I_1(\gamma R)}{R^2} + \frac{B'_{21}}{\gamma^2} \frac{K_1(\gamma R)}{R^2} + \frac{C'_{21}}{R} + \frac{D'_{21}}{R^3} + \frac{\Gamma'_{21}}{2} \frac{\ln(R)}{R} \right]. \quad (3.75)$$

Since  $A_{11}$ ,  $B_{11}$ ,  $C_{11}$ ,  $D_{11}$ ,  $A_{21}$ ,  $B_{21}$ ,  $C_{21}$ , and  $D_{21}$  are functions of  $\Gamma_{11}$  and  $\Gamma_{22}$ , which are  $\theta$ -dependent, it is helpful to know the derivative and transform of  $\Gamma_{11}$  and  $\Gamma_{22}$ . It is found that

$$\Gamma'_{11} = \frac{\partial \Gamma_{11}}{\partial \theta} = -\frac{q}{2} \cos \theta, \quad \text{and} \quad \Gamma'_{21} = \frac{\partial \Gamma_{21}}{\partial \theta} = \frac{k_1}{k_2} Da q \cos \theta. \quad (3.76a, b)$$

Notice that  $\Gamma_{11}$  and  $\Gamma_{22}$  in equations (3.76) are functions of  $\cos \theta$ . According to Appendix D, the transform of equations (3.76) are

$$\bar{\Gamma}'_{11} = \bar{\Gamma} \{ \Gamma'_{11} \} = \begin{cases} -\frac{q}{2} \pi \cos \sigma, & n = 1 \\ 0, & n \neq 1 \end{cases}, \text{ and}$$



$$\bar{F}'_{21} = \bar{F} \{ \Gamma'_{21} \} = \begin{cases} \frac{k_1}{k_2} Da q \pi \cos \sigma, & n = 1 \\ 0, & n \neq 1 \end{cases}. \quad (3.76c, d)$$

Once again, the non-homogeneous terms become zero for  $n \neq 1$ . Analogous to the previous solutions, only  $n = 1$  will provide a non-trivial solution. Hence, for  $n = 1$ , the energy equations (3.74) and (3.75) are transformed to

$$\frac{d^2 \bar{\Theta}_{111}}{dR^2} + \frac{1}{R} \frac{d\bar{\Theta}_{111}}{dR} - \frac{1}{R^2} \bar{\Theta}_{111} = q \left[ \frac{\bar{A}'_{111}}{8} R + \frac{\bar{B}'_{111}}{2} \frac{\ln(R)}{R} + \frac{\bar{C}'_{111}}{R} + \frac{\bar{D}'_{111}}{R^3} + \left( \frac{\ln(R)}{8} - \frac{3}{32} \right) \bar{F}'_{11} R \right], \text{ and} \quad (3.77)$$

$$\frac{d^2 \bar{\Theta}_{211}}{dR^2} + \frac{1}{R} \frac{d\bar{\Theta}_{211}}{dR} - \frac{1}{R^2} \bar{\Theta}_{211} = q \left( \frac{k_1}{k_2} \right)^2 \left[ \frac{\bar{A}'_{211}}{\gamma^2} \frac{I_1(\gamma R)}{R^2} + \frac{\bar{B}'_{211}}{\gamma^2} \frac{K_1(\gamma R)}{R^2} + \frac{\bar{C}'_{211}}{R} + \frac{\bar{D}'_{211}}{R^3} + \frac{\bar{F}'_{21}}{2} \frac{\ln(R)}{R} \right]. \quad (3.78)$$

The corresponding boundary and interface conditions are (for  $n = 1$ )

$$\text{at } R = a/b, \quad \bar{\Theta}_{111} = 0, \quad (3.79a)$$

$$\text{at } R = c/b, \quad \bar{\Theta}_{211} = 0, \quad (3.79b)$$

$$\text{at } R = 1, \quad \bar{\Theta}_{111} = \bar{\Theta}_{211}, \quad \text{and} \quad \frac{k_1}{k_2} \frac{d\bar{\Theta}_{111}}{dR} = \frac{d\bar{\Theta}_{211}}{dR}. \quad (3.79c, d)$$

The solutions to the above equations are

$$\bar{\Theta}_{111} = q \left[ \frac{\bar{A}'_{111}}{64} R^3 + \frac{\ln(R)^2 - \ln(R)}{8} \bar{B}'_{111} R + \frac{\bar{C}'_{111}}{2} R \ln(R) - \frac{\bar{D}'_{111}}{2} \frac{\ln(R)}{R} + \bar{E}_{111} R + \bar{F}_{111} R^{-1} + \left( \frac{\ln(R)}{64} - \frac{3}{128} \right) \bar{F}'_{11} R^3 \right], \text{ and} \quad (3.80)$$

$$\begin{aligned}\bar{\Theta}_{21,1} = q \left( \frac{k_1}{k_2} \right)^2 & \left[ \frac{\bar{A}'_{21,1}}{\gamma^3} R \int_1^R \frac{I_0(\gamma \xi)}{\xi^3} d\xi - \frac{\bar{B}'_{21,1}}{\gamma^3} R \int_1^R \frac{K_0(\gamma \xi)}{\xi^3} d\xi + \frac{\bar{C}'_{21,1}}{2} R \ln(R) \right. \\ & \left. - \frac{\bar{D}'_{21,1}}{2} \frac{\ln(R)}{R} + \bar{E}_{21,1} R + \bar{F}_{21,1} R^{-1} + \frac{\ln(R)^2 - \ln(R)}{8} \bar{F}'_{21,1} R \right],\end{aligned}\quad (3.81)$$

where

$$\bar{A}'_{11,1} = -\bar{B}'_{11,1} + I_1(\gamma) \bar{A}'_{21,1} + K_1(\gamma) \bar{B}'_{21,1} + \bar{F}'_{21,1}, \quad (3.82a)$$

$$\begin{aligned}\bar{B}'_{11,1} = & \left[ a'_{r1} (b_{A21} c_{B21} - b_{B21} c_{A21}) + b'_{r1} (a_{B21} c_{A21} - a_{A21} c_{B21}) \right. \\ & \left. + c'_{r1} (a_{A21} b_{B21} - a_{B21} b_{A21}) \right] / d_1,\end{aligned}\quad (3.82b)$$

$$\bar{C}'_{11,1} = -\frac{(a/b)^2}{4} \bar{A}'_{11,1} - \left( \frac{\ln(a/b)}{2} + \frac{1}{4} \right) \bar{B}'_{11,1} - (a/b)^2 \left( \frac{\ln(a/b)}{4} - \frac{1}{8} \right) \bar{F}'_{11,1}, \quad (3.82c)$$

$$\bar{D}'_{11,1} = \frac{(a/b)^4}{8} \bar{A}'_{11,1} + \frac{(a/b)^2}{4} \bar{B}'_{11,1} + (a/b)^4 \left( \frac{\ln(a/b)}{8} - \frac{1}{32} \right) \bar{F}'_{11,1}, \quad (3.82d)$$

$$\bar{E}_{11,1} = -\bar{F}_{11,1} + (k_1/k_2)^2 (\bar{E}_{21,1} + \bar{F}_{21,1}) - \frac{1}{64} \bar{A}'_{11,1} + \frac{3}{128} \bar{F}'_{11,1}, \quad (3.82e)$$

$$\begin{aligned}\bar{F}_{11,1} = & \left\{ a_{r2} \left[ (c/b) \left( (k_1/k_2)^2 + 1 \right) - \frac{(k_1/k_2)^2 - 1}{c/b} \right] - 2b_{r2} (k_1/k_2)^2 (a/b) \right. \\ & \left. - c_{r2} (k_1/k_2)^2 \frac{a/b}{c/b} \left[ (c/b)^2 - 1 \right] \right\} / d_2,\end{aligned}\quad (3.82f)$$

$$\begin{aligned}\bar{A}'_{21,1} = & \left[ a'_{r1} (b_{B21} c_{B11} - b_{B11} c_{B21}) + b'_{r1} (a_{B11} c_{B21} - a_{B21} c_{B11}) \right. \\ & \left. + c'_{r1} (a_{B21} b_{B11} - a_{B11} b_{B21}) \right] / d_1,\end{aligned}\quad (3.82g)$$

$$\begin{aligned}\bar{B}'_{21,1} = & \left[ a'_{r1} (b_{B11} c_{A21} - b_{A21} c_{B11}) + b'_{r1} (a_{A21} c_{B11} - a_{B11} c_{A21}) \right. \\ & \left. + c'_{r1} (a_{B11} b_{A21} - a_{A21} b_{B11}) \right] / d_1,\end{aligned}\quad (3.82h)$$

$$\bar{C}'_{211} = -\frac{I_0(\gamma c/b)}{2\gamma} \bar{A}'_{211} + \frac{K_0(\gamma c/b)}{2\gamma} \bar{B}'_{211} - \left( \frac{\ln(c/b)}{2} + \frac{1}{4} \right) \bar{F}'_{211}, \quad (3.82i)$$

$$\begin{aligned} \bar{D}'_{211} &= \left[ (c/b)^2 \frac{I_0(\gamma c/b)}{2\gamma} - (c/b) \frac{I_1(\gamma c/b)}{\gamma^2} \right] \bar{A}'_{211} \\ &- \left[ (c/b)^2 \frac{K_0(\gamma c/b)}{2\gamma} + (c/b) \frac{K_1(\gamma c/b)}{\gamma^2} \right] \bar{B}'_{211} + \frac{(c/b)^2}{4} \bar{F}'_{211}, \end{aligned} \quad (3.82j)$$

$$\begin{aligned} \bar{E}_{211} &= \left\{ -\frac{2}{c/b} a_{r2} + \left[ \left( (k_1/k_2)^2 - 1 \right) (a/b) + \frac{(k_1/k_2)^2 + 1}{a/b} \right] b_{r2} \right. \\ &\quad \left. + \frac{(a/b)^2 - 1}{(a/b)(c/b)} c_{r2} \right\} / d_2, \end{aligned} \quad (3.82k)$$

$$\begin{aligned} \bar{F}_{211} &= \left\{ 2(c/b) a_{r2} - \left[ \left( (k_1/k_2)^2 + 1 \right) (a/b) + \frac{(k_1/k_2)^2 - 1}{a/b} \right] b_{r2} \right. \\ &\quad \left. - \left[ (a/b)^2 - 1 \right] \frac{c/b}{a/b} c_{r2} \right\} / d_2, \end{aligned} \quad (3.82l)$$

$$\begin{aligned} a_{r2} &= \frac{(a/b)^3 - (a/b)}{64} \bar{A}'_{111} + \frac{a/b}{8} \left[ \ln(a/b)^2 - \ln(a/b) \right] \bar{B}'_{111} + \frac{a/b}{2} \ln(a/b) \bar{C}'_{111} \\ &- \frac{\ln(a/b)}{2(a/b)} \bar{D}'_{111} + \left[ \frac{3}{128} (a/b) + \frac{(a/b)^3}{64} \left( \ln(a/b) - \frac{3}{2} \right) \right] \bar{F}'_{111}, \end{aligned} \quad (3.83a)$$

$$\begin{aligned} b_{r2} &= \frac{c/b}{\gamma^3} \left[ \bar{A}'_{211} \int_1^b \frac{I_0(\gamma \xi)}{\xi^3} d\xi - \bar{B}'_{211} \int_1^b \frac{K_0(\gamma \xi)}{\xi^3} d\xi \right] + \frac{c/b}{2} \ln(c/b) \bar{C}'_{211} \\ &- \frac{\ln(c/b)}{2(c/b)} \bar{D}'_{211} + \frac{c/b}{8} \left[ \ln(c/b)^2 - \ln(c/b) \right] \bar{F}'_{211}, \end{aligned} \quad (3.83b)$$

$$\begin{aligned} c_{r2} &= \frac{1}{32} \bar{A}'_{111} - \frac{1}{8} \bar{B}'_{111} + \frac{1}{2} \bar{C}'_{111} - \frac{1}{2} \bar{D}'_{111} - \frac{1}{32} \bar{F}'_{111} - \frac{I_0(\gamma)}{\gamma^3} \bar{A}'_{211} + \frac{K_0(\gamma)}{\gamma^3} \bar{B}'_{211} \\ &- \frac{1}{2} \bar{C}'_{211} + \frac{1}{2} \bar{D}'_{211} + \frac{1}{8} \bar{F}'_{211}, \text{ and} \end{aligned} \quad (3.83c)$$

$$d_2 = \left[ \left( 1 - (k_1/k_2)^2 \right) (c/b) + \frac{1 + (k_1/k_2)^2}{(c/b)} \right] (a/b) - \left[ \left( 1 + (k_1/k_2)^2 \right) (c/b) + \frac{1 - (k_1/k_2)^2}{(c/b)} \right] (a/b)^{-1}. \quad (3.83d)$$

Recall that the solutions for  $n \neq 1$  are trivial, the inverse transforms are thus reduced to

$$\Theta_{11} = \frac{1}{\pi} \bar{\Theta}_{11,1} \quad \text{and} \quad \Theta_{21} = \frac{1}{\pi} \bar{\Theta}_{21,1}. \quad (3.84 - 85)$$

Therefore, the solutions become

$$\Theta_{11} = q \left[ \frac{A'_{11}}{64} R^3 + \frac{\ln(R)^2 - \ln(R)}{8} B'_{11} R + \frac{C'_{11}}{2} R \ln(R) - \frac{D'_{11}}{2} \frac{\ln(R)}{R} + E_{11} R + F_{11} R^{-1} + \left( \frac{\ln(R)}{64} - \frac{3}{128} \right) \Gamma'_{11} R^3 \right], \text{ and} \quad (3.86)$$

$$\Theta_{21} = q \left( \frac{k_1}{k_2} \right)^2 \left[ \frac{A'_{21}}{\gamma^3} R \int_1^R \frac{I_0(\gamma \xi)}{\xi^3} d\xi - \frac{B'_{21}}{\gamma^3} R \int_1^R \frac{K_0(\gamma \xi)}{\xi^3} d\xi + \frac{C'_{21}}{2} R \ln(R) - \frac{D'_{21}}{2} \frac{\ln(R)}{R} + E_{21} R + F_{21} R^{-1} + \frac{\ln(R)^2 - \ln(R)}{8} \Gamma'_{21} R \right]. \quad (3.87)$$

The  $\theta$ -dependent functions,  $A'_{11}$ ,  $B'_{11}$ ,  $C'_{11}$ ,  $D'_{11}$ ,  $E_{11}$ ,  $F_{11}$ ,  $A'_{21}$ ,  $B'_{21}$ ,  $C'_{21}$ ,  $D'_{21}$ ,  $E_{21}$ , and  $F_{21}$  can be derived directly from  $\bar{A}'_{11,1}$ ,  $\bar{B}'_{11,1}$ ,  $\bar{C}'_{11,1}$ ,  $\bar{D}'_{11,1}$ ,  $\bar{E}_{11,1}$ ,  $\bar{F}_{11,1}$ ,  $\bar{A}'_{21,1}$ ,  $\bar{B}'_{21,1}$ ,  $\bar{C}'_{21,1}$ ,  $\bar{D}'_{21,1}$ ,  $\bar{E}_{21,1}$  and  $\bar{F}_{21,1}$  by replacing the function  $\pi \sin \sigma$  with the function  $\sin \theta$ , respectively.

#### (d) Second Leading Terms in the Velocity Field ( $Ra^2$ )

Collect the terms that correspond to the second order of  $Ra$ , one obtains

$$\bar{\nabla}^4 \Psi_{12} = \frac{1}{Pr} \frac{1}{R} \left( \frac{\partial \Psi_{11}}{\partial R} \frac{\partial \bar{\nabla}^2 \Psi_{11}}{\partial \theta} - \frac{\partial \Psi_{11}}{\partial \theta} \frac{\partial \bar{\nabla}^2 \Psi_{11}}{\partial R} \right) - \left( \sin \theta \frac{\partial \Theta_{11}}{\partial R} + \frac{\cos \theta}{R} \frac{\partial \Theta_{11}}{\partial \theta} \right), \text{ and } \quad (3.88)$$

$$\bar{\nabla}^4 \Psi_{22} - \frac{1}{Da} \bar{\nabla}^2 \Psi_{22} = \frac{1}{Pr} \frac{1}{R} \left( \frac{\partial \Psi_{21}}{\partial R} \frac{\partial \bar{\nabla}^2 \Psi_{21}}{\partial \theta} - \frac{\partial \Psi_{21}}{\partial \theta} \frac{\partial \bar{\nabla}^2 \Psi_{21}}{\partial R} \right) - \left( \sin \theta \frac{\partial \Theta_{21}}{\partial R} + \frac{\cos \theta}{R} \frac{\partial \Theta_{21}}{\partial \theta} \right). \quad (3.89)$$

with the corresponding boundary and interface conditions.

$$\text{at } R = a/b, \quad \frac{\partial \Psi_{12}}{\partial R} = \frac{\partial \Psi_{12}}{\partial \theta} = 0, \quad (3.90a, b)$$

$$\text{at } R = c/b, \quad \frac{\partial \Psi_{22}}{\partial R} = \frac{\partial \Psi_{22}}{\partial \theta} = 0, \quad (3.90c, d)$$

$$\text{at } R = l, \quad \frac{\partial \Psi_{12}}{\partial R} = \frac{\partial \Psi_{22}}{\partial R}, \quad \frac{\partial \Psi_{12}}{\partial \theta} = \frac{\partial \Psi_{22}}{\partial \theta}, \quad (3.90e, f)$$

$$\bar{\nabla}^2 \Psi_{12} = \bar{\nabla}^2 \Psi_{22}, \quad \text{and} \quad \frac{\partial \bar{\nabla}^2 \Psi_{12}}{\partial R} = \frac{\partial \bar{\nabla}^2 \Psi_{22}}{\partial R} - \frac{1}{Da} \frac{\partial \Psi_{22}}{\partial R}. \quad (3.90g, h)$$

Before one proceeds, it is advantageous to examine each term so that one can predict how these terms behave after the transform. Substitute the solution of stream function and temperature at the lower level into equations (3.88) and (3.89), one obtains

$$\begin{aligned} \bar{\nabla}^4 \Psi_{12} = \bar{\nabla}^2 \Omega_{12} = & X_1 R^2 \ln(R)^2 + X_2 R^2 \ln(R) + X_3 R^2 + X_4 \ln(R)^2 \\ & + X_5 \ln(R) + X_6 + X_7 R^{-2} \ln(R) + X_8 R^{-2} + X_9 R^{-4}, \text{ and} \end{aligned} \quad (3.91)$$

$$\bar{\nabla}^4 \Psi_{22} - \frac{1}{Da} \bar{\nabla}^2 \Psi_{22} = \bar{\nabla}^2 \Omega_{22} - \gamma^2 \Omega_{22} = Z(R, \theta), \quad (3.92)$$

where

$$X_1 = \frac{1}{Pr} \frac{\Gamma_{11} \Gamma'_{11}}{4}, \quad (3.93a)$$

$$X_2 = \frac{1}{Pr} \left( \frac{A_{11} \Gamma'_{11} + A'_{11} \Gamma_{11}}{4} - \frac{3 \Gamma_{11} \Gamma'_{11}}{16} \right) - q \left( \frac{3}{64} \sin \theta \Gamma'_{11} - \frac{1}{64} \cos \theta \Gamma_{11} \right), \quad (3.93b)$$

$$X_3 = \frac{1}{Pr} \left[ \frac{A_{11} A'_{11}}{4} + \frac{3}{32} (A_{11} \Gamma'_{11} - 3A'_{11} \Gamma_{11} + \Gamma_{11} \Gamma'_{11}) \right] \\ + q \left[ \sin \theta \left( -\frac{3}{64} A'_{11} + \frac{1}{8} B'_{11} + \frac{7}{128} \Gamma'_{11} \right) + \cos \theta \left( \frac{1}{64} A_{11} - \frac{3}{128} \Gamma_{11} \right) \right]. \quad (3.93c)$$

$$X_4 = \frac{1}{Pr} \frac{B_{11} \Gamma'_{11} - B'_{11} \Gamma_{11}}{2} - q \left( \frac{1}{8} \sin \theta B'_{11} - \frac{1}{8} \cos \theta B_{11} \right). \quad (3.93d)$$

$$X_5 = \frac{1}{Pr} \left( \frac{-A_{11} B'_{11} + A'_{11} B_{11}}{2} + \frac{5B_{11} \Gamma'_{11} - B'_{11} \Gamma_{11}}{8} + C_{11} \Gamma'_{11} - C'_{11} \Gamma_{11} \right) \\ - q \left[ \sin \theta \left( \frac{1}{8} B'_{11} + \frac{1}{2} C'_{11} \right) + \cos \theta \left( \frac{1}{8} B_{11} - \frac{1}{2} C_{11} \right) \right]. \quad (3.93e)$$

$$X_6 = \frac{1}{Pr} \left( \frac{3A_{11} B'_{11} + 5A'_{11} B_{11}}{8} - A_{11} C'_{11} + A'_{11} C_{11} - \frac{3B_{11} \Gamma'_{11} + 5B'_{11} \Gamma_{11}}{32} - C'_{11} \Gamma_{11} \right) \\ - q \left[ \sin \theta \left( \frac{1}{2} C'_{11} + E_{11} \right) + \cos \theta E'_{11} \right]. \quad (3.93f)$$

$$X_7 = \frac{1}{Pr} (B_{11} B'_{11} - D_{11} \Gamma'_{11} - D'_{11} \Gamma_{11}) - q \left( \frac{1}{2} \sin \theta D'_{11} + \frac{1}{2} \cos \theta D_{11} \right). \quad (3.93g)$$

$$X_8 = \frac{1}{Pr} \left( -A_{11} D'_{11} - A'_{11} D_{11} + \frac{B_{11} B'_{11}}{2} + B_{11} C'_{11} + B'_{11} C_{11} - D'_{11} \Gamma_{11} \right) \\ + q \left[ \sin \theta \left( \frac{1}{2} D'_{11} + F_{11} \right) - \cos \theta F'_{11} \right]. \quad (3.93h)$$

$$X_9 = \frac{1}{Pr} (B_{11} D'_{11} - B'_{11} D_{11}). \quad (3.93i)$$

$$Z(R, \theta) = Y_1 \int_1^R \xi^{-1} I_0(\gamma \xi) d\xi + Y_2 \int_1^R \xi^{-1} K_0(\gamma \xi) d\xi + Y_3 \ln(R)^2 \\ + [Y_4 I_0(\gamma R) + Y_5 K_0(\gamma R) + Y_6] \ln(R) + Y_7 I_0(\gamma R) + Y_8 K_0(\gamma R) + Y_9$$

$$\begin{aligned}
& + \left\{ \left[ Y_{10} I_1(\gamma R) + Y_{11} K_1(\gamma R) \right] \ln(R) + Y_{12} I_1(\gamma R) + Y_{13} K_1(\gamma R) \right\} R^{-1} \\
& + \left\{ Y_{14} \ln(R) + Y_{15} I_0(\gamma R) + Y_{16} K_0(\gamma R) + Y_{17} \right\} R^{-2} + \left\{ Y_{18} I_1(\gamma R) + Y_{19} K_1(\gamma R) \right\} R^{-3} + Y_{20} R^{-4}.
\end{aligned} \tag{3.94}$$

$$Y_1 = q(k_1/k_2) \gamma^{-3} (-\sin \theta A'_{21} + \cos \theta A_{21}), \tag{3.95a}$$

$$Y_2 = q(k_1/k_2) \gamma^{-3} (\sin \theta B'_{21} - \cos \theta B_{21}), \tag{3.95b}$$

$$Y_3 = \frac{1}{8} q(k_1/k_2) (-\sin \theta \Gamma'_{21} + \cos \theta \Gamma_{21}), \tag{3.95c}$$

$$Y_4 = -\frac{\gamma}{2} A_{21} \Gamma'_{21}, \tag{3.95d}$$

$$Y_5 = -\frac{\gamma}{2} B_{21} \Gamma'_{21}, \tag{3.95e}$$

$$Y_6 = -q(k_1/k_2) \left[ \sin \theta \left( \frac{1}{2} C'_{21} + \frac{1}{8} \Gamma'_{21} \right) + \cos \theta \left( -\frac{1}{2} C_{21} + \frac{1}{8} \Gamma_{21} \right) \right], \tag{3.95f}$$

$$Y_7 = -\gamma A_{21} C'_{21}, \tag{3.95g}$$

$$Y_8 = \gamma B_{21} C'_{21}, \tag{3.95h}$$

$$Y_9 = -q(k_1/k_2) \left[ \sin \theta \left( \frac{1}{2} C'_{21} + E_{21} - \frac{1}{8} \Gamma'_{21} \right) + \cos \theta E'_{21} \right], \tag{3.95i}$$

$$Y_{10} = \frac{1}{2} (A_{21} \Gamma'_{21} + A'_{21} \Gamma_{21}), \tag{3.95j}$$

$$Y_{11} = \frac{1}{2} (B_{21} \Gamma'_{21} + B'_{21} \Gamma_{21}), \tag{3.95k}$$

$$Y_{12} = A_{21} C'_{21} + A'_{21} \left( C_{21} + \frac{\Gamma_{21}}{2} \right), \tag{3.95l}$$

$$Y_{13} = B_{21} C'_{21} + B'_{21} \left( C_{21} + \frac{\Gamma_{21}}{2} \right), \tag{3.95m}$$

$$Y_{14} = \Gamma_{21} \Gamma'_{21} - \frac{1}{2} q(k_1 / k_2) (\sin \theta D'_{21} + \cos \theta D_{21}), \quad (3.95n)$$

$$Y_{15} = A_{21} (-\gamma D'_{21} + \gamma^{-1} \Gamma'_{21}) - q(k_1 / k_2) \gamma^{-3} \sin(\theta) A'_{21}, \quad (3.95o)$$

$$Y_{16} = B_{21} (\gamma D'_{21} - \gamma^{-1} \Gamma'_{21}) + q(k_1 / k_2) \gamma^{-3} \sin(\theta) B'_{21}, \quad (3.95p)$$

$$Y_{17} = q(k_1 / k_2) \left[ \sin \theta \left( \frac{1}{2} D'_{21} + F_{21} \right) - \cos \theta F'_{21} \right], \quad (3.95q)$$

$$Y_{18} = A_{21} (D'_{21} - \gamma^{-2} \Gamma'_{21}) - A'_{21} (D_{21} - \gamma^{-2} \Gamma_{21}), \quad (3.95r)$$

$$Y_{19} = B_{21} (D'_{21} - \gamma^{-2} \Gamma'_{21}) - B'_{21} (D_{21} - \gamma^{-2} \Gamma_{21}), \text{ and} \quad (3.95s)$$

$$Y_{20} = -D_{21} \Gamma'_{21} + D'_{21} \Gamma_{21}. \quad (3.95t)$$

It is very helpful if one looks into the nature of these coefficients. Recognize that while  $A_{11}$ ,  $B_{11}$ ,  $C_{11}$ ,  $D_{11}$ ,  $A_{21}$ ,  $B_{21}$ ,  $C_{21}$ ,  $D_{21}$ ,  $E'_{21}$ , and  $F'_{21}$  are functions of  $\sin \theta$ ,  $A'_{11}$ ,  $B'_{11}$ ,  $C'_{11}$ ,  $D'_{11}$ ,  $A'_{21}$ ,  $B'_{21}$ ,  $C'_{21}$ ,  $D'_{21}$ ,  $E_{21}$ , and  $F_{21}$  are functions of  $\cos \theta$ . Consequently, the above functions  $X_1, X_2, \dots, X_9$  and  $Y_1, Y_2, \dots, Y_{20}$  are functions of the product of  $\sin \theta$  and  $\cos \theta$ . From Appendix D, it is clear that the solutions are not trivial only if  $n = 2$ . The transformed governing equations become

$$\begin{aligned} \frac{1}{R} \frac{d}{dR} \left( R \frac{d\bar{\Omega}_{12,2}}{dR} \right) - \frac{4}{R^2} \bar{\Omega}_{12,2} &= \bar{X}_1 R^2 \ln(R)^2 + \bar{X}_2 R^2 \ln(R) + \bar{X}_3 R^2 + \bar{X}_4 \ln(R)^2 \\ &+ \bar{X}_5 \ln(R) + \bar{X}_6 + \bar{X}_7 R^{-2} \ln(R) + \bar{X}_8 R^{-2} + \bar{X}_9 R^{-4}, \text{ and} \end{aligned} \quad (3.96)$$

$$\frac{1}{R} \frac{d}{dR} \left( R \frac{d\bar{\Omega}_{22,2}}{dR} \right) - \left( \frac{4}{R^2} + \frac{1}{Da} \right) \bar{\Omega}_{22,2} = \bar{Z}(R), \quad (3.97)$$

which are subject to the following interface condition

$$\text{at } R = 1, \quad \bar{\Omega}_{12} = \bar{\Omega}_{22}. \quad (3.98)$$



where

$$\bar{Z}(R) = \bar{F}\{Z(R, \theta)\}. \quad (3.99)$$

The coefficients  $\bar{X}_i$  and  $\bar{Y}_i$  in Eqs. (3.96) and (3.99) can be derived directly from  $X_i$  and  $Y_i$  in Eqs. (3.93) and (3.95). For example,

$$X_1 = \frac{1}{Pr} \frac{\Gamma_{11} \Gamma'_{11}}{4}. \quad (3.100)$$

Substitute Eq. (3.66a) into Eq. (3.93a) to yield

$$X_1 = \frac{1}{4Pr} \left( -\frac{q}{2} \sin \theta \right) \left( -\frac{q}{2} \cos \theta \right). \quad (3.101)$$

Rearranging Eq. (3.101), one obtains

$$X_1 = \frac{q^2}{16Pr} \cos \theta \sin \theta. \quad (3.102)$$

The transformation of Eq. (3.102) becomes

$$\bar{X}_1 = \frac{\pi q^2}{16Pr} \cos \sigma \sin \sigma, \text{ or} \quad (3.103)$$

$$\bar{X}_1 = \frac{1}{4\pi Pr} \bar{\Gamma}_{11} \bar{\Gamma}'_{11}. \quad (3.104)$$

The general solutions of the vorticity equations are

$$\begin{aligned} \bar{\Omega}_{12,2} = & \left[ \frac{\bar{X}_1}{12} \ln(R)^2 + \left( -\frac{\bar{X}_1}{9} + \frac{\bar{X}_2}{12} \right) \ln(R) + \left( \frac{13\bar{X}_1}{216} - \frac{\bar{X}_2}{18} + \frac{\bar{X}_3}{12} \right) \right] R^4 \\ & + \left[ \frac{\bar{X}_4}{12} \ln(R)^3 + \left( -\frac{\bar{X}_4}{16} + \frac{\bar{X}_5}{8} \right) \ln(R)^2 + \left( \frac{\bar{X}_4}{32} - \frac{\bar{X}_5}{16} + \frac{\bar{X}_6}{4} \right) \ln(R) + \bar{A}_{12,2} \right] R^2 \\ & - \left[ \frac{\bar{X}_7}{4} \ln(R) + \frac{\bar{X}_8}{4} \right] + \left[ -\frac{\bar{X}_9}{4} \ln(R) + \bar{B}_{12,2} \right] R^{-2}, \text{ and} \end{aligned} \quad (3.105)$$

$$\bar{\Omega}_{22,2} = \left( \bar{A}_{22,2} - \int_1^R \xi \bar{Z}(\xi) K_2(\gamma \xi) d\xi \right) I_2(\gamma R) + \left( \bar{B}_{22,2} + \int_1^R \xi \bar{Z}(\xi) I_2(\gamma \xi) d\xi \right) K_2(\gamma R). \quad (3.106)$$

where  $\bar{Z}(\xi)$  is the function defined in (3.99),  $I_2(\gamma \xi)$  and  $K_2(\gamma \xi)$  are the second order modified Bessel functions of the first and second kinds, respectively. They are related to the zeroth and first order of their kind in the following fashions,

$$I_2(\gamma \xi) = I_0(\gamma \xi) - \frac{2}{\gamma \xi} I_1(\gamma \xi), \text{ and} \quad (3.107a)$$

$$K_2(\gamma \xi) = K_0(\gamma \xi) + \frac{2}{\gamma \xi} K_1(\gamma \xi). \quad (3.107b)$$

Because no close-form solution is available for the integrals that appear in the above solution (3.106), numerical integration must be performed. Associated with the above vorticity solutions, the stream functions are governed by the following equations,

$$\frac{1}{R} \frac{d}{dR} \left( R \frac{d\bar{\Psi}_{12,2}}{dR} \right) - \frac{4}{R^2} \bar{\Psi}_{12,2} = \bar{\Omega}_{12,2}, \text{ and} \quad (3.108)$$

$$\frac{1}{R} \frac{d}{dR} \left( R \frac{d\bar{\Psi}_{22,2}}{dR} \right) - \frac{4}{R^2} \bar{\Psi}_{22,2} = \bar{\Omega}_{22,2}, \quad (3.109)$$

which are subject to the boundary and interface conditions given below,

$$\text{at } R = a/b, \quad \frac{d\bar{\Psi}_{12}}{dR} = \bar{\Psi}_{12} = 0, \quad (3.110a, b)$$

$$\text{at } R = c/b, \quad \frac{d\bar{\Psi}_{22}}{dR} = \bar{\Psi}_{22} = 0, \quad (3.110c, d)$$

$$\text{at } R = 1, \quad \frac{d\bar{\Psi}_{12}}{dR} = \frac{d\bar{\Psi}_{22}}{dR}, \quad \bar{\Psi}_{12} = \bar{\Psi}_{22}, \text{ and} \quad (3.110e, f)$$

$$\frac{d\bar{\Omega}_{12}}{dR} = \frac{d\bar{\Omega}_{22}}{dR} - \frac{1}{Da} \frac{d\bar{\Psi}_{22}}{dR}. \quad (3.110g, h)$$

After some manipulations and careful calculations, one yields the following solutions for the above equations. Because of the absence of a close-form solution for the vorticity in the porous layer, the stream function in the porous layer is also expressed in an integral form. The solutions are

$$\begin{aligned} \bar{\Psi}_{12,2} = & \frac{\bar{X}_1}{384} R^6 \ln(R)^2 + \left( -\frac{25\bar{X}_1}{4608} + \frac{\bar{X}_2}{384} \right) R^6 \ln(R) + \left( \frac{415\bar{X}_1}{110592} - \frac{25\bar{X}_2}{9216} + \frac{\bar{X}_3}{384} \right) R^6 \\ & + \frac{\bar{X}_4}{144} R^4 \ln(R)^3 + \left( -\frac{11\bar{X}_4}{576} + \frac{\bar{X}_5}{96} \right) R^4 \ln(R)^2 + \left( \frac{85\bar{X}_4}{3456} - \frac{11\bar{X}_5}{576} + \frac{\bar{X}_6}{48} \right) R^4 \ln(R) \\ & + \left( -\frac{137\bar{X}_4}{10368} + \frac{19\bar{X}_5}{1728} - \frac{\bar{X}_6}{72} + \frac{\bar{A}_{12,2}}{12} \right) R^4 - \frac{\bar{X}_7}{32} R^2 \ln(R)^2 + \left( \frac{\bar{X}_7}{64} - \frac{\bar{X}_8}{16} \right) R^2 \ln(R) \\ & + \bar{C}_{12,2} R^2 + \frac{\bar{X}_9}{16} \ln(R) - \frac{\bar{B}_{12,2}}{4} + \bar{D}_{12,2} R^{-2}, \text{ and} \end{aligned} \quad (3.111)$$

$$\bar{\Psi}_{22,2} = \bar{C}_{22,2} R^2 + \bar{D}_{22,2} R^{-2} + \frac{R^2}{4} \int_1^R \frac{\bar{\Omega}_{22,2}(\xi)}{\xi} d\xi - \frac{R^{-2}}{4} \int_1^R \xi^3 \bar{\Omega}_{22,2}(\xi) d\xi, \quad (3.112)$$

where

$$\bar{A}_{12,2} = -\frac{13X_1}{216} + \frac{X_2}{18} - \frac{X_3}{12} + \frac{X_8}{4} - \bar{B}_{22,2} + I_2(\gamma) \bar{A}_{22,2} + K_2(\gamma) \bar{B}_{22,2}, \quad (3.113a)$$

$$\begin{aligned} \bar{B}_{12,2} = & \left[ a_{k3} (b_{A22} c_{H22} - b_{H22} c_{A22}) + b_{k3} (a_{H22} c_{A22} - a_{A22} c_{H22}) \right. \\ & \left. + c_{k3} (a_{A22} b_{H22} - a_{H22} b_{A22}) \right] / d_3, \end{aligned} \quad (3.113b)$$

$$\bar{C}_{12,2} = -\frac{(a/b)^2}{8} \bar{A}_{12,2} + \frac{1}{8(a/b)^2} (\bar{B}_{12,2} - 4k_1 - 2(a/b)k_2), \quad (3.113c)$$

$$\bar{D}_{12,2} = \frac{(a/b)^6}{24} \bar{A}_{12,2} + \frac{(a/b)^2}{2} \left( \frac{\bar{B}_{12,2}}{4} - k_1 + \frac{1}{2}(a/b)k_2 \right). \quad (3.113d)$$

$$\begin{aligned} \bar{A}_{22,2} = & \left[ -a_{k3} (4b_{B22} + b_{H12} c_{B22}) + b_{k3} (a_{H12} c_{B22} + 4a_{B22}) \right. \\ & \left. + c_{k3} (a_{B22} b_{H12} - a_{H12} b_{B22}) \right] / d_3. \end{aligned} \quad (3.113e)$$

$$\begin{aligned} \bar{B}_{21,2} = & \left[ a_{k3} (b_{H12} c_{A22} + 4b_{A22}) - b_{k3} (4a_{A22} + a_{H12} c_{A22}) \right. \\ & \left. + c_{k3} (a_{H12} b_{A22} - a_{A22} b_{H12}) \right] / d_3. \end{aligned} \quad (3.113f)$$

$$\bar{C}_{22,2} = k_{AC} \bar{A}_{22,2} + k_{BC} \bar{B}_{22,2} + k_{CC}. \quad (3.113g)$$

$$\bar{D}_{22,2} = k_{AD} \bar{A}_{22,2} + k_{BD} \bar{B}_{22,2} + k_{CD}. \quad (3.113h)$$

$$a_{H12} = -\frac{(a/b)^6}{24} + \frac{(a/b)^2}{4} - \frac{1}{3} + \frac{1}{8(a/b)^2}. \quad (3.114a)$$

$$a_{A22} = \left[ \frac{(a/b)^6}{24} - \frac{(a/b)^2}{8} + \frac{1}{12} \right] I_2(\gamma) - k_{AC} - k_{AD}, \quad (3.114b)$$

$$a_{B22} = \left[ \frac{(a/b)^6}{24} - \frac{(a/b)^2}{8} + \frac{1}{12} \right] K_2(\gamma) - k_{BC} - k_{BD}, \quad (3.114c)$$

$$\begin{aligned} a_{k3} = & \left( -\frac{13(a/b)^6}{5184} + \frac{13(a/b)^2}{1728} - \frac{419}{331776} \right) \bar{X}_1 \\ & + \left( \frac{(a/b)^6}{432} - \frac{(a/b)^2}{144} + \frac{53}{27648} \right) \bar{X}_2 + \left( -\frac{(a/b)^6}{288} + \frac{(a/b)^2}{96} - \frac{5}{1152} \right) \bar{X}_3 \\ & - \frac{137}{10368} \bar{X}_4 + \frac{19}{1728} \bar{X}_5 - \frac{1}{72} \bar{X}_6 + \left( \frac{(a/b)^6}{96} - \frac{(a/b)^2}{32} + \frac{5}{48} \right) \bar{X}_8 \\ & - \left( \frac{(a/b)^2}{2} + \frac{1}{2(a/b)^2} \right) k_1 + \left( \frac{(a/b)^3}{4} - \frac{1}{4(a/b)} \right) k_2 - k_{CC} - k_{CD}. \end{aligned} \quad (3.114d)$$

$$b_{H12} = \frac{1}{12}(a/b)^6 - \frac{1}{3} + \frac{1}{4(a/b)^2}, \quad (3.114e)$$

$$b_{A22} = \left[ -\frac{(a/b)^6}{12} - \frac{(a/b)^2}{4} + \frac{1}{3} \right] I_2(\gamma) - 2k_{Ac} + 2k_{AD}, \quad (3.114f)$$

$$b_{H22} = \left[ -\frac{(a/b)^6}{12} - \frac{(a/b)^2}{4} + \frac{1}{3} \right] K_2(\gamma) - 2k_{Hc} + 2k_{HD}, \quad (3.114g)$$

$$\begin{aligned} b_{k3} = & \left( -\frac{13(a/b)^6}{2592} + \frac{13(a/b)^2}{864} - \frac{419}{165888} \right) \bar{X}_1 \\ & + \left( -\frac{(a/b)^6}{216} - \frac{(a/b)^2}{72} + \frac{67}{13824} \right) \bar{X}_2 + \left( \frac{(a/b)^6}{144} + \frac{(a/b)^2}{48} - \frac{7}{576} \right) \bar{X}_3 \\ & - \frac{293}{10368} \bar{X}_4 + \frac{43}{1728} \bar{X}_5 - \frac{5}{144} \bar{X}_6 + \left( -\frac{(a/b)^6}{48} - \frac{(a/b)^2}{16} + \frac{1}{48} \right) \bar{X}_8 + \frac{1}{16} \bar{X}_9 \\ & + \left( (a/b)^2 - \frac{1}{(a/b)^2} \right) k_1 - \left( \frac{(a/b)^3}{2} + \frac{1}{2(a/b)} \right) k_2 - 2k_{c'} + 2k_{cD}, \end{aligned} \quad (3.114h)$$

$$c_{A22} = 4I_2(\gamma) - \gamma I_1(\gamma) + \frac{2}{Da} k_{Ac} - \frac{2}{Da} k_{AD}, \quad (3.114i)$$

$$c_{H22} = 4K_2(\gamma) + \gamma K_1(\gamma) + \frac{2}{Da} k_{Hc} - \frac{2}{Da} k_{HD}, \quad (3.114j)$$

$$\begin{aligned} c_{k3} = & \frac{1}{108} \bar{X}_1 - \frac{1}{36} \bar{X}_2 + \frac{1}{6} \bar{X}_3 + \frac{1}{32} \bar{X}_4 - \frac{1}{16} \bar{X}_5 + \frac{1}{4} \bar{X}_6 - \frac{1}{4} \bar{X}_7 \\ & + \frac{1}{2} \bar{X}_8 - \frac{1}{4} \bar{X}_9 + \frac{2}{Da} k_{c'} - \frac{2}{Da} k_{cD}. \end{aligned} \quad (3.114k)$$

$$\begin{aligned} d_3 = & a_{H12} (b_{H22} c_{A22} - b_{A22} c_{H22}) + a_{A22} (b_{H12} c_{H22} + 4b_{H22}) \\ & - a_{H22} (4b_{A22} + b_{H12} c_{A22}), \end{aligned} \quad (3.114l)$$

$$k_1 = \left[ \frac{\bar{X}_1}{384} \ln(a/b)^2 + \left( -\frac{25\bar{X}_1}{4608} + \frac{\bar{X}_2}{384} \right) \ln(a/b) + \frac{415\bar{X}_1}{110592} - \frac{25\bar{X}_2}{9216} + \frac{\bar{X}_3}{384} \right] (a/b)^6$$

$$\begin{aligned}
& + \left[ \frac{\bar{X}_4}{144} \ln(a/b)^3 + \left( -\frac{11\bar{X}_4}{576} + \frac{\bar{X}_5}{96} \right) \ln(a/b)^2 \right. \\
& + \left. \left( \frac{85\bar{X}_4}{3456} - \frac{11\bar{X}_5}{576} + \frac{\bar{X}_6}{48} \right) \ln(a/b) - \frac{137\bar{X}_4}{10368} + \frac{19\bar{X}_5}{1728} - \frac{\bar{X}_6}{72} \right] (a/b)^4 \\
& + \left[ -\frac{\bar{X}_7}{32} \ln(a/b)^2 + \left( \frac{\bar{X}_7}{64} - \frac{\bar{X}_8}{16} \right) \ln(a/b) \right] (a/b)^2 + \frac{\bar{X}_9}{16} \ln(a/b), \quad (3.115a)
\end{aligned}$$

$$\begin{aligned}
k_2 = & \left[ \frac{\bar{X}_1}{64} \ln(a/b)^2 + \left( -\frac{7\bar{X}_1}{265} + \frac{\bar{X}_2}{64} \right) \ln(a/b) + \frac{35\bar{X}_1}{2048} - \frac{7\bar{X}_2}{512} + \frac{\bar{X}_3}{64} \right] (a/b)^5 \\
& + \left[ \frac{\bar{X}_4}{36} \ln(a/b)^3 + \left( -\frac{\bar{X}_4}{18} + \frac{\bar{X}_5}{24} \right) \ln(a/b)^2 \right. \\
& + \left. \left( \frac{13\bar{X}_4}{216} - \frac{\bar{X}_5}{18} + \frac{\bar{X}_6}{12} \right) \ln(a/b) - \frac{293\bar{X}_4}{10368} + \frac{43\bar{X}_5}{1728} - \frac{5\bar{X}_6}{144} \right] (a/b)^3 \\
& + \left[ -\frac{\bar{X}_7}{16} \ln(a/b)^2 - \left( \frac{\bar{X}_7}{32} + \frac{\bar{X}_8}{8} \right) \ln(a/b) + \frac{\bar{X}_7}{64} - \frac{\bar{X}_8}{16} \right] (a/b) + \frac{\bar{X}_9}{16(a/b)}, \quad (3.115b)
\end{aligned}$$

$$k_{A1} = -\frac{1}{4} \int_1^b \xi^{-1} I_2(\gamma\xi) d\xi, \quad (3.115c)$$

$$k_{B1} = -\frac{1}{4} \int_1^b \xi^{-1} K_2(\gamma\xi) d\xi, \quad (3.115d)$$

$$k_{C1} = -\frac{1}{4} \int_1^b \xi^{-1} G(\xi) d\xi, \quad (3.115e)$$

$$k_{A2} = \frac{1}{4} \int_1^b \xi^3 I_2(\gamma\xi) d\xi, \quad (3.115f)$$

$$k_{hl} = \frac{1}{4} \int_1^c \int_1^b \xi^3 K_2(\gamma \xi) d\xi, \quad (3.115g)$$

$$k_{cl} = -\frac{1}{4} \int_1^c \int_1^b \xi^3 G(\xi) d\xi, \text{ and} \quad (3.115h)$$

$$G(\xi) = K_2(\gamma \xi) \int_1^\xi \bar{Z}(\zeta) I_2(\gamma \zeta) d\zeta - I_2(\gamma \xi) \int_1^\xi \bar{Z}(\zeta) K_2(\gamma \zeta) d\zeta. \quad (3.116)$$

Similar to the first order solutions, one needs to perform inverse Finite Fourier Transform to obtain solutions in the physical domain. Recall that the inverse transforms are given by

$$\Psi_{12} = \frac{1}{2\pi} \bar{\Psi}_{12,0} + \frac{1}{\pi} \sum_{n=1}^{\infty} \bar{\Psi}_{12,n} \quad \text{and} \quad \Psi_{22} = \frac{1}{2\pi} \bar{\Psi}_{22,0} + \frac{1}{\pi} \sum_{n=1}^{\infty} \bar{\Psi}_{22,n}. \quad (3.117 - 118)$$

Since, in this case, only  $n = 2$  gives non-trivial solutions, the solutions for the stream functions are

$$\begin{aligned} \Psi_{12} = & \frac{X_1}{384} R^6 \ln(R)^2 + \left( -\frac{25X_1}{4608} + \frac{X_2}{384} \right) R^6 \ln(R) + \left( \frac{415X_1}{110592} - \frac{25X_2}{9216} + \frac{X_3}{384} \right) R^6 \\ & + \frac{X_4}{144} R^4 \ln(R)^3 + \left( -\frac{11X_4}{576} + \frac{X_5}{96} \right) R^4 \ln(R)^2 + \left( \frac{85X_4}{3456} - \frac{11X_5}{576} + \frac{X_6}{48} \right) R^4 \ln(R) \\ & + \left( -\frac{137X_4}{10368} + \frac{19X_5}{1728} - \frac{X_6}{72} + \frac{A_{12,2}}{12} \right) R^4 - \frac{X_7}{32} R^2 \ln(R)^2 + \left( \frac{X_7}{64} - \frac{X_8}{16} \right) R^2 \ln(R) \\ & + C_{12,2} R^2 + \frac{X_9}{16} \ln(R) - \frac{B_{12,2}}{4} + D_{12,2} R^{-2}, \text{ and} \end{aligned} \quad (3.119)$$

$$\Psi_{22} = C_{22,2} R^2 + D_{22,2} R^{-2} + \frac{R^2}{4} \int_1^R \frac{\Omega_{22,2}(\xi)}{\xi} d\xi - \frac{R^{-2}}{4} \int_1^R \xi^3 \Omega_{22,2}(\xi) d\xi. \quad (3.120)$$

A rather complete sample calculation at  $\theta = 30^\circ$  is shown in Appendix E. Profiles of the first and second leading terms for stream function, vorticity, and temperature were plotted to prove the validity of the solutions. Moreover, checks for the boundary and interface conditions were performed to further verify the correctness of these solutions.

### (e) Evaluation of Heat Transfer Results

To evaluate the heat transfer results, the local and average Nusselt numbers defined respectively in Eqs. (2.68) and (2.69) are employed. Substitute the temperature profiles (3.18b, d) into equation (2.69) and evaluate at the inner and out cylinders, one obtains

$$\overline{Nu}_{in} = \frac{q}{a/b} - Ra \frac{q}{\pi} \int_0^\pi \tilde{\Theta}'_{11} \Big|_{R=a/b} d\theta + \dots \text{ and} \quad (3.121)$$

$$\overline{Nu}_{out} = \frac{k_1}{k_2} \frac{q}{c/b} - Ra \frac{k_1}{k_2} \frac{q}{\pi} \int_0^\pi \tilde{\Theta}'_{21} \Big|_{R=c/b} d\theta + \dots \quad (3.122)$$

where

$$\begin{aligned} \tilde{\Theta}'_{11} = & \frac{3R^2}{64} A'_{11} + \frac{\ln(R)^2 + \ln(R) - 1}{8} B'_{11} + \frac{\ln(R) + 1}{2} C'_{11} - \frac{\ln(R) - 1}{2R^2} D'_{11} \\ & + E_{11} - \frac{F_{11}}{R^2} + \frac{\Gamma'_{11} R^2}{64} \left( 3\ln(R) - \frac{7}{2} \right), \text{ and} \end{aligned} \quad (3.123a)$$

$$\begin{aligned} \tilde{\Theta}'_{21} = & \frac{A'_{21}}{\gamma^3} \left( \int_1^R \frac{I_0(\gamma \xi)}{\xi^3} d\xi + \frac{I_0(\gamma R)}{R^2} \right) - \frac{B'_{21}}{\gamma^3} \left( \int_1^R \frac{K_0(\gamma \xi)}{\xi^3} d\xi + \frac{K_0(\gamma R)}{R^2} \right) \\ & + \frac{C'_{21}}{2} [\ln(R) + 1] + \frac{D'_{21}}{2R^2} (\ln(R) - 1) + E_{21} - \frac{F_{21}}{R^2} + \frac{\Gamma'_{21}}{8} [\ln(R)^2 + \ln(R) - 1]. \end{aligned}$$



Since Eqs. (3.123) are even functions, the limit of integration in Eqs. (3.121) and (3.122) can be evaluated from 0 to  $\pi$ .

### 3.6 Results and Discussion

The present study is focused on the effects of Rayleigh number, porous sleeve thickness, Darcy number, Prandtl number, and the effective thermal conductivity ratio on the flow and temperature fields in concentric annular spaces. Among the parameters considered, Rayleigh number signifies the thermal buoyancy induced by the differential heating between the inner and outer cylinders. Since the Rayleigh number is assumed small in the present study, the annulus is only slightly heated. Therefore, the buoyancy-induced flow is small but finite. Also, it is important to note that the Prandtl number for liquids such as water, methyl alcohol, and gasoline has a value on the order of  $10$  while for lubricant oils, it is about  $10^4$ . For the discussion that follows, we again limit our attention to a specific configuration of  $a = 1$ ,  $b = 1.5$ ,  $c = 2$ , unless specified otherwise.

Unlike the previous chapter, the velocity and temperature fields in this chapter are presented in terms of stream functions and isotherms. Figure 3.2 shows the velocity fields for various Rayleigh and Prandtl numbers. Apparently, the velocity fields are symmetrical about the vertical axis. On each side of the symmetrical axis, there exists a convective cell. On the left, the cell rotates in the counter-clockwise direction while on the right, another cell of equal strength rotates in the clockwise direction. It is surprising to find that the Prandtl number has insignificant effect on the solution. Observe that in the formulation, the Prandtl number only appears in the equations with the second order

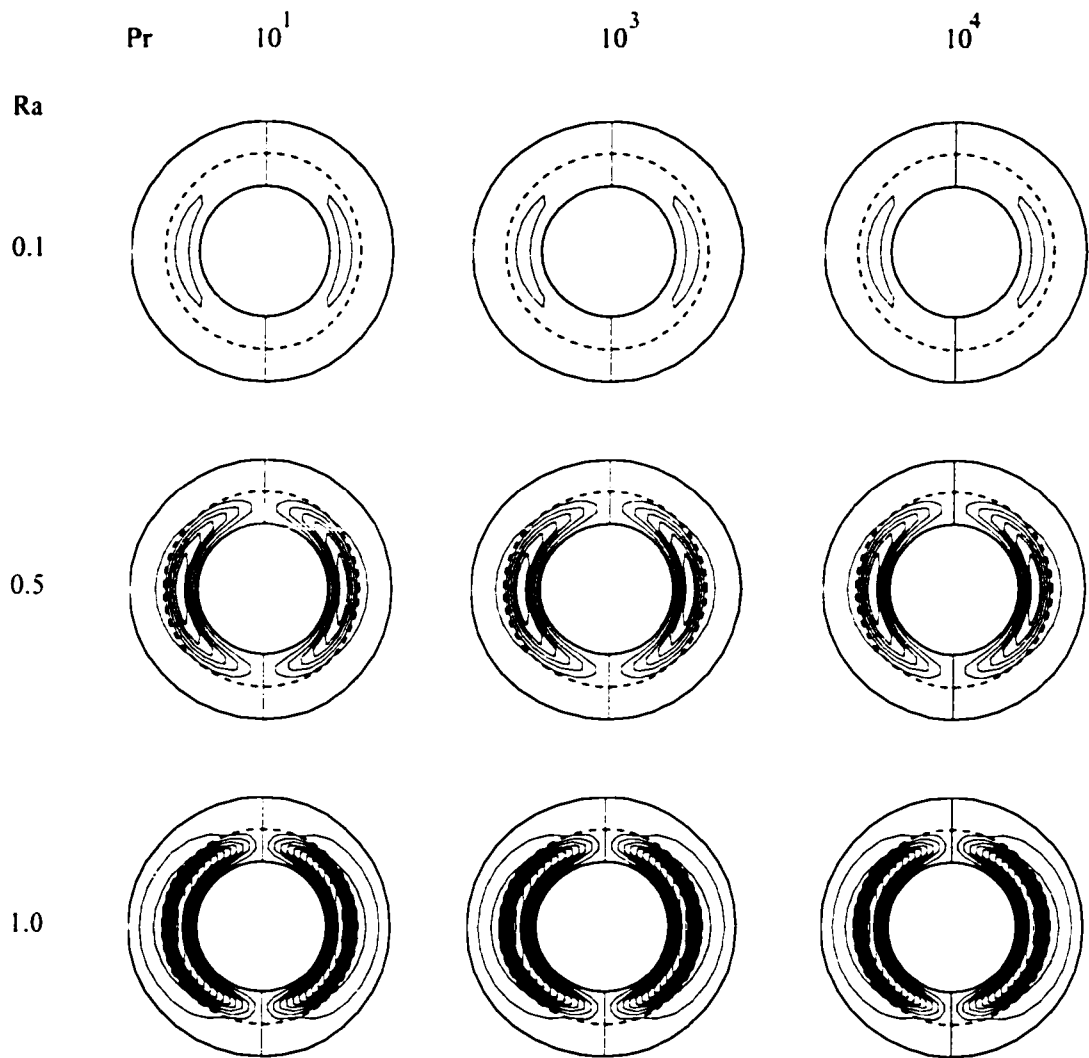


Figure 3.2 Flow fields in a concentric annulus with a porous sleeve for  $h = 1.50$ ,  $Da = 10^{-4}$ , and  $k_1/k_2 = 1.0$  ( $\Delta\Psi = 5.0 \times 10^{-6}$ ).

or higher. This in turn implies that the terms corresponding to  $Ra^2$  have a negligible effect on the final result even if  $Ra = 1$ . As the Rayleigh number increases, the strength of the convective cells grows accordingly. Since the flow fields are identical among the cases with different values of the Prandtl number, it proves that the Prandtl number effect is negligible, or in other words,  $\Psi_{12}$  and  $\Psi_{22}$  are relatively small compared with their preceding terms. Strictly speaking, a regular perturbation technique would not have a converged solution when the perturbed quantity ( $Ra$  in the present study) has a value greater than unity. However, in the literature, it has been reported that Mack and Bishop (1968) utilized perturbation technique to obtain solutions in which the Rayleigh number was as high as  $10^3$ . In addition, Huetz and Petit (1974) as well as Custer and Shaughnessy (1977) all performed a similar study in which the perturbed quantity, the Grashof number  $Gr$ , was in an order up to  $10^4$ .

Figure 3.3 shows the temperature fields which correspond to the cases presented in Figure 3.2. Obviously, the temperature fields for all combinations of the Rayleigh and Prandtl numbers considered are almost the same. The temperature profiles are independent of the azimuthal angle because the isotherms appear to be a family of concentric circles. These isotherms are placed in an interval that is proportional to the logarithm of the radial distance. It suggests that heat conduction is the dominant heat transfer mode in the entire annulus space. This is consistent with the assumption made at the beginning of this study, that is, the study is limited to a small value of the Rayleigh number. A small Rayleigh number indicates that heat convection is insignificant, or in other words, heat conduction is the dominant heat transfer mechanism in the system. This observation is also consistent with what Kuehn and Goldstein (1976) reported. They

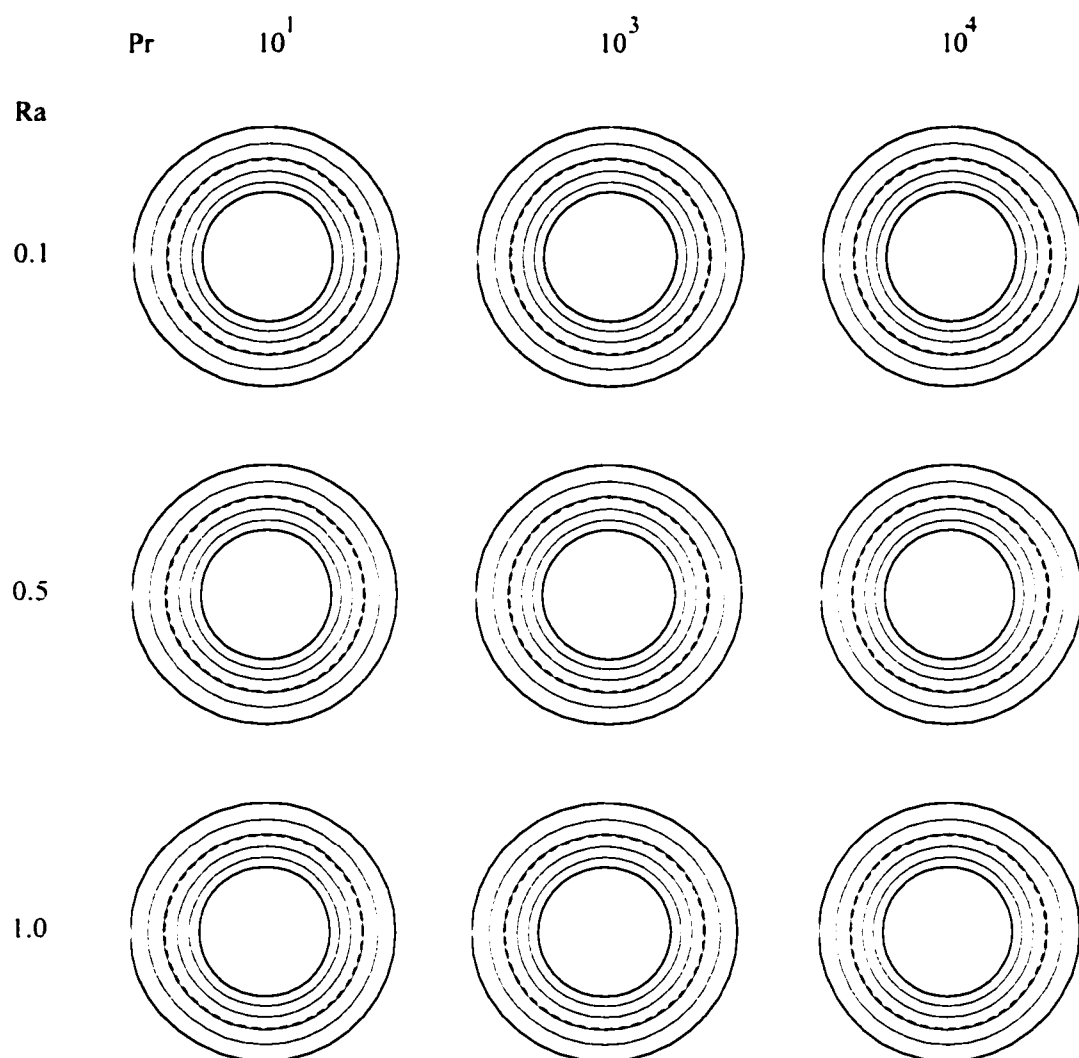


Figure 3.3 Temperature fields in a concentric annulus with a porous sleeve for  $h = 1.50$ ,  $Da = 10^{-4}$ , and  $k_1/k_2 = 1.0$  ( $\Delta\Theta = 0.2$ ).

have shown that the critical Rayleigh number  $Ra_L$  for the onset of heat convection in concentric cylinders is about  $10^3$ , where  $Ra_L$  is defined based on the gap width,  $L$ . As concluded in the previous chapter, the presence of a porous sleeve suppresses convective flow and thus demotes heat convection. Therefore, it is reasonable to expect that the critical Rayleigh number for the onset of heat convection in a concentric annulus with a porous sleeve would be higher than  $10^3$ .

Figure 3.4 presents the flow fields for various Rayleigh numbers and sleeve thicknesses. Consistent with what observed in Figure 3.2, the strength of the convective cell increases with the Rayleigh number. Recall from the last chapter that an increase in the value of  $b$  from 1.25 to 1.75 implies a reduction in the porous sleeve thickness. This can be clearly observed by the locations of the interface (dashed line) between the inner and outer cylinders. As  $b$  increases, the thickness of the porous sleeve reduces and the flow resistance in the entire system decreases accordingly. As a result, less energy is lost to flow resistance which leads to more energy to drive the convective flow. In general, the eyes of the convective cells are located within the fluid layer. Also noticed is that the flow patterns depend strongly on  $b$ . At  $b = 1.75$ , the porous sleeve is almost impermeable and the main flow is confined within the fluid layer. As  $b$  decreases, the convective cells penetrate the porous sleeve. At  $b = 1.25$ , the fluid layer is too thin to contain the convective cells. As a result, the cells penetrate the porous sleeve, but their strength decreases. It is interesting to point out that the streamlines experience a change in the direction across the interface. This change in the direction is less obvious for smaller  $b$ .

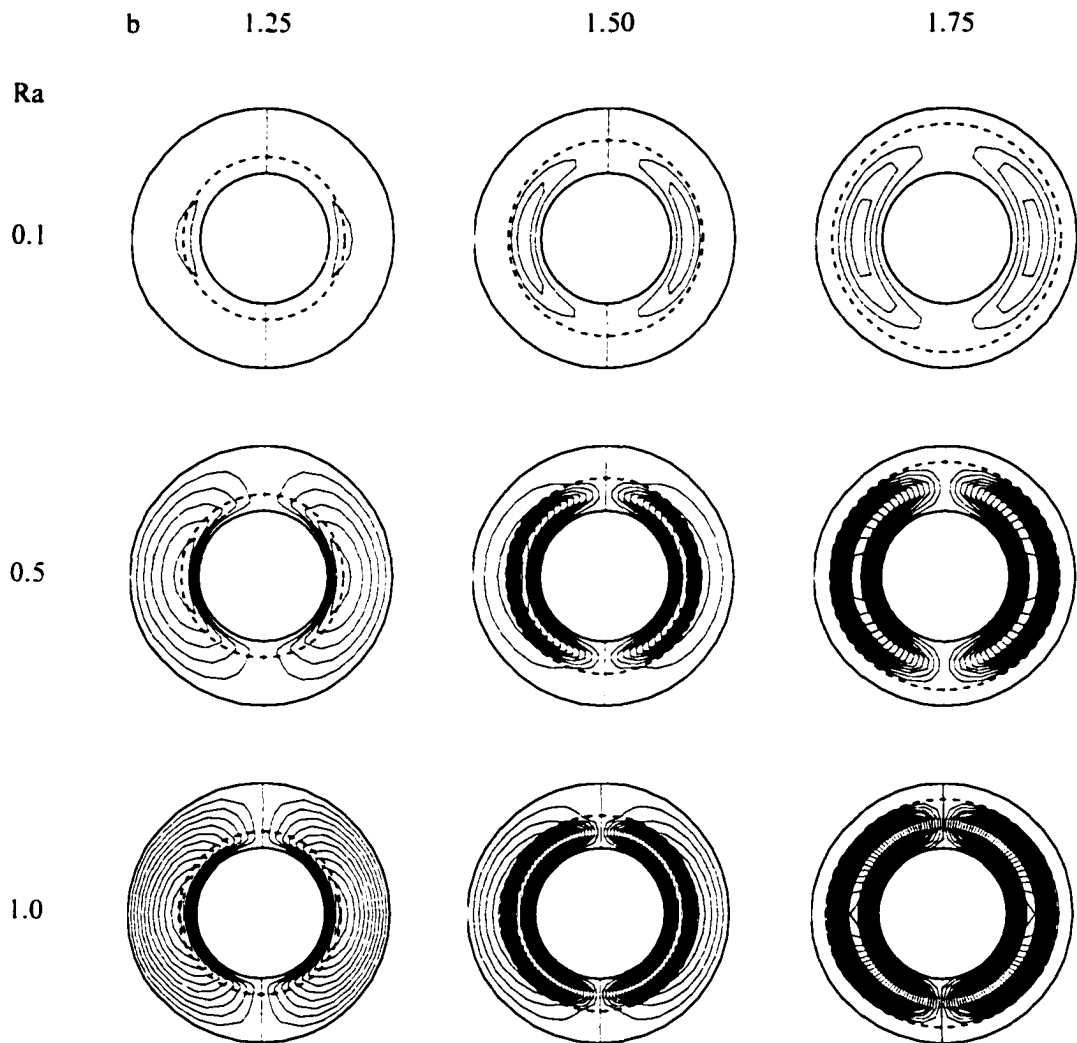
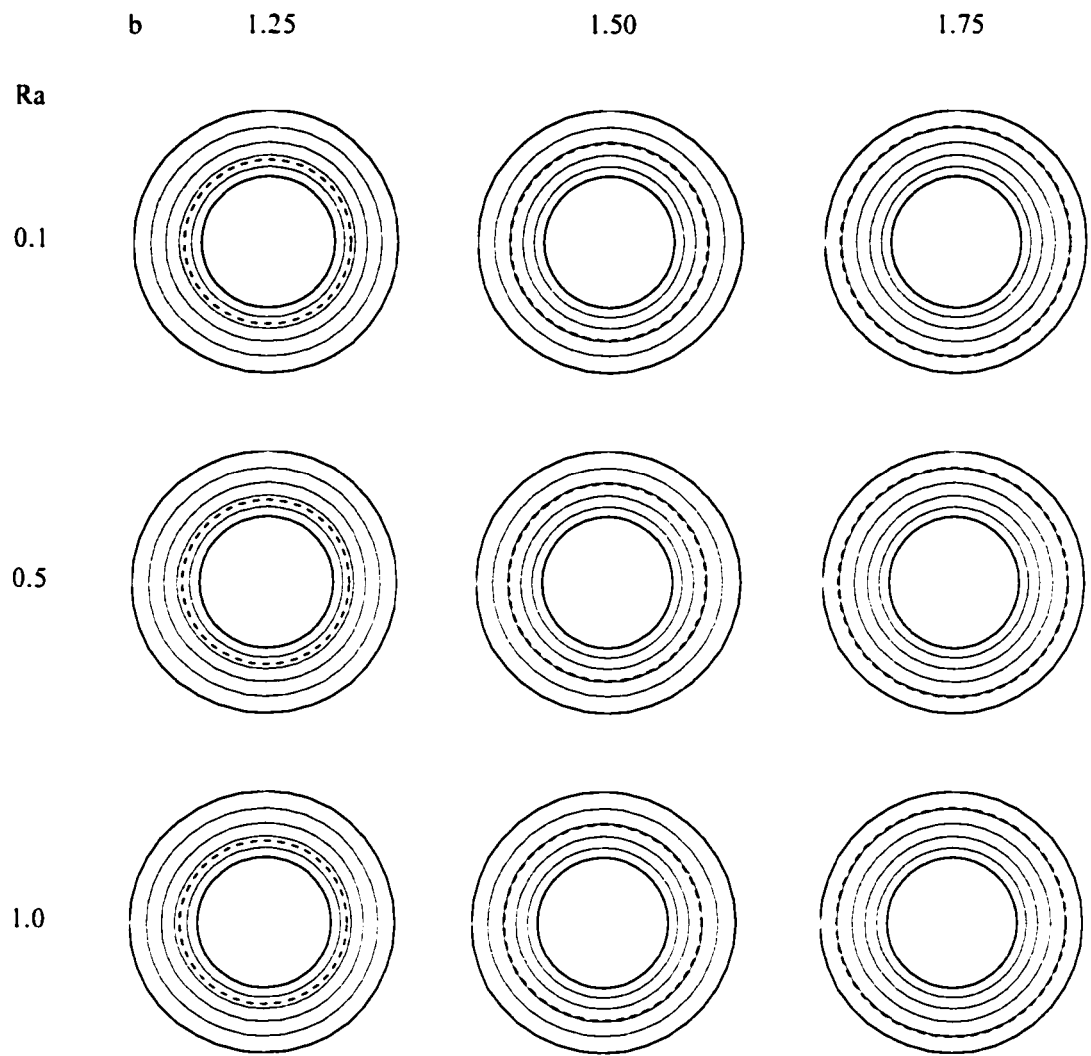


Figure 3.4 Flow fields in a concentric annulus with a porous sleeve for  $Da = 10^4$ ,  $k_1/k_2 = 1.0$ , and  $Pr = 20,000$  ( $\Delta\Psi = 2.0 \times 10^{-6}$  for  $b = 1.25$ ,  $\Delta\Psi = 2.5 \times 10^{-6}$  for  $b = 1.50$ , and  $\Delta\Psi = 5.0 \times 10^{-6}$  for  $b = 1.75$ ).

The isotherms shown in Figure 3.5 are nearly identical in patterns. Regardless of the location of the interface, the spacing between isotherms remains unchanged. This indicates that the sleeve thickness has nearly no effect on the temperature distribution. Since it is assumed that  $k_1/k_2 = 1.0$  in these cases, the temperature gradient in the annulus is proportional to the logarithm of the radial distance. Recognize that the porous sleeve thickness only affects the flow structure because heat transfer is in a very weak heat convection mode. Because it is heat conduction that dominates the heat transfer in these cases, there is no reason for the temperature fields shown in Figure 3.5 to be different from each other.

Presented in Figure 3.6 are the flow fields for various Darcy and Rayleigh numbers. Again, the convective cells grow stronger with an increase in the Rayleigh number. A unity Darcy number implies that the pore size in the porous sleeve is of the same order of the gap width. This in turn signifies the flow resistance effect in the porous sleeve is basically non-existent. As such, the flow structures for  $Da = 10^0$  resemble those in an annulus without the porous sleeve. As the Darcy number decreases, the flow resistance becomes more significant and it is more difficult for the convective flow to penetrate the porous sleeve. This leads to weaker convective cells for a smaller Darcy number. This trend is observed for all the Rayleigh number considered. Also, it is clearly observed that the eye of the convective cells moves inward as the Darcy number decreases. Since the flow penetration decreases with a reduction in the Darcy number, the cells are mostly confined in the fluid layer and thus the eyes are pushed inward. At  $Da = 10^0$ , the eyes lie right on the interface between the fluid and porous sleeve, which locates at the center of the gap. This is mainly because the presence of a porous sleeve



**Figure 3.5**      Temperature fields in a concentric annulus with a porous sleeve for  $Da = 10^{-4}$ ,  $k_1/k_2 = 1.0$ , and  $Pr = 20,000$  ( $\Delta\Theta = 0.2$ ).



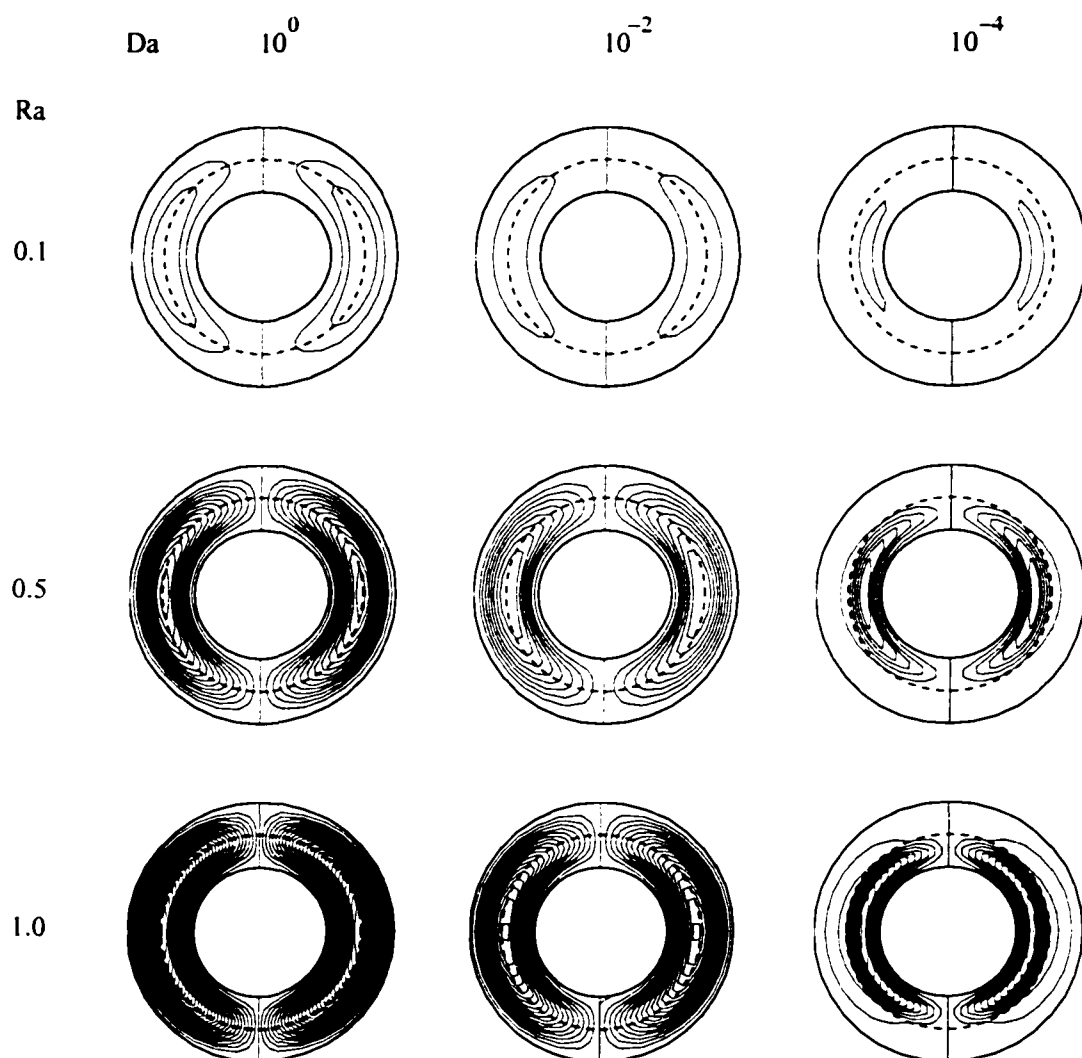


Figure 3.6 Flow fields in a concentric annulus with a porous sleeve for  $b = 1.50$ ,  $k_1/k_2 = 1.0$ , and  $Pr = 20,000$  ( $\Delta\Psi = 5.0 \times 10^{-6}$  for  $Da = 10^{-4}$ , and  $\Delta\Psi = 2.5 \times 10^{-5}$  otherwise).

has basically no effect on the flow field at this value of the Darcy number. Figure 3.7 shows the corresponding temperature fields for the cases presented in Figure 3.6. Since the conductivity ratio is unity for all the cases considered here, the isotherm patterns are identical. This also shows that the temperature gradients are too small to induce significant heat convection.

The effects of thermal conductivity ratio  $k_1/k_2$  are examined from Figures 3.8 to 3.11. The flow fields illustrated in Figure 3.8 show similar trends discovered in Figure 3.6. At small Rayleigh numbers, the convective cells are confined within the fluid layer. As the Rayleigh number increases, the cells gain more strength and eventually penetrate the porous sleeve ( $Ra = 1.0$ ). With an increase in the thermal conductivity ratio, the convective cells become weaker. However, it can be observed that flow penetration is enhanced for  $k_1/k_2 > 1$ , but suppressed for  $k_1/k_2 < 1$ . At low Rayleigh numbers, the porous sleeve behaves as if it were impermeable. As the Rayleigh number increases, additional thermal energy promotes convective flow and these cells eventually gain enough strength to penetrate the porous layer ( $Ra = 1.0$ ). Notice that the streamlines change their directions across the interface. It is also seen that the flow structures in the porous layer depend on  $k_1/k_2$ . For  $k_1/k_2 > 1$ , the porous sleeve has a smaller thermal conductivity and thus leads to a larger temperature gradient in the porous sleeve to promote convection and flow penetration. At  $Ra = 1.0$ , flow penetrates the porous sleeve through a larger portion of the interface for  $k_1/k_2 = 2.0$  than that for  $k_1/k_2 = 0.5$ .

Figure 3.9 shows the corresponding temperature fields for the cases presented in Figure 3.8. The results indicate that the temperature fields depend mostly on the thermal conductivity ratio but not the Rayleigh number. Because the dominant heat transfer

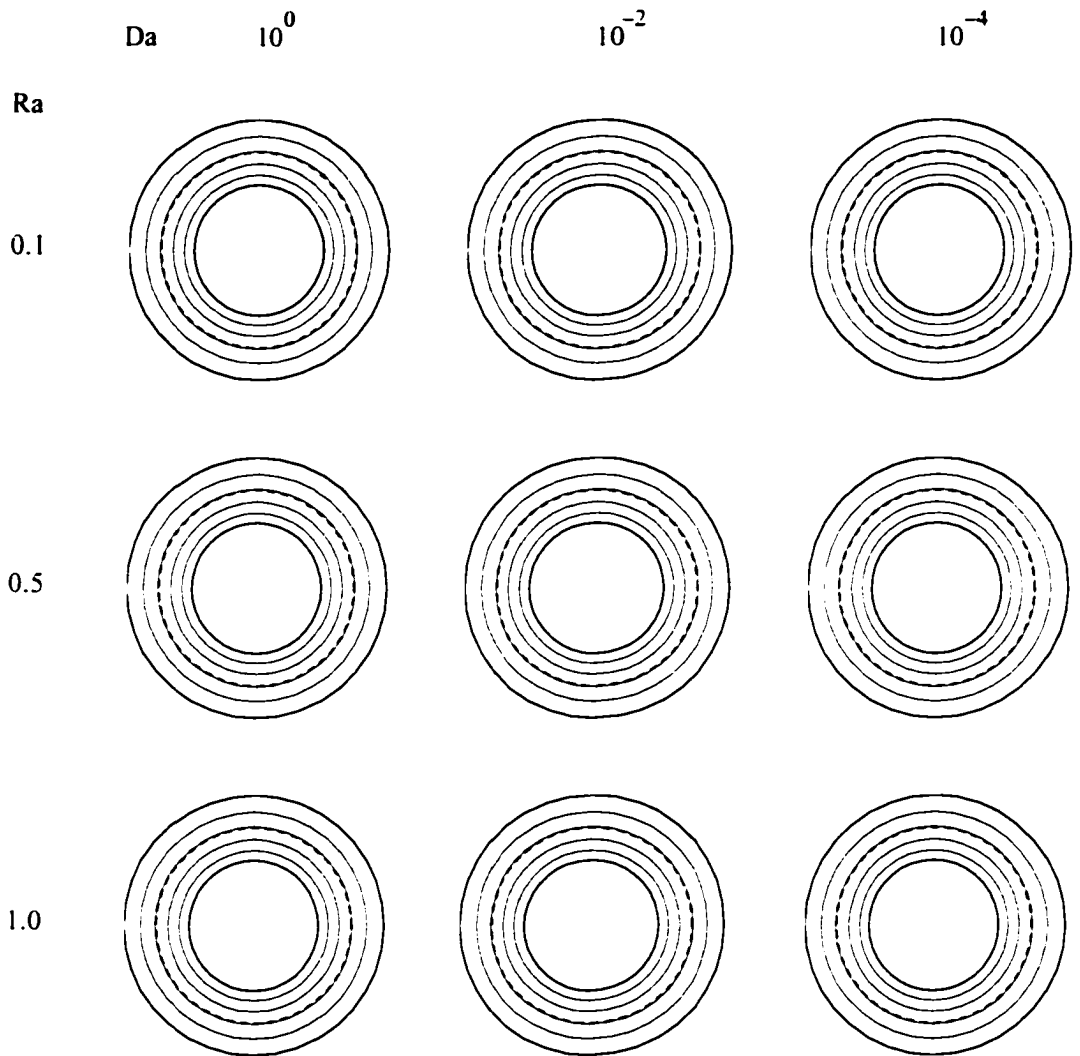
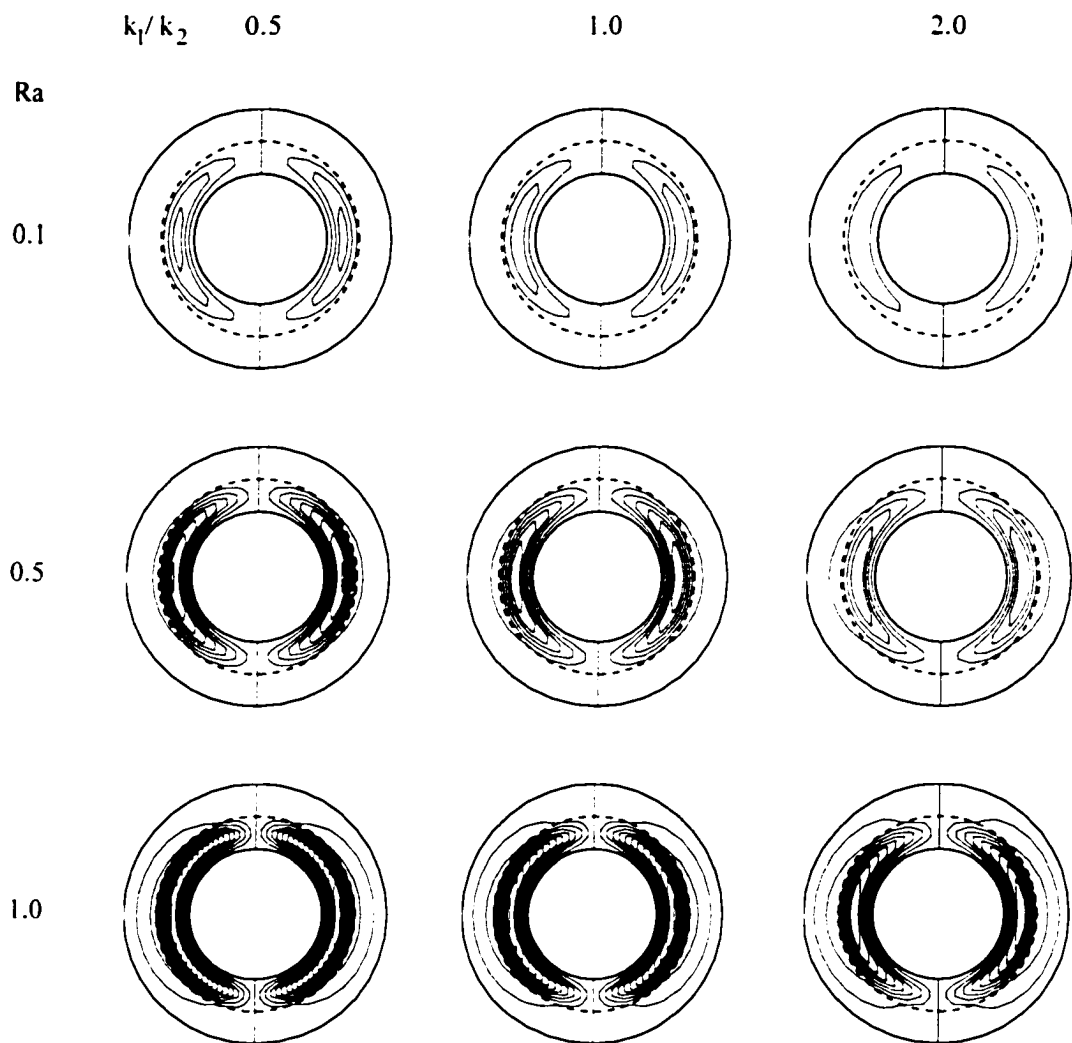


Figure 3.7 Temperature fields in a concentric annulus with a porous sleeve for  $b = 1.50$ ,  $k_1/k_2 = 1.0$ , and  $Pr = 20,000$  ( $\Delta\Theta = 0.2$ ).



**Figure 3.8** Flow fields in a concentric annulus with a porous sleeve for  $b = 1.50$ ,  $Da = 10^{-4}$ , and  $Pr = 20,000$  ( $\Delta\Psi = 2.5 \times 10^{-6}$  for  $Ra = 0.1$ , and  $\Delta\Psi = 5.0 \times 10^{-6}$  otherwise).

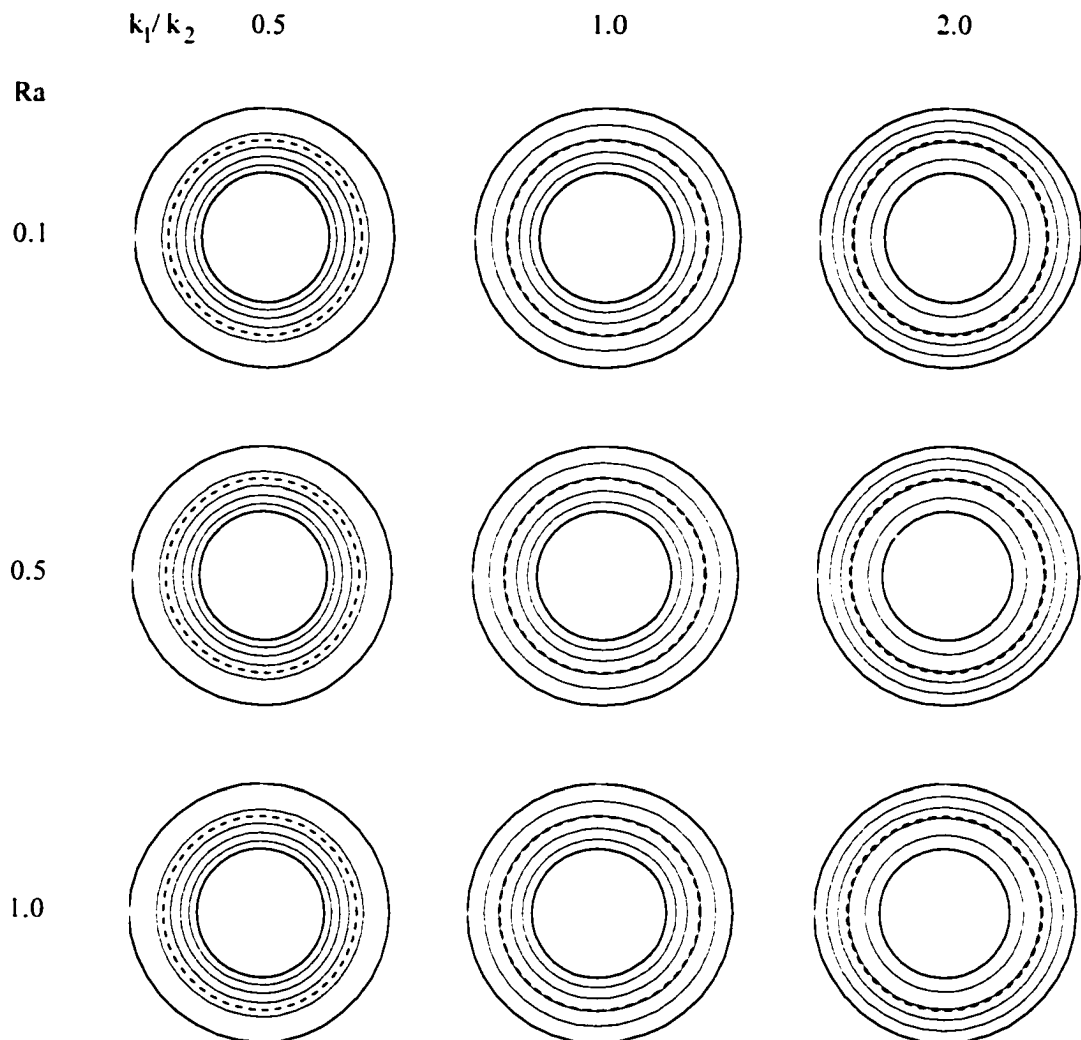


Figure 3.9 Temperature fields in a concentric annulus with a porous sleeve for  $h = 1.50$ ,  $Da = 10^{-4}$ , and  $Pr = 20,000$  ( $\Delta\Theta = 0.2$ ).

mode for these cases ( $Ra \leq 1.0$ ) is heat conduction, the Rayleigh number only plays a minor role. When  $k_1/k_2 = 1.0$ , the isotherms are relatively evenly distributed within the gap because there is no distinction between the fluid and porous sleeve as far as pure conduction is concerned. For  $k_1/k_2 < 1.0$ , the porous sleeve is more conductive than the fluid layer. As a result, a large temperature gradient is found in the fluid layer while temperature is almost uniform in the porous sleeve. Conversely, for  $k_1/k_2 > 1.0$ , the temperature in the fluid layer is more uniform than that in the porous sleeve.

Flow fields for various combinations of  $k_1/k_2$  and  $b$  are presented in Figure 3.10. First of all, one observes that the strength of the convective cells is relatively the same for a given porous sleeve thickness, but it increases with  $b$ . Recall from Figures 3.8 and 3.9, a larger  $k_1/k_2$  results in a smaller temperature gradient in the fluid layer to initiate a strong convection. As  $k_1/k_2$  reduces, the temperature gradient in the fluid layer increases and eventually provokes the convective cell whose eye is located in the fluid layer. For example, at  $b = 1.25$ , the change in the thermal conductivity ratio modifies the temperature field that in turn affects the strength of buoyancy force. For  $k_1/k_2 = 2.0$ , a greater temperature gradient takes place in the porous sleeve, which promotes convection in the porous sleeve and thus allows more flow penetration to the porous sleeve. On the other hand, for  $k_1/k_2 = 0.5$ , the temperature gradient in the fluid layer is greater. Consequently, the convective cells take up more space in the fluid layer when compared with the case of  $k_1/k_2 = 2.0$ . In brief, one can conclude that an increase in the thermal conductivity ratio  $k_1/k_2$  promotes convective flows in the porous sleeve but demotes that in the fluid layer.

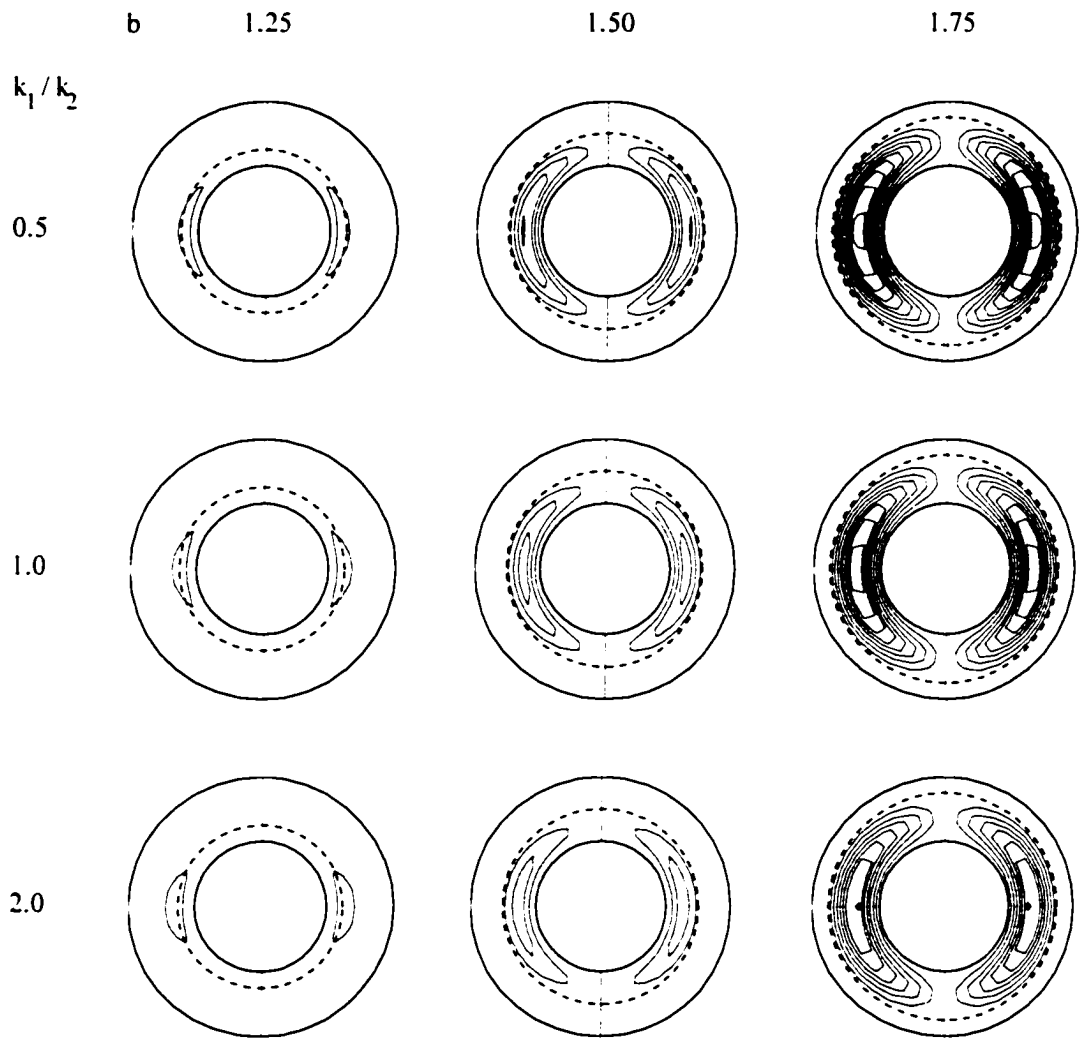


Figure 3.10 Flow fields in a concentric annulus with a porous sleeve for  $Da = 10^{-4}$ ,  $Pr = 20,000$ , and  $Ra = 0.1$  ( $\Delta\Psi = 2.0 \times 10^{-6}$ ).

Figure 3.11 presents the temperature fields for the cases discussed above. Obviously, heat conduction is still the dominant heat transfer mode. For a given porous sleeve thickness, it is apparent that the temperature gradient in the fluid layer decreases with the thermal conductivity ratio  $k_1/k_2$ , but that in the porous sleeve increases. This is exactly what is expected because heat transfer across any annular cross-section is constant. As such, a layer with a larger thermal conductivity experiences a smaller temperature gradient. For a fixed thermal conductivity ratio  $k_1/k_2$ , the number of isotherms in the fluid layer increases while that in the porous sleeve decreases as the value of  $b$  increases. Among all the isotherms shown, it is seen that only those of  $k_1/k_2 = 1.0$  are independent of the porous sleeve thickness.

The flow fields presented in Figure 3.12 show a similar trend that was observed in Figure 3.6. As the Darcy number decreases, the convective cell weakens in strength along with its eye moving toward the fluid layer. Notice that the increment of the stream function  $\Delta\Psi$  for the case of  $Da = 10^{-4}$  is only half of the other cases. Therefore, its strength is actually much weaker than it appears in the figure. It is interesting to note that the change in strength of the convective cells does not follow a certain rule when  $k_1/k_2$  changes. When the porous sleeve is less permeable ( $Da = 10^{-4}$ ), a smaller thermal conductivity ratio ( $k_1/k_2 < 1$ ) leads to a larger temperature gradient in the fluid layer. A larger temperature gradient represents a stronger driving force to produce a more vigorous convective flow. As such, the strength of the convective flow decreases with an increase in the conductivity ratio. When the porous sleeve is considerably permeable ( $Da = 10^0$  and  $10^{-2}$ ), the strength of the convective cells on the other hand grows with the thermal conductivity ratio  $k_1/k_2$ . Remember that, at this range of Darcy numbers, the



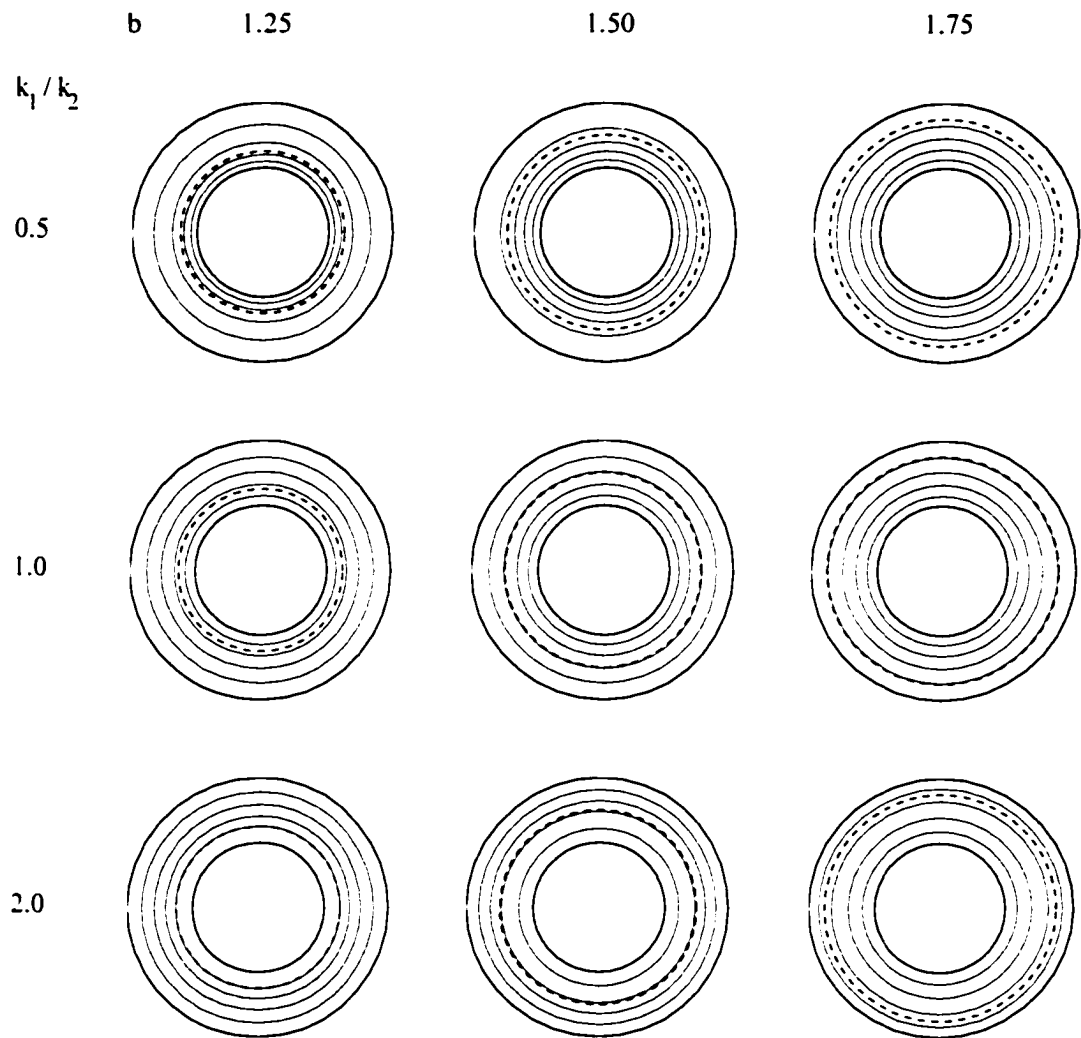


Figure 3.11 Temperature fields in a concentric annulus with a porous sleeve for  $Da = 10^{-4}$ ,  $Pr = 20,000$ , and  $Ra = 0.1$  ( $\Delta\theta = 0.2$ ).

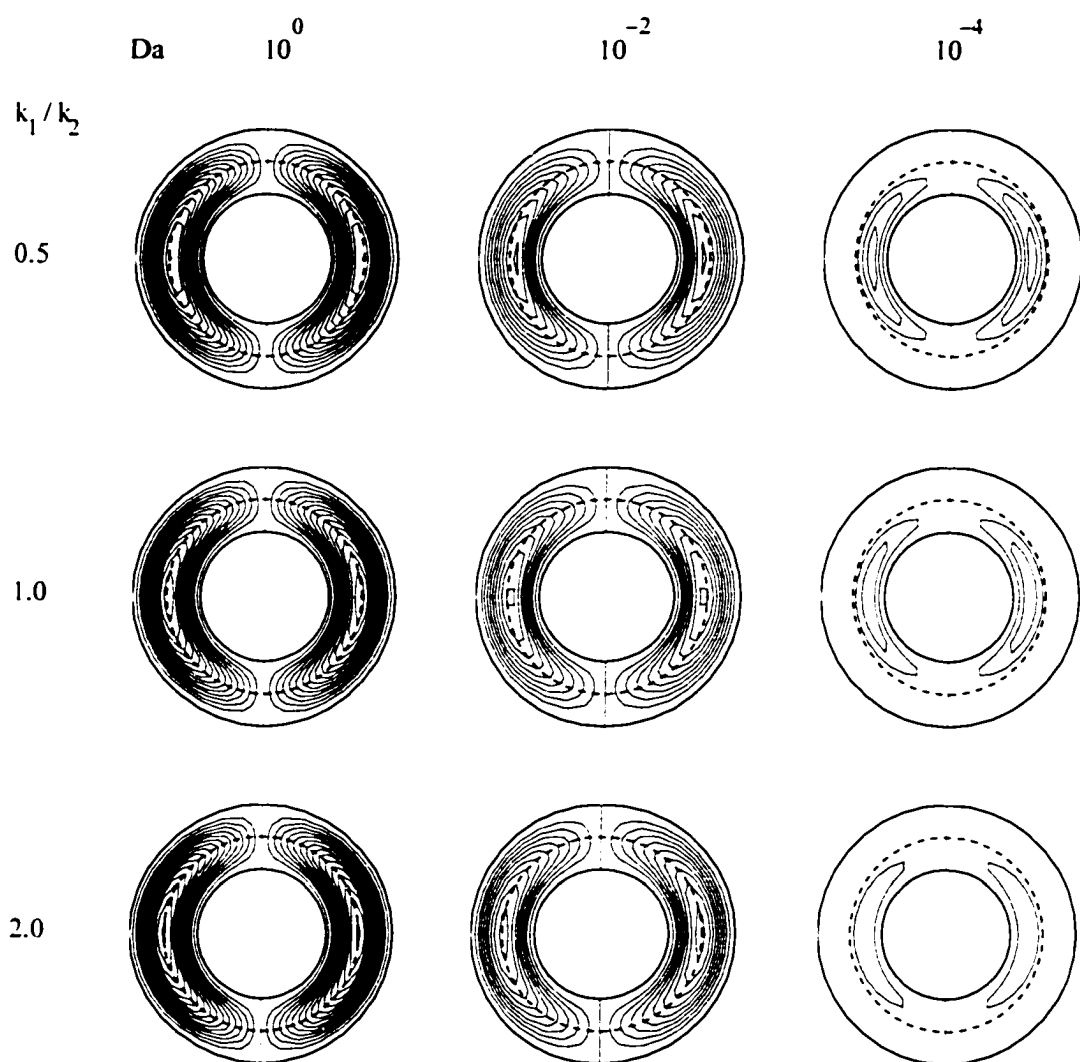


Figure 3.12 Flow fields in a concentric annulus with a porous sleeve for  $b = 1.50$ ,  $Pr = 20,000$ , and  $Ra = 0.1$  ( $\Delta\Psi = 2.5 \times 10^{-6}$  for  $Da = 10^{-4}$ , and  $\Delta\Psi = 5.0 \times 10^{-6}$  otherwise).

flow in the annulus behave as if it were in a single fluid layer. At  $k_1/k_2 = 0.5$ , a higher temperature gradient appears in the fluid layer, leaving the porous sleeve almost isothermal. As  $k_1/k_2$  increases, the temperature gradient in the porous sleeve increases, leading to a stronger convective cell.

Figure 3.13 shows the corresponding temperature fields for the cases presented in Figure 3.12. Again the results suggest that for a given conductivity ratio the temperature field is independent of the Darcy number. When  $k_1/k_2 = 1.0$ , there is no distinction between the fluid and porous layers as far as heat transfer is concerned. For  $k_1/k_2 < 1$ , the porous sleeve is more conductive than the fluid layer. For this reason, the porous sleeve is almost uniform in temperature. Conversely, for  $k_1/k_2 > 1$ , the temperature in the fluid layer is more uniform than that in the porous sleeve. Unlike the flow fields, the temperature fields for  $Da = 10^0$  depend heavily on  $k_1/k_2$ . Although there is almost no flow resistance in the porous sleeve for  $Da = 10^0$ , the presence of a porous sleeve does promote ( $k_1/k_2 > 1.0$ ) or demote ( $k_1/k_2 < 1.0$ ) the heat flow. For low Rayleigh numbers, heat conduction is the dominant heat transfer mechanism. The Darcy number, although dictates the flow structure, has very little effect on the temperature field. The dependence of the temperature field on the Darcy number is expected to become important for highly convective flows that occur at high Rayleigh numbers.

The average Nusselt numbers on the inner and outer cylinders are presented in Figure 3.14. It is observed that the average Nusselt numbers for the inner cylinder is always double of those for the outer cylinders. However, after multiplying both average Nusselt numbers by their corresponding surface areas, one finds that they are equal because the radius of the outer cylinder is twice of that of the inner cylinder. This shows

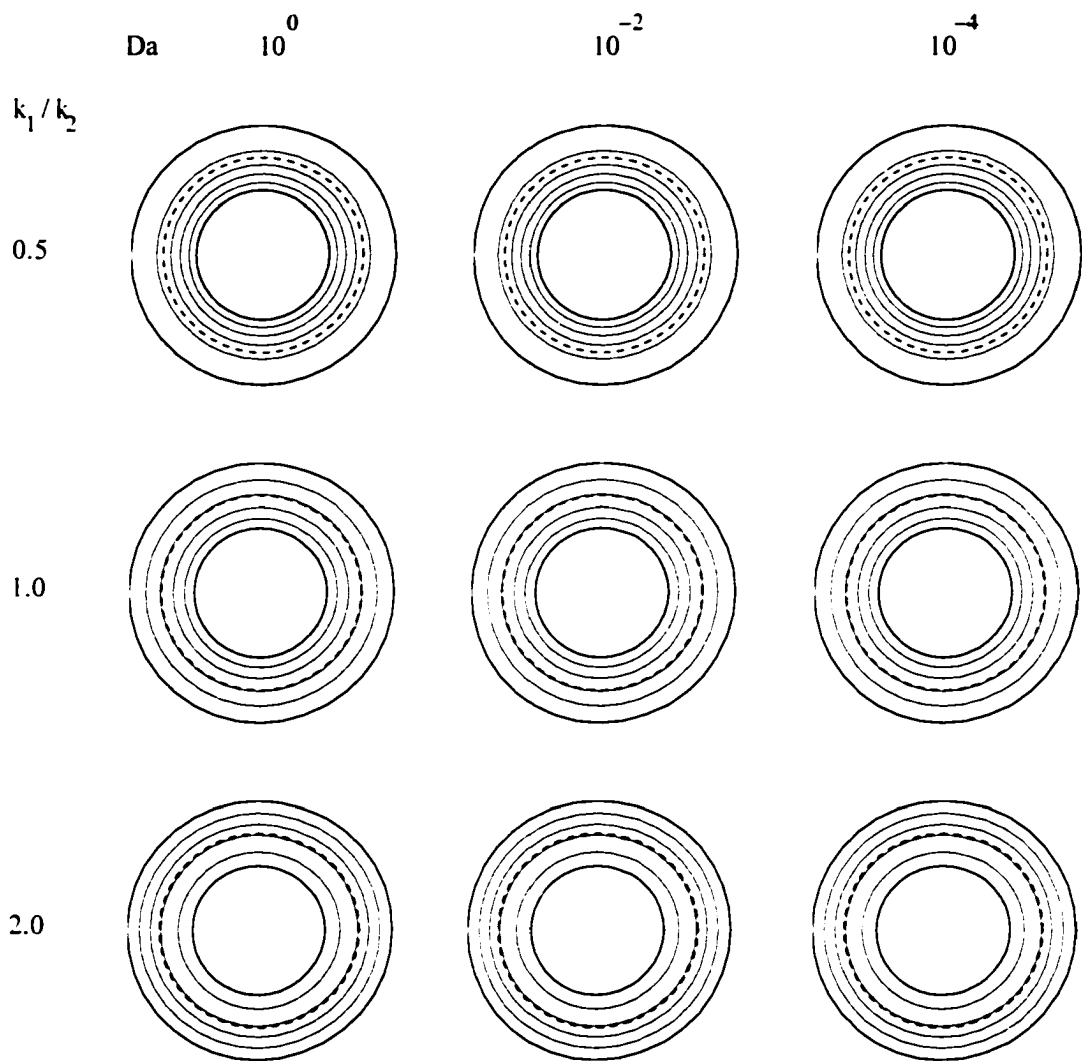


Figure 3.13 Temperature fields in a concentric annulus with a porous sleeve for  $b = 1.50$ ,  $Pr = 20,000$ , and  $Ra = 0.1$  ( $\Delta\Theta = 0.2$ ).

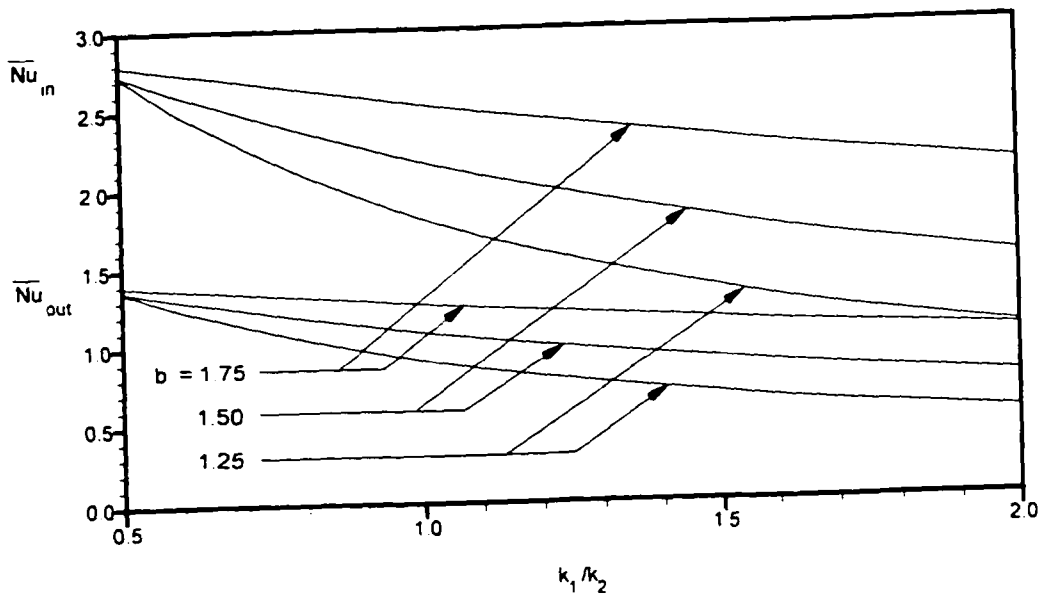


Figure 3.14 Average Nusselt numbers on the inner and outer cylinders for various values of  $b$  and  $k_1/k_2$  ( $Da = 10^{-4}$  and  $Ra = 0.1$ ).

that energy is balance between the inner and outer cylinders. It is observed that the average Nusselt numbers decreases monotonously with  $k_1/k_2$ . The highest average Nusselt numbers are associated with the largest value of  $b$ . In other words, the thinner the porous sleeve, the better the heat transfer result. At  $k_1/k_2 = 0.5$ , the average Nusselt numbers for  $b = 1.25$  and  $1.50$  become identical. Based on this observation, one may expect that for a smaller thermal conductivity ratio  $k_1/k_2$ , the average Nusselt numbers for all three values of  $b$  would be the same.

### 3.7 Conclusion

A theoretical study was performed using the regular perturbation method and Finite Fourier Transform. From the results obtained, it is found that there are two convective cells induced by the differential heating between the inner and outer cylinders. The strength of these cells increases with the Rayleigh number. Also found is that the Prandtl number has a very insignificant effect on the flow and temperature fields when the Rayleigh number is small. Although there is a finite flow induced by the temperature difference between the shaft and the housing, the lubricant in these bearings does not require special attention if the temperature difference between the shaft and the housing is small.

The thinner a porous sleeve, the greater the strength of a convective cell. For a sufficiently thin porous sleeve, the porous sleeve behaves as if it were impermeable. Typically, the porous sleeve thickness of a sintered journal bearing is very thin. Therefore, it is reasonable to expect that the convective flow generated solely by the differential heating is comparatively weak. At low Rayleigh numbers, the heat removal

from the inner cylinder is mainly by conduction. However, at a high Rayleigh number when heat convection becomes more important, it is believed that the porous sleeve thickness will play a much more critical role in heat transfer from the cylinder to the outer cylinder.

As the pore size in the porous sleeve decreases (i.e., the Darcy number decreases), the flow strength weakens. If the Darcy number is of the order of unity, the flow field reaches its asymptotic profile. At this end, the effect of the porous sleeve is negligible because its pore size is of the order of the cylinder diameters. In practical applications, the Darcy number associated with porous bearings is on the order of  $10^{-8}$  to  $10^{-9}$ . Accordingly, the convective flow in actual bearings due to differential heating between the non-rotating shaft and housing is significantly small.

Because conduction is the dominant heat transfer mode for the present study, the parameter  $k_1/k_2$  does not significantly affect the flow field. Instead, it has a profound effect on the temperature distribution. For a given porous sleeve thickness, the temperature gradient in the fluid layer decreases with  $k_1/k_2$  but it increases in the porous sleeve. Consequently, for a typical porous bearing ( $Da < 10^{-4}$ ), an increase in the thermal conductivity ratio weakens the convective cells. Also, the effects of thermal conductivity ratio on the temperature gradients lead to a reduction of the average Nusselt numbers with  $k_1/k_2$ . Other than the thermal conductivity ratio, a thinner porous sleeve will also lead to a larger average Nusselt number. For sintered bearings, it is always the case that  $k_1/k_2 < 1.0$  and  $b/c \rightarrow 1$ . This study suggests that the heat dissipation by pure conduction is effective and sufficient when the sintered bearings are not in operation.

# **CHAPTER FOUR**

## **MIXED CONVECTION IN ROTATING CONCENTRIC CYLINDERS WITH A POROUS SLEEVE**

### **4.1 Introductory Remarks**

Heat transfer in rotating bodies has various applications in industry. Some of the most commonly encountered applications include the cooling of motor shafts, turbine blades, and high speed gas bearings. The cooling of rotating condensers for seawater distillation is a less common example. In these systems, buoyancy and centrifugal forces are the two most important factors to consider because their combined effect dictates the flow structure and the heat transfer mechanism. The rotational flow pattern in unheated rotating cylinders will end up with the Taylor vortices if the critical Reynolds (or Taylor) number is reached. DiPrima and Swinney (1985) have comprehensively reviewed the analytical and experimental studies for annuli whose inner cylinder rotates. Ball and Farouk (1987) and Ball (1987) investigated the development of Taylor vortices and heat transfer in a vertical annulus with a heated rotating inner cylinder. They found that the flow field in a vertical annulus whose inner cylinder rotates at a moderate speed is axisymmetric. However, in a horizontal annulus, the strong centrifugal force will trigger the formation of the Taylor cells and yield a fully three-dimensional flow structure. Fusegi et al. (1986b) carried out a numerical study of two-dimensional mixed convection in horizontal concentric cylinders with the inner one maintained at a higher temperature and rotating at a low speed. Fusegi and Farouk (1986a) also presented numerical results



for three-dimensional natural convection in an annulus with an aspect ratio of unity. Later, in their study of three-dimensional mixed convection in a horizontal rotating annulus, Yang and Farouk (1992) attempted to quantify the interaction between buoyancy and centrifugal forces and to determine the effects of secondary flows (i.e., the Taylor cells) on the heat transfer.

#### 4.2 Objective of the Present Study

As an extension of the previous study by Fusegi et al. (1986b), this study considers an application in which an additional porous layer is added to the outer cylinder (Figure 4.1). The purpose of the present study is to numerically investigate the combined effect due to the presence of the porous layer, centrifugal, and buoyancy forces on the flow pattern and temperature distribution in the annulus. In contrast to the previous chapter that consider only weak natural convection in a concentric annulus with a porous sleeve, the present study considers a full range of convection regimes ranging from natural, mixed, to forced convection and thus covers a wider range of parameters.

#### 4.3 Governing Equations

With the definition of vorticity given below

$$\omega_t = \frac{1}{r} \frac{\partial}{\partial r} (r u_\theta) - \frac{1}{r} \frac{\partial u_r}{\partial \theta} \quad (4.1)$$

the momentum and energy equations for both fluid layer and porous sleeve become

$$\frac{1}{r} \frac{\partial}{\partial r} \left( \omega_t \frac{\partial \psi_1}{\partial \theta} \right) - \frac{1}{r} \frac{\partial}{\partial \theta} \left( \omega_t \frac{\partial \psi_1}{\partial r} \right) = g \beta \left( \sin \theta \frac{\partial T_1}{\partial r} + \frac{\cos \theta}{r} \frac{\partial T_1}{\partial \theta} \right)$$

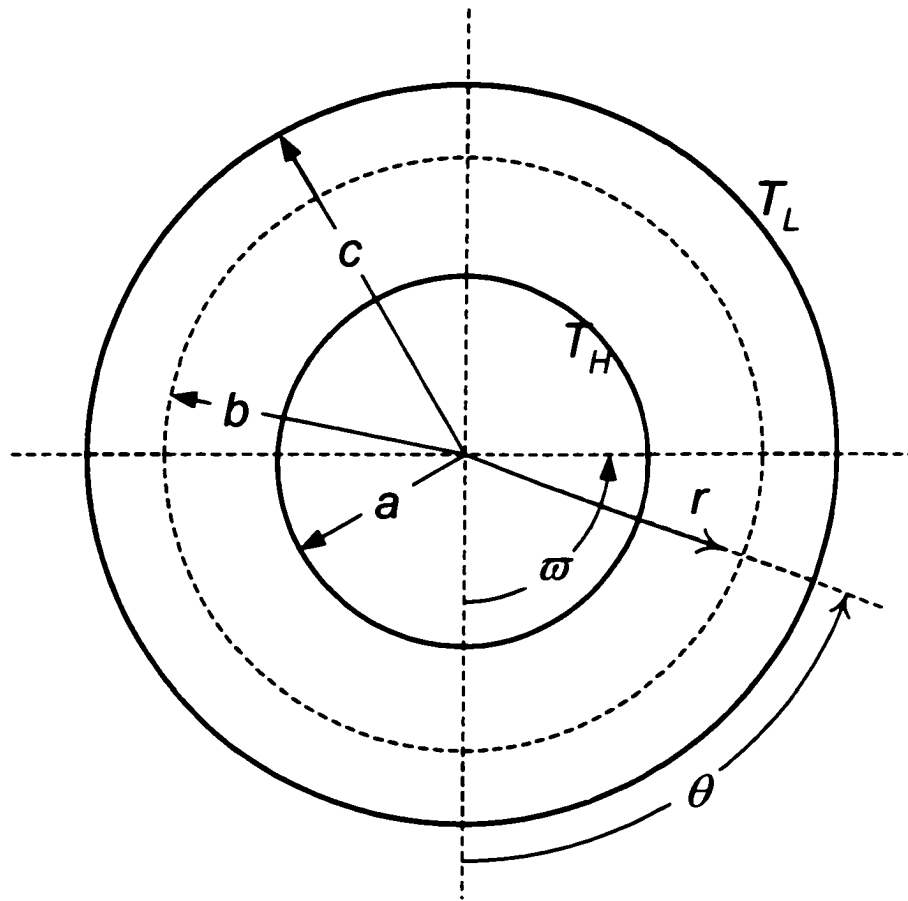


Figure 4.1 Concentric rotating cylinders with a porous sleeve.

$$+ \nu \left[ \frac{1}{r} \frac{\partial}{\partial r} \left( r \frac{\partial \omega_1}{\partial r} \right) + \frac{1}{r^2} \frac{\partial^2 \omega_1}{\partial \theta^2} \right], \quad (4.2)$$

$$\frac{1}{r} \frac{\partial}{\partial r} \left( T_1 \frac{\partial \psi_1}{\partial \theta} \right) - \frac{1}{r} \frac{\partial}{\partial \theta} \left( T_1 \frac{\partial \psi_1}{\partial r} \right) = \alpha_1 \left[ \frac{1}{r} \frac{\partial}{\partial r} \left( r \frac{\partial T_1}{\partial r} \right) + \frac{1}{r^2} \frac{\partial^2 T_1}{\partial \theta^2} \right]. \quad (4.3)$$

$$\begin{aligned} \frac{1}{r} \frac{\partial}{\partial r} \left( \omega_2 \frac{\partial \psi_2}{\partial \theta} \right) - \frac{1}{r} \frac{\partial}{\partial \theta} \left( \omega_2 \frac{\partial \psi_2}{\partial r} \right) &= g \beta \left( \sin \theta \frac{\partial T_2}{\partial r} + \frac{\cos \theta}{r} \frac{\partial T_2}{\partial \theta} \right) \\ &- \frac{\nu}{K} \omega_2 + \nu \left[ \frac{1}{r} \frac{\partial}{\partial r} \left( r \frac{\partial \omega_2}{\partial r} \right) + \frac{1}{r^2} \frac{\partial^2 \omega_2}{\partial \theta^2} \right], \text{ and} \end{aligned} \quad (4.4)$$

$$\frac{1}{r} \frac{\partial}{\partial r} \left( T_2 \frac{\partial \psi_2}{\partial \theta} \right) - \frac{1}{r} \frac{\partial}{\partial \theta} \left( T_2 \frac{\partial \psi_2}{\partial r} \right) = \alpha_2 \left[ \frac{1}{r} \frac{\partial}{\partial r} \left( r \frac{\partial T_2}{\partial r} \right) + \frac{1}{r^2} \frac{\partial^2 T_2}{\partial \theta^2} \right]. \quad (4.5)$$

where

$$u_n = \frac{1}{r} \frac{\partial \psi_i}{\partial \theta}, \quad \text{and} \quad u_{\theta} = -\frac{\partial \psi_i}{\partial r}. \quad (4.6a, b)$$

Note that the definition of stream function in Eq. (4.6) is different from that in the previous chapter. This definition (Eq. (4.6)) is preferred because it is more commonly adopted in numerical formulation.

Introduce the following dimensionless parameters

$$\begin{aligned} \Psi_i &= \frac{\psi_i}{\alpha_1}, & \Omega_i &= \frac{b^2}{\alpha_1} \omega_i, \\ R &= \frac{r}{b}, & \Theta_i &= \frac{T_i - T_l}{\Delta T}. \end{aligned} \quad (4.7a, b, c, d)$$

where the subscript  $i$  is the index referring to the sublayer and

$$\Delta T = T_H - T_L. \quad (4.8)$$

The governing equations are normalized to give

$$\begin{aligned} \frac{1}{R} \frac{\partial}{\partial R} \left( \Omega_1 \frac{\partial \Psi_1}{\partial \theta} \right) - \frac{1}{R} \frac{\partial}{\partial \theta} \left( \Omega_1 \frac{\partial \Psi_1}{\partial R} \right) &= Ra Pr \left( \sin \theta \frac{\partial \Theta_1}{\partial R} + \frac{\cos \theta}{R} \frac{\partial \Theta_1}{\partial \theta} \right) \\ &+ Pr \left[ \frac{1}{R} \frac{\partial}{\partial R} \left( R \frac{\partial \Omega_1}{\partial R} \right) + \frac{1}{R^2} \frac{\partial^2 \Omega_1}{\partial \theta^2} \right], \end{aligned} \quad (4.9)$$

$$\frac{1}{R} \frac{\partial}{\partial R} \left( \Theta_1 \frac{\partial \Psi_1}{\partial \theta} \right) - \frac{1}{R} \frac{\partial}{\partial \theta} \left( \Theta_1 \frac{\partial \Psi_1}{\partial R} \right) = \frac{1}{R} \frac{\partial}{\partial R} \left( R \frac{\partial \Theta_1}{\partial R} \right) + \frac{1}{R^2} \frac{\partial^2 \Theta_1}{\partial \theta^2}. \quad (4.10)$$

$$\begin{aligned} \frac{1}{R} \frac{\partial}{\partial R} \left( \Omega_2 \frac{\partial \Psi_2}{\partial \theta} \right) - \frac{1}{R} \frac{\partial}{\partial \theta} \left( \Omega_2 \frac{\partial \Psi_2}{\partial R} \right) &= Ra Pr \left( \sin \theta \frac{\partial \Theta_2}{\partial R} + \frac{\cos \theta}{R} \frac{\partial \Theta_2}{\partial \theta} \right) \\ &- \frac{Pr}{Da} \Omega_2 + Pr \left[ \frac{1}{R} \frac{\partial}{\partial R} \left( R \frac{\partial \Omega_2}{\partial R} \right) + \frac{1}{R^2} \frac{\partial^2 \Omega_2}{\partial \theta^2} \right], \text{ and} \end{aligned} \quad (4.11)$$

$$\frac{\alpha_1}{\alpha_2} \left[ \frac{1}{R} \frac{\partial}{\partial R} \left( \Theta_2 \frac{\partial \Psi_2}{\partial \theta} \right) - \frac{1}{R} \frac{\partial}{\partial \theta} \left( \Theta_2 \frac{\partial \Psi_2}{\partial R} \right) \right] = \frac{1}{R} \frac{\partial}{\partial R} \left( R \frac{\partial \Theta_2}{\partial R} \right) + \frac{1}{R^2} \frac{\partial^2 \Theta_2}{\partial \theta^2}. \quad (4.12)$$

where

$$Ra = \frac{g \beta \Delta T h^3}{\nu \alpha_1}, \quad Da = \frac{K}{b^2}, \text{ and} \quad (4.13a, b)$$

$$Pr = \frac{\nu}{\alpha_1}. \quad (4.13c)$$

Recognize that there are six variables, namely  $\Psi_1$ ,  $\Psi_2$ ,  $\Omega_1$ ,  $\Omega_2$ ,  $\Theta_1$ , and  $\Theta_2$ , in four governing equations. Hence, two more equations are needed to make this problem complete. These additional equations are the definitions of the vorticity in terms of stream functions (Eq. (4.1)) for the fluid layer and the porous sleeve, respectively. Their dimensionless forms are

$$\Omega_1 = - \left[ \frac{1}{R} \frac{\partial}{\partial R} \left( R \frac{\partial \Psi_1}{\partial R} \right) + \frac{1}{R^2} \frac{\partial}{\partial \theta} \left( \frac{\partial \Psi_1}{\partial \theta} \right) \right], \text{ and} \quad (4.14)$$

$$\Omega_2 = - \left[ \frac{1}{R} \frac{\partial}{\partial R} \left( R \frac{\partial \Psi_2}{\partial R} \right) + \frac{1}{R^2} \frac{\partial}{\partial \theta} \left( \frac{\partial \Psi_2}{\partial \theta} \right) \right]. \quad (4.15)$$

#### 4.4 Boundary and Interface Conditions

The boundary and interface conditions for the problem under consideration are given as follow. The derivation of these interface conditions is similar to that shown in Appendix C.

On the surface of the inner cylinder.

$$r = a, \quad u_{r1} = 0, \quad u_{\theta1} = U, \quad \text{and} \quad T_1 = T_H. \quad (4.16a, b, c)$$

On the surface of the outer cylinder.

$$r = c, \quad u_{r2} = 0, \quad u_{\theta2} = 0, \quad \text{and} \quad T_2 = T_L. \quad (4.17a, b, c)$$

On the interface between the fluid layer and the porous sleeve.

$$r = b, \quad u_{r1} = u_{r2}, \quad u_{\theta1} = u_{\theta2}, \quad (4.18a, b)$$

$$\omega_1 = \omega_2, \quad \frac{\partial \omega_1}{\partial r} = \frac{\partial \omega_2}{\partial r} - \frac{u_{\theta2}}{Da}, \quad (4.18c, d)$$

$$T_1 = T_2, \quad \text{and} \quad k_1 \frac{\partial T_1}{\partial r} = k_2 \frac{\partial T_2}{\partial r}. \quad (4.18e, f)$$

Conditions (4.16) to (4.18) are normalized using the dimensionless parameters defined in Eq. (4.7) and the dimensionless forms are given below.

$$\begin{aligned} \text{At } R = a/b, \quad \frac{\partial \Psi_1}{\partial \theta} &= 0, \quad \frac{\partial \Psi_1}{\partial R} = -Pe, \quad \text{and} \\ \Theta_1 &= 1. \end{aligned} \quad (4.19a, b, c)$$

$$\begin{aligned} \text{At } R = c/b, \quad \frac{\partial \Psi_2}{\partial \theta} &= 0, \quad \frac{\partial \Psi_2}{\partial R} = 0, \quad \text{and} \\ \Theta_2 &= 0. \end{aligned} \quad (4.20a, b, c)$$

$$\text{At } R = 1, \quad \frac{\partial \Psi_1}{\partial \theta} = \frac{\partial \Psi_2}{\partial \theta}, \quad \frac{\partial \Psi_1}{\partial R} = \frac{\partial \Psi_2}{\partial R}, \quad (4.21a, b)$$

$$\Omega_1 = \Omega_2, \quad \frac{\partial \Omega_1}{\partial R} = \frac{\partial \Omega_2}{\partial R} + \frac{1}{Da} \frac{\partial \Psi_2}{\partial R}, \quad (4.21c, d)$$

$$\Theta_1 = \Theta_2, \quad \text{and} \quad \frac{\partial \Theta_1}{\partial R} = \frac{k_2}{k_1} \frac{\partial \Theta_2}{\partial R}, \quad (4.21e, f)$$

where

$$Pe = Re Pr = \frac{U'b}{\alpha_1}. \quad (4.22)$$

Notice that Eq. (4.21d) is different from the corresponding interface condition derived in Appendix C because of the difference in the definition of stream function.

#### 4.5 Finite Difference Method

Finite Difference Method is employed in this work because of its ease of use. In this approach, the governing equations are first integrated over a control volume and then discretized to form a set of six algebraic equations. A control volume is shown in Figure 4.2. Consequently, these algebraic equations are solved simultaneously subject to the prescribed boundary and interface conditions. These algebraic equations are

$$\begin{aligned} & \int_0^n \int_0^c \left[ \frac{1}{R} \frac{\partial}{\partial R} \left( \Omega_1 \frac{\partial \Psi_1}{\partial \theta} \right) - \frac{1}{R} \frac{\partial}{\partial \theta} \left( \Omega_1 \frac{\partial \Psi_1}{\partial R} \right) \right] R dR d\theta \\ &= Ra Pr \int_0^n \int_0^c \left[ \sin \theta \frac{\partial \Theta_1}{\partial R} + \frac{\cos \theta}{R} \frac{\partial \Theta_1}{\partial \theta} \right] R dR d\theta \\ &+ Pr \int_0^n \int_0^c \left[ \frac{1}{R} \frac{\partial}{\partial R} \left( R \frac{\partial \Omega_1}{\partial R} \right) + \frac{1}{R^2} \frac{\partial^2 \Omega_1}{\partial \theta^2} \right] R dR d\theta. \end{aligned} \quad (4.23)$$

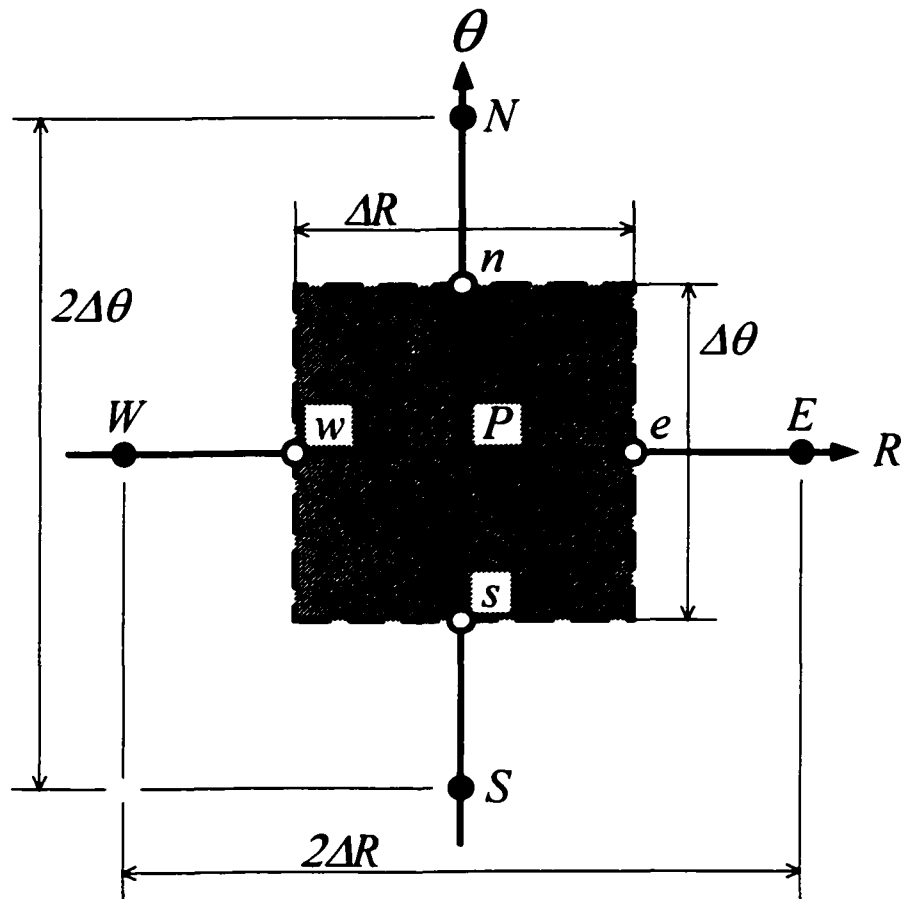


Figure 4.2 Control volume for the node  $P$ .

$$\begin{aligned}
& \int_1^n \int_w^c \left[ \frac{1}{R} \frac{\partial}{\partial R} \left( \Theta_1 \frac{\partial \Psi_1}{\partial \theta} \right) - \frac{1}{R} \frac{\partial}{\partial \theta} \left( \Theta_1 \frac{\partial \Psi_1}{\partial R} \right) \right] R dR d\theta \\
&= \int_1^n \int_w^c \left[ \frac{1}{R} \frac{\partial}{\partial R} \left( R \frac{\partial \Theta_1}{\partial R} \right) + \frac{1}{R^2} \frac{\partial^2 \Theta_1}{\partial \theta^2} \right] R dR d\theta, \tag{4.24}
\end{aligned}$$

$$-\int_1^n \int_w^c \Omega_1 R dR d\theta = \int_1^n \int_w^c \left[ \frac{1}{R} \frac{\partial}{\partial R} \left( R \frac{\partial \Psi_1}{\partial R} \right) + \frac{1}{R^2} \frac{\partial}{\partial \theta} \left( \frac{\partial \Psi_1}{\partial \theta} \right) \right] R dR d\theta. \tag{4.25}$$

$$\begin{aligned}
& \int_1^n \int_w^c \left[ \frac{1}{R} \frac{\partial}{\partial R} \left( \Omega_2 \frac{\partial \Psi_2}{\partial \theta} \right) - \frac{1}{R} \frac{\partial}{\partial \theta} \left( \Omega_2 \frac{\partial \Psi_2}{\partial R} \right) \right] R dR d\theta \\
&= Ra Pr \int_1^n \int_w^c \left[ \sin \theta \frac{\partial \Theta_2}{\partial R} + \frac{\cos \theta}{R} \frac{\partial \Theta_2}{\partial \theta} \right] R dR d\theta \\
&- \frac{Pr}{Da} \int_1^n \int_w^c \Omega_2 R dR d\theta + Pr \int_1^n \int_w^c \left[ \frac{1}{R} \frac{\partial}{\partial R} \left( R \frac{\partial \Omega_2}{\partial R} \right) + \frac{1}{R^2} \frac{\partial^2 \Omega_2}{\partial \theta^2} \right] R dR d\theta. \tag{4.26}
\end{aligned}$$

$$\begin{aligned}
& \int_1^n \int_w^c \left[ \frac{1}{R} \frac{\partial}{\partial R} \left( \Theta_2 \frac{\partial \Psi_2}{\partial \theta} \right) - \frac{1}{R} \frac{\partial}{\partial \theta} \left( \Theta_2 \frac{\partial \Psi_2}{\partial R} \right) \right] R dR d\theta \\
&= \tilde{\alpha} \int_1^n \int_w^c \left[ \frac{1}{R} \frac{\partial}{\partial R} \left( R \frac{\partial \Theta_2}{\partial R} \right) + \frac{1}{R^2} \frac{\partial^2 \Theta_2}{\partial \theta^2} \right] R dR d\theta, \text{ and} \tag{4.27}
\end{aligned}$$

$$-\int_1^n \int_w^c \Omega_2 R dR d\theta = \int_1^n \int_w^c \left[ \frac{1}{R} \frac{\partial}{\partial R} \left( R \frac{\partial \Psi_2}{\partial R} \right) + \frac{1}{R^2} \frac{\partial}{\partial \theta} \left( \frac{\partial \Psi_2}{\partial \theta} \right) \right] R dR d\theta. \tag{4.28}$$

where  $\tilde{\alpha} = \alpha_2 / \alpha_1 = k_2 / k_1$ .



Note that the terms in Eqs. (4.23) to (4.28) can be classified into three categories, namely the source, the diffusive and the convective terms (Patankar, 1980). For simplicity, these terms are presented separately in the generic forms in the following sections excluding their constant coefficients.

#### 4.5.1 Source Terms

Source terms  $[S]$  are the terms representing the thermal buoyancy effect that appear in the vorticity transport equations. In numerical formulation, these terms are the simplest in form and thus the easiest to deal with. To be brief, only the integrals are considered here. The source terms in Eqs. (4.23) and (4.26) take the following form.

$$[S] = \int_{\psi}^n \int_{\theta}^c \left[ \sin \theta \frac{\partial \Theta_i}{\partial R} + \frac{\cos \theta}{R} \frac{\partial \Theta_i}{\partial \theta} \right] R dR d\theta. \quad (4.29)$$

Remember that both source terms have coefficients  $RaPr$ , which are not included here for derivation. The integral in Eq. (4.29) can be numerically represented as

$$[S] = a_w^S \Theta_w + a_E^S \Theta_E + a_S^S \Theta_S + a_N^S \Theta_N, \quad (4.30a)$$

where

$$a_w^S = -\frac{1}{2} R_p \sin \theta_p \Delta \theta, \quad a_E^S = \frac{1}{2} R_p \sin \theta_p \Delta \theta, \quad (4.30b, c)$$

$$a_S^S = -\frac{1}{2} \cos \theta_p \Delta R, \quad \text{and} \quad a_N^S = \frac{1}{2} \cos \theta_p \Delta R. \quad (4.30d, e)$$

#### 4.5.2 Diffusive Terms

The diffusive terms appear in the right hand side of Eqs. (4.23) to (4.28). They represent viscous dissipation in the vorticity transport equation and heat conduction in the

energy equation. Integrating the diffusive terms in Eqs. (4.23) to (4.28) over a control volume yields

$$[D] = \int_{\psi}^n \int_{\theta}^e \left[ \frac{1}{R} \frac{\partial}{\partial R} \left( R \frac{\partial \Phi}{\partial R} \right) + \frac{1}{R^2} \frac{\partial^2 \Phi}{\partial \theta^2} \right] R dR d\theta. \quad (4.31)$$

Equation (4.31) is a general form. The variable  $\Phi$  represents  $\Omega$ ,  $\Theta$ , and  $\Psi$  in Eqs. (4.23) to (4.28). The algebraic form of Eq. (4.31) can be expressed as

$$[D] = a_w^D \Phi_w + a_E^D \Phi_E + a_S^D \Phi_S + a_N^D \Phi_N - a_p^D \Phi_p, \quad (4.32a)$$

where

$$a_w^D = \frac{R_w \Delta \theta}{\Delta R}, \quad a_E^D = \frac{R_e \Delta \theta}{\Delta R}, \quad (4.32b, c)$$

$$a_S^D = \frac{\Delta R}{R_p \Delta \theta}, \quad a_N^D = \frac{\Delta R}{R_p \Delta \theta}, \text{ and} \quad (4.32d, e)$$

$$a_p^D = a_w^D + a_E^D + a_S^D + a_N^D. \quad (4.32f)$$

### 4.5.3 Convective Terms

Among all the terms in the transport equations, the convective terms  $[C]$  are the most complicated ones. They describe the transport phenomenon of a property  $\Phi$ . Not only are they more complex in physics, but also they are more difficult to handle numerically. For decades, various numerical algorithms have been proposed and applied for these terms (Patankar, 1980). The integral of the general form of the convective terms in Eqs. (4.23), (4.24), (4.26), and (4.27) is given by

$$[C] = \int_{\psi}^n \int_{\theta}^e \left[ \frac{1}{R} \frac{\partial}{\partial R} \left( \Phi \frac{\partial \Psi}{\partial \theta} \right) - \frac{1}{R} \frac{\partial}{\partial \theta} \left( \Phi \frac{\partial \Psi}{\partial R} \right) \right] R dR d\theta. \quad (4.33)$$

Using the upwind scheme, the above equations can be cast into the following form (Gosman et al., 1969),

$$[C] = a_p^C \Phi_p - a_w^C \Phi_w - a_e^C \Phi_e - a_s^C \Phi_s - a_n^C \Phi_n, \quad (4.34a)$$

in which the coefficients are given by

$$a_w^C = \frac{1}{8} \left[ (\Psi_N + \Psi_{NW} - \Psi_S - \Psi_{SE}) + |\Psi_N + \Psi_{NW} - \Psi_S - \Psi_{SE}| \right], \quad (4.34b)$$

$$a_e^C = \frac{1}{8} \left[ (\Psi_S + \Psi_{SE} - \Psi_N - \Psi_{NE}) + |\Psi_S + \Psi_{SE} - \Psi_N - \Psi_{NE}| \right], \quad (4.34c)$$

$$a_s^C = \frac{1}{8} \left[ (\Psi_W + \Psi_{SW} - \Psi_E - \Psi_{SE}) + |\Psi_W + \Psi_{SW} - \Psi_E - \Psi_{SE}| \right], \quad (4.34d)$$

$$a_n^C = \frac{1}{8} \left[ (\Psi_E + \Psi_{NE} - \Psi_W - \Psi_{NW}) + |\Psi_E + \Psi_{NE} - \Psi_W - \Psi_{NW}| \right], \text{ and} \quad (4.34e)$$

$$a_p^C = a_e^C + a_w^C + a_s^C + a_n^C. \quad (4.34f)$$

#### 4.5.4 Finite Difference Equations

Substitute the convective, diffusive, and source terms into Eqs. (4.23) to (4.28), one obtains the finite difference equations that are preferred for computation.

For the vorticity transport equation in the fluid layer (4.23), one obtains the following algebraic equation.

$$\begin{aligned} & a_p^C \Omega_{1P} - a_w^C \Omega_{1W} - a_e^C \Omega_{1E} - a_s^C \Omega_{1S} - a_n^C \Omega_{1N} \\ & = Ra Pr \left( a_w^S \Theta_{1W} + a_e^S \Theta_{1E} + a_s^S \Theta_{1S} + a_n^S \Theta_{1N} \right) \\ & + Pr \left( a_w^D \Omega_{1W} + a_e^D \Omega_{1E} + a_s^D \Omega_{1S} + a_n^D \Omega_{1N} - a_p^D \Omega_{1P} \right). \end{aligned} \quad (4.35)$$

Collecting the terms at node  $P$ , one obtains

$$\Omega_{1P} = c_{\Omega,W} \Omega_{1W} + c_{\Omega,E} \Omega_{1E} + c_{\Omega,S} \Omega_{1S} + c_{\Omega,N} \Omega_{1N} + S_{\Omega}, \quad (4.36a)$$

where

$$c_{\Omega W} = \frac{a_W^C + Pr a_W^D}{a_P^C + Pr a_P^D}, \quad c_{\Omega E} = \frac{a_E^C + Pr a_E^D}{a_P^C + Pr a_P^D}, \quad (4.36b, c)$$

$$c_{\Omega S} = \frac{a_S^C + Pr a_S^D}{a_P^C + Pr a_P^D}, \quad c_{\Omega N} = \frac{a_N^C + Pr a_N^D}{a_P^C + Pr a_P^D}, \text{ and} \quad (4.36d, e)$$

$$S_{\Omega} = \frac{Ra Pr \kappa}{Pr a_P^D + a_P^C} (a_W^S \Theta_{1W} + a_E^S \Theta_{1E} + a_S^S \Theta_{1S} + a_N^S \Theta_{1N}). \quad (4.36f)$$

In the fluid layer, the energy equation (4.24) is discretized to give

$$\begin{aligned} & a_P^C \Theta_{1P} - a_W^C \Theta_{1W} - a_E^C \Theta_{1E} - a_S^C \Theta_{1S} - a_N^C \Theta_{1N} \\ & = a_W^D \Theta_{1W} + a_E^D \Theta_{1E} + a_S^D \Theta_{1S} + a_N^D \Theta_{1N} - a_P^D \Theta_{1P}. \end{aligned} \quad (4.37)$$

Collecting the terms at node  $P$ , the above equation becomes

$$\Theta_{1P} = c_{\Theta W} \Theta_{1W} + c_{\Theta E} \Theta_{1E} + c_{\Theta S} \Theta_{1S} + c_{\Theta N} \Theta_{1N}, \quad (4.38a)$$

where

$$c_{\Theta W} = \frac{a_W^C + a_W^D}{a_P^C + a_P^D}, \quad c_{\Theta E} = \frac{a_E^C + a_E^D}{a_P^C + a_P^D}, \quad (4.38b, c)$$

$$c_{\Theta S} = \frac{a_S^C + a_S^D}{a_P^C + a_P^D}, \quad \text{and} \quad c_{\Theta N} = \frac{a_N^C + a_N^D}{a_P^C + a_P^D}. \quad (4.38d, e)$$

The definition of vorticity in the fluid layer (4.25) is discretized as

$$-\Omega_{1P} R_P \Delta R \Delta \theta = a_W^D \Psi_{1W} + a_E^D \Psi_{1E} + a_S^D \Psi_{1S} + a_N^D \Psi_{1N} - a_P^D \Psi_{1P}. \quad (4.39)$$

The above equation can be rearranged to give

$$\Psi_{1P} = c_{\Psi W} \Psi_{1W} + c_{\Psi E} \Psi_{1E} + c_{\Psi S} \Psi_{1S} + c_{\Psi N} \Psi_{1N} + S_{\Psi}, \quad (4.40a)$$

where

$$c_{\Psi W} = \frac{a_W^D}{a_P^D}, \quad c_{\Psi E} = \frac{a_E^D}{a_P^D}, \quad (4.40b, c)$$

$$c_{\psi_1 S} = \frac{a_S^D}{a_p^D}, \quad c_{\psi_1 W} = \frac{a_W^D}{a_p^D}, \text{ and} \quad (4.40d, e)$$

$$S_{\psi_1} = \frac{\Omega_{1p} R_p \Delta R \Delta \theta}{a_p^D}. \quad (4.40f)$$

The governing equations for the porous sleeve are discretized in the same way. Substitute the terms accordingly, the vorticity transport equation in the porous sleeve (4.26) is given by

$$\begin{aligned} & a_p^C \Omega_{2p} - a_W^C \Omega_{2W} - a_E^C \Omega_{2E} - a_S^C \Omega_{2S} - a_N^C \Omega_{2N} \\ &= Ra Pr \left( a_W^S \Theta_{2W} + a_E^S \Theta_{2E} + a_S^S \Theta_{2S} + a_N^S \Theta_{2N} \right) - \frac{Pr}{Da} \Omega_{2p} R_p \Delta R \Delta \theta_p \\ &+ Pr \left( a_W^D \Omega_{2W} + a_E^D \Omega_{2E} + a_S^D \Omega_{2S} + a_N^D \Omega_{2N} - a_p^D \Omega_{2p} \right), \end{aligned} \quad (4.41)$$

which can be rewritten as follows

$$\Omega_{2p} = c_{\Omega_2 W} \Omega_{2W} + c_{\Omega_2 E} \Omega_{2E} + c_{\Omega_2 S} \Omega_{2S} + c_{\Omega_2 N} \Omega_{2N} + S_{\Omega_2}, \quad (4.42a)$$

where

$$c_{\Omega_2 W} = \frac{a_W^C + Pr a_W^D}{a_p^C + (Pr/Da) R_p \Delta R \Delta \theta_p + Pr a_p^D}, \quad (4.42b)$$

$$c_{\Omega_2 E} = \frac{a_E^C + Pr a_E^D}{a_p^C + (Pr/Da) R_p \Delta R \Delta \theta_p + Pr a_p^D}, \quad (4.42c)$$

$$c_{\Omega_2 S} = \frac{a_S^C + Pr a_S^D}{a_p^C + (Pr/Da) R_p \Delta R \Delta \theta_p + Pr a_p^D}, \quad (4.42d)$$

$$c_{\Omega_2 N} = \frac{a_N^C + Pr a_N^D}{a_p^C + (Pr/Da) R_p \Delta R \Delta \theta_p + Pr a_p^D}, \text{ and} \quad (4.42e)$$

$$S_{\Omega_2} = Ra Pr \frac{a_W^S \Theta_{2W} + a_E^S \Theta_{2E} + a_S^S \Theta_{2S} + a_N^S \Theta_{2N}}{a_p^C + (Pr/Da) R_p \Delta R \Delta \theta_p + Pr a_p^D}. \quad (4.42f)$$

The energy equation in the porous sleeve (4.27) is given by

$$\begin{aligned} & a_p^C \Theta_{2P} - a_w^C \Theta_{2W} - a_E^C \Theta_{2E} - a_S^C \Theta_{2S} - a_N^C \Theta_{2N} \\ & = \tilde{\alpha} (a_w^D \Theta_{2W} + a_E^D \Theta_{2E} + a_S^D \Theta_{2S} + a_N^D \Theta_{2N} - a_p^D \Theta_{2P}) . \end{aligned} \quad (4.43)$$

Rearranging Eq. (4.43) gives

$$\Theta_{2P} = c_{\Theta;W} \Theta_{2W} + c_{\Theta;E} \Theta_{2E} + c_{\Theta;S} \Theta_{2S} + c_{\Theta;N} \Theta_{2N} , \quad (4.44a)$$

where

$$c_{\Theta;W} = \frac{a_w^C + \tilde{\alpha} a_w^D}{a_p^C + \tilde{\alpha} a_p^D} , \quad c_{\Theta;E} = \frac{a_E^C + \tilde{\alpha} a_E^D}{a_p^C + \tilde{\alpha} a_p^D} , \quad (4.44b, c)$$

$$c_{\Theta;S} = \frac{a_S^C + \tilde{\alpha} a_S^D}{a_p^C + \tilde{\alpha} a_p^D} , \quad \text{and} \quad c_{\Theta;N} = \frac{a_N^C + \tilde{\alpha} a_N^D}{a_p^C + \tilde{\alpha} a_p^D} . \quad (4.44d, e)$$

Finally, the definition of vorticity in the porous sleeve (4.28) is given by

$$-\Omega_{2P} R_p \Delta R \Delta \theta = a_w^D \Psi_{2W} + a_E^D \Psi_{2E} + a_S^D \Psi_{2S} + a_N^D \Psi_{2N} - a_p^D \Psi_{2P} . \quad (4.45)$$

Rearranging the above equation yields

$$\Psi_{2P} = c_{\Psi;W} \Psi_{2W} + c_{\Psi;E} \Psi_{2E} + c_{\Psi;S} \Psi_{2S} + c_{\Psi;N} \Psi_{2N} + S_{\Psi;P} , \quad (4.46a)$$

where

$$c_{\Psi;W} = \frac{a_w^D}{a_p^D} , \quad c_{\Psi;E} = \frac{a_E^D}{a_p^D} , \quad (4.46b, c)$$

$$c_{\Psi;S} = \frac{a_S^D}{a_p^D} , \quad c_{\Psi;N} = \frac{a_N^D}{a_p^D} , \quad \text{and} \quad (4.46d, e)$$

$$S_{\Psi;P} = \frac{\Omega_{2P} R_p \Delta R \Delta \theta}{a_p^D} . \quad (4.46f)$$

#### 4.5.5 Discretization of Interface Conditions

The discretization of interface conditions along the interface between the fluid and the porous layers requires some additional attentions. They are derived with the help of imaginary nodal points (Figure 4.3). This approach has been employed successfully in the past (Pan and Lai, 1995; Leong and Lai, 2001). The interface conditions for vorticity, temperature, and stream function can be reduced and represented in the following algebraic forms.

$$\Omega_{1P} = \frac{Da(4 - \Delta R^2)(\Omega_{1W} + \Omega_{2E})}{\Delta R^3 + 2Da\Delta R^2 - 8Da} + \frac{(2 - \Delta R)\Psi_{1W} - (2 + \Delta R)\Psi_{2E} + 2\Delta R(\delta + 1)\Psi_{1P} - \Delta R\delta(\Psi_{1N} + \Psi_{1S})}{\Delta R^3 + 2Da\Delta R^2 - 8Da}, \quad (4.47)$$

$$\Theta_{1P} = \frac{4(\Theta_{1W} + \tilde{\alpha}\Theta_{2E}) - (\Theta_{1WW} + \tilde{\alpha}\Theta_{2EE})}{3(1 + \tilde{\alpha})}, \text{ and} \quad (4.48)$$

$$\Psi_{1P} = \frac{2 - \Delta R}{4(\delta + 1)}\Psi_{1W} + \frac{2 + \Delta R}{4(\delta + 1)}\Psi_{2E} + \frac{\delta}{2(\delta + 1)}(\Psi_{1N} + \Psi_{2S}) + \frac{(\Delta R)^2}{2(\delta + 1)}\Omega_{1P}. \quad (4.49)$$

where  $\delta = (\Delta R / \Delta \theta)^2$ . *WW* and *EE* are the nodes further west and east to the nodes of *W* and *E*, respectively.

#### 4.5.6 Convergence Criteria

Gauss-Seidel iterative scheme is employed in this numerical study. In this study, correction of the stream function on the inner cylinder is performed based on the prescribed velocity on the inner cylinder. This correction scheme bears some similarity with that Launder and Ying (1972, 1974) suggested. Unlike the scheme used in this study, their scheme involved the implementation of correction for the guess stream

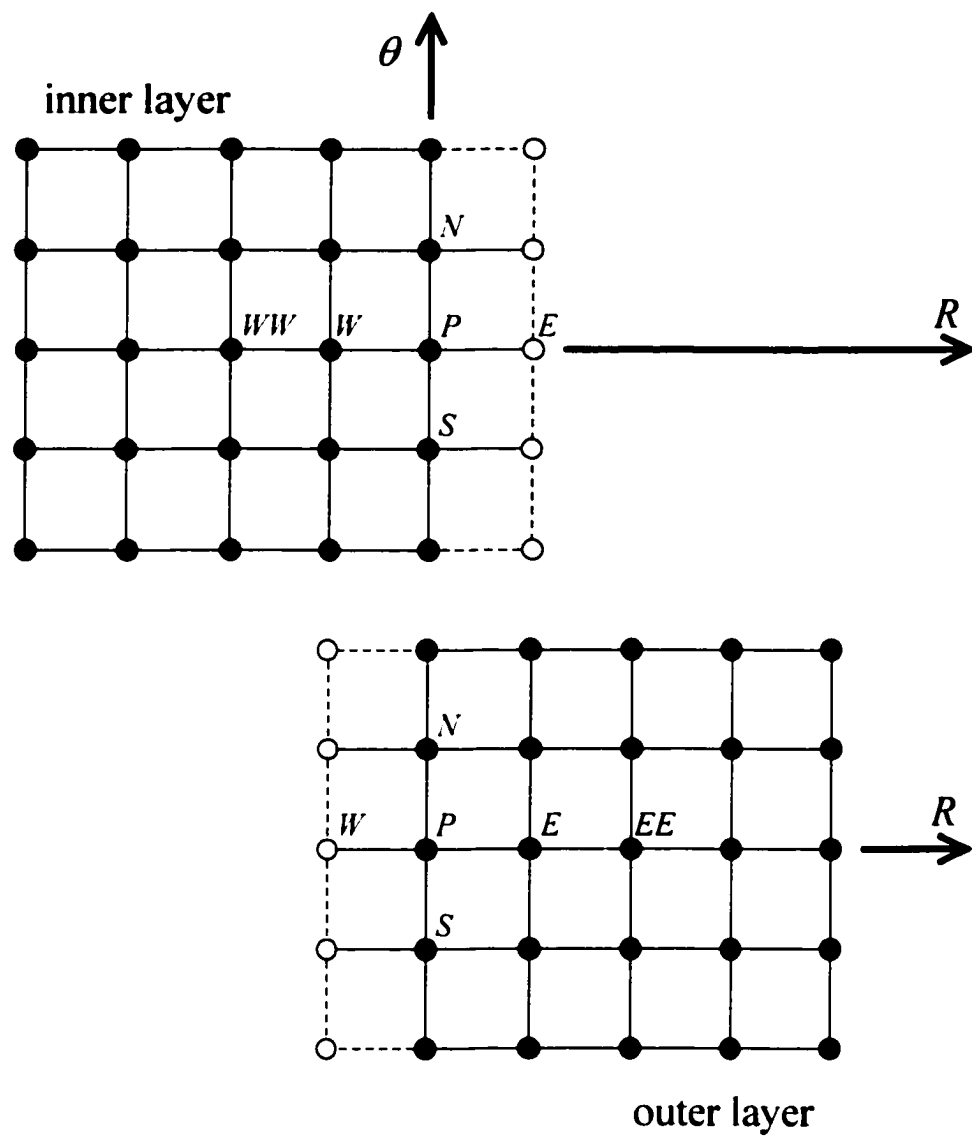


Figure 4.3 Imaginary nodal points for the implementation of interface conditions.



function on the inner cylinder based on pressure terms. As shown in Figure 4.4, the relative error of property  $\Phi$  at node  $P$  and iterative step  $n$  is defined as

$$\varepsilon_{\Phi_P} = \left| \frac{\Phi_P^n - \Phi_P^{n-1}}{\Phi_P^n} \right|. \quad (4.50)$$

The numerical code will not stop running until the relative errors for the stream function, vorticity and temperature are simultaneously less than  $10^{-4}$ . Because the inner cylinder rotates, the value of the stream function on the inner cylinder is not known a priori. For this reason, an initial guess for this value is needed to initiate the iterative process. After a converged solution is obtained, the gradient of the stream function on the inner cylinder (i.e., the rotational speed of the inner cylinder) is evaluated. If the calculated speed agrees with the given one, then the computation is complete. Otherwise, the procedure repeats with a new guessed value of the stream function on the inner cylinder. Based on the gradient previously obtained, a linear interpolation is performed to determine the corrected guessed value. The relative error of this corrected guessed value with respect to the previous one is estimated. Once again, the computation will only stop if the relative error of this corrected guess value is less than  $10^{-4}$ .

#### 4.5.7 Evaluation of Heat Transfer Performance

The heat transfer results are evaluated through the Nusselt number on each surface of the cylinders. By definition, the local Nusselt number represents the local heat flux and is given by

$$Nu = \frac{hb}{k_i} = -\frac{\partial \Theta_i}{\partial R}. \quad (4.51)$$

On the surfaces of the inner and outer cylinders, they are given by

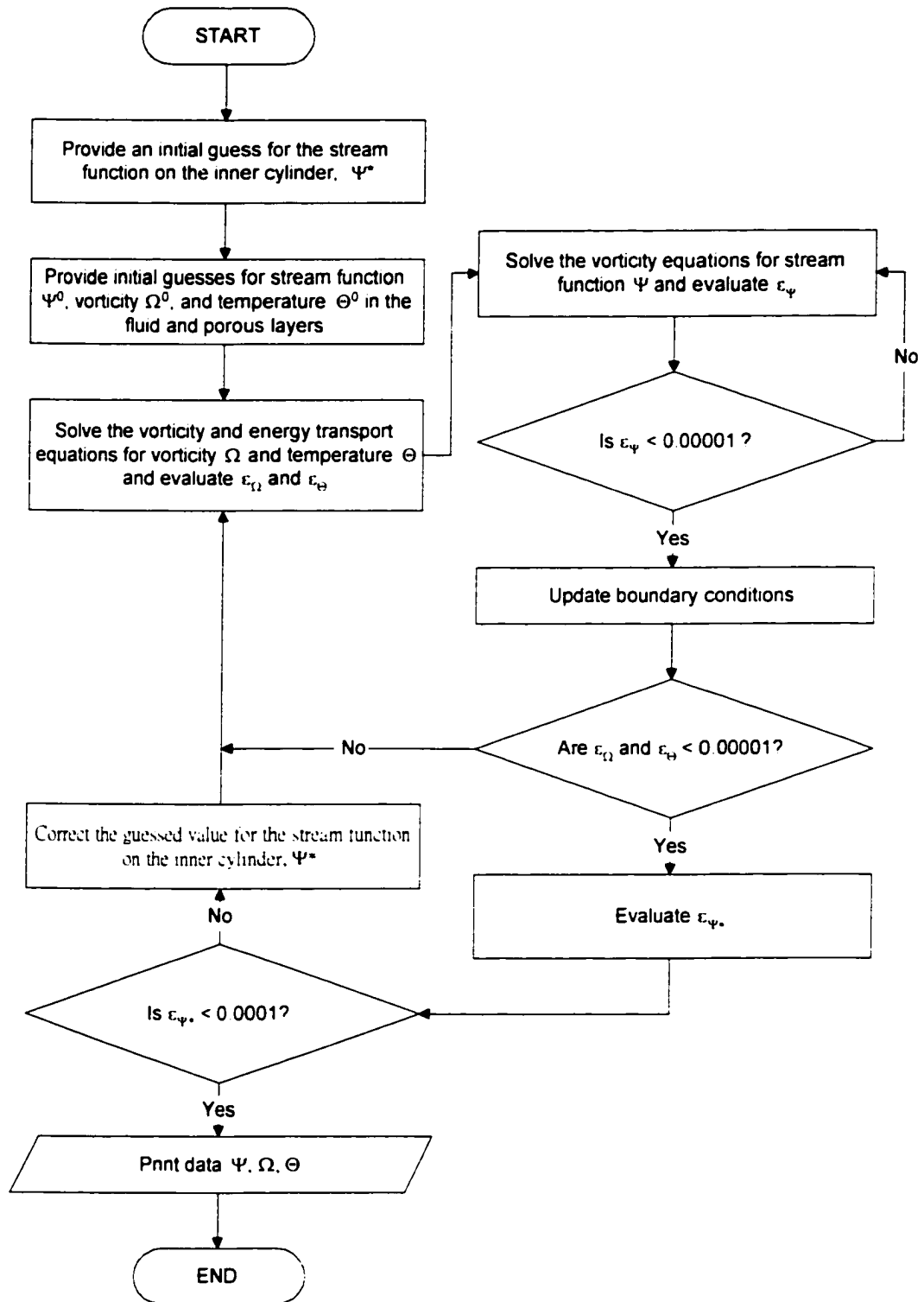


Figure 4.4 Algorithm of the numerical approach.

$$Nu_{in} = \frac{hb}{k_1} = -\frac{\partial \Theta_1}{\partial R}, \text{ and} \quad (4.52a)$$

$$Nu_{out} = \frac{hb}{k_2} = -\frac{\partial \Theta_2}{\partial R}. \quad (4.52b)$$

These local Nusselt numbers not only can provide us the information about heat transfer in the annular space, but also a means to evaluate the accuracy of the numerical results. To perform the energy balance between the inner and outer cylinders, one rewrites Eq. (4.52b) as

$$\frac{hb}{k_1} = -\frac{k_2}{k_1} \frac{\partial \Theta_2}{\partial R} = \frac{k_2}{k_1} Nu_{out}, \quad (4.53)$$

so that the quantity  $hb/k_1$  can serve as the basis for comparison. The percentage error of Nusselt numbers is given by

$$\% \mathcal{E} = \frac{c(k_2/k_1)\overline{Nu_{out}} - a\overline{Nu_{in}}}{a\overline{Nu_{in}}}, \quad (4.54)$$

where the Nusselt numbers are the average Nusselt numbers evaluated at each surface (which are defined below in Eq. (2.69)) and their coefficients  $a$  and  $c$  take into account the surface areas of the inner and outer cylinders.

## 4.6 Results and Discussion

A numerical code has been successfully developed to solve Eqs. (4.9) to (4.12), (4.14) and (4.15) simultaneously subject to the boundary and interface conditions. A grid refinement test has been performed to determine the optimal grid size. It is found that the optimal grid size is 61x73 for most of the cases considered. Although a finer grid would generally yield an improvement in solution, it would consume much more computational

time. In some cases, the time required could be more than double of the time it takes for the grid size of 61x73. Because of the marginal improvement yielded and enormous computational effort required, the grid size of 61x73 is obviously the most appropriate grid size that provide reliable results. For some highly convective cases, it was found that finer grids, 71x91 and 81x91, were needed to ensure better solutions.

The code has been validated against several natural convection cases. The results obtained were found to agree very well with those presented in the previous chapter. A comparison of these solutions is shown in Figure 4.5. Table 4.1 lists the details of the parameters used in the study. As shown in the figure, the streamlines from the analytical solution are not as smooth as those from the numerical solution because the grid used for the former ones was far less than that for the latter ones. A finer grid has not been attempted for the analytical solutions because the analytical approach requires a large amount of computational effort.

Table 4.1 Numerical parameters used for the comparison effort.

Analytical Approach*	Numerical Approach
<u>Case (a1)</u> grid size: 11x37	<u>Case (a2)</u> grid size: 81x91 $b = 1.25, Da = 10^{-4}, k_1/k_2 = 1, Pr = 2 \times 10^4, Pe = 0, Ra = 0.5$
<u>Case (b1)</u> grid size: 11x37	<u>Case (b2)</u> grid size: 81x91 $b = 1.50, Da = 10^{-4}, k_1/k_2 = 1, Pr = 10^4, Pe = 0, Ra = 0.5$
<u>Case (c1)</u> grid size: 11x37	<u>Case (c2)</u> grid size: 81x91 $b = 1.75, Da = 10^{-4}, k_1/k_2 = 1, Pr = 2 \times 10^4, Pe = 0, Ra = 0.1$

\* These cases are solved using perturbation method and Fourier Transform, as reported in Chapter Three.

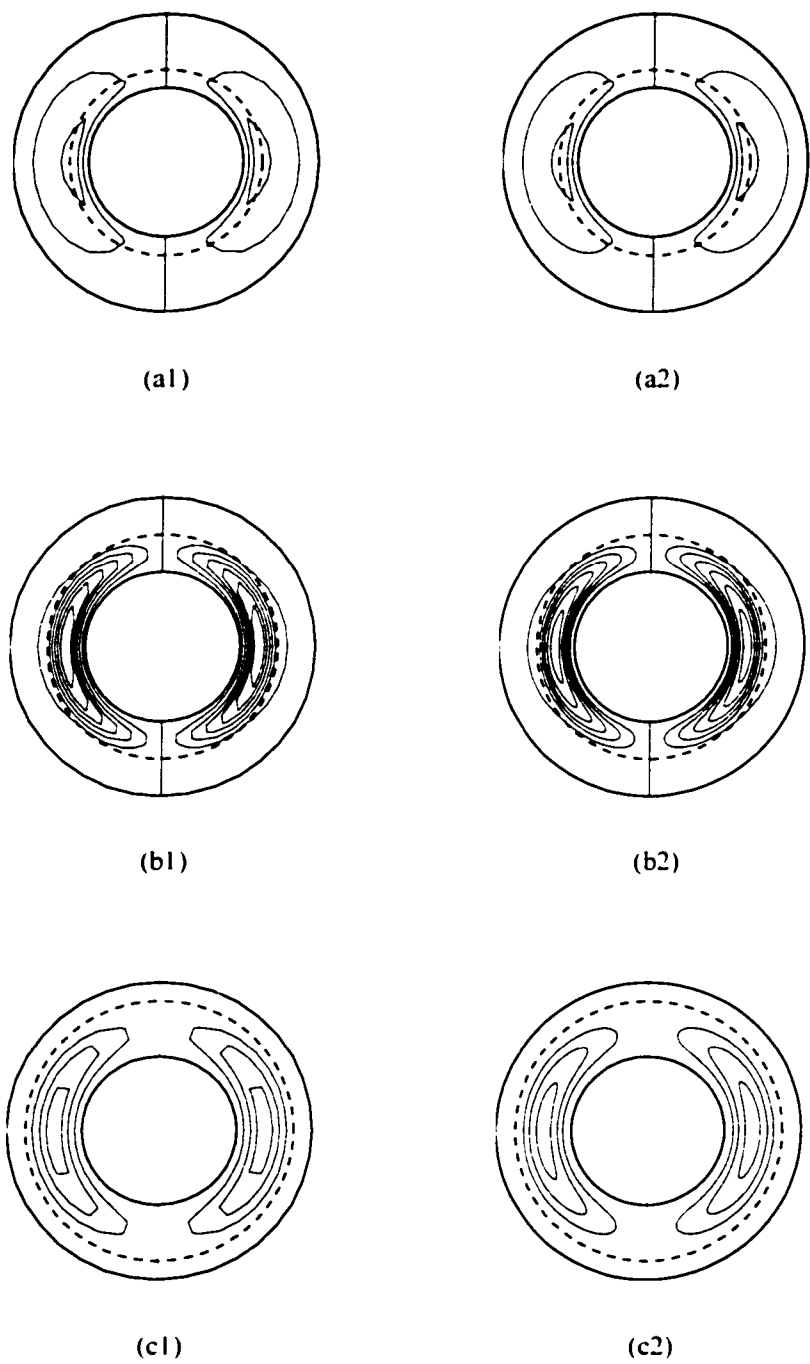


Figure 4.5 Code validation: a comparison of solutions obtained using analytical (the previous chapter) and numerical approaches ( $\Delta\psi = 5 \times 10^{-6}$ ).

The flow and temperature fields for laminar natural convection between horizontal circular cylinders at high Rayleigh numbers can be divided into five physically distinctive regions (Jischke and Farshchi, 1980; Himasekhar and Bau, 1986).

(i) Inner boundary layer

This is a very thin layer next to the inner cylinder in which buoyancy and viscous forces are dominant. Here, gradients in the angular direction are negligible compared to those in the radial direction.

(ii) Outer boundary layer

Similar to the inner boundary layer, this is a very thin layer next to the outer cylinder and is dominated by buoyancy and viscous forces.

(iii) Plume

It exists along the vertical line of symmetry above the inner cylinder and joins the inner and outer thermal boundary layers. Buoyancy is the force that drives it.

(iv) Core region

This region refers to the region bounded by the other four regions. The outer boundary layer empties into the inner one through this core region.

(v) Stagnant region

This region is located beneath the inner cylinder. Here, the buoyancy inhibits fluid motion and heat transfer takes place mainly by conduction.

Different from the previous studies (Jischke and Farshchi, 1980; Himasekhar and Bau, 1986), the governing parameters in the current study, in addition to the Rayleigh number, include the Peclet number. At low Peclet numbers, the regions mentioned above

are distorted as they will be shown later. At high Peclet numbers, the regions corresponding to the inner and outer boundary layers grow, merge, and eventually replace other regions.

Figure 4.6 shows the flow field of a mixed convection case, which corresponds to a relatively high Rayleigh number and a low Peclet number. If the Peclet number is zero, the case reduces to that of natural convection. When the Peclet number is small, this case can be viewed as natural convection perturbed by a small shear effect induced by the inner cylinder. Because of this rotational effect, the flow pattern will no longer be symmetric. In the figure, streamlines are plotted to illustrate the flow pattern in the annulus. Apparently, the streamlines are nearly symmetrical along the vertical axis. Since there exist buoyancy and shear effects in this case, their combined effect leads to a flow structure that is relatively complicated. To confirm and better understand the velocity distribution, the angular velocity profiles in the vector form are superimposed on the figure at several cross-sections. Clearly, there appear two convective cells on each side of the annulus. Also noticed is that the angular velocity profiles are almost symmetrical along the vertical axis, implying the dominance of natural convection. In the porous sleeve, it can be seen that there is a flow with a finite velocity.

Since a shear layer is not clearly shown in Figure 4.6, the velocity profiles at different cross-sections ( $\theta = 0^\circ, 90^\circ, 180^\circ$ , and  $270^\circ$ ) are further examined in Figure 4.7. In these plots, the variation of the angular velocity in the radial direction is presented from the surface of the inner cylinder to that of the outer cylinder. The region for  $R < 1.0$  is the fluid layer while the region for  $R > 1.0$  is the porous sleeve. The first thing observed is that the slip velocity is not allowed on both the outer cylinder and the

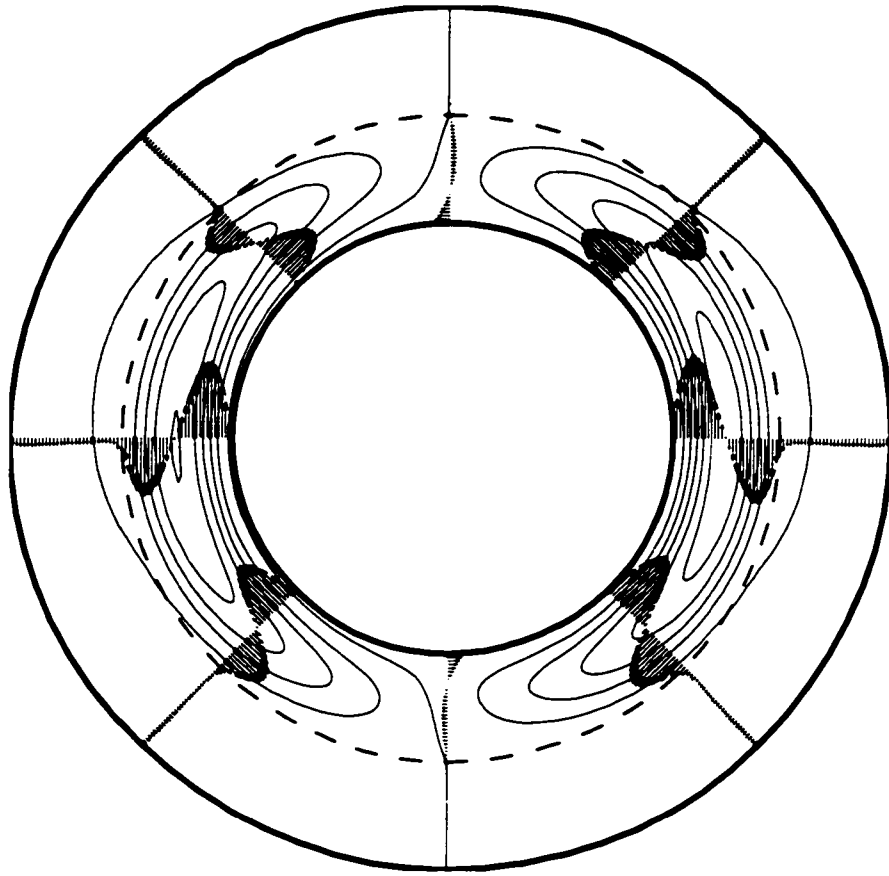


Figure 4.6 Velocity field in the forms of streamlines and angular velocity profiles at various cross-sections ( $b = 1.5$ ,  $Da = 10^{-4}$ ,  $k_1/k_2 = 1$ ,  $Pr = 2 \times 10^4$ ,  $Ra = 10^5$ , and  $Pe = 10$ ).



interface. Furthermore, the velocity gradient is continuous across the interface. These results are consistent with the assumptions of the Darcy-Lapwood-Brinkman extended model. On the inner cylinder, the magnitude of azimuthal velocity is estimated to be

$$U_{\theta} = -\frac{\Psi_2 - \Psi_1}{\Delta R}. \quad (4.55)$$

Theoretically, the magnitude of the angular velocity should equal to the Peclet number, which is 10 in this case. Since the approximation using Eq. (4.55) has a truncation error on the order of  $(\Delta R)^2$ , the estimated velocity on the inner cylinder is not exact. For this reason, the plots presented in Figure 4.7 only serves as a qualitative proof showing the existence of the shear layer surrounding the inner cylinder. At  $\theta = 0^\circ$ , it is seen that the inner cylinder induces a shear flow in the positive angular counter-clockwise direction. A nearly identical velocity profile is observed at  $\theta = 180^\circ$ . Based on the velocity profile along the cross-section at  $\theta = 90^\circ$ , it can be seen that the fluid next to the inner cylinder rises as a result of buoyancy and shear effects. The flow on this side of the inner boundary layer region is aided by the buoyancy force due to the differential heating and the shear effect due to the rotation of the inner cylinder. At  $\theta = 270^\circ$ , an opposing flow is observed. On this side of the inner boundary layer region, the buoyancy force tends to raise the fluid, but the rotation of the inner cylinder tends to entrain the fluid downward. As a result, the fluid particle near the inner cylinder is found to flow downward with a small but finite angular velocity in the counter-clockwise direction. Whereas, the fluid particle at the outer edge of the inner boundary layer, although still has a negative angular velocity, is getting a lift from buoyancy. It is observed that the shear flow only exists in a very thin layer between the convective cell and the inner cylinder. At the plume region, the shear flow from the right hand side splits into two streams, one

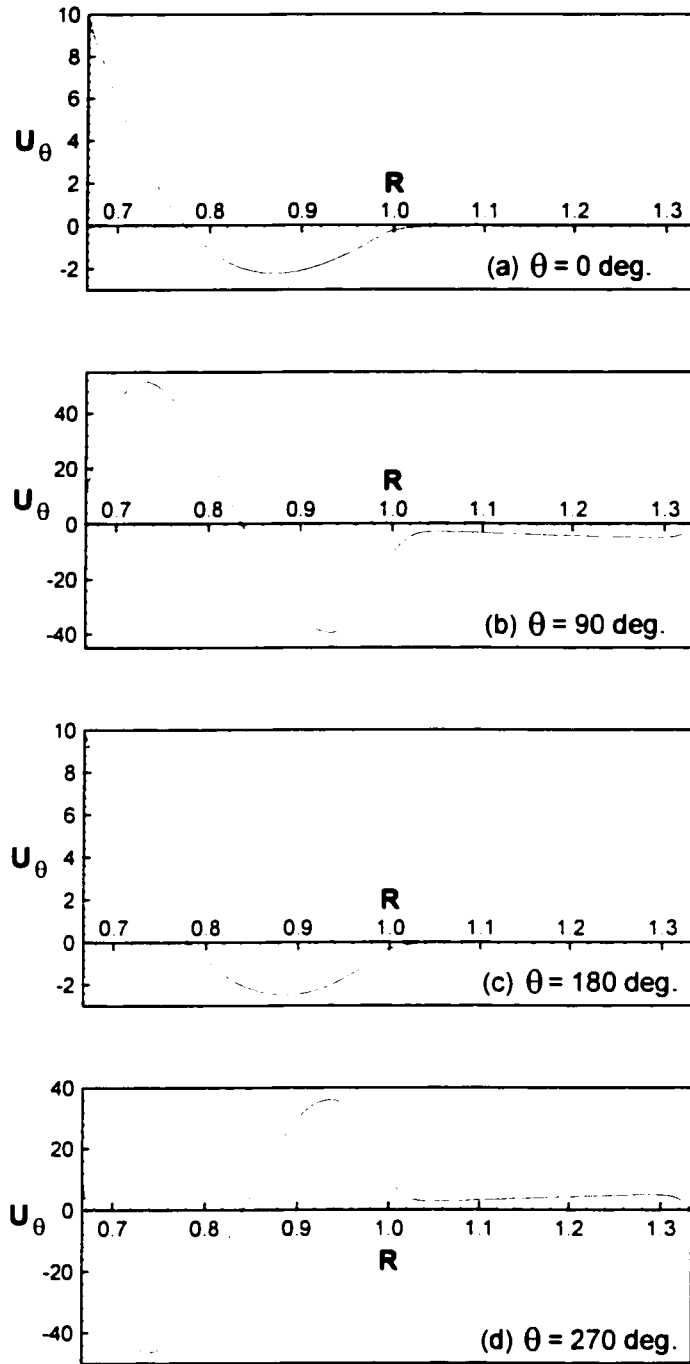
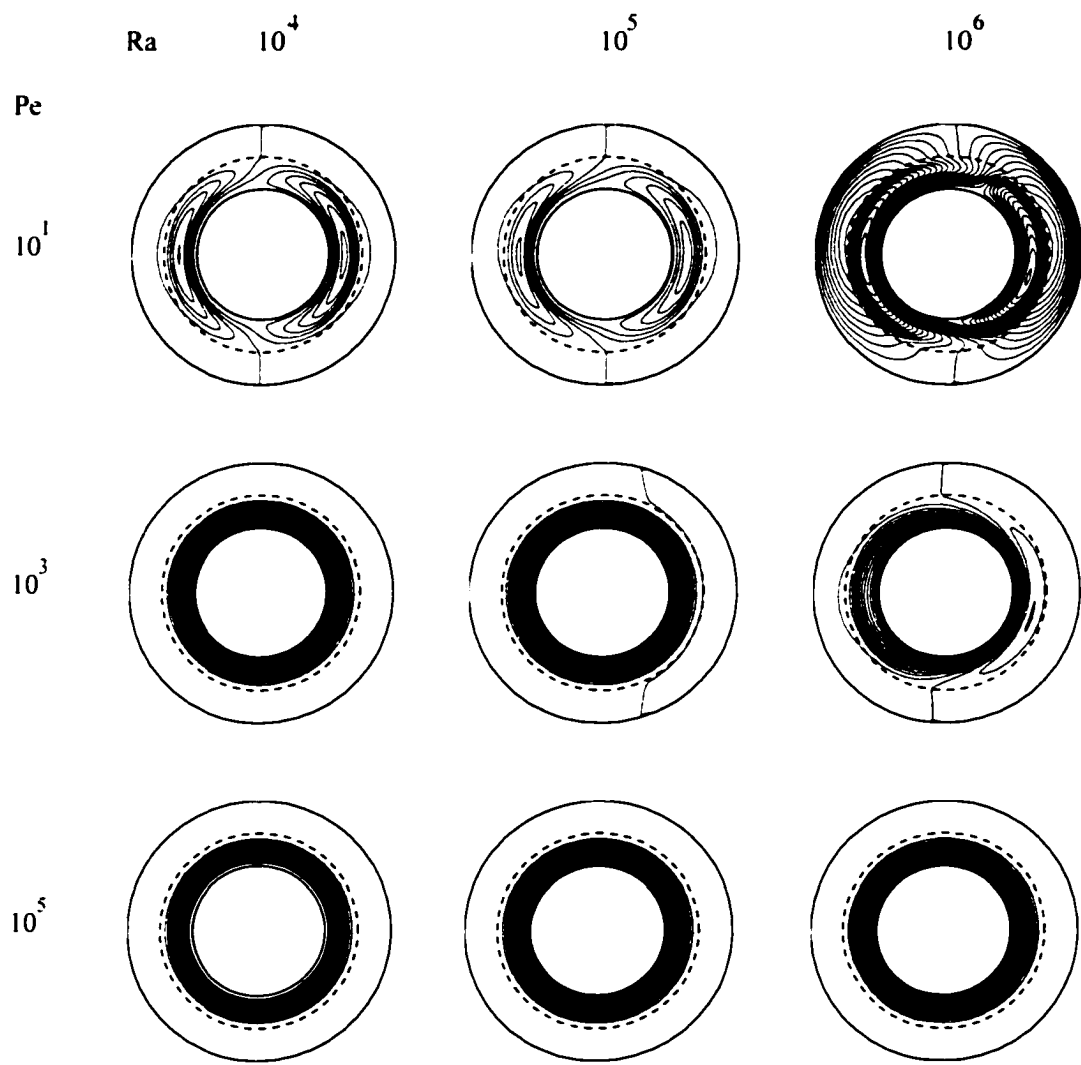


Figure 4.7 Angular velocity profiles at various cross-sections ( $b = 1.5$ ,  $Da = 10^4$ ,  $k_1/k_2 = 1$ ,  $Pr = 2 \times 10^4$ ,  $Ra = 10^5$ , and  $Pe = 10$ ).

of which follows the inner cylinder and enters the left shear layer while the other flows around the right convective cell and penetrates the porous sleeve. At the lower section, these two streams merge and flow into the right shear layer again.

In Figure 4.8, the flow fields at various Rayleigh and Peclet numbers are presented in the form of streamline contours. As the Peclet number increases, it implies that the rotational speed of the inner cylinder increases. This leads to a thicker shear flow layer immediately next to the inner cylinder as well as a finite shear flow in the porous sleeve. Also noticed is the sharper gradient of streamlines with an increase of the Peclet number, which indicates that the shear flow is becoming stronger. Because of the increasing shear effect, the shear flow dominates in the fluid layer and suppresses the formation of the convective cells. An increase in the Rayleigh number signifies the dominance of buoyancy effect. As the buoyancy grows, the convective cells evidently become stronger. At a relatively low Rayleigh number, the convective cells only occupy the fluid layer. As the Rayleigh number increases, the cells gain more strength and penetrate the porous layer. When  $Pe = 10$ , the system is dominated by the buoyancy effect. Somewhat similar to the plots presented in the earlier study of natural convection, there exist two primary convective cells of almost equal strength in the annular space. Also, the flow patterns are almost symmetrical except for the region immediately next to the rotating inner cylinder. Because of the rotational effect, the convective cells are deformed by the shearing action. As the Peclet number increases to  $10^3$ , the buoyancy effect is almost overcome by the shear effect. Therefore, the convective cells are suppressed and will eventually disappear if the rotational speed is further increased. At  $Ra = 10^6$ , the left convective cell is completely suppressed and the right convective cell



**Figure 4.8** Flow fields in concentric rotating cylinders with a porous sleeve for  $h = 1.5$ ,  $Da = 10^{-4}$ ,  $k_1/k_2 = 1$ , and  $Pr = 20,000$  ( $\Delta\Psi = 0.1$  for  $Pe = 1$  and  $Ra = 10^4$ ,  $\Delta\Psi = 1$  for  $Pe = 1$  and  $Ra = 10^5$  and  $10^6$ ,  $\Delta\Psi = 10$  for  $Pe = 10^3$ , and  $\Delta\Psi = 2000$  for  $Pe = 10^5$ ).

becomes so weak that it barely survives in the fluid layer. A further increase of the Peclet number to  $10^5$  causes the entire flow field to rotate like a rigid body. This is a clear evidence that the flow is dominated by the shear effect. From the plots shown in this figure, one observes that flow penetration is more likely to occur at low Peclet and high Rayleigh numbers, which suggests that the buoyancy effect assists flow penetration whereas the shear effect limits flow penetration.

The corresponding isotherms are shown in Figure 4.9 to demonstrate the dependence of temperature fields on the Rayleigh and Peclet numbers. As the Rayleigh number increases, the uniform distribution of isotherms is disturbed. The thermal plume is seen to tilt to one side and the development of the five natural convection regions is more complete. This signifies the growing importance of heat convection. In contrast, the Peclet number has a completely opposite effect. Clearly, the distribution of the isotherms become more and more proportional to the logarithm of the radial distance in the annulus and eventually form a family of concentric circles. Consequently, the thermal plume diminishes. In other words, an increase in the Peclet number suppresses the buoyancy effect. As shown in the previous chapter, if the annulus remains stationary, there is always a thermal plume developing vertically upward from the inner cylinder. Here, the uprising thermal plume is distorted by the shear effect resulted from the rotation of the inner cylinder. When the buoyancy effect is much stronger than the shear effect, the very thin layer of shear flow causes the thermal plume shifted to the right. Recall from Figures 4.6 and 4.7 that the velocity component is greater on the right hand side of the annulus. Therefore, a larger temperature gradient is also found on this side of annulus. As the shear layer grows, the isotherms become more circular and its thermal plume

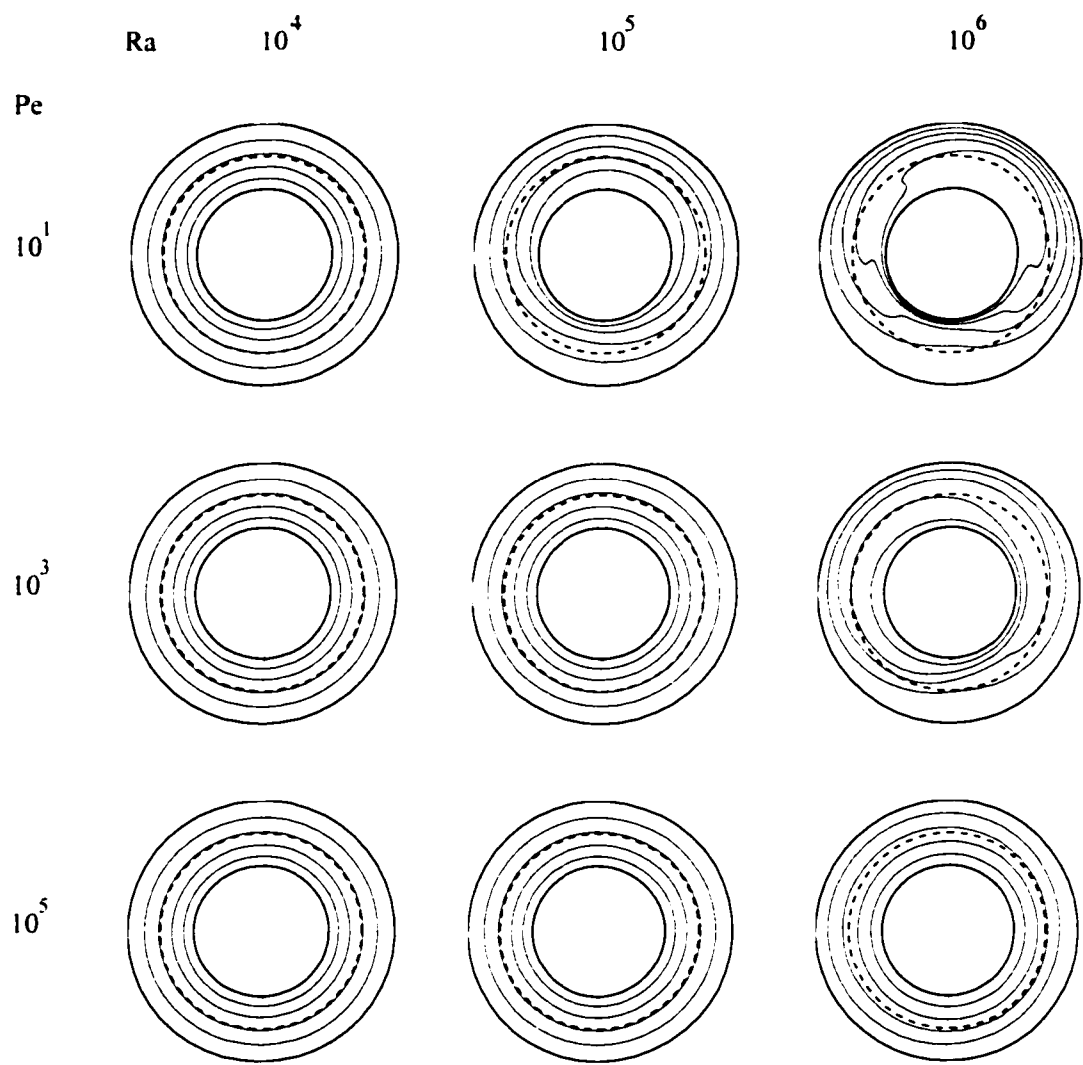


Figure 4.9 Temperature fields in concentric rotating cylinders with a porous sleeve for  $b = 1.5$ ,  $Da = 10^4$ ,  $k_1/k_2 = 1$ , and  $Pr = 20,000$  ( $\Delta\Theta = 0.2$ ).

points to the left, which is closely related to the flow structure. At a high Peclet number, the flow rotates like a solid body, contributing nearly no flow in the radial direction. As a result, the flow does not contribute to heat removal in the radial direction. Hence, the heat transfer mechanism is mainly by conduction. The temperature distribution for this case is evidently very similar to that of purely conduction. From this figure, it was shown that the onset of convection in rotating cylinders dependent on both Rayleigh and Peclet number. Mack and Bishop (1968) reported that the onset of natural convection in a non-rotating annulus takes place at  $Ra = 10^3$ . From the present results, one can conclude that the rotation of inner cylinder delays the onset of natural convection.

Figure 4.10 shows the flow fields for various values of  $b$  and Rayleigh number. Since  $b$  is the inner radius of the porous sleeve, an increase in  $b$  implies a decrease in the porous sleeve thickness. As the porous sleeve becomes thinner, the fluid layer is thicker. Since the flow resistance in the porous sleeve is greater than that in the fluid layer, the overall flow resistance reduces when the porous sleeve is thinner and the fluid layer is thicker. Not only does this thicker fluid layer offer more space for the shear flow and convective cells to develop, but also it imposes a lower overall flow resistance that the shear flow and convective cells must overcome. As a result, the strength of the shear flow and convective cells both increases with  $b$ . Since there is more space for the flow to develop in the annulus, the flow is less likely to penetrate the porous sleeve. In this case, the porous sleeve would behave as if it were impermeable. In general, the eyes of the convective cells tend to locate in the fluid layer. For a thicker porous sleeve ( $b = 1.25$ ), it is possible that the eyes of the cells fall on the interface. When this happens, it is found that the strength of the convective cells decreases tremendously. Even at  $Ra = 10^6$ , the

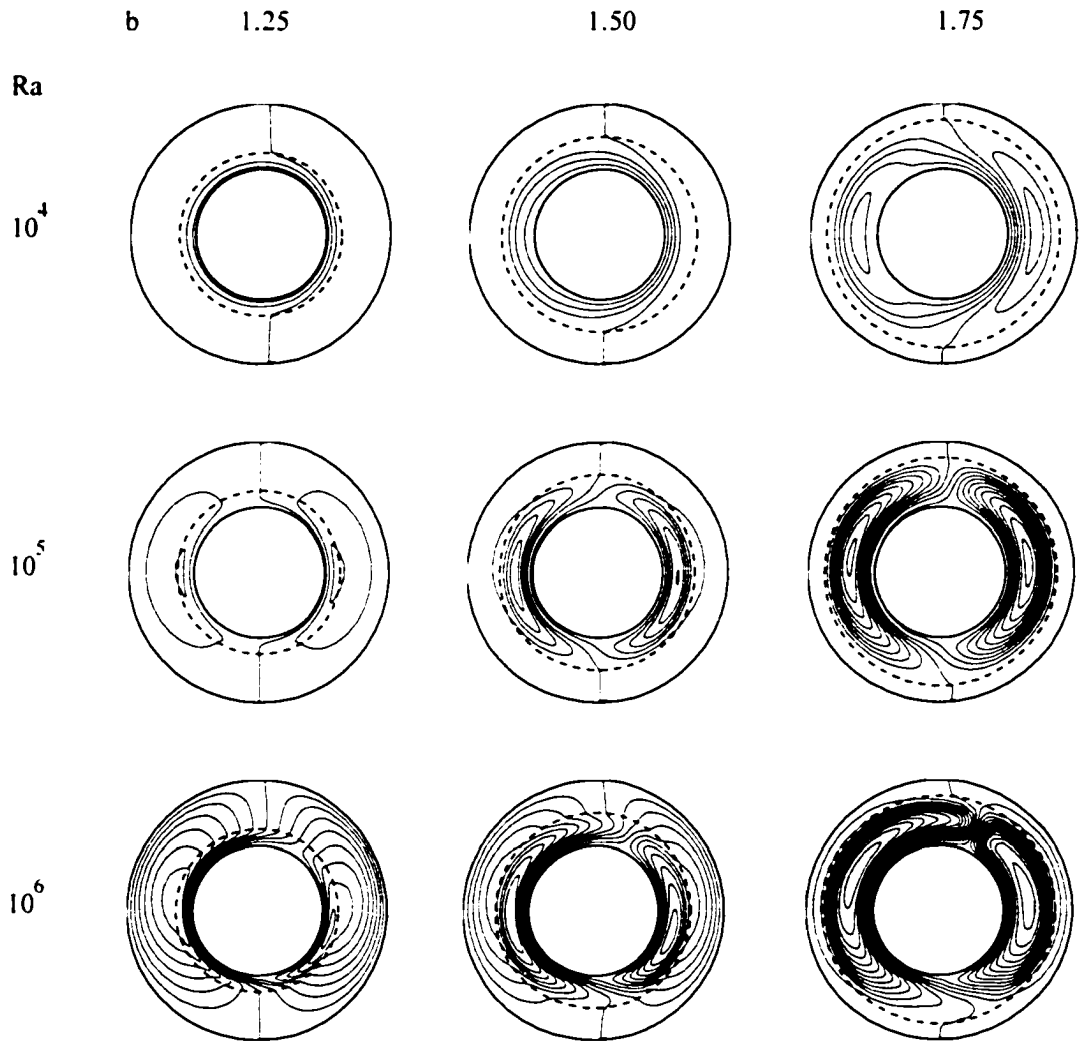


Figure 4.10 Flow fields in concentric rotating cylinders with a porous sleeve for  $Da = 10^{-4}$ ,  $k_1/k_2 = 1$ ,  $Pe = 10$ , and  $Pr = 20,000$  ( $\Delta\Psi = 0.5$  for  $Ra = 10^4$ ,  $\Delta\Psi = 1$  for  $Ra = 10^5$ , and  $\Delta\Psi = 2$  for  $Ra = 10^6$ ).



shear layer is thin and the convective cell is weak. As the porous layer thickness decreases (i.e.,  $b$  increases), both convective cell strength and shear layer thickness increase.

From Figure 4.11, it is obvious that convection increases with  $b$ . When the porous sleeve is thin, the overall flow resistance is low and therefore a small amount of energy is needed to initiate a convective flow. For example, heat convection is already present at  $Ra = 10^4$  when  $b = 1.75$ . As  $b$  decreases, it is seen that the isotherms become more circular. Eventually, the heat transfer mode at  $b = 1.25$  is dominated by conduction. This clearly indicates that porous sleeve thickness delays the onset of natural convection. By the same reason, at  $Ra = 10^5$ , only a small perturbation in the isotherms is observed when  $b = 1.25$ . As  $b$  increases to 1.75, it is noticed that a thermal plume rises from the inner cylinder. At  $Ra = 10^6$ , a thermal plume rises upward and grows into a mushroom-like cloud that points to the upper right. As  $b$  increases, the isotherms are further twisted. Because of the presence of the thermal plume, the highest heat transfer rate occurs at the top upper portion of the outer cylinder and the lower portion of the inner cylinder. Although the heat transfer mode at  $Ra = 10^6$  is convection, the stagnant region is much greater for  $b = 1.25$  than  $b = 1.75$ .

The flow fields for various Rayleigh and Darcy numbers are shown in Figure 4.12. Recall that Darcy number signifies the relative pore size in the porous sleeve. As the Darcy number decreases, the strength of the convective cells decreases. This is because the flow experiences a higher resistance in the porous layer as the pore size reduces. When  $Da = 10^0$ , the presence of the porous sleeve becomes irrelevant because the pore size of the porous sleeve is on the same order of the gap width. In reality, this case does

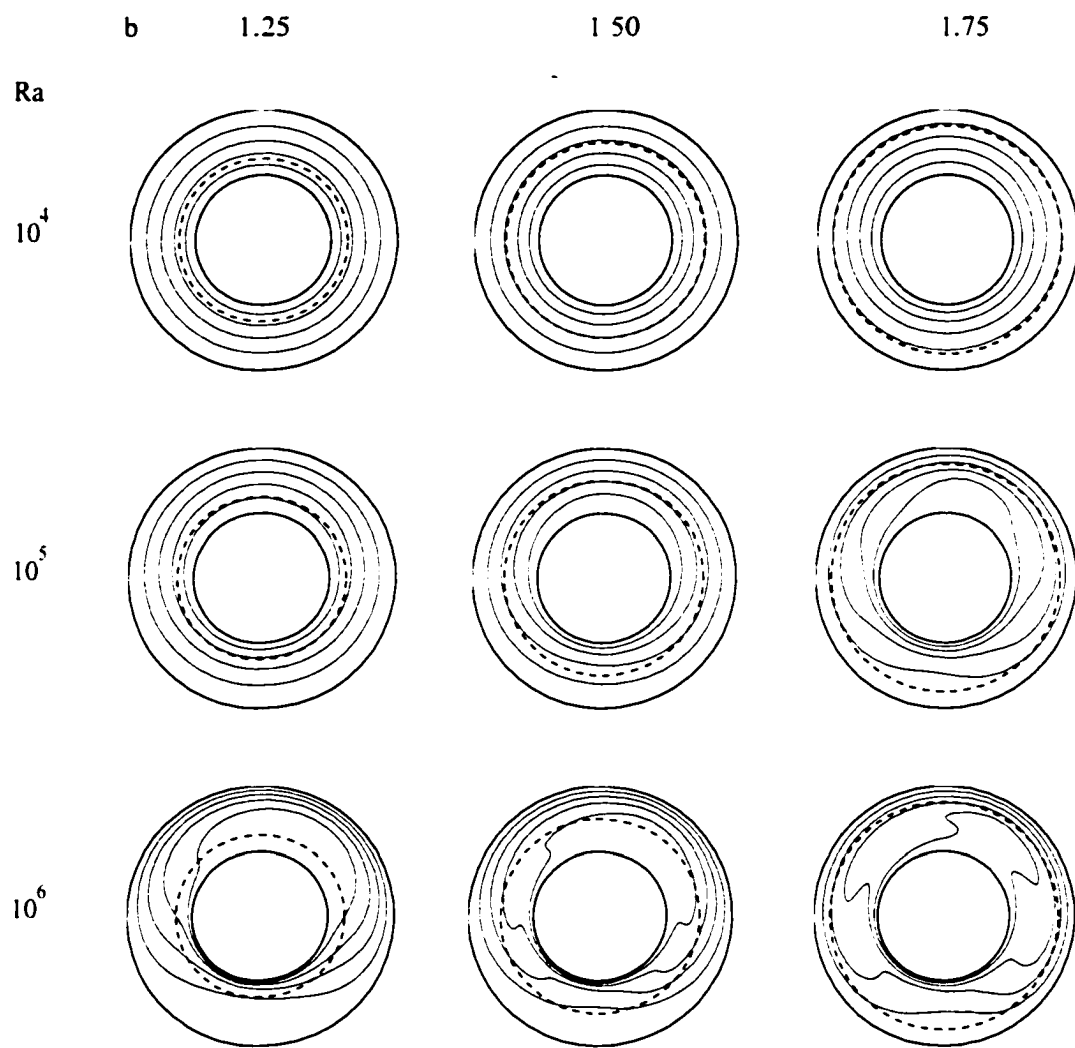


Figure 4.11 Temperature fields in concentric rotating cylinders with a porous sleeve for  $Da = 10^4$ ,  $k_1/k_2 = 1$ ,  $Pe = 10$ , and  $Pr = 20,000$  ( $\Delta\Theta = 0.2$ ).

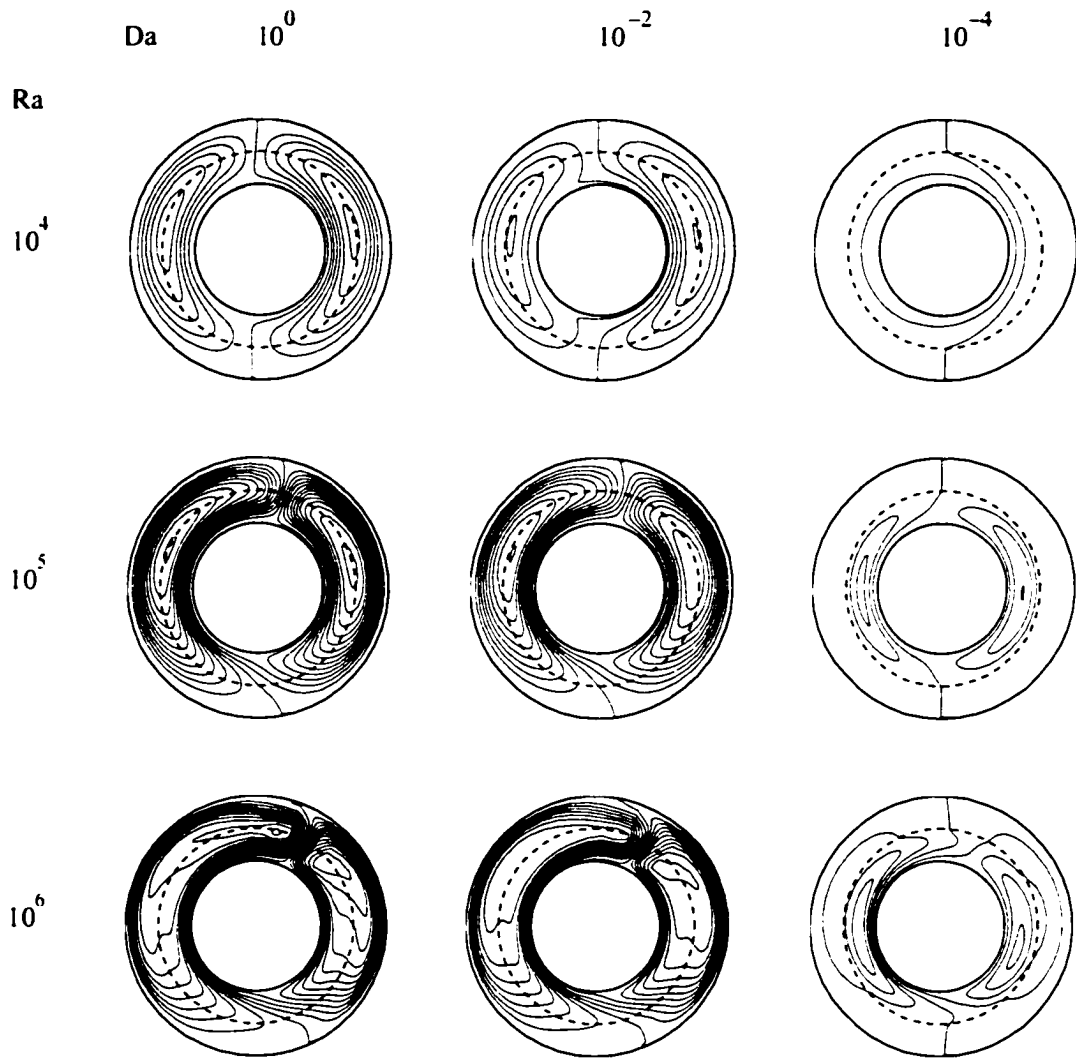


Figure 4.12 Flow fields in concentric rotating cylinders with a porous sleeve for  $b = 1.5$ ,  $k_1/k_2 = 1$ ,  $Pe = 10$ , and  $Pr = 20,000$  ( $\Delta\Psi = 1$  for  $Ra = 10^4$ ,  $\Delta\Psi = 2$  for  $Ra = 10^5$ , and  $\Delta\Psi = 5$  for  $Ra = 10^6$ ).

not have too much physical meaning. For the present study, it represents a limiting case for the cylinders without a porous sleeve. On the other end, when  $Da = 10^{-4}$ , the pore size is greatly reduced. At  $Ra = 10^4$ , there is only one convective cell in the annulus, but it is too weak to be shown in the figure. As the Rayleigh number increases, two convective cells develop in the fluid layer. For a fixed Rayleigh number, the strength of the convective cells reduces with a decrease in the Darcy number. At the same time, the eyes of the cells shift downward and move toward the inner cylinder. At  $Ra = 10^4$  and  $Da = 10^0$ , the convective cells are strong, but the shear layer is thin. However, when the Darcy number is reduced to  $10^{-4}$ , the convective cells diminish and the shear layer grows thicker. For  $Da \geq 10^{-2}$ , the eyes of the convective cells always fall on the interface because the porous layer effect is insignificant. When  $Da = 10^{-4}$ , the eyes of the convective cells are always in the fluid layer because the primary flow is squeezed in the fluid layer.

Figure 4.13 shows the temperature distributions for the corresponding cases in Figure 4.12. Apparently, an increase in the Darcy number promotes heat convection. When  $Ra = 10^4$  and  $Da = 10^{-4}$ , the distribution of isotherms, which is proportional to the logarithm of the radial distance, indicates the onset of heat convection. As the pore size increases, a thermal plume develops from the inner cylinder. The isotherms are compressed against the outer cylinder. In other words, the local Nusselt number increases with the Darcy number. As the Rayleigh number increases ( $Ra \geq 10^5$ ), there is a sudden change in heat transfer mode (from conduction to convection) when the Darcy number increases from  $10^{-4}$  to  $10^{-2}$ . A further increase in the Darcy number from  $10^{-2}$  to  $10^0$  leads to a stronger convection. The temperature gradient around the inner cylinder

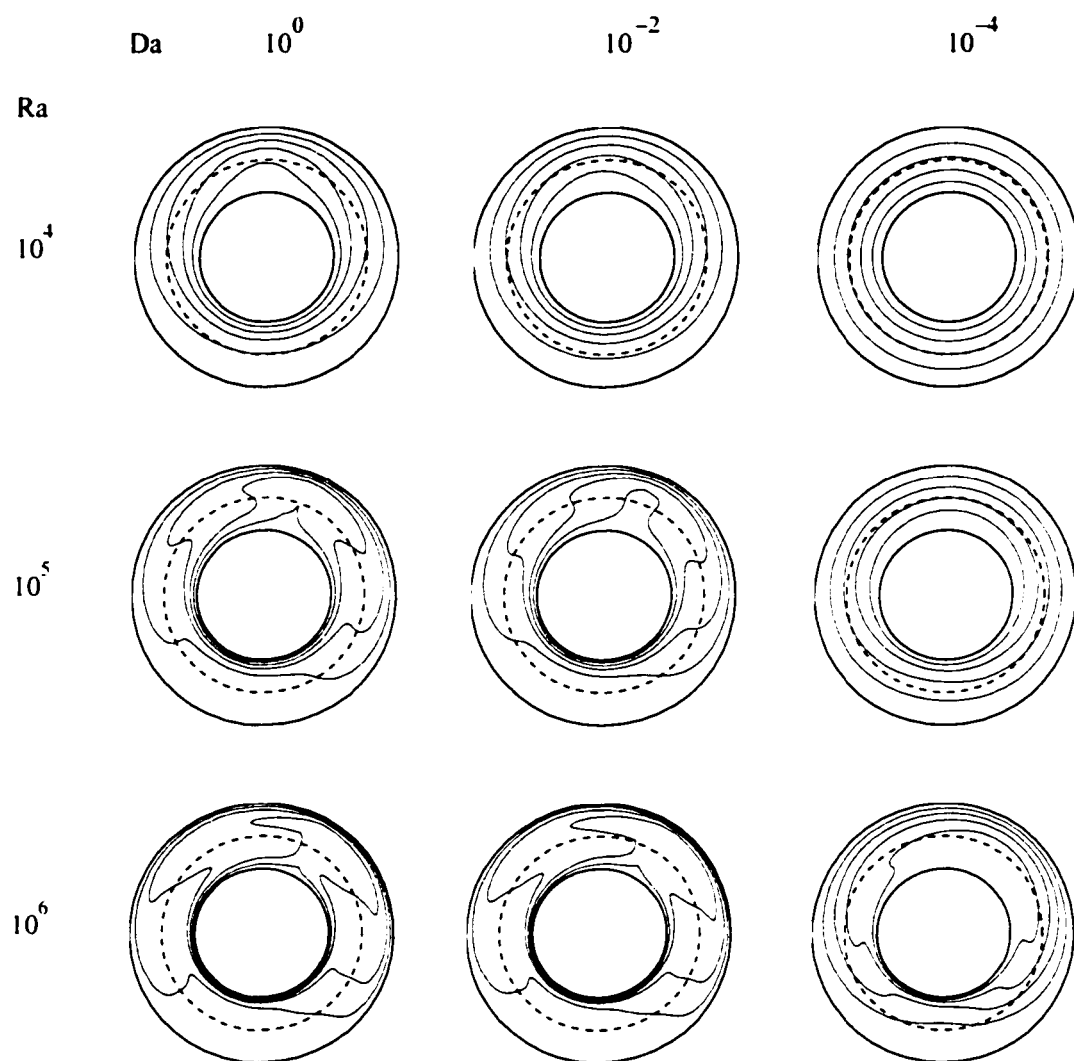


Figure 4.13 Temperature fields in concentric rotating cylinders with a porous sleeve for  $b = 1.5$ ,  $k_1/k_2 = 1$ ,  $Pe = 10$ , and  $Pr = 20,000$  ( $\Delta\Theta = 0.2$ ).

increases and the thermal buoyancy layer becomes thinner. Notice that the differences in temperature distribution between  $Da = 10^0$  and  $Da = 10^{-2}$  are relatively small.

The dependence of flow field on the Peclet number and thermal conductivity ratio is shown in Figure 4.14. The appearance of two convective cells at  $Pe \leq 10^2$  has clearly implied that the flow field is dominated by buoyancy effect whereas the thick shear layer at  $Pe = 10^3$  indicates that the flow field is taken over by the shear effect when the Peclet number increases. Notice that the shear layer extends into the porous sleeve at the left portion of the annular space. On the right, the shear layer is squeezed in the annular space and coexists with a secondary cell. For  $k_1/k_2 = 0.5$ , the porous sleeve is twice more conductive than the fluid. Conversely, for  $k_1/k_2 = 2.0$ , the thermal conductivity of the fluid is twice as large as the effective conductivity of the porous sleeve. In most engineering applications,  $k_1/k_2$  is less than unity because the porous sleeve is mostly made of metals or ceramics. It is found that the convective cell is stronger when the porous sleeve is more conductive than the fluid layer. When  $k_1/k_2 < 1$ , the temperature gradient in the fluid layer is greater than that in the porous sleeve. It is this temperature gradient that produces stronger convective cells. If  $k_1/k_2 > 1$ , the reversed trend is observed. It is interesting to observe that the strength of the shear flow actually grows with  $k_1/k_2$  at  $Pe = 10^3$ .

Shown in Figure 4.15 are the temperature fields for the corresponding flow fields discussed previously in Figure 4.14. At  $Pe = 10^2$ , it is remarkable to notice that the thermal plume rises vertically from the inner cylinder. These patterns look somewhat similar to those of natural convection at different Rayleigh numbers (Kuehn and Goldstein, 1976; Date, 1986). However, it is noticed that isotherms at the lower portion

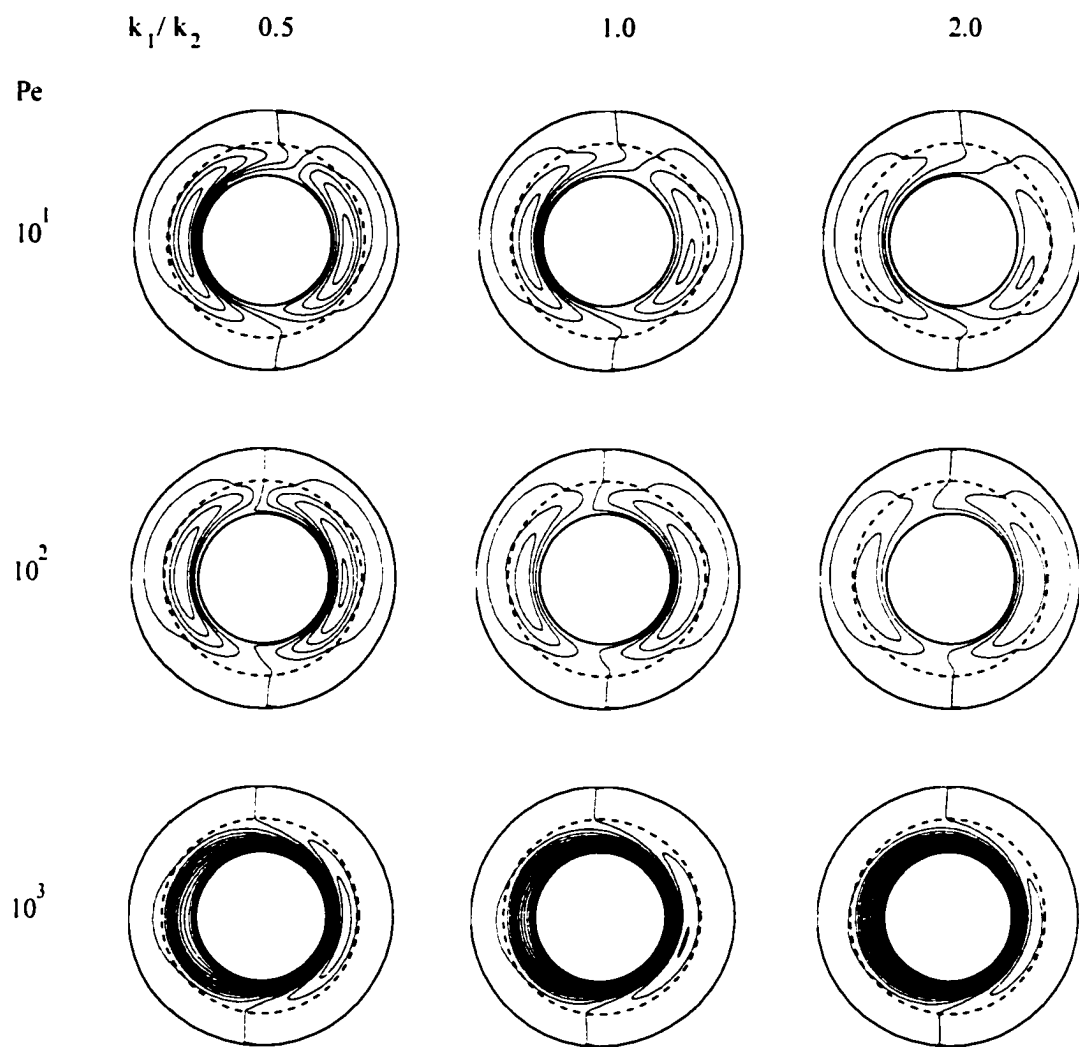


Figure 4.14 Flow fields in concentric rotating cylinders with a porous sleeve for  $h = 1.5$ ,  $Da = 10^{-4}$ ,  $Pr = 20,000$ , and  $Ra = 10^6$  ( $\Delta\Psi = 10$  for  $Pe = 10^3$ , and  $\Delta\Psi = 0.5$  otherwise).

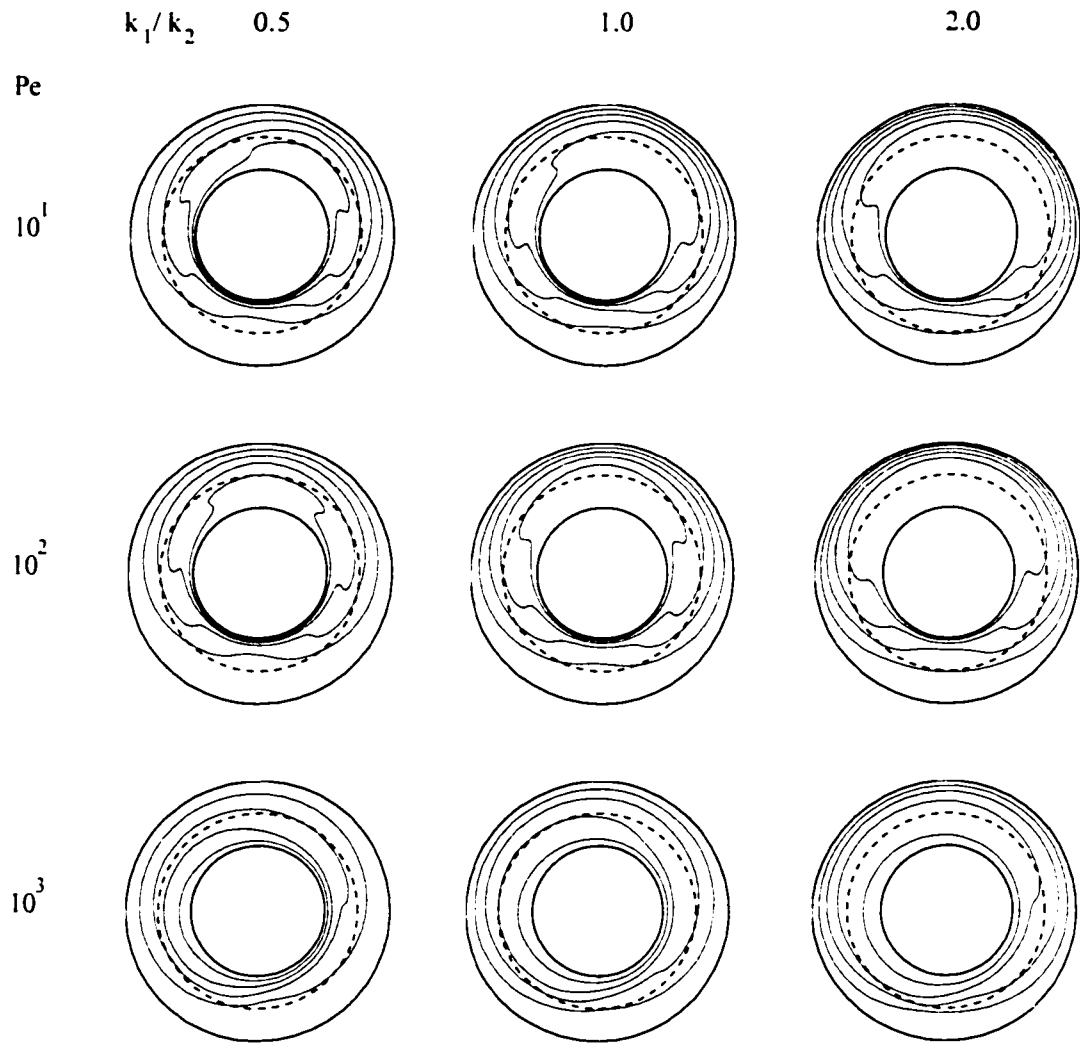


Figure 4.15 Temperature fields in concentric rotating cylinders with a porous sleeve for  $b = 1.5$ ,  $Da = 10^{-4}$ ,  $Pr = 20,000$ , and  $Ra = 10^6$  ( $\Delta\Theta = 0.2$ ).



of the annulus are more distorted. In these cases, buoyancy seems to completely offset the shear effect. When the rotational speed is smaller ( $Pe = 10$ ), the thermal plume arises from the inner cylinder but is slightly tilted to the right. As  $k_1/k_2$  increases, the thermal plume grows into a more noticeable mushroom like dome. As a result, a relatively large portion above the inner cylinder is at a higher temperature. On the other hand, if the flow field is dominated by shear effect ( $Pe = 10^3$ ), the thermal plume is hardly noticeable. Instead, the isotherms look like a family of eccentric circles with some of them bent near the interface. In general, the isotherms are more closely packed in the porous sleeve if  $k_1/k_2 > 1$ , but they are more spread out in the entire annulus if  $k_1/k_2 < 1$ .

The average Nusselt numbers on the inner cylinder, which is normalized by its conduction value, is shown in Figure 4.16. The normalized Nusselt number depends on both Rayleigh and Peclet numbers. When  $Ra \leq 10^3$ , it is found that the normalized Nusselt number remains unchanged (i.e., remains at unity). This means the conduction Nusselt number is the lowest limit for the average Nusselt number on the inner cylinder ( $\overline{Nu}_{cond} = 2.1640$ ) and the heat transfer mechanism is purely conduction. As the Rayleigh number increases, heat convection takes place around  $Ra = 10^4$ . The cases for which the Peclet number is zero correspond to purely natural convection. The average Nusselt number for these cases increases exponentially with the Rayleigh number. As the Peclet number increases, the shear flow tends to suppress heat convection such that the average Nusselt number decreases. As shown in the plot, the average Nusselt numbers for  $Pe = 0$  and  $Pe = 10$  are different only slightly because the flow fields at  $Pe = 10$  remains buoyancy dominant. When the Peclet number increases further, there is a great reduction in the average Nusselt number. Obviously, the onset of heat convection is

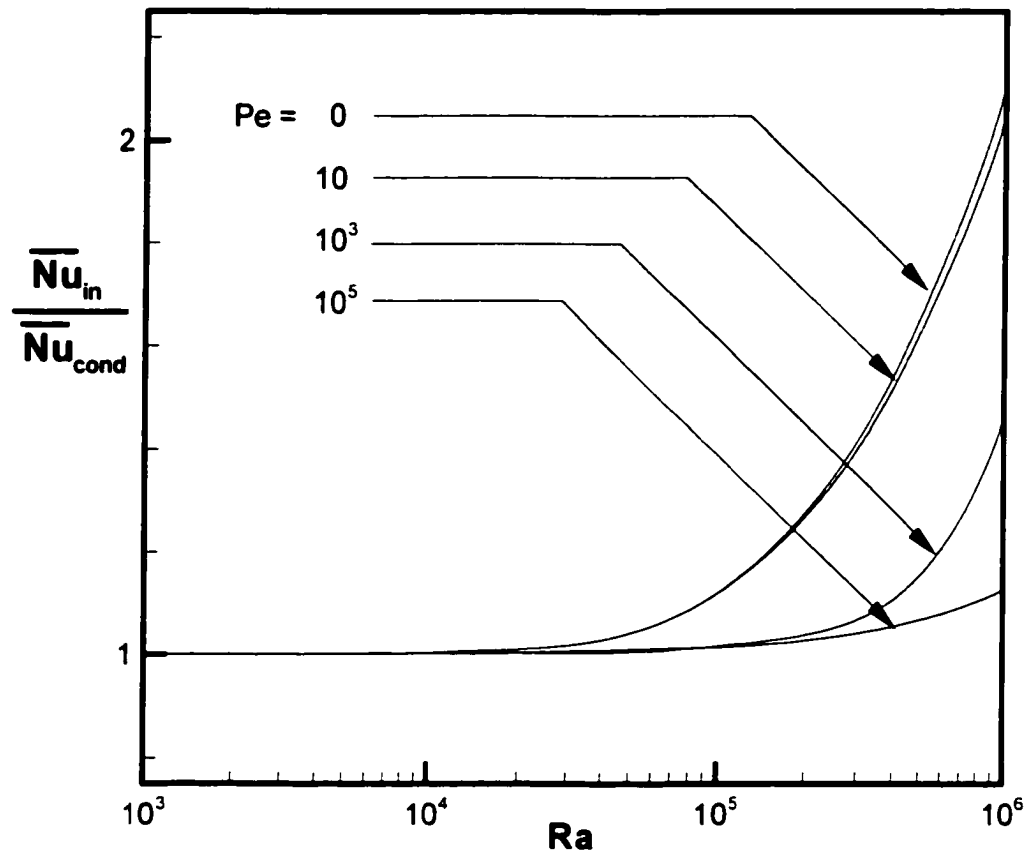


Figure 4.16 The dependence of average Nusselt number on Rayleigh and Peclet numbers for  $b = 1.5$ ,  $Da = 10^{-4}$ ,  $k_1/k_2 = 1$ , and  $Pr = 20,000$ .

shifted to a larger Rayleigh number when the Peclet number increases. Also noticed is that the average Nusselt number approaches the asymptotic value of heat conduction as the Peclet number continues to increase. In other words, heat conduction tends to be the main heat transfer mode for a porous journal bearing operating at a very high speed.

Figure 4.17 shows the dependence of the average Nusselt number on the Rayleigh number for various porous sleeve thicknesses. Consistent with Figure 4.16, the transition of heat transfer mechanism from forced convection to mixed convection and natural convection is apparent. For a fixed porous sleeve thickness, the normalized Nusselt number for  $Ra \leq 10^3$  remains unity. If the average Nusselt numbers were not normalized, one would find that they, as the Rayleigh number reduces, approach different constants that are proportional to the value of  $b$ . Recall from the definition of Nusselt number (Eq. (4.51)) that it is directly proportional to the value of  $b$ . Therefore, even if conduction is the only heat transfer mode, the Nusselt number is still dependent of the value of  $b$ . If the normalized Nusselt numbers is used, the confusion due to definition can be avoided. Clearly, the only effect the porous sleeve thickness has on the heat transfer performance is the onset of convection. The thinner the porous sleeve thickness (the larger the value of  $b$ ), the lower the critical Rayleigh number at which convection occurs. Moreover, the thicker the porous sleeve thickness, the steeper the rate of increase in the average Nusselt number in the natural convection regime.

Apparently, the average Nusselt number also depends on the Darcy number. In Figure 4.18, the normalized Nusselt numbers for four Darcy numbers are presented. The curve that corresponds to a Darcy number of  $10^0$  implies that the effect due to the presence of the porous sleeve is negligible and thus it marks the upper bound for the

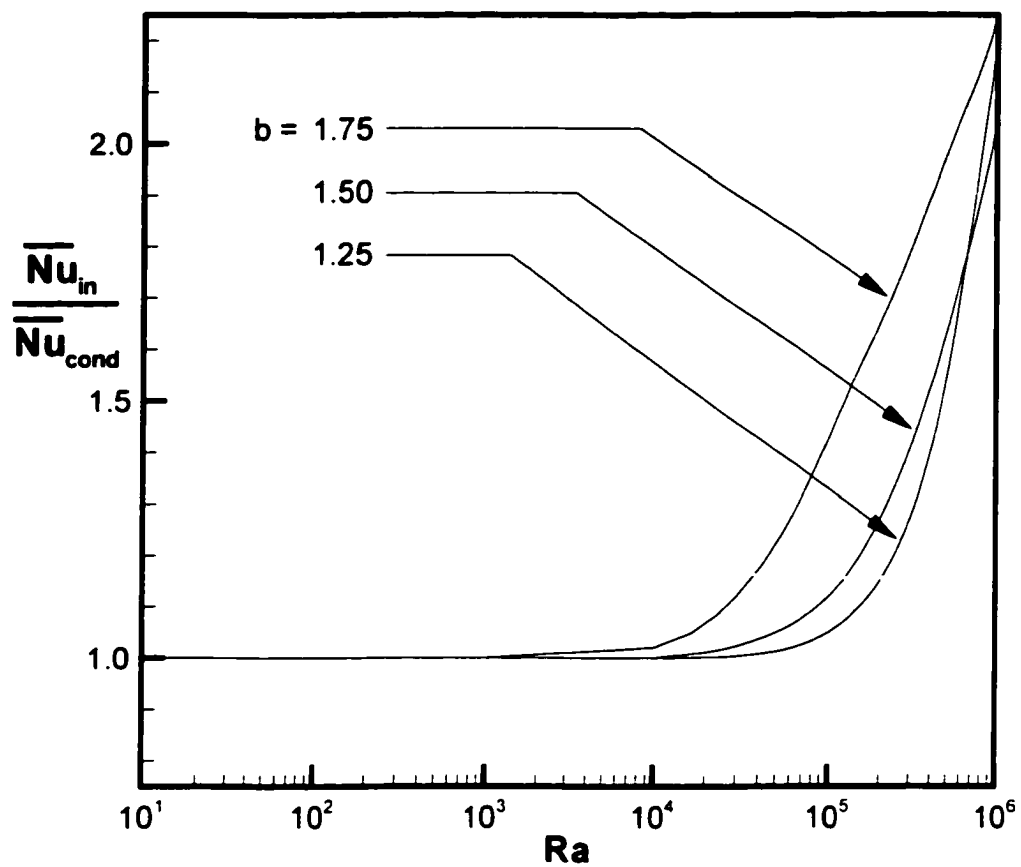


Figure 4.17 The dependence of average Nusselt number on Rayleigh number and  $b$  for  $Da = 10^{-4}$ ,  $k_1/k_2 = 1$ ,  $Pe = 10$ , and  $Pr = 20,000$ .

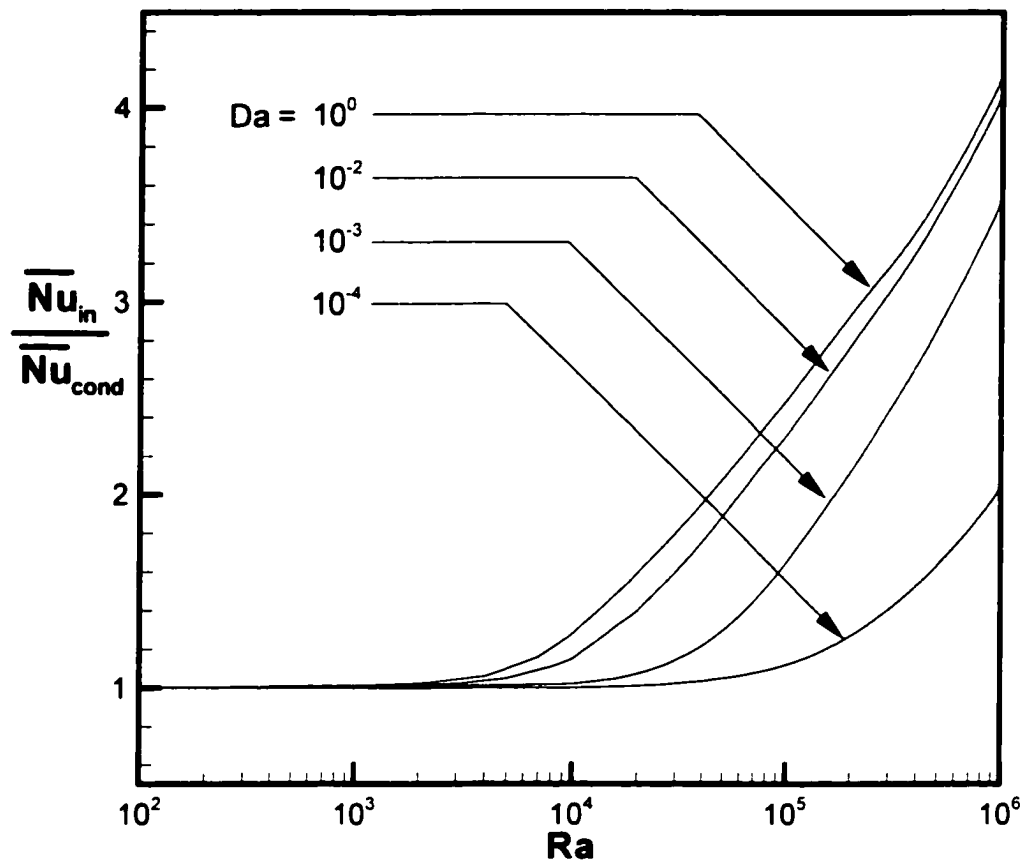


Figure 4.18 The dependence of average Nusselt number on Rayleigh and Darcy numbers for  $b = 1.5$ ,  $k_1/k_2 = 1$ ,  $Pe = 10$ , and  $Pr = 20,000$ .

average Nusselt numbers. Similar to the previous figures, the normalized Nusselt number is unity for  $Ra \leq 10^3$ . With the absence of the porous sleeve, onset of convection takes place as early as  $Ra = 2 \times 10^3$ . As the pore size in the porous sleeve reduces, the greater flow resistance delays the onset of convection. Eventually, the forced convection region extends to greater values of Rayleigh number.

For a fixed porous sleeve thickness, the average Nusselt number for  $Ra \leq 10^3$  is solely a function of  $k_1/k_2$ . In a pure conduction mode, according to Fourier's law, the temperature gradient is directly related to the thermal conductivity. For a given heat flux, thermal conductivity is inversely proportional to the temperature gradient. Hence, the asymptotic average Nusselt number is expected to follow the same trend. If the normalized Nusselt numbers are plotted, these asymptotic values will approach unity as shown in Figure 4.19. As the Rayleigh number increases, the heat transfer mode moves into the mixed convection regime. Also noticed is that a more conductive porous sleeve promotes the onset of convection. When the system is in the natural convection regime, it is observed that the average Nusselt number increases at almost the same rate for all values of  $k_1/k_2$ .

#### **4.7 Conclusions**

The present study has been successfully performed using a numerical approach. Extensive runs have been performed to study the effects of several governing parameters on the flow and temperature fields in rotating cylinders with a porous sleeve.

In general, the flow and temperature fields in the annulus can be clearly divided into two main categories, the buoyancy dominant regime and the shear dominant

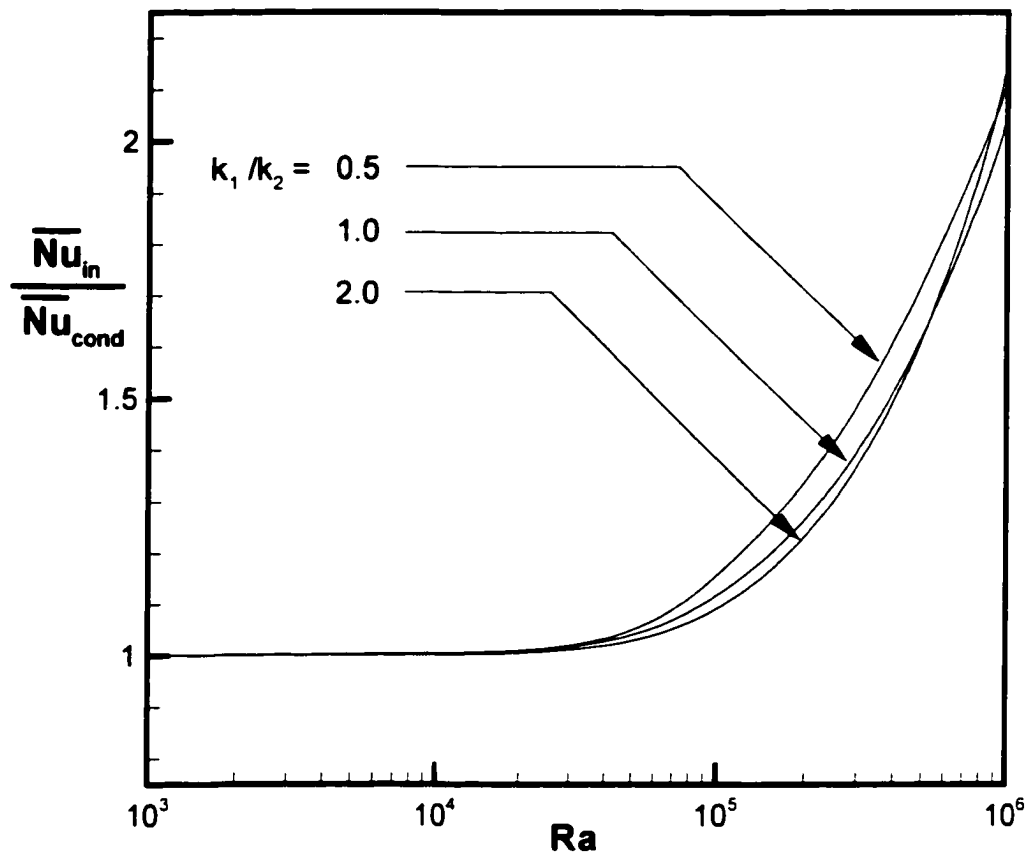


Figure 4.19 The dependence of average Nusselt number on Rayleigh number and thermal conductivity ratio for  $b = 1.5$ ,  $Da = 10^{-4}$ ,  $Pe = 10$ , and  $Pr = 20,000$ .

regime. If the system is dominated by buoyancy effect, there always exist two convective cells of almost equal strength on each side of the annulus. Similar to the results in the previous chapter, the strength of these cells increases with the Rayleigh number. When the Rayleigh number is relatively small, the convective cells are contained in the fluid layer. If the Rayleigh number is large, the convective cells will gain enough strength to penetrate the porous sleeve.

On the other hand, if the flow and temperature fields are shear dominant, there exists only a shear layer in the annulus. This shear layer is particularly strong in the fluid layer. As the Peclet number increases, both the strength and thickness of the shear layer increases accordingly. When the shear layer is thick, the convective cells diminish. It is interesting to note that the Rayleigh number does not have any significant effect on the shear layer in this flow regime. Based on this observation, one would expect a shear flow in a high-speed concentric porous bearing. Its flow field is barely influenced by the differential heating between the shaft and the housing. When the bearing is not in operation, some weak circulation due to the differential heating between the shaft and the housing is possible.

When the porous sleeve thickness is thin, the reduction in overall flow resistance leads to an increase in the flow strength. This eventually promotes heat convection. For a typical sintered journal bearing, the porous sleeve is usually very thin. Therefore, it is expected that convective cells are more readily to develop in the fluid layer. The development of these cells enhances the flow circulation in the bearing and thus the heat removal from the shaft through the bearing. As a result, a porous sleeve in a sintered journal bearing should be made as thin as possible within the design constraints.



Since the Darcy number represents the relative pore size in a porous sleeve, a small Darcy number implies that the flow resistance needs to be overcome for penetration to the porous sleeve is large. As shown in this study, the strength of the convective cells or the shear layer reduces tremendously when the Darcy number is small. For  $Da \leq 10^{-4}$ , it is found that heat conduction is the dominant heat transfer mechanism. In practice, a typical Darcy number for a sintered journal bearing is on the order of  $10^{-8}$ . Hence, the heat transfer mode is most likely heat conduction as long as the Darcy number is concerned. However, an absolute prediction is difficult based on this study because, for a practical sintered bearing, the porous sleeve is thin and less permeable. Since a thin porous sleeve promotes heat convection, but a low permeability demotes heat convection, the combined result of these two opposite effects needs further investigation.

As shown in the present study, the strength of the convective cells decreases with the thermal conductivity ratio while the strength of the shear flow increases with the thermal conductivity ratio. Typically, the thermal conductivity ratio of a bronze sintered journal bearing lubricated by SAE engine oil is on the order of  $10^{-3}$ . When the bearing is not in operation, it is expected that the thermal energy is mainly transferred through convection. If the bearing is under normal operation, especially when the shaft rotates at high speed, the flow field is mainly controlled by shear effect and thus the heat transfer mode changes to heat conduction.

The isotherms for temperature field at high Peclet numbers are generally concentric. This distribution of isotherms look very similar to that corresponds to a purely conduction case. This result is consistent with the heat transfer analysis. In terms of heat transfer results, it is found that the average Nusselt number deviates from that of

the natural convection and approaches that for pure conduction as the Peclet number increases. Also, it is noticed that the presence of a porous sleeve delays the onset of natural convection. These findings suggest that the heat transfer performance of a sintered journal bearing may be poor because the onset of heat convection is delayed and its heat transfer mode tends to be pure conduction.

## **CHAPTER FIVE**

### **FLOW VISUALIZATION USING A HELE-SHAW CELL**

#### **5.1 Introductory Remarks**

Throughout the years, a great deal of effort has been devoted to understanding the lubrication mechanism in sintered journal bearings. Aiming at obtaining a better design, many lubrication engineers have performed various experimental studies to improve the bearing performance by focusing on the shaft rotational speed, the pressure distribution in the bearings and its load capacity. In contrast, flow visualization in the bearings is rarely reported in literature.

To date, many experimental observations reported in the literature were commonly found inconsistent. In some instances, they even contradicted with each other leading to a state of confusion. This undesirable situation occurred because of the nature involved in the experiment of porous bearings. Besides the fact that all experiments are subject to human factors, experiments dealing with sintered bearings face an additional challenge in which identical sintered bearings are almost impossible to manufacture in the metallurgical process. Consequently, it is difficult to find quantitative agreement among experimental results especially from different research groups.

Flow visualization is favorable in many experimental studies in fluid mechanics because it provides a clear picture of the flow field and can lend support to results obtained from theoretical and numerical studies. Yang (1989, 1994) has compiled some of the most common flow visualization techniques with or without the help of computer

facilities. Unfortunately, flow visualization experiment in porous journal bearings is rather scarce. One of the difficulties the lubrication engineers face is to visualize the flow patterns in a porous bushing without affecting the operation of bearing itself. On top of this, to visualize the flow within the porous sleeves without the obstruction of porous material is almost impossible or too costly to perform.

The earliest flow visualization study related to porous bearings was done more than twenty years ago. Using optical interferometry, Yung and Cameron (1979) visualized the lubrication of porous bearings. However, their findings were against the existence of a continuous oil film in the bearing. Later, Braun (1982) observed that the porous journal bearings, after a short time of operation, were filled partially by air causing the hydrodynamic lubrication to break down.

To verify the results reported by Yung and Cameron (1979) as well as Braun (1982), Kaneko and Obara (1990) visualized the mechanism of lubrication in porous journal bearings using fluorescent-dyed oil. Based on the pictures they took through the windows on the journal housing, they confirmed the existence of an oil circulation through the porous matrix. Although their study was a great success, their pictures only showed the growth of dyed oil in the windows. Their study couldn't show the complete flow interactions between the fluid and porous layers. This shortcoming of their experiment has motivated the current experimental study with the goal to fully understand the fluid flow within the annular space and the porous sleeve.

## 5.2 Hele-Shaw Analogy

One of the difficulties in the study of flow in porous media is to actually visualize the flow pattern within the medium. In fact, visualizing the flow pattern in a porous medium is more challenging than that in a fluid layer because the presence of the porous structure blocks the view of the flow pattern. For this reason, a direct visualization of the flow in porous media is almost impossible. As such, various analogies have been developed and used successfully to visualize the flow pattern in a porous medium. There are several techniques that enable the study of flow in a porous medium. The popular ones include the Sand Box Analogy, the Electric Analogy, the Membrane Analogy, and the Hele-Shaw Analogy (Bear, 1972). Among these analogies, the Hele-Shaw Analogy is found to be most appropriate for the current study.

In the early last century, Henry S. Hele-Shaw, an English engineer, discovered the analogy that could be used to model the flows important to the applications in petroleum and chemical industry. The main advantage of his model is that it is very simple in design and thus relatively inexpensive to build. A Hele-Shaw cell is constructed by placing two parallel plates very close to each other separated by a gap of thickness  $h$  to render visible streamlines of a two-dimensional potential flow (Hele-Shaw 1898a, 1898b; Hele-Shaw and Hay 1900). In this analogy, the Hele-Shaw cell is filled with a fluid of known viscosity to enable the modeling of flows in porous media. The flow occurs within the cell is known as a Hele-Shaw flow. In this analogy, the gap width between the two parallel plates is related to the permeability of the porous medium to be simulated. With this method, the flow in porous media is analogous to a two-dimensional flow in a very thin layer.

Saffman and Taylor (1958) recognized the value of this analogy and used this approach to perform theoretical and experimental investigations to understand the stability of the interface between two immiscible viscous fluids in a porous medium under the gravitational effect. Recently, McCloud and Maher (1996) experimentally studied the steady-state Saffman-Taylor flow in an anisotropic Hele-Shaw cell.

Wooding (1960) employed the concept of Hele-Shaw analogy to examine the instability of a viscous liquid of variable density in a long vertical channel of a rectangular cross-section. He also analyzed the problem through theoretical means and found that the experimental results were slightly higher than those obtained using the asymptotic expansion and the simple approximate theory.

Bear et al. (1968) and Van Dyke (1982) have made use of Hele-Shaw cells to study low velocity flows around bodies and the hydrodynamics of beds while Elder (1965), Horne and O'Sullivan (1974), Williams et al. (1974), and Hartline and Lister (1977) have made use of them to model thermal convection in porous media. Bychkov (1980, 1981) investigated more practical industrial applications by optimizing the geometry of internal channels and pipeline accessories using the flow in thin fluid layers.

Koster and Muller have performed a series of studies related to flow visualization using the Hele-Shaw analogy and holographic real-time interferometry. They divided the Hele-Shaw box into two categories based on its geometry (i.e., its height ( $l$ ) and width ( $w$ )). If  $l/w \ll 1$ , the box is named the Hele-Shaw cell while it is referred to as the Hele-Shaw slot if  $l/w > 1$ . They have considered both the Hele-Shaw slots (1980, 1981, and 1984) and Hele-Shaw cells of different dimensions (1982, 1983). They visualized natural convection flows in both vertical and horizontal Hele-Shaw cells induced by a heated

plate at the bottom (1983). The fluids used were 3 cSt silicone oil and water. In addition, Koster (1983) discussed the temperature-dependent reflective index and the so-called “thermal memory” of Plexiglas. He also pointed out the advantages and disadvantages of the visualization technique he employed.

Nakoryakov et al. (1991) proposed a two-dimensional model of the flow in a Hele-Shaw cell, taking into account the convective terms in the momentum equations. The results of laser Doppler velocity measurements and flow visualization with submerged jet and flow around a cylinder in a Hele-Shaw cell were reported. A suspension of aluminum particles in spirit solution was added to the water for visualization.

The Hele-Shaw cell was also modified to study the bubble behavior in a fluid under a magnetic field. Ishimoto et al. (1995) employed an ultrasonic wave echo and image processing technique to visualize the translational motion and deformation of a single gas bubble in magnetic fluid.

Carrillo et al. (1996) considered a modified classical viscous fingering problem in a circular Hele-Shaw cell consisting of a controlled rotation of the cell around its vertical axis. With this modification, the instability can be driven by both the density difference and the viscosity contrast between the two fluids. Their experiments in a rotating cell laid the foundation of an analogy to be used for gravity-driven experiments in the channel geometry.

### 5.3 Problem Statement

The objective of this work is to experimentally visualize the flow patterns in a porous journal bearing using Hele-Shaw analogy. The enclosure has two different gap widths, the one with a wider gap simulates the fluid layer while the narrower one simulates the porous layer. The beauty of this Hele-Shaw analogy is that no porous medium is actually needed to simulate the porous layer. Thus, better visual results can be expected. Flow fields will be visualized for several cases when the shaft is oriented vertically. Using tracing particles, the flow patterns can be visualized through time-elapse photography.

### 5.4 Theory of Hele-Shaw Analogy

The Hele-Shaw analogy that is used to simulate the flow in porous media can actually be derived through mathematical means. For a steady highly viscous flow in a Hele-Shaw cell, the Navier-Stoke equations reduce to

$$\rho g_x - \frac{\partial p}{\partial x} + \mu \left( \frac{\partial^2 u_x}{\partial x^2} + \frac{\partial^2 u_x}{\partial y^2} + \frac{\partial^2 u_x}{\partial z^2} \right) = 0, \text{ and} \quad (5.1)$$

$$\rho g_y - \frac{\partial p}{\partial y} + \mu \left( \frac{\partial^2 u_y}{\partial x^2} + \frac{\partial^2 u_y}{\partial y^2} + \frac{\partial^2 u_y}{\partial z^2} \right) = 0. \quad (5.2)$$

Since the gap in a Hele-Shaw cell is very small, the second derivatives of velocity components with respect to  $x$  and  $y$  are significantly smaller than those with respect to  $z$ . In the absence of body forces, Eqs. (5.1) and (5.2) are simplified to give

$$\frac{\partial p}{\partial x} = \mu \frac{\partial^2 u_x}{\partial z^2}, \text{ and} \quad (5.3)$$



$$\frac{\partial p}{\partial y} = \mu \frac{\partial^2 u_x}{\partial z^2}. \quad (5.4)$$

Integrating the above equations twice and applying the no-slip boundary condition at walls,  $z = h/2$  and  $z = -h/2$  (Figure 5.1), one yields

$$u_x = \frac{h^2}{8\mu} \frac{\partial p}{\partial x} \left[ \left( \frac{2z}{h} \right)^2 - 1 \right], \text{ and} \quad (5.5)$$

$$u_y = \frac{h^2}{8\mu} \frac{\partial p}{\partial y} \left[ \left( \frac{2z}{h} \right)^2 - 1 \right]. \quad (5.6)$$

The average velocities in the cell can be evaluated by

$$\bar{u}_x = \frac{1}{h} \int_{-\frac{h}{2}}^{\frac{h}{2}} u_x \, dz, \text{ and} \quad (5.7)$$

$$\bar{u}_y = \frac{1}{h} \int_{-\frac{h}{2}}^{\frac{h}{2}} u_y \, dz, \quad (5.8)$$

which lead to the expressions given below,

$$\bar{u}_x = -\frac{h^2}{12\mu} \frac{\partial p}{\partial x}, \text{ and} \quad (5.9)$$

$$\bar{u}_y = -\frac{h^2}{12\mu} \frac{\partial p}{\partial y}. \quad (5.10)$$

According to Darcy's law, the bulk velocities are given by

$$\bar{u}_x = -\frac{K}{\mu} \frac{\partial p}{\partial x}, \text{ and} \quad (5.11)$$

$$\bar{u}_y = -\frac{K}{\mu} \frac{\partial p}{\partial y}. \quad (5.12)$$

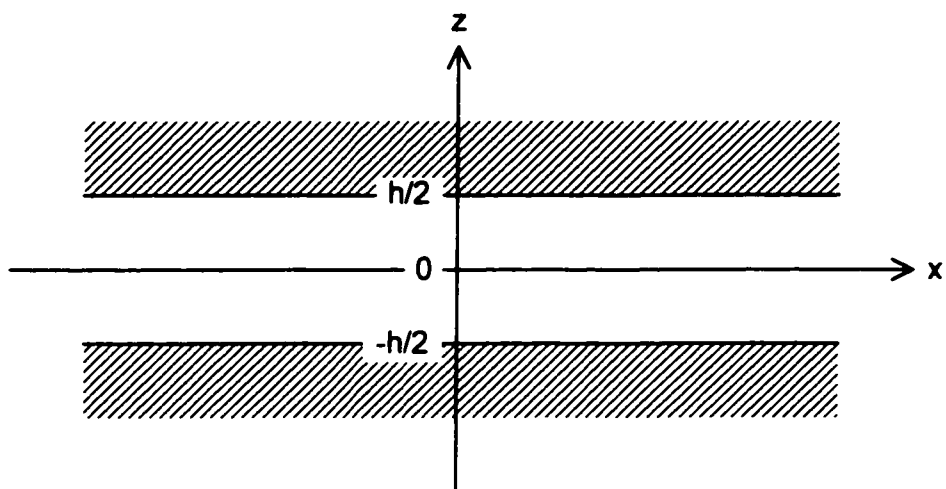


Figure 5.1 Coordinate system used in the derivation of Hele-Shaw analogy.

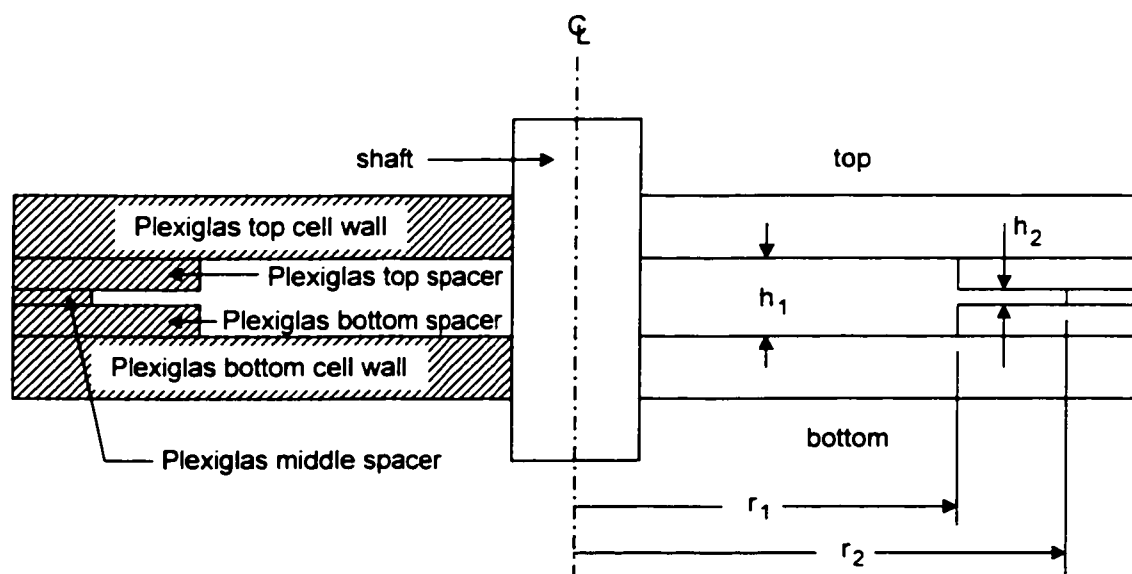


Figure 5.2 Cross-section of the modified Hele-Shaw cell constructed for the current experiment.

Recognize that Eqs. (5.11) and (5.12) are similar in form with Eqs. (5.9) and (5.10). Apparently, there is a direct correspondence between a two-dimensional flow in the Hele-Shaw cell and the flow in a porous medium if the gap width  $h$  in the Hele-Shaw cell is carefully chosen such that it is related to the permeability  $K$  given in Eqs. (5.11) and (5.12) in the following fashion.

$$h = \sqrt{12K} . \quad (5.13)$$

Using the Hele-Shaw analogy, the porous sleeve in a journal bearing can be represented by a channel with a very narrow gap. As shown in Figure 5.2, the Hele-Shaw cell for the present study has two cross-sections of different gap width, where the wider one ( $h_1$ ) represents the fluid layer and the narrower one ( $h_2$ ) simulates the porous sleeve. A practical value for the permeability  $K$  of a porous sleeve can be as small as  $10^{-8} \text{ m}^2$ . From Eq. (5.13), the corresponding gap width in a Hele-Shaw cell is calculated to be on the order of  $1 \text{ mm}$ . After the cell is constructed, it is filled with silicone oil and suspended with tracing particles. When the shaft rotates, a shear flow is induced in the cell. As the silicone oil circulates in the cell, it carries the tracing particles with it which makes the flow visualization possible through time-elapse photography.

## 5.5 Experimental Setup

The experimental apparatus has four major units, namely the cell, the reservoir, the rotor, and the imaging unit. Figure 5.3 shows the schematics of the experimental setup whereas Table 5.1 lists the components and their specifications.

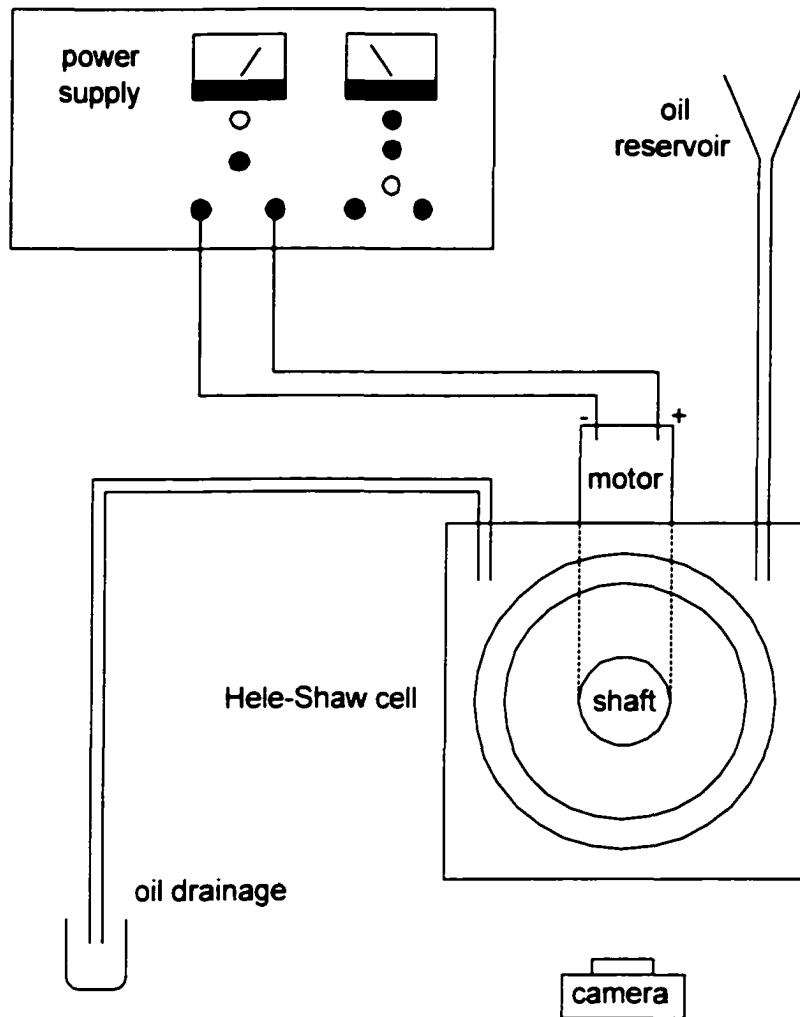


Figure 5.3 Sketch of the experimental setup for flow visualization.

**Table 5.1 List of the components of the experimental apparatus and their specifications.**

Item	Specification / Manufacturer	Unit
Hele-Shaw Cell	Five Plexiglas of different dimensions, as shown in Figure 5.2, glued together by Ace clear 100% silicone sealant (Item # 11316), tightened with Midwest Fastener Corp. stainless steel 6-32x2 Phillips pan machine screws (Item # 07097), 6-32 finished hex nuts (Item # 05265), and Flat washers (Item # 05320).	Cell
Seals	Two 1-7/8 ID x 2-1/16 OD c/s 3/32 washers Flanco Gasket and Manuf., Inc. (Item # 2-134-70)	Cell
Lubricants	Fisher silicone oil (Item # S159-500)	Cell
Tracer	Jones Tones, Inc. craft glitter (Item # CHG – 308 Silver)	Cell
Funnel	One Flotool spill saver (Item # 3220010701)	Reservoir
Tubing	One 1-3/8 ID x 1/2 OD vinyl tube Two 5-1/4 ID x 3/8 OD vinyl tube	Reservoir
Valve	One Assembles in Motion ball valve (Item # SGL-0500-T)	Reservoir
Shaft	One 1.95" diameter stainless steel shaft	Rotor
Couplings	One Dayton 1/2 ID x 1-1/8 OD x 2-1/2 flexible shaft couplings (Item # 2X497)	Rotor
Motor	One DeWalt 18 Volt DC gear motor (Item # 393111-01)	Rotor
Gear system	One DeWalt transmission box (Item # 380264-08)	Rotor
Power supply	Trilectron Industries power supply (PP-2309 c/u; serial # 4162-115AA) Input: 115/220V, 50/60Hz, 1PH, 10/5A Output: 2-36 VDC, 0-15 Amp.	Rotor
Wiring	Two 2' long 12-gauge Radio Shack hookup wire 600V, 80C, 1/32 PVC, stranded, type: AWM (Item # 278-565) Four 1-3/8 Radio Shack test clips Solder terminals, rated 3 Amp (Item # 270-1545)	Rotor
Camera	One Minolta Maxxum 7000i autofocus SLR	Imaging
Tripod	Samsonite	Imaging
Films	Kodak black & white 24x400 35mm films	Imaging

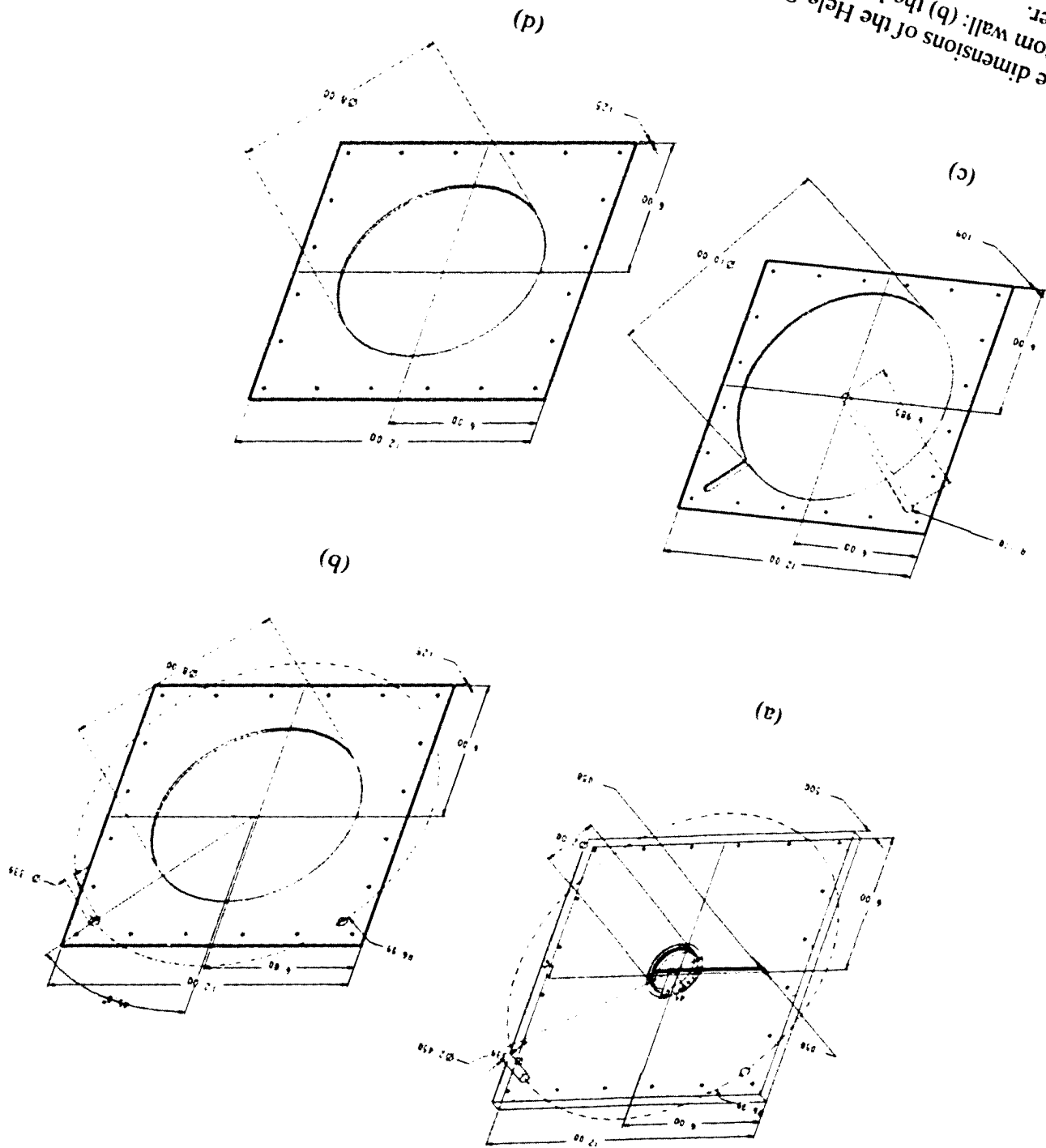
### 5.5.1 The Cell Unit

For the present study, the conventional Hele-Shaw cell is modified to meet the special need of the present study. A conventional Hele-Shaw cell consists of several walls, two of which are placed very close to each other to simulate the flow in a porous medium. Because of the presence of the fluid layer, two distinctive gaps must be incorporated in the present model. To achieve this, the Hele-Shaw cell was constructed using two 1/2", two 1/4", and a 7/64" thick Plexiglas plates cut into proper dimensions. The 7/64" thick Plexiglas plate served as a spacer in the Hele-Shaw cell to represent the porous sleeve whereas the two 1/4" thick Plexiglas plates were the spacers to represent the fluid layer.

Unlike the conventional Hele-Shaw cell that has no moving part, a shaft is included in the present model to produce a shear flow in the fluid layer. To facilitate the experiment, a stainless steel shaft was custom-made to run perpendicular through the cell. To prevent leakage, precise o-rings were used to seal the gaps between the shaft and the walls. To enable the visualization of the flow patterns, transparent Plexiglas plates were chosen for the cell walls. A black cardboard was attached to the back of the cell to enhance the visibility of the tracing particles and better improve the visual effects.

Figure 5.4 shows the dimensions of the Plexiglas plates and stainless steel shaft. Additional dimensions are shown in Figure 5.4(a) and (e) for the grooves where the o-rings sit. With this setup,  $h = 1.8''$ , the corresponding permeability is  $K = 6.505 \times 10^{-7} m^2$ . Before these five plates were assembled together with 20 bolts, a thin layer of silicone glue was applied around the edges of all plates to further prevent leakage. These through

Figure 5.4  
The dimensions of the Hele-Shaw cell and the shaft (in inches) (a) the bottom wall; (b) the bottom spacer; (c) the middle spacer; and (d) the top spacer.



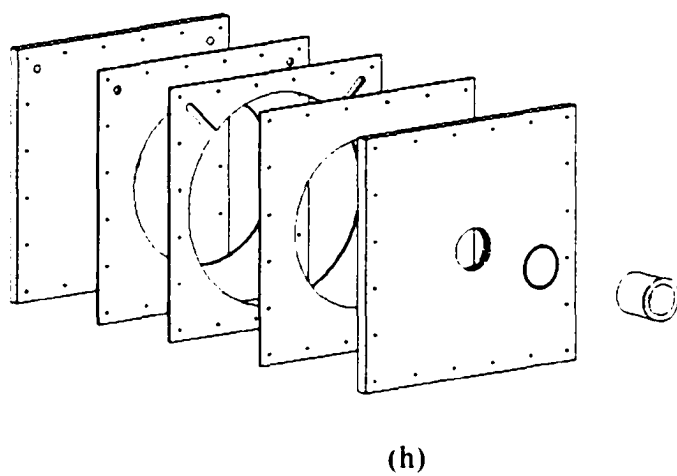
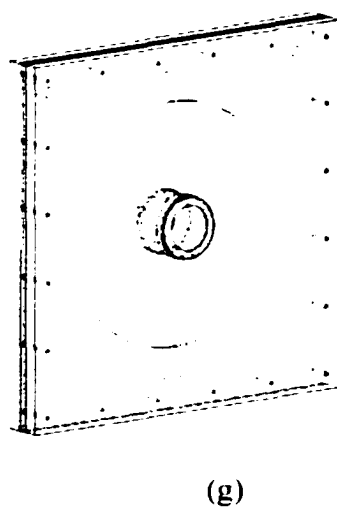
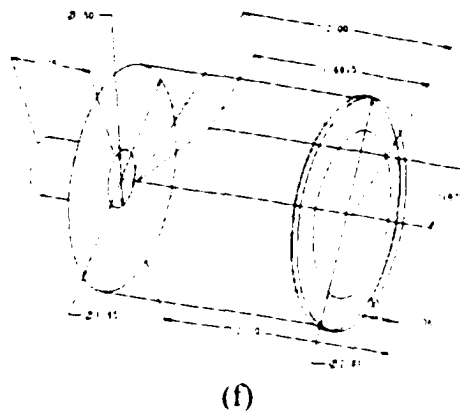
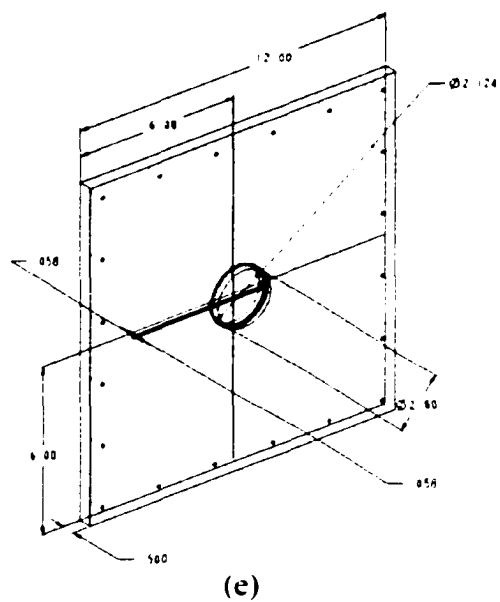


Figure 5.4 continued. (e) the top wall, (f) the shaft, (g) the assembled cell, and (h) the extended cell.



holes have a diameter of  $7/32$ " and are 2.2" apart from each other and 0.5" away from all edges.

### **5.5.2 The Reservoir Unit**

The reservoir unit was built to feed the silicone oil with suspended tracing particles into the cell unit. In this unit, silicone oil is poured into a funnel that is connected to the Hele-Shaw cell with tubing. A valve is used to regulate the flow rate into the cell. By the same token, both the cell and the reservoir can be drained easily by a hydrostatic head due to elevation when the valve is opened.

### **5.5.3 The Rotor Unit**

The rotor unit consisted of a custom-made shaft, a flexible coupling, a transmission box, a gear motor, a power supply, and wiring. This was the only unit in this experiment setup that had moving parts. The power supply converts A.C. to D.C. and regulates the power output to the gear motor to produce various rotational speeds. A transmission box was utilized to increase the power output of the motor. Instead of a solid coupling, a flexible coupling was preferred here so that a slight misalignment between the rotor and the cell could be tolerated. The stainless steel shaft was custom-made in the Machine Shop of the School of Aerospace and Mechanical Engineering. To reduce the dynamic friction between the shaft and the o-rings, the shaft was made partially hollow. The dimensions of the shaft are shown in Figure 5.4(f).

#### **5.5.4 The Imaging Unit**

To visualize the flow patterns, a camera aiming at the cell is securely attached to a tripod. Two light sources are provided on either side of the setup. Black and white films were used in this case. An SLR camera is chosen for this experiment because it allows greater flexibility in the art of photography. The important adjustable factors to produce the best pictures were the aperture size, the shutter speed, and the exposure time of the camera.

### **5.6 Experimental Procedure**

Prior to running the experiment, it is necessary to assemble the model, calibrate the power supply, and test the camera settings. Only after the above preparation was completed, the flow patterns in the cell was visualized and documented by means of a camera.

#### **5.6.1 Model Assembly**

A thin layer of clear Silicone Sealant was first applied on the Plexiglas plates evenly. Later, bolts, washers, and nuts were fastened to apply uniform pressure on the plates to ensure that the cell was completely sealed off. The cell was then left overnight to cure. Once the cell was ready, two rubber o-rings were inserted into the groove in the holes of the outermost plates. A drop of clean silicone oil was applied to the o-rings so that they could seal the cell better. The rotor assembly was put together with its shaft inserted into the cell. Then, both the cell and the rotor assembly were safely secured to a

frame with predrilled holes to align the cell and the rotor assembly within a acceptable tolerance.

The reservoir unit was assembled and tubing was hooked up in sequence. Silicone oil was premixed with a small amount of particle tracers (in this case, glitter) in a beaker. Then, the silicone oil with suspended tracers was poured into the funnel at a proper height. Slowly, the ball valve was opened to feed the silicone oil in the funnel to the cell. Once, the oil filled up the entire cell, the valve was closed. Extra care was taken to remove any undesirable air bubbles trapped inside the cell. The cell was then thoroughly checked for leakage. Figure 5.5 shows a picture of the complete setup of this experiment.

### **5.6.2 Calibration of Rotational Speed**

To calibrate the rotational speed, an rpm gauge (Shimpo DT-105 Hand Digital Tachometer) was used to measure the rotational speed as a function of the current output from the power supply. The calibration curve is shown in Figure 5.6. Notice that the curve is only valid for currents in the range between  $6.5\text{ A}$  and  $10.5\text{ A}$ . When the electric current was close to or less than  $6.5\text{ A}$ , the motor would not run because the power was too low to overcome the static friction between the shaft and the o-rings. Also, running the motor beyond  $10\text{ A}$  was very unstable. The current fluctuated vigorously causing the motor to spin at unsteady rotational speeds. A further increase in the current eventually shuts down the operation of the motor. Based on the calibration curve, a specific current output from the power supply can drive the motor to a specific rotational speed. Using a

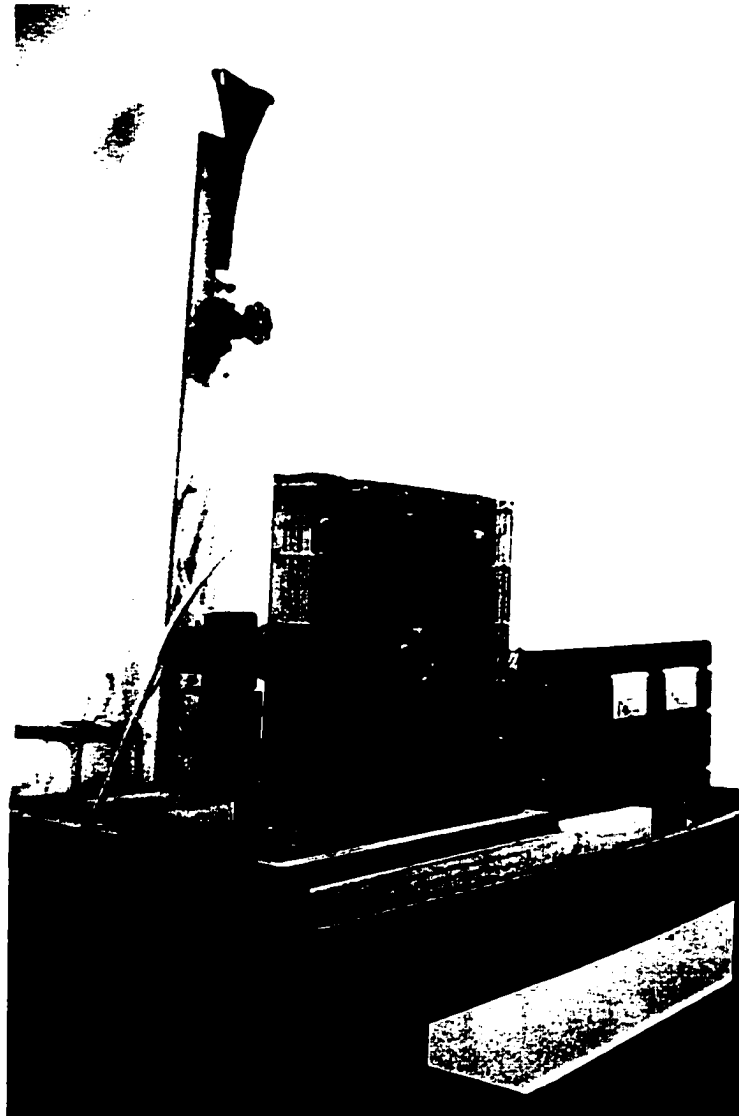


Figure 5.5 Photograph of the modified Hele-Shaw cell.

second degree polynomial curve fit, it was determined that the rotational speed could be estimated by

$$\omega = 5.2717 I^2 - 18.323 I - 19.47. \quad (5.14)$$

The above correlation yields a correlation coefficient  $R^2$  value of  $0.9891$ . From either Eq. (5.14) or Figure 5.6, any desirable rotational speed of the shaft can be readily obtained by adjusting the current output from the power supply.

### 5.6.3 Adjustment of Camera Settings

An autofocus SLR camera was chosen over a fully automatic digital camera for this experiment because an SLR camera provides more control for the photo takings. Lightings were placed at the most appropriate locations. Trials for different combinations of aperture sizes, shutter speeds, and degrees of exposure were performed to ensure the best quality of images.

### 5.6.4 Flow Visualization

After everything was finely tuned, the rotor assembly was switched on. When switching on the power supply, the current output was always turned to the minimum to avoid overrunning the motor with excessive electrical power. Right after the power supply was switched on, the current output was gradually turned to approximately  $9\text{ A}$ . Because of the high static friction, the shaft was manually turned initially. As soon as the shaft started to rotate, the current output displayed on the power supply quickly dropped to  $6.5\text{ A}$ . Normally, reducing the current output below this threshold value would cause the motor to halt. The current output was then gradually increased which led to an

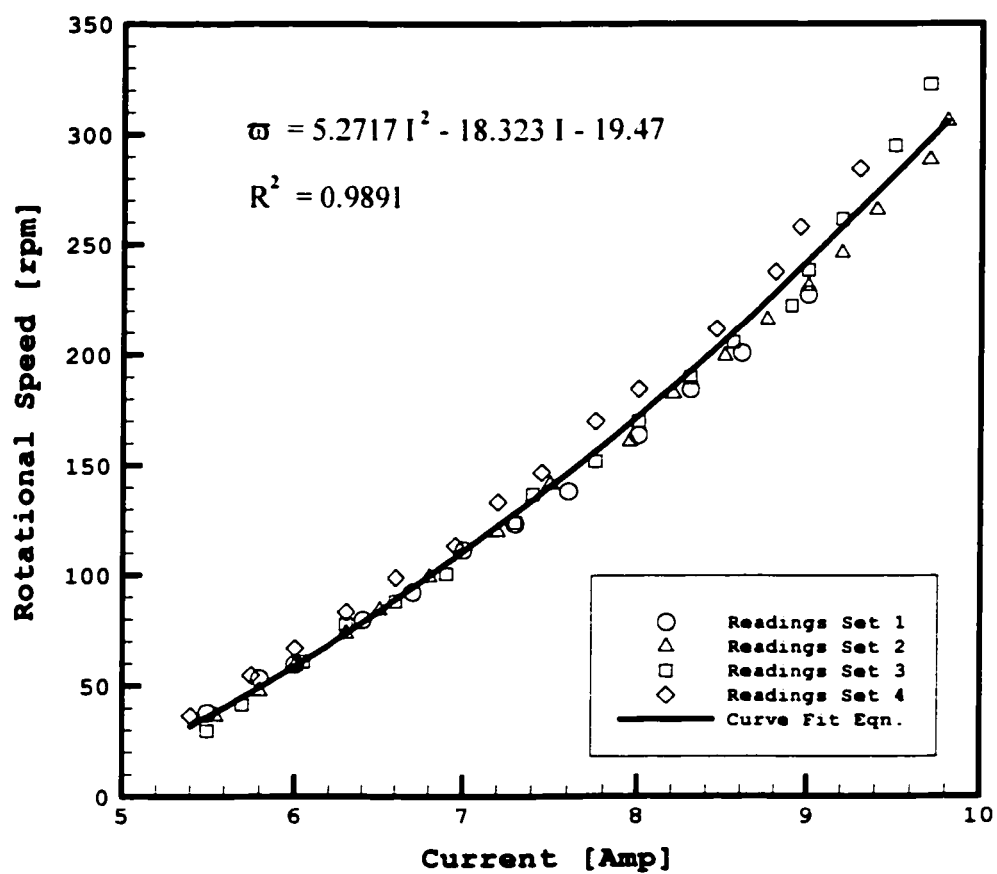


Figure 5.6 Calibration curve of the rotational speed as a function of the electric current from the power supply.

increase in the shaft rotational speed. Referring to the calibration curve, the shaft rotating speed was fixed for a specific current output. After the desirable rotational speed was reached, pictures were taken with sufficient exposure time so that the path lines of tracing particles could be captured.

It was found that the temperature of the shaft rised if the shaft rotated more than 5 minutes. The rate of temperature rise increased tremendously especially when the shaft rotational speed was high. It is believed that this increase in shaft temperature is mainly due to the friction between the shaft and the o-rings. After a long period of operation about an hour, the temperature of the shaft could reach as high as  $34.3 \pm 1.2$  °C while its initial temperature was  $21.4 \pm 0.1$  °C.

## **5.7 Results and Discussion**

Figure 5.7 shows the comparison of the flow patterns obtained from experimental and numerical studies. This is a relatively isothermal case. Experimentally, this case is more difficult to accomplish than any other cases. To obtain the result, one must try every effort to minimize the heat generation from the shaft. Generally, the amount of heat generated is mainly proportional to how fast the shaft rotates and how long the shaft has operated. In this case, a low rotational speed was preferred over a higher speed because it generates less heat from the friction between the shaft and the o-rings. Specifically, the shaft rotational speed was  $60 \pm 9$  rpm from measurement. The picture was taken as soon as the flow pattern became quasi-steady, i.e., as soon as the flow pattern did not change significantly. Typically, this had to be done about 3 minutes after the start of operation. After the power supply was switched off, temperatures were

measured at different locations of the shaft. They were in the range between  $24.6 \pm 0.1$  °C to  $24.8 \pm 0.1$  °C. The temperature of the silicone oil was measured to be  $24.5 \pm 0.1$  °C. Based on these temperature measurements, the heating due to friction between the shaft and the o-rings was proven negligible.

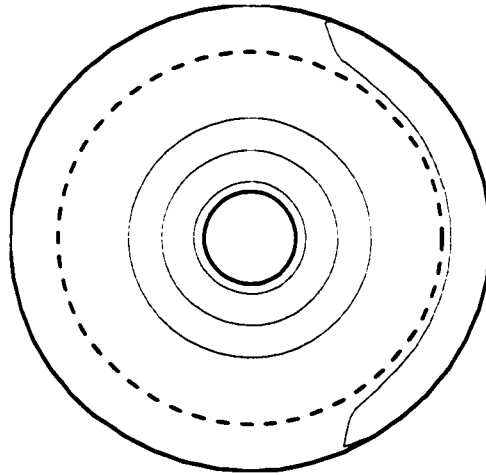
Figure 5.7(a) shows that the flow field was relatively isothermal. Only a ring of shear flow appeared directly next to the rotating shaft. Away from this shear layer, the fluid in other parts of the cell was nearly motionless. For comparison, a numerical run was performed with equivalent  $Pe = 233,100$  and  $Ra = 1,469,000$ . These values were determined using the mechanical and thermal properties listed in Table 5.2. Table 5.3 provides some typical values of the Peclet and Rayleigh numbers based on the values listed in Table 5.2. The flow field obtained through numerical simulation is shown in Figure 5.7(b). Clearly, the flow structure in the annulus is similar to that from experiment. According to the numerical result, there is a very weak recirculation cell at the right hand side of the porous sleeve. However, its existence could not be verified from experiment because of its extremely weak strength.

A non-isothermal case was also considered. The comparison of experimental and numerical results is presented in Figure 5.8. In this case, the shaft rotated at  $39\text{ rpm}$ . Its flow pattern is shown in Figure 5.8(a). Because of the buoyancy effect, there was a jet of fluid issuing radially outward from the shaft. Also, because of the shear effect, this jet was tilted to the left. Figure 5.8(b) shows a similar flow pattern obtained through numerical simulation. This pattern corresponds to  $Pe = 10^3$  and  $Ra = 10^6$ . Both approaches predict two weak convective cells and a strong shear flow. The shear flow is so strong that the buoyancy-induced flow is swept away from inner cylinder in the





(a)



(b)

Figure 5.7 Comparison of isothermal flow fields between (a) experimental observation at a rotational speed of  $\omega = 60 \text{ rpm}$ , and (b) numerical result at  $Pe = 2.33 \times 10^5$  and  $Ra = 0$  ( $\Delta\Psi = 5 \times 10^4$ ).

Table 5.2 List of mechanical and thermal properties used in the experiment.

Properties	Values
Density of silicone oil at (20 °C), $\rho$	$963 \text{ kg/m}^3$ <sup>[*1]</sup> ; $(962 \pm 0) \text{ kg/m}^3$ <sup>[*3]</sup>
Thermal diffusivity of silicone oil at (20 °C), $\alpha$	$7 \times 10^{-8} \text{ m}^2/\text{s}$ <sup>[*2]</sup>
Thermal conductivity of silicone oil at (20 °C), $k$	$0.1 \text{ W/m } ^\circ\text{C}$ <sup>[*2]</sup>
Volumetric heat capacity of silicone oil at (20 °C), $C_p$	$1.37 \times 10^6 \text{ J/m}^3$ <sup>[*2]</sup>
Dynamic viscosity of silicone oil, $\mu$	$(48.35 \pm 1.23) \text{ cP}$ <sup>[*3]</sup>
Kinematic viscosity of silicone oil, $\nu$	$(50.26 \pm 1.28) \times 10^{-4} \text{ m}^2/\text{s}$ <sup>[*3]</sup>
Coefficient of Thermal Expansion, $\beta$	$0.00104 \text{ } ^\circ\text{C}^{-1}$ <sup>[*4]</sup>

Ref: <sup>[\*1]</sup> <https://fscimage.fishersci.com/msds/40237.htm>

<sup>[\*2]</sup> <http://www.hukseflux.com/thermal%20conductivity/thermal.htm>

<sup>[\*3]</sup> based on experimental measurements:

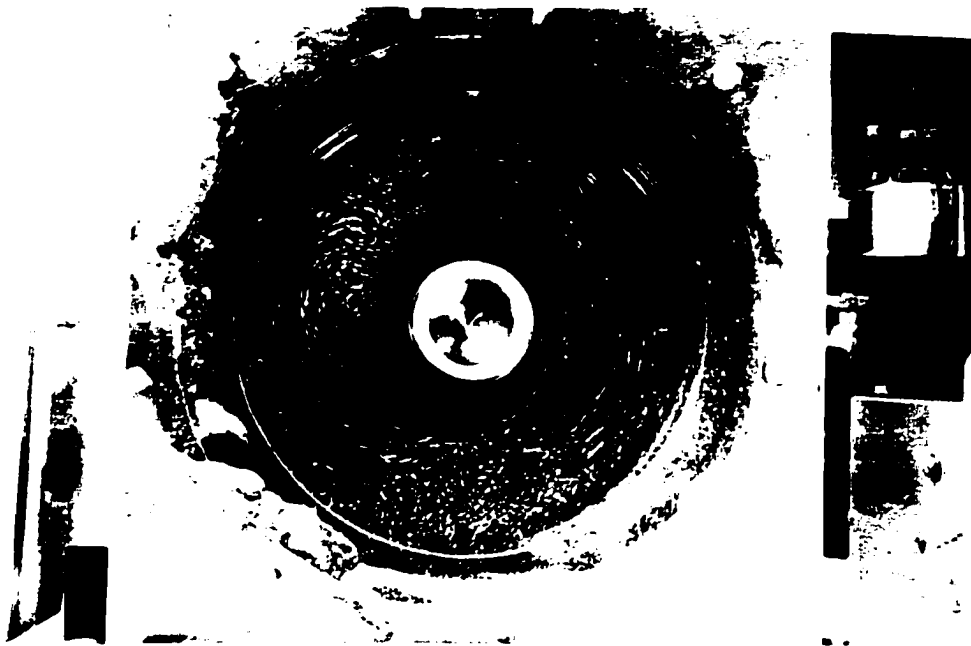
density measurement: Fisher brand Hydrometer (Catalog # 11-583 B)

viscosity measurement: Cole-Parmer 98936 Series Rotational Viscometer  
(with 95% confidence)

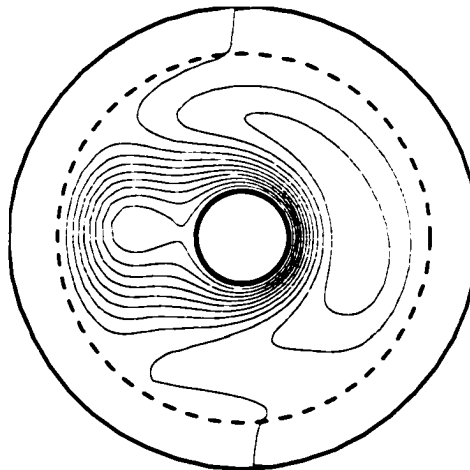
<sup>[\*4]</sup> conversation with technical support from Fisher Scientific Co.

Table 5.3 List of parameters and their corresponding values in experiment.

Tabulated Equivalent Parameters		Values
Permeability, $K = h^2/12$	$h = 0.11 \text{ in}$	$6.505 \times 10^{-7} \text{ m}^2$
Darcy number, $Da = K/b^2$		$6.302 \times 10^{-5}$
Prandtl number, $Pr = \nu/\alpha$		718
Rayleigh number, $Ra = g\beta\Delta Tb^3/\nu\alpha$	$\Delta T = 0.5 \text{ } ^\circ\text{C}$	$1.5201 \times 10^6$
	$\Delta T = 1.0 \text{ } ^\circ\text{C}$	$3.0403 \times 10^6$
	$\Delta T = 2.0 \text{ } ^\circ\text{C}$	$6.0806 \times 10^6$
	$\Delta T = 5.0 \text{ } ^\circ\text{C}$	$15201 \times 10^7$
	$\Delta T = 10.0 \text{ } ^\circ\text{C}$	$3.0403 \times 10^7$
Peclet number, $Pe = Ub/\alpha$	$I = 5.5 \text{ A}$	$\omega = 39.2224 \text{ rpm}$
	$I = 6.0 \text{ A}$	$\omega = 60.3732 \text{ rpm}$
	$I = 6.5 \text{ A}$	$\omega = 84.1598 \text{ rpm}$
	$I = 7.0 \text{ A}$	$\omega = 110.5823 \text{ rpm}$
	$I = 7.5 \text{ A}$	$\omega = 139.6406 \text{ rpm}$
	$I = 8.0 \text{ A}$	$\omega = 171.3348 \text{ rpm}$
	$I = 8.5 \text{ A}$	$\omega = 205.6648 \text{ rpm}$
	$I = 9.0 \text{ A}$	$\omega = 242.6307 \text{ rpm}$
	$I = 9.5 \text{ A}$	$\omega = 282.2324 \text{ rpm}$
	$I = 10.0 \text{ A}$	$\omega = 324.4700 \text{ rpm}$



(a)



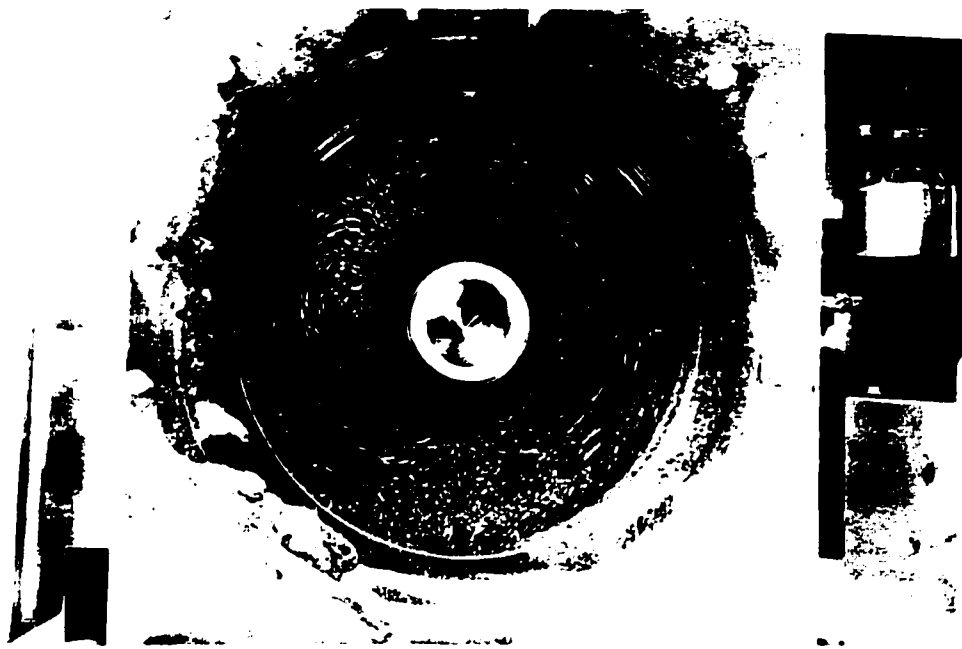
(b)

Figure 5.8 Comparison of non-isothermal flow fields between (a) experimental observation at a rotational speed of  $\varpi = 39 \text{ rpm}$ , and (b) numerical result at  $Pe = 10^3$  and  $Ra = 10^6$  ( $\Delta\Psi = 20$ ).

counter-clockwise direction. Before the fluid particles arrive at the interface, they are split into two streams, one to the left and another to the right. Generally, the left convective cell merge with the shear flow to become a stronger recirculation cell. Basically, the experimental and numerical results exhibit the same trend. However, it should be pointed out that the numerical result shown corresponds to an operating condition at approximately  $\Delta T = 0.5^\circ\text{C}$  and  $\varpi = 0.26\text{ rpm}$ . If the exact experimental condition was implemented, the flow pattern would be similar to that presented in Figure 5.7(b).

A series of pictures for flow fields at various rotational speeds are presented in Figure 5.9. Obviously, the shear layer continued to present. Unfortunately, the paths of the tracers cannot be clearly observed through the picture, but the presence of shear layer can still be detected. As displayed in Figure 5.9(a), the flow pattern for a rotational speed of  $32 \pm 4\text{ rpm}$ , the shear flow immediately next to the shaft was represented by a ring of gray band and some shorter white lines whereas the convective flow was recognized by longer white lines. This does not mean that the flow in the shear layer was slower than that in the convective cell. In fact, the flow in the shear layer was much faster. To capture the convective flow patterns, a much slower shuffle speed had to be used. When this shuffle speed was used, the trace of the faster shear flow blended into rings of white lines, leading to a wrong impression that the convective flow was faster than the shear flow.

When the rotational speed was further increased, as shown in Figure 5.9(b) and (c), it is noticed that the shorter white lines in the shear layer disappeared and were replaced by a darker hole. It was observed that the higher the speed the shaft rotated, the



(a)



(b)

Figure 5.9 Flow patterns in the modified Hele-Shaw cell at various shaft rotational speeds (a)  $\varpi = 39 \text{ rpm}$  ( $Pe = 1.506 \times 10^5$ ), (b)  $\varpi = 100 \text{ rpm}$  ( $Pe = 3.861 \times 10^5$ ), (c)  $\varpi = 158 \text{ rpm}$  ( $Pe = 6.100 \times 10^5$ ), and (d)  $\varpi = 333 \text{ rpm}$  ( $Pe = 1.286 \times 10^6$ ).



(c)



(d)

Figure 5.9 continued.

more ambiguous the shorter white lines, the darker the shear layer, and the larger its size. The shear layers depicted in Figure 5.9(a), (b), and (c) were circular in shape. As soon as the rotational speed was increased beyond a threshold value, the shear layer became unstable. When this happened, the shear layer rotated in a spiral fashion, which was somewhat vaguely captured in Figure 5.9(d).

As shown in these figures, there were two convective cells circulating in opposite directions. The smaller one on the left rotated in the counter-clockwise direction while the larger one on the right rotated in the clockwise direction. Based on the observation from the previous chapter, there is always a thermal plume rising from the shaft. The flow pattern shown in Figure 5.9(a) suggests that the thermal plume was no longer rising vertically upward from the shaft. Instead, it was tilted to the left. Along this direction, fluid particles flow radially outward and make a relatively sharp turn before they reached the porous sleeve. Those fluid particles that followed the left convective cell traveled in the convective region for a short distance and reentered the shear flow region smoothly. On the other hand, those fluid particles that followed the right convective cell went through a longer distance before they merged into the shear flow again. Before leaving the convective region, they made another sharp turn (almost  $360^\circ$  this time).

Also observed is that the line that separated two convective cells became more tilted as the shaft rotational speed increased. If this speed increased beyond a critical value, the flow evidently became turbulent as shown in Figure 5.9(d). Unlike the flow structures presented in Figures 5.9(a), (b), and (c), the longer white lines are no longer smooth. Instead, these lines became either spiral or circular depending on their locations.

This proves that the instability of the shear layer produced eddies that were later carried along by the convective flows and spread all over the flow field.

The side effect from an extensive run of experiment was the increase of shaft temperature. The rate of temperature rise was proportional to the shaft rotational speed. Because of the rise in the shaft temperature, the buoyancy effect became more and more pronounced. As such, the cases in which the rotational speed was high, the combined shear and buoyancy effects had led to a rather complicated flow pattern in the Hele-Shaw cell. The most apparent change in the flow field was the presence of two convective cells right next to the shear flow. As reported in the literature and Chapter Three of this work, the flow field of natural convection has two convective cells of equal strength rotating in opposite direction. From this flow visualization study, it was observed that not only were these convective cells not equal in strength, but also their orientations were distorted tremendously. Clearly, the right cell had grown considerably by expanding to the top portion, squeezing the left one to a smaller size. What unaccounted for was the presence of a motionless region below the rotating shaft. Consistent observations suggested that the flow structure could be divided into four flow regions.

The suggested four flow regions are shown in Figure 5.10. The innermost region corresponds to the shear layer. The middle section is the region where convective flow takes place. The outermost section is generally associated with the porous sleeve. The lowest triangular section is the region where flow is almost stationary.

At a relatively low rotational speed, the particles in the shear region experienced the highest velocity, but they generally traveled only in the angular direction. The flow pattern in this region resembled that of the polar Couette flow in rotating cylinders. As



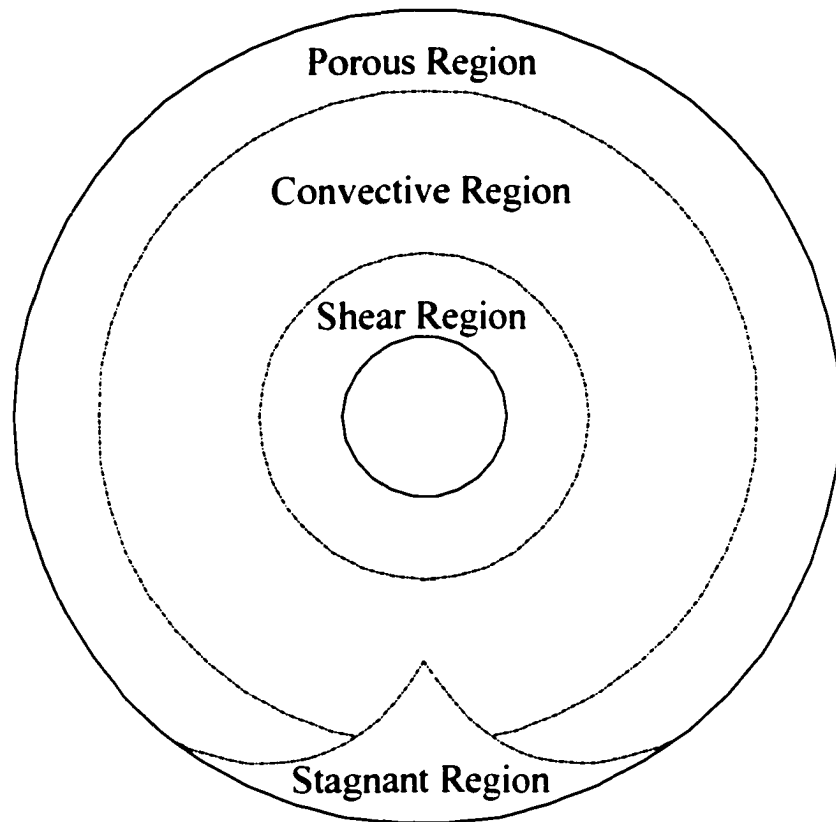


**Figure 5.10** Various flow regions observed from the experimental study at high rotational speeds.

the rotational speed increased, the corresponding Taylor number would exceed the threshold Taylor number in which rotational instability was triggered (Taylor, 1923; Coles, 1965; Kataoka and Takigawa, 1981; Ohmura et al., 1997). When this happened, the flow no longer behaved like a polar Couette flow. In fact, the flow pattern evolved into a spiral pattern (Figure 5.9(d)). Accompanied by this spiral flow pattern was that the fluid particles also traveled in the axial direction, causing the trace of the particles to be helical in shape. The observation of this pattern has been well documented and this flow instability is referred to as Taylor instability or sometimes Taylor cells (Ohmura et al., 1995).

As Måløy and Goldberg (1993) pointed out, the Taylor-Couette flow becomes chaotic when  $Re/Re_c \sim 11$ . For the present study, the critical Reynolds  $Re_c$  number based on the gap width is 125. The unsteady flow field shown in Figure 5.9(d) was for a rotational speed of  $333 \pm 17 \text{ rpm}$  or  $Re/Re_c = 10.3$ . At this high speed, the flow was chaotic and definitely became three-dimensional, which can be confirmed from the observation that the flow particles were thrown away from the shaft as it span. As the flow particles were moving away from the shaft, they were drawn back towards the shaft by recirculation. This process repeated until the flow particles reached the edge of the cell. There, they stuck close to the wall and flowed outward away from the shear region. In short, the flow inertia in the shear layer is much greater than thermal buoyancy in the range of this study.

The flow structure in the convective region is mainly resulted from the combination of the shear and buoyancy effects. There were two convective cells circulating in this region. Because of the shear effect, these cells were no longer

symmetrical about the vertical axis. As shown in Chapter Three, when the shaft does not rotate, the cells are symmetrical, in which the flow particles in the cells rise directly upward from the heated inner shaft. Because of the distortion by the rotational effect, the convective cells were severely deformed and pushed downstream in the shaft rotational direction. In this region, the flow pattern can be considered as in the mixed convective regime. When the shaft temperature is the same as that of the fluid, this region is force-convection driven.

The flow field in the porous region was difficult to observe because the number of particle tracers was small and the velocity in this region was insignificantly small. The distribution of the particle tracers was relatively even only right after the cell was filled with the silicone oil and its tracers. As the shaft rotated, most of the tracing particles were drawn towards the convective region, leaving behind very little tracers in the porous region. Because of the abrupt change in the gap width, very few tracers were able to penetrate the porous region when they reentered the porous region from the convective region. In addition, the slow motion of the particles in the porous layer was much more difficult to be captured even using a longer exposure time of *30 sec*. Even though recognizing the flow pattern through the pictures was still possible, especially when the flow particles left the porous region and entered the convective region at the lower portion of the cell. In this porous region, capillary effect is much greater than that in the shear and convective regions. As a result, the flow in this region is much slower than that in the shear and convective regions.

The stagnant region is relatively small in size as compared to other regions discussed above. In this region, the fluid particles remained relatively motionless

throughout the entire experiment. In fact, this region was not anticipated before the experiment was performed. Also, the presence of this region has never been foreseen from both theoretical and numerical studies. Its presence is mainly due to the experimental conditions. Because of settling, the number of tracing particles in this region was higher than any other region. Within this region, the weight of additional particle tracers balances the thermal buoyancy force. Since this concentration effect has not been included in the theoretical and numerical studies, its presence is not expected in their results.

## **5.8 Experimental Discrepancy**

Although the flow visualization has clarified some doubts about the flow field in an annulus with a porous sleeve, it has also cast some doubts in the comparison between the numerical and experimental results obtained from this study. It is believed that the inherent difference between the numerical and experimental models and experimental error have contributed to the discrepancy observed between the numerical and experimental results.

In the formulation of numerical model, it is assumed that the flow is two-dimensional and laminar throughout the range of study. Also, the properties of the fluid are uniform and independent of temperature, and the Taylor instability is absent.

To satisfy the two-dimensional flow assumption, the annulus has to be infinitely long. However, for the Hele-Shaw analogy to be valid, its gap width must be thin enough so that the second order terms in the governing equations can be neglected. To accommodate this condition, the gap width for the fluid layer was also made relatively

small. With this configuration, the two-dimensional flow assumption was not exactly met. In addition, the abrupt change in the gap width across the interface might have induced undesirable secondary flows. As a result, the flow in the experimental model was not completely described by the numerical formulation.

Although the numerical formulation was based on the assumption of laminar flow, this is not always the case in experiment, especially when the rotational speed is high. Although the Reynolds number based on the highest rotational speed in this experiment was calculated to be less than the critical Reynolds number, turbulence could be originated from the rough surfaces. Because of the imperfect fabrication of the shaft and the cell, the production of eddies from the solid wall might be critical in leading to the transition to turbulent flow.

The assumption of constant properties was also not exactly met in experiment. This idealized situation is made only for the ease of numerical study. It is doubtful that the thermal properties of the fluid and cell walls remain constant within the range of temperature experienced in this experiment.

The onset of Taylor instability that leads to Taylor cells is not anticipated from the present numerical formulation. Since the Taylor instability is transient and propagates in the axial direction, the present study as well as many other publications in the literature, which dealt with two-dimensional Reynolds equation, may need further justification.

Some experimental errors are simply unavoidable. One of the errors was introduced by the tracing particles. Since the density of the tracing particle is greater than that of the silicone oil, the particles tend to settle after some time. As these particles were settling down, they dragged along the fluid particles and thus induced a downward flow.

In addition, it is very difficult to have the particle tracers mixed evenly with the silicone oil. When the particles start to settle, the distribution of the tracers was far denser at the lower portion of the cell than in any other portion. This contributed to the fact that the silicone oil with its suspended particle tracers was highly non-uniform. As a result, the fluid was not isotropic and its density was highly non-uniform. This is the main reason that leads to the formation of the stagnant region in the Hele-Shaw cell.

After the power supply was switched off at the end of the experiment, several temperature measurements were made on the shaft surface. It was found that the temperature distribution on the shaft was not uniform. This temperature distribution not only depended on the friction between the shaft and the o-rings, but also on how heat was removed from the rotor unit. Several temperature measurements had shown that the difference in temperature on the shaft could be as large as  $1.2^{\circ}\text{C}$ . This temperature difference was normally proportional to the average temperature of the shaft.

Perhaps the most serious discrepancy between the numerical and experimental models was the thermal boundary condition. As mentioned earlier, the shaft temperature was not constant and uniform in the experiment. In addition, the thermal boundary condition on the outer cylinder (i.e., the journal housing) in the numerical model was not exactly implemented in the experiment. Unlike the numerical model, the temperature on the radius  $c$  in the modified Hele-Shaw cell was not exactly at a constant temperature.

## **5.9 Conclusions**

Although the flow visualization experiment could not perfectly duplicate the conditions in the numerical study, it did provide some insights to the problem considered

in the present study. Observations from this experiment have drawn the following conclusions.

The flow in the Hele-Shaw cell can be divided into four regions, the shear, the convective, the porous, and the stagnant regions. These regions can be easily recognized from the flow patterns captured in the photographs.

The shear region is located right next to the rotating shaft, which is driven by the shear effect. In this region, the fluid particles rotate due to the shearing action that the shaft induces. The faster the shaft rotates, the thicker the shear layer becomes and the faster the tracing particles travel. Flow becomes instable when the shaft rotational speed increases. When the shaft rotates at *333 rpm*, the flow becomes chaotic.

The convective region is driven by the buoyancy effect. In this region, the appearance of two convective cells is possible if there exists a significant temperature difference between the shaft and the fluid. This temperature difference increases with the shaft rotational speed and its operational time. If the convective cells appear, the left one is always smaller in size and rotates in the counter-clockwise direction. In contrast, the right one is always larger but rotates in the clockwise direction. Their strength is proportional to the temperature difference between the shaft and the fluid. When the shaft rotates at *333 rpm*, the flow in this region becomes oscillatory in the radial direction.

In the porous region, the flow is finite but is too insignificant to be captured in photography. Careful examinations from several experimental runs have confirmed the finite flow in this region. The effect of chaotic flow also affects the flow in this region when the shaft rotational speed was *333 rpm*.

The stagnant region has never been disclosed in the theoretical or numerical results in this study. It is probably caused by the concentration effect due to the presence of tracing particles. In this region, the large number of the tracing particles damps the action from buoyancy and shear force. Therefore, there is almost no flow motion in this region. As the shaft rotates faster or the temperature difference becomes larger, the size of this region reduces.



## **CHAPTER SIX**

### **CONCLUSIONS**

#### **6.1 Introductory Remarks**

The study of flow and temperature fields in rotating cylinders with a porous sleeve has been successfully performed. This study includes theoretical, numerical, and experimental investigations.

Using the theoretical approach, two distinctive cases were investigated. The first case considered eccentric rotating cylinders with a porous sleeve while the second case focused on natural convection in concentric non-rotating cylinders with a porous sleeve. A regular perturbation method was employed in these investigations. The perturbed terms in these cases were the eccentricity ratio and the Rayleigh number, respectively.

For the numerical investigation, a finite difference code was developed to solve for the flow and temperature fields in concentric rotating cylinders with a porous sleeve. The effects of various parameters were investigated in great detail. Among the most important ones were the rotational speed of the inner cylinder, the strength of buoyancy force, the thickness of the porous sleeve, and its permeability.

An experimental study was conducted to visualize the flow patterns in rotating cylinders with a porous sleeve using a modified Hele-Shaw cell. Silicone oil with suspended particle tracers was used to fill the cell to reveal the flow patterns as the shaft rotated.

## **6.2 Effects of Various Parameters**

The effects of some of the most critical governing parameters on the overall performance of sintered journal bearings are summarized in this section.

### **(a) Buoyancy Effect**

The buoyancy effect is represented by the Rayleigh number. It was found that the greater the Rayleigh number, the more important the buoyancy effect. For a specific configuration and material, a greater Rayleigh number implies a larger temperature difference between the inner and outer cylinders.

The results show that the existence of one or two convective cells is possible, depending on the shaft rotational speed. The strength of convective cells increases with the Rayleigh number. When the Rayleigh number is small, the convective cells only appear in the fluid layer and the heat removal from the inner cylinder is mainly by conduction. In contrast, when the Rayleigh number is large, the convective cells may penetrate the porous sleeve and the heat removal is more effective by convection.

### **(b) Shear Effect**

The shear effect is directly related to the shaft rotational speed. In literature, two dimensionless parameters, the Reynolds number and the Taylor number, are normally used to signify the effect of rotational speed, depending on the nature of the problems or the applications. For non-isothermal cases (such as the present study), the Peclet number is used instead. The Peclet number is similar to the Reynolds and Taylor numbers in the sense that it is also a representation of speed.

Generally, the flow and temperature fields in the annulus are affected by both buoyancy and shear effects. If the system is dominated by buoyancy effect, as in a natural convection case, there are two convective cells of nearly equal strength appearing on each side of the annulus. When the inner cylinder rotates (a finite Peclet number), it produces a layer of fluid next to the inner cylinder. Obviously, the strength and the thickness of the shear layer increases with the Peclet number. With an increase in the Peclet number, the system becomes more and more dominated by the shear effect. Consequently, the growth of shear layer suppresses the size of convective cells until the cells completely disappear from the flow field.

#### **(c) Thickness of Porous Sleeve**

In this study, both inner and outer radii are fixed. The porous sleeve thickness is represented by the porous sleeve inner radius  $b$ . As  $b$  increases, the porous sleeve thickness decreases. When  $b$  increases, the reduction in flow resistance leads to an increase in the flow strength. This increase in the flow strength can produce a stronger shear flow, a stronger convective cell, or a combination of both.

If the porous sleeve is thick, a large velocity gradient appears along the rotating inner cylinder. This in turn produces high stresses and high heat generation rate due to large viscous dissipation in the fluid. If the porous sleeve is thin, the velocity gradient reduces and thus the heat generation through viscous dissipation also reduces. For a sufficiently thin porous sleeve, the porous sleeve behaves as if it were an impermeable wall that the porous journal bearing is no different from a solid journal bearing.

#### **(d) Permeability of Porous Sleeve**

The Darcy number represents the permeability of the porous sleeve, an indirect measure of pore size in the porous sleeve. By definition, the greater the Darcy number, the larger the pores in the porous sleeve.

As the Darcy number approaches unity, the presence of the porous sleeve becomes insignificant. Both velocity and temperature profiles approach those in a solid journal bearing. On the other hand, if the Darcy number approaches zero, the porous sleeve becomes so impermeable that it behaves like a solid wall. In this study, it was found that a porous sleeve with a Darcy number less than  $10^{-4}$  can be considered impermeable.

As the Darcy number decreases, flow penetration to the porous sleeve is less likely to take place because of the increase in the flow resistance. As a result, some flow energy was dissipated by the flow resistance, which led to a weaker shear layer and convective cells.

#### **(e) Thermal Conductivity Ratio**

The thermal conductivity ratio is defined as the ratio of the thermal conductivity of the fluid layer  $k_f$  to that of the porous sleeve  $k_2$ . The effective thermal conductivity of the porous sleeve can be estimated by

$$k_2 = \phi k_f + (\phi - 1) k_p, \quad (6.1)$$

where  $\phi$  is the porosity of the porous medium,  $k_f$  is the thermal conductivity of the fluid, and  $k_p$  is the thermal conductivity of the porous medium.

At a very small Rayleigh number, heat conduction is the dominant heat transfer mode. The thermal conductivity ratio does not have any significant effect on the flow field, but it does have a profound effect on the temperature distribution. Since this ratio is a material property of the annulus, it has close relationship with the porous sleeve thickness. For a given porous sleeve thickness, the temperature gradient in the fluid layer decreases with  $k_1/k_2$  but increases in the porous sleeve.

At a large Rayleigh number, the thermal conductivity ratio plays a vital role in the flow field when thermal buoyancy effect is important. It is found that the strength of the convective cells decreases with the thermal conductivity ratio, but that of the shear flow increases with it.

#### **(f) Eccentricity**

To study the effect of the eccentricity of the inner cylinder on the flow and temperature fields in the annulus, the eccentricity ratio, defined as the ratio of the eccentricity to the inner radius of the porous sleeve, is used.

The most significant effect resulting from the eccentricity ratio is that it modifies the velocity and temperature distributions in the gap between the inner and the outer cylinders. As the eccentricity ratio increases, the inner cylinder moves vertically downward. Across the narrowest gap, the velocity and temperature gradients are greater than those at other locations. The reverse trend was observed across the widest gap.

Although the above conclusion is drawn based on the observation from the cases that the eccentricity ratio is very small, it is expected that the actual flow and temperature

distributions in an eccentric annular space with a porous sleeve will be qualitatively similar to what observed here.

### **6.3 Heat Transfer Performance**

The heat transfer performance is evaluated through the Nusselt number. Since the local heat transfer is not of particular interest, the local Nusselt number has not been investigated. To evaluate the overall heat transfer performance of the entire system, the average Nusselt number was calculated.

The average Nusselt number increases when the porous sleeve thickness reduces. Therefore, one can conclude that the presence of a porous sleeve delays the onset of natural convection. The average Nusselt number also increases with the Darcy number and approaches some asymptotic values that depend on the effective thermal conductivity ratio  $k_1/k_2$ . On the other hand, the average Nusselt number decreases monotonously with  $k_1/k_2$ . The smaller the thermal conductivity ratio, the greater the average Nusselt number. On the other hand, a larger average Nusselt number on the outer cylinder always corresponds to a larger thermal conductivity ratio. The dependency of Nusselt number on the Darcy number diminishes with a decrease in the porous sleeve thickness.

Based on the numerical results, the average Nusselt number increases with the Rayleigh number. Clearly, the heat transfer mode changes from forced convection regime to mixed convection regime and eventually to natural convection regime when the Rayleigh number increases. The transition of these regimes depends on both Peclet and Rayleigh numbers. When the Peclet number is zero, the flow and temperature fields in a non-rotating annulus with a porous sleeve are dominated by natural convection and have

the highest average Nusselt numbers. As the Peclet number increases, heat transfer is in transition to forced convection and the average Nusselt number reduces.

#### **6.4 The Design of Porous Journal Bearings**

The main goals in the design of porous journal bearings are high load capacity, low frictional factor, and long operational life. Since the above goals have been attempted for decades, it is not the objective of the present study to re-iterate their importance. Nowadays, high performance sintered journal bearings are more commonly used in engineering applications. These bearings are smaller in size, operate at higher speeds, and generate less noise as they have a lower vibration level. However, these high performance bearings are more likely to subject to thermal seizure failure in operation. For a successful design, the heat generated in the bearing ought to be removed efficiently to avoid thermal seizure. It is the objective of this study to identify the major parameters that influence the heat removal.

Since the shaft rotates at a high speed, there is always a shear layer inside the porous journal bearing. When the bearing is in operation, the flow field is dominated by shear effect. As a result, convective cells are not likely to appear and the Rayleigh number does not have any significant effect on the shear layer. For this reason, the flow field is barely influenced by the differential heating between the shaft and the housing when the shaft rotates at high speeds. When the bearing is not in operation or the shaft rotates at low speeds, a weak circulation is possible due to the temperature difference between the shaft and the housing. Based on this observation, one should not overrun the bearing in application. Particularly for porous bearings, the shaft rotational speed should

not be too high so that heat removal by convection can be promoted between the shaft and the housing.

For a typical sintered journal bearing, the porous sleeve thickness is very thin. Since the sleeve thickness promotes heat convection, the development of convective cells in the fluid layer is less likely than the conventional solid journal bearings. Clearly, these cells enhance the flow circulation in the bearing as well as the heat removal from the shaft. As a result, in designing a sintered journal bearing, its porous sleeve should be made as thin as possible.

For a practical sintered journal bearing, the Darcy number is on the order of  $10^{-8}$  to  $10^{-9}$ . Hence, the heat transfer mode is mainly by heat conduction as far as the Darcy number is concerned. However, an absolute prediction is impossible based on this study because, in a practical sintered bearing, the porous sleeve is thin and not very permeable. Since a thin porous sleeve promotes heat convection, but a less permeable porous sleeve demotes heat convection, the combined effect of these two factors needs further investigation.

For a typical porous bearing ( $Da < 10^{-4}$ ), an increase in the thermal conductivity ratio weakens the convective cells. Also, the effects of thermal conductivity ratio on the temperature gradients lead to a reduction of the average Nusselt numbers with  $k_1/k_2$ . Other than the thermal conductivity ratio, a thinner porous sleeve will also lead to a larger average Nusselt number.

Since the porous sleeve in the sintered journal bearings is normally made of bronze, it is generally true that  $k_1/k_2 < 1.0$  and  $b/c \rightarrow 1$ . A typical thermal conductivity ratio of a bronze sintered journal bearing lubricated by SAE engine oil is on the order of



$10^{-3}$ . When the bearing is not in operation, heat is removed from the inner shaft mainly by convection. When the bearing operates at high speeds, its corresponding flow field is mainly a shear layer and thus its heat transfer mechanism is heat conduction.

These observations suggest that the heat transfer performance of a sintered journal bearing is not optimal because the onset of heat convection is delayed and its heat transfer mode tends to be pure conduction.

## **6.5 Future Work**

Although the present study has successfully investigated some issues related to the performance of porous journal bearings, there are still many questions remained to be explored. The present work can be extended to address some of these questions from experimental or numerical approaches.

To improve the experimental study, the tracing particles need to be replaced with more suitable ones. One of the critical properties of these tracing particles is that their density should be close to that of the silicone oil. By doing so, it is believed that the size of the stagnant region can be minimized or even eliminated. Other than the quick fix related to the tracers, the current experiment can be easily modified to visualize the flow pattern in rotating eccentric annulus with a porous sleeve. In addition, the measurement of the temperature distribution should be added to better understand and describe the physics behind rotating annulus with a porous sleeve.

With the success in the present numerical solution, the code can be modified to accommodate the investigation of the flow and temperature fields in eccentric rotating cylinders with a porous sleeve.

To this end, the numerical formulation may require to use both cylindrical and bipolar coordinate systems. As shown in Figure 6.1, the computational domain of an eccentric porous journal bearing is demarcated by three circles. The inner domain lies between the two inner (eccentric) circles and the outer domain is enclosed by the two (outer) concentric circles. A bipolar coordinate system is used in the inner domain, while the cylindrical coordinate system is used in the outer domain. A sample of the grid distribution is shown in Figure 6.2. This approach is discussed in the following sections in greater detail.

### 6.5.1 Bipolar Coordinate System

Bipolar coordinate system is a body-fitted coordinate system in which two coordinates maintain orthogonal. It is especially good for problems involving one or two circles (cylinders). Cho et al. (1982) and Bau (1984) have shown that this coordinate system is perfect for problems dealing with eccentric cylinders.

In this coordinate system, the computational domain is bounded by two eccentric circles,  $\eta_a$  of the inner circle and  $\eta_b$  of the outer circle. According to Moon and Spencer (1971), these variables are related to  $x$  and  $y$  by the following expression.

$$q^1 = \eta, \quad q^2 = \varphi, \quad (6.2a, b)$$

$$x = \frac{\ell \sinh \eta}{\cosh \eta - \cos \varphi}, \quad y = \frac{\ell \sin \varphi}{\cosh \eta - \cos \varphi}, \quad (6.3a, b)$$

$$h = h_1 = h_2 = \frac{\ell}{\cosh \eta - \cos \varphi}, \quad \text{and} \quad g_{11} = g_{22} = \frac{\ell^2}{(\cosh \eta - \cos \varphi)^2}, \quad (6.4a, b)$$

where

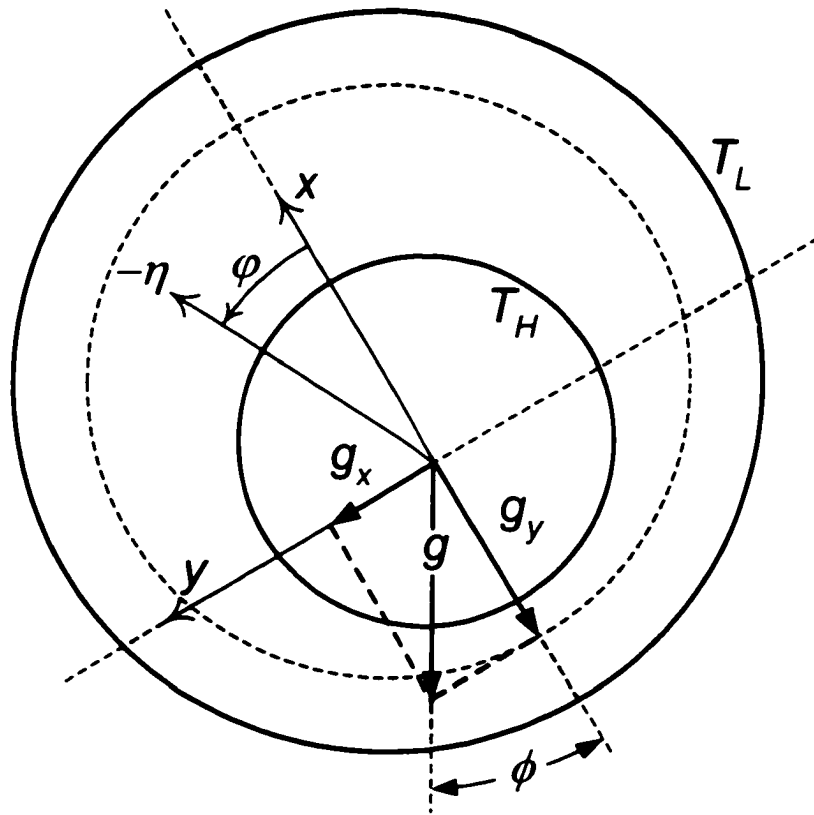


Figure 6.1 The coordinate systems for an eccentric porous journal bearing.

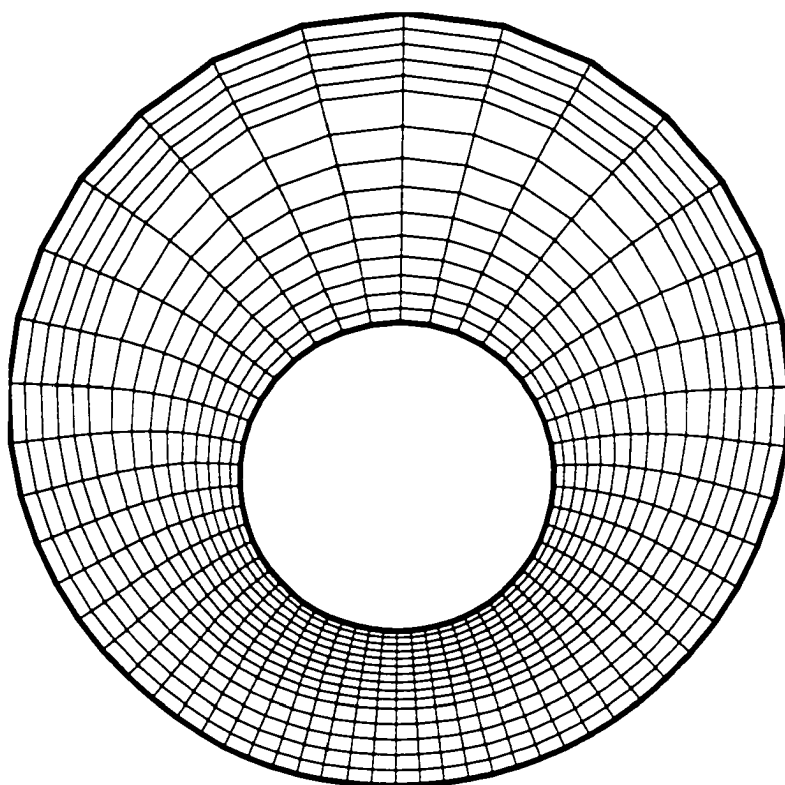


Figure 6.2 The computational domain for an eccentric porous journal bearing.

$$\ell = \sinh \eta_u, \quad (6.5)$$

is a scale factor in the bipolar coordinate system. In Eqs. (6.4),  $h_i$  and  $g_{ii}$  are the scale factors and the diagonal components of the fundamental metric tensor with respect to the orthogonal coordinate component  $q^i$  (Reddy and Rasmussen, 1990).

Making use of the principles in vector transformation between two orthogonal coordinate systems, the following identities between the Cartesian and bipolar coordinate systems can be derived.

$$\hat{e}_\tau = \frac{1 - \cosh \eta \cos \varphi}{\cosh \eta - \cos \varphi} \hat{e}_\eta - \frac{\sinh \eta \sin \varphi}{\cosh \eta - \cos \varphi} \hat{e}_\varphi, \text{ and} \quad (6.6a)$$

$$\hat{e}_\nu = -\frac{\sinh \eta \sin \varphi}{\cosh \eta - \cos \varphi} \hat{e}_\eta - \frac{1 - \cosh \eta \cos \varphi}{\cosh \eta - \cos \varphi} \hat{e}_\varphi. \quad (6.6b)$$

In a bipolar coordinate system,  $\eta_u$  is generally chosen to be greater than  $\eta_b$ . These two values mark the inner and outer limits of the bipolar coordinate system. By varying these two values, the coordinate system can produce three distinctive computational domains as shown in Figure 6.3.

- (a) Setting  $\eta_b$  to zero implies that  $b$  is infinite. In this case, a bipolar coordinate system produces a computational domain between a circle and a line as shown in Figure 6.3(a). This configuration is best used for simulation of the transport phenomena of buried heated pipe (Bau, 1984; Cheng and Lai, 1997).
- (b) If  $\eta_b$  has the same sign as  $\eta_u$ , it generates a computational domain between two circles (a smaller circle corresponding to  $\eta_u$  and a larger circle corresponding to  $\eta_b$ , as shown in Figure 6.3(b)). This configuration is the most suitable for eccentric annuli. This configuration has been employed in

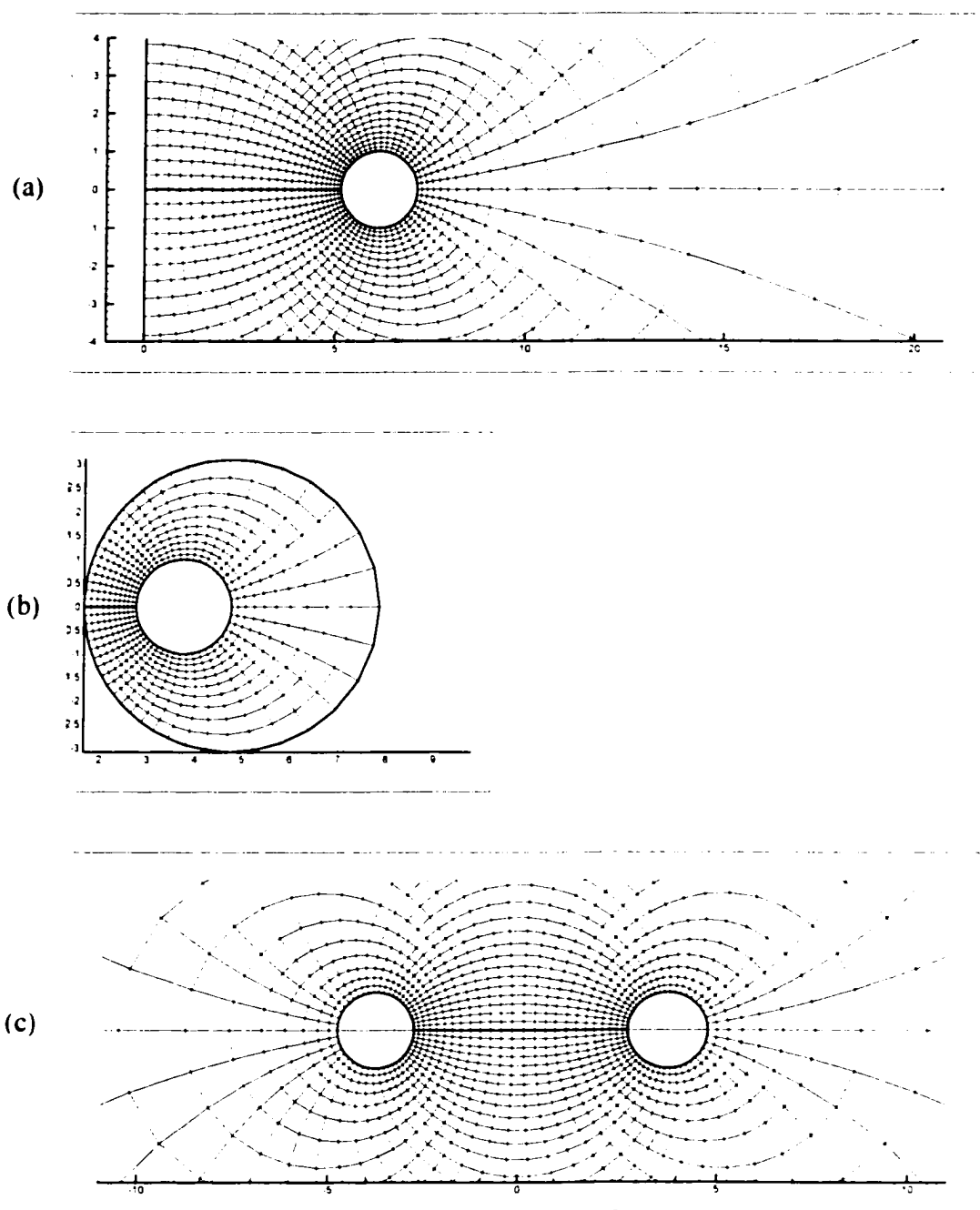


Figure 6.3 Three computational domains in the bipolar coordinate system.

the study of pipes insulation, heat exchangers, and eccentric solid journal bearings (Himasekhar and Bau, 1986).

- (c) If  $\eta_h$  has the opposite sign as  $\eta_u$ , it generates a computational domain between two separated circles. In this case, as depicted in Figure 6.3(c), the smaller circle is no longer inside the larger circle. This configuration can be used to study bio heat transfer. For example, the two circles are the blood vessels whereas the computational domain represents the tissues.

### 6.5.2 Governing Equations

As shown in Figure 6.1, the journal surface and the interface between the fluid and porous layers are eccentric. However, this interface is concentric with the housing surface. To fully describe the configuration, the values of  $a$ ,  $b$ ,  $c$ , and  $e$  are prescribed.

For a Boussinesq fluid, the steady-state invariant forms of the continuity, momentum and energy equations are

$$\text{div } \vec{V}_1 = 0, \quad (6.7)$$

$$\text{div}(\omega_1 \vec{V}_1) = -\beta \text{grad } T_1 \times \vec{g} \cdot \hat{e}_z + \nu \nabla^2 \omega_1, \text{ and} \quad (6.8)$$

$$\text{div}(T_1 \vec{V}_1) = \alpha_1 \nabla^2 T_1, \quad (6.9)$$

where

$$\vec{V}_1 = u_{r1} \hat{e}_r + u_{\theta 1} \hat{e}_\theta, \text{ and} \quad (6.10)$$

$$\omega_1 = \vec{\omega}_1 \cdot \hat{e}_z = (\text{curl } \vec{V}_1) \cdot \hat{e}_z. \quad (6.11)$$

Here, only the z-component of the vorticity is considered because the x- and y-components of vorticity are zero for any two-dimensional flow. Recognize that the actual vector notation for stream function is given as

$$\bar{V} = \text{grad } \psi \times \hat{e}_z. \quad (6.12)$$

Equations (6.8), (6.9), and (6.11) can be expressed in terms of the bipolar polar coordinate system using the vector operators that Moon and Spencer (1971) have compiled for the bipolar coordinate system. The following identities are adopted from their work and have been simplified for two-dimensional problems.

$$\text{grad } \Phi = \frac{\cosh \eta - \cos \varphi}{\ell} \left( \hat{e}_\eta \frac{\partial \Phi}{\partial \eta} + \hat{e}_\varphi \frac{\partial \Phi}{\partial \varphi} \right). \quad (6.13a)$$

$$\text{div } \bar{E} = \frac{(\cosh \eta - \cos \varphi)^2}{\ell} \left[ \frac{\partial}{\partial \eta} \left( \frac{E_\eta}{\cosh \eta - \cos \varphi} \right) + \frac{\partial}{\partial \varphi} \left( \frac{E_\varphi}{\cosh \eta - \cos \varphi} \right) \right]. \quad (6.13b)$$

$$\text{curl } \bar{E} = \hat{e}_\eta \left[ \frac{\cosh \eta - \cos \varphi}{\ell} \frac{\partial E_z}{\partial \varphi} - \frac{\partial E_\varphi}{\partial z} \right] + \hat{e}_\varphi \left[ \frac{\partial E_\eta}{\partial z} - \frac{\cosh \eta - \cos \varphi}{\ell} \frac{\partial E_z}{\partial \eta} \right], \text{ and} \quad (6.13c)$$

$$\nabla^2 \Phi = \frac{(\cosh \eta - \cos \varphi)^2}{\ell^2} \left( \frac{\partial^2 \Phi}{\partial \eta^2} + \frac{\partial^2 \Phi}{\partial \varphi^2} \right). \quad (6.13d)$$

where  $\Phi$  is a scalar and  $\bar{E}$  is a vector defined as  $\bar{E} = E_\eta \hat{e}_\eta + E_\varphi \hat{e}_\varphi$ .

The governing equations for the porous layer are

$$\text{div } \bar{V}_2 = 0. \quad (6.14)$$

$$\text{div}(\omega_2 \bar{V}_2) = -\beta \text{grad } T_2 \times \bar{g} \cdot \hat{e}_z - \frac{\mu}{\rho K} \omega_2 + \frac{\bar{\mu}}{\rho} \nabla^2 \omega_2, \text{ and} \quad (6.15)$$

$$\text{div}(T_2 \bar{V}_2) = \alpha_2 \nabla^2 T_2. \quad (6.16)$$

Since this layer is concentric, it is more appropriate to use the cylindrical coordinate system to formulate the governing equations. Reddy and Rasmussen (1990) and Moon and Spencer (1971) have listed the appropriate identities for this case.



Recognize that there are six variables, namely  $\psi_1$ ,  $\psi_2$ ,  $\omega_1$ ,  $\omega_2$ ,  $T_1$ , and  $T_2$ , in the four governing equations presented above. Hence, two more equations are needed to make this problem well posed. These two additional equations are the definitions of the vorticity in terms of stream functions for both layers. For the fluid layer, it is given in Eq. (6.11) whereas that for the porous layer is given below.

$$\omega_2 = \bar{\omega}_2 \cdot \hat{e}_z = (\text{curl } \bar{V}_2) \cdot \hat{e}_z. \quad (6.17)$$

### 6.5.3 Boundary and Interface Conditions

The dimensional boundary and interface conditions for the problem are given as follow. Here, the boundary conditions are prescribed and  $U = \varpi a$ .

On the surface of the journal,

$$\eta = \eta_a, \quad u_{\eta 1} = 0, \quad u_{\varphi 1} = U, \quad \text{and} \quad T_1 = T_H. \quad (6.18a, b, c)$$

On the surface of the housing,

$$r = c, \quad u_{r 2} = 0, \quad u_{\theta 2} = 0, \quad \text{and} \quad T_2 = T_L. \quad (6.19a, b, c)$$

On the interface between the fluid and porous layers,

$$\eta = \eta_b \text{ or } r = b, \quad u_{\eta 1} = u_{r 2}, \quad u_{\varphi 1} = u_{\theta 2}, \quad (6.20a, b)$$

$$\tau_1 = \tau_2, \quad P_1 = P_2, \quad (6.20c, d)$$

$$T_1 = T_2, \quad \text{and} \quad q_1 = q_2. \quad (6.20e, f)$$

### 6.5.4 Method of Solution

To reduce the governing equations presented above, suitable definitions of  $\psi_1$  and  $\psi_2$  must be predetermined using Eq. (6.12). With these definitions, Eqs. (6.8), (6.9),

(6.11), (6.15), (6.16), and (6.17), as well as their boundary and interface conditions, can be greatly reduced to the streamfunction-vorticity formulation (Gosman et al., 1977).

Algorithm outlined in Chapter Four can be adopted for this extended work to solve for the values of  $\psi_1$ ,  $\psi_2$ ,  $\omega_1$ ,  $\omega_2$ ,  $T_1$ , and  $T_2$ . Similar to Chapter Four, the employment of imaginary nodal points in this study is mandatory. However, unlike that in Chapter Four, a more complicated derivation, which involves interpolations, is anticipated due to the fact that the governing equations for fluid and porous regions are expressed in different coordinate systems.

## REFERENCES

Ball, K. S., 1987. *Mixed Convection Heat Transfer in Rotating System*, Ph. D. Dissertation, Department of Mechanical Engineering and Mechanics, Drexel University, Philadelphia, PA.

Ball, K. S., and Farouk, B., 1987, On the Development of Taylor Vortices in a Vertical Annulus with a Heated Rotating Inner Cylinder, *International Journal for Numerical Methods in Fluids*, Vol. 7, No. 8, pp. 857 - 867.

Bau, H. H., 1984, Low Rayleigh Number Thermal Convection in a Saturated Porous Medium Bounded by Two Horizontal, Eccentric Cylinders, *Journal of Heat Transfer*, Vol. 106, No.1, pp. 166 - 175.

Bear, J., 1972, *Dynamics of Fluids in Porous Media*, American Elsevier Publishing Company, Inc., New York.

Bear, J., Zaslavsky, D., and Irmay, S., 1968, *Physical Principles of Water Percolation and Seepage*, UNESCO.

Beavers, G. S., and Joseph, D. D., 1967, Boundary Conditions at a Naturally Permeable Wall, *Journal of Fluid Mechanics*, Vol. 30, No. 1, pp. 197 - 207.

Beavers, G. S., Sparrow, E. M., and Magnuson, R. A., 1970, Experiments on Coupled Parallel Flows in a Channel and a Bounding Porous Medium, *Journal of Basic Engineering*, Vol. 92, No. 4, pp. 843 - 848.

Beavers, G. S., Sparrow, E. M., and Masha, B. A., 1974, A Boundary Condition at a Porous Surface Which Bounds a Fluid Flow, *AIChE Journal*, Vol. 20, No. 3, pp. 596 - 597.

Berman, A. S., 1958, Laminar Flow in an Annulus with Porous Walls, *Journal of Applied Physics*, Vol. 29, pp. 71 - 75.

Bertrand, P. A., and Carré, D. J., 1997, Oil Exchange between Ball Bearings and Porous Polyimide Ball Bearing Retainers, *Tribology Transactions*, Vol. 40, No. 2, pp. 294 - 302.

Bertrand, P. A., Carré, D. J., and Bauer, R., 1995, Oil Exchange between Ball Bearings and Cotton-Phenolic Ball-Bearing Retainers, *Tribology Transaction*, Vol. 38, No. 2, pp. 342 - 352.

Bishop, E. H., and Carley, C. T., 1966, Photographic Studies of Natural Convection between Concentric Cylinders, *Proceedings of the 1966 Heat Transfer and Fluid Mechanics Institute*, Stanford University Press, pp. 63 - 78.

Braun, A. L., 1982, Porous Bearings, *Tribology International*, Vol. 15, No. 5, pp. 235 - 242.

Braun, J. T., and Groenhof, E. D., 1975, Silicone Lubrication of Porous Bronze Bearing, *Lubrication Engineering*, Vol. 31, No. 4, pp. 176 - 181.

Brinkman, H. C., 1947a, A Calculation of the Viscous Force Exerted by a Flowing Fluid on a Dense Swarm of Particles, *Applied Scientific Research*, Vol. A1, pp. 27 - 34.

Brinkman, H. C., 1947b, On the Permeability of Media Consisting of Closely Packed Porous Particles, *Applied Scientific Research*, Vol. A1, pp. 81 - 86.

Bujurke, N. M., and Naduvanamami, N. B., 1991, On the Performance of Narrow Porous Journal Bearing Lubricated with Couple Stress Fluid, *Acta Mechanica*, Vol. 86, pp. 179 - 191.

Bujurke, N. M., and Patil, H. P., 1992, The Effect of Variable Permeability and Rotation on the Performance Characteristics of Porous Bearings, *Wear*, Vol. 155, pp. 7 - 14.

Burton, R. A., 2000, *Heat, Bearings, and Lubrication: Engineering Analysis of Thermally Coupled Shear Flows and Elastic Solid Boundaries*, Springer-Verlag, New York.

Bychkov, Y. M., 1980, *Visualization of Thin Flows of Incompressible Fluid*, Shiitza, Kishinev.

Bychkov, Y. M., 1981, *Hydrodynamics of Thin Flows of Incompressible Fluid*, Shiitza, Kishinev.

Caltagirone, J. P., 1976, Thermoconvective Instabilities in a Porous Medium Bounded by Two Concentric Horizontal Cylinders, *Journal of Fluid Mechanics*, Vol. 76, Part 2, pp. 337 - 362.

Cameron, A., Morgan, V. T., and Stainsby, A. E., 1962, Critical Conditions for Hydrodynamic Lubrication of Porous Metal Bearings, Lubrication and Wear Group, *Proceedings of the Institution of Mechanical Engineers*, Vol. 176, No. 28, pp. 761 - 770.

Cameron, A., and Wood, W. L., 1949, The Full Journal Bearing, *Proceedings of the Institution of Mechanical Engineers*, London, Vol. 161, pp. 59 - 72.

Capone, E., 1970, Lubrication of Axially Undefined Porous Bearing, *Wear*, Vol. 15, No. 3, pp. 157 - 170.

Capone, E., and D'Agostino, V., 1974, Oil Whirl in Porous Metal Bearings, *Mechanica*, Vol. 9, No. 2, pp. 121 - 129.

Capone, E., Niola, V., and Bocchini, G. F., 1980, Further Developments in Porous Bearing Technology: The 20 Permeability Step Bearing, *Tribology*, Vol. 13, pp. 294 - 296.

Carrillo, L., Magdaleno, F. X., Casademunt, J., and Ortin, J., 1996, Experiments in a rotating Hele-Shaw Cell, *Physical Review E*, Vol. 54, No. 6, pp. 6260 - 6267.

Carson, R. W., 1964, A Special Review of All Self-Lubricated Bearings, *Product Engineering*, Vol. 35, No. 8, pp. 79 - 90.

Chandra, M., Malik, M., and Sinhasan, R., 1981, Investigation of Slip Effects in Plane Porous Journal Bearings, *Wear*, Vol. 73, No. 1, pp. 61 - 72.

Charrier-Mojtabi, M. C., Mojtabi, A., and Caltagirone, J. P., 1979, Numerical Solution of a Flow due to Natural Convection in Horizontal Cylindrical Annulus, *Journal of Heat Transfer*, Vol. 101, pp. 171 - 173.

Chattopadhyay, A. K., 1995, Steady State Characteristics of Finite Porous Oil Journal Bearings of Arbitrary Wall Thickness, *Indian Journal of Engineering and Materials Sciences*, Vol. 2, No. 6, pp. 257 - 260.

Chattopadhyay, A. K., and Majumdar, B. C., 1984a, Steady State Solution of Finite Hydrostatic Porous Oil Journal Bearings with Tangential Velocity Slip, *Tribology International*, Vol. 17, No. 6, pp. 317 - 323.

Chattopadhyay, A. K., and Majumdar, B. C., 1984b, Dynamic Characteristics of Finite Porous Journal Bearings Considering Tangential Velocity Slip, *Journal of Tribology*, Vol. 106, No. 4, pp. 534 - 536.

Chattopadhyay, A. K., and Majumdar, B. C., 1986, On the Stability of Rigid Rotor in Finite Porous Journal Bearings with Slip, *Journal of Tribology*, Vol. 108, No. 2, pp. 190 - 194.

Chattopadhyay, A. K., Majumdar, B. C., and Rao, N. S., 1987, Stability of a Rigid Rotor in Finite Externally Pressurized Oil Journal Bearing with Slip, *Journal of Tribology*, Vol. 109, No. 2, pp. 301 - 306.

Cheng, E. S., and Lai, F. C., 1996, Coupled Heat and Mass Transfer from a Buried Pipe, *32nd AIAA Thermophysics Conference*, AIAA Paper 97-2517.

Cho, C. H., Chang, K. S., and Park, K. H., 1982, Numerical Simulation of Natural Convection in Concentric and Eccentric Horizontal Cylindrical Annuli, *Journal of Heat Transfer*, Vol. 104, No. 4, pp. 624 - 630.

Cieslicki, K. M., 1993, On a Static and Dynamical Evaluation of Permeability of Porous Bearing Sleeves, *Wear*, Vol. 167, pp. 69 - 72.

Cieslicki, K. M., 1994, Investigations of the Effect of Inertia on Flow of Air Through Porous Bearing Sleeves, *Wear*, Vol. 172, pp. 73 - 78.

Cieslicki, K. M., and Krzeminski, K., 1995a, Influence of the Geometrical Structure of Porous Sleeve on Some Tribological Parameters of Porous Bearings, *21<sup>st</sup> Leeds-Lyon Symposium on Tribology "Lubricants and Lubrication"*, ed. D. Dowson et al., pp. 595 - 603.

Cieslicki, K. M., and Krzeminski, K., 1995b, Spatial Anisotropy of Permeability of Porous Bearing Sleeves, *International Journal of Powder Metallurgy*, Vol. 31, pp. 221 - 229.

Cieslicki, K. M., and Krzeminski, K., 1996, Porous Sleeve Bearings: Air and Oil Permeability, *International Journal of Powder Metallurgy*, Vol. 32, No. 2, pp. 175 - 183.

Coles, D., 1965, Transition in Circular Couette Flow, *Journal of Fluid Mechanics*, Vol. 21, part 3, pp. 385 - 425.

Conry, T. F., and Cusano, C., 1974, On the Stability of Porous Journal Bearings, *Journal of Engineering for Industry*, Vol. 96, No. 2, pp. 585 - 590.

Corbett, J., Almond, R. J., Stephenson, D. J., and Kwan, Y. B. B., 1998, Porous Ceramic Water Hydrostatic Bearings for Improved Accuracy Performance, *CIRP Annals Manufacturing Technology*, Vol. 47, No. 1, pp. 467 - 470.

Cusano, C., 1967, *Design of a Machine for the Experimental Investigation of Porous Metal Bearings*, M.S. Thesis, Cornell University, Ithaca, NY.

Cusano, C., 1970, *Theoretical and Experimental Analyses of Porous Metal Bearings*, Ph.D. Dissertation, Cornell University, Ithaca, NY.

Cusano, C., 1972a, Lubrication of Porous Journal Bearings, *Journal of Lubrication Technology*, Vol. 94, No. 1, pp. 69 - 73.

Cusano, C., 1972b, Lubrication of a Two-Layer Porous Journal Bearing, *Journal of Mechanical Engineering Science*, Vol. 14, No. 5, 335 - 339.

Cusano, C., 1972c, Analytical Investigation of an Infinitely Long, Two-Layer Porous Bearing, *Wear*, Vol. 22, pp. 59 - 67.

Cusano, C., 1973, The Effect of Variable Permeability on the Performance Characteristics of Porous Bearings, *Wear*, Vol. 23, pp.55 - 62.

Cusano, C., 1979, An Analytical Study of Starved Porous Bearings, *Journal of Lubrication Technology*, Vol. 101, No. 1, pp. 38 - 47.



Cusano, C., and Conry, T. F., 1978, On the Transmissibility of Short Porous Journal Bearings, *Journal of Lubrication Technology*, Vol. 100, No. 2, pp. 296 - 302.

Cusano, C., and Phelan, R. M., 1973, Experimental Investigation of Porous Bronze Bearings, *Journal of Lubrication Technology*, Vol. 95, No. 2, pp. 173 - 180.

Custer, J. R., and Shaughnessy, E. J., 1977, Thermoconvective Motion of Low Prandtl Number Fluids within a Horizontal Cylindrical Annulus, *Journal of Heat Transfer*, Vol. 99, No. 4, pp. 596 - 602.

Date, A. W., 1986, Numerical Prediction of Natural Convection Heat Transfer in Horizontal Annulus, *International Journal of Heat and Mass Transfer*, Vol. 29, No. 10, pp. 1457 - 1464.

Diprima, R. C., and Stuart, W. H., 1972a, Flow between Eccentric Rotating Cylinders, *Journal of Lubrication Technology*, Vol. 94, No. 3, pp. 266 - 274.

Diprima, R. C., and Stuart, W. H., 1972b, Non-local Effects in the Stability of Flow between Eccentric Rotating Cylinders, *Journal of Fluid Mechanics*, Vol. 54, Part 3, pp. 393 - 415.

Diprima, R. C., and Swinney, H. L., 1985, Instability and Transition in Flow between Concentric Rotating Cylinders, *In Hydrodynamic Instability and the Transition to Turbulence*, ed. H. L. Swinney and J. P. Gollub, Springer, New York, pp. 139 - 186.

DuBois, G. B., Mabie, H. H., and Ocvirk, F. W., 1951, Experimental Investigation of Oil Film Pressure Distribution for Misaligned Plain Bearings, National Advisory Committee for Aeronautics NACA, Technical Note 2507.

DuBois, G. B., and Ocwick, F. W., 1952, Experimental Investigation of Eccentricity Ratio, Friction, and Oil Flow of Short Journal Bearings, National Advisory Committee for Aeronautics NACA, Technical Note 2809.

Dubois, G. B., and Ocwick, F. W., 1953, Analytical Derivation and Experimental Evaluation of Short Bearing Approximation of Full Journal Bearings, National Advisory Committee for Aeronautics NACA, Report 1157.

Elder, J. W., 1965, Physical Processes in Geothermal Areas, *Am. Geophys. Un. Mon.*, Vol. 8, pp. 211 - 239.

Elrod, H. G., 1981, A Cavitation Algorithm, *Journal of Lubrication Technology*, Vol. 103, No. 3, pp. 350 - 354.

Eudier, M., and Margerand, R., 1969, Practical Working Conditions for Sintered Bearings, *Powder Metallurgy*, Vol. 12, No.24, pp. 417 - 425.

Fuller, D. D., 1984, *Theory and Practice of Lubrication for Engineers*, 2 ed., Wiley, New York.

Fusegi, T., and Farouk, B., 1986, A Three-dimensional Study of Natural Convection in the Annulus in between Horizontal Concentric Cylinders, *8<sup>th</sup> International Heat Transfer Conference*, Hemisphere, San Francisco, CA, pp. 1575 - 1579.

Fusegi, T., Farouk, B., and Ball, K. S., 1986, Mixed Convection Flows within a Horizontal Concentric Annulus with a Heated Rotating Inner Cylinder, *Numerical Heat Transfer*, Vol. 9, pp. 591 - 604.

Geotzel, C. G., 1950, *Treatise on Powder Metallurgy*, Vol. 2, Interscience Publications, New York, pp. 504 - 541.

Gnanaraj, S. D., and Raman, R., 1992, Experimental Studies on Wear in Oil-Impregnated Sintered Bearings, *Wear*, Vol. 155, pp. 73 - 81.

Gohart, R., and So, H., 1981, Porous Retainers for Rolling Bearings, *Journal of Mechanical Engineering Science*, Vol. 23, No. 6, pp. 263 - 271.

Goldstein, M. E., and Braun, W. H., 1971, Effect of Velocity Slip at a Porous Boundary on the Performance of an Incompressible Porous Bearing, NASA Technical Note D-6181, pp. 1 - 36.

Gosman, A. D., Pun, W. M., Runchal, A. K., Spalding, D. B., and Wolfshtein, M., 1969, *Heat and Mass Transfer in Recirculating Flows*, Academic Press, London.

Guha, S. K., 1986, Study of Conical Whirl Instability of Externally Pressurized Porous Oil Bearings with Tangential Velocity Slip, *Journal of Tribology*, Vol. 108, No. 2, pp. 256 - 261.

Gururajan, K., and Prakash, J., 1999, Surface Roughness Effects in Infinitely Long Porous Journal Bearings, *Journal of Tribology*, Vol. 121, No. 1, pp. 139 - 147.

Hartline, B., and Lister, C. R. B., 1977, Thermal Convection in a Hele-Shaw Cell, *Journal of Fluid Mechanics*, Vol. 79, pp. 379 - 389.

Hele-Shaw, H. S., 1898a, The Flow of Water, *Nature*, Vol. 58, No. 1489, pp. 34 - 36.

Hele-Shaw, H. S., 1898b, Investigation of the Nature of Surface Resistances of Water and of Streamline Motion under Certain Experimental Conditions, *Transaction of Institute of Naval Architect*, London, Vol. 40, pp. 218 - 221.

Hele-Shaw, H. S., and Hay, A., 1900, *Philosophical Transactions, Royal Society of London Series A*, Vol. 195, pp. 303 - 308.

Heuberger, J. H., 1961, Behavior of Lubricants in Porous Bearings, *Powder Metallurgy*, ed. W. Leszynski, Wiley Interscience, New York, pp. 819 - 823.

Himasekhar, K., and Bau, H. H., 1986, Large Rayleigh Number Convection in a Horizontal, Eccentric Annulus Containing Saturated Porous Media, *International Journal of Heat and Mass Transfer*, Vol. 29, No. 5, pp. 703 - 712.

Horne, R. N., and O'Sullivan, M. J., 1974, Oscillatory Convection in a Porous Medium Heated From Below, *Journal of Fluid Mechanics*, Vol. 66, pp. 339 - 352.

Huetz, J., and Petit, J. P., 1974, Natural and Mixed Convection in Concentric Annular Spaces – Experimental and Theoretical Results for Liquid Metals, *5<sup>th</sup> International Heat Transfer Conference*, Tokyo, Vol. 3, pp. 169 - 172.

Ishimoto, J., Okubo, M., Kamiyama, S., and Higashitani, M., 1995, Bubble Behavior in Magnetic Fluid under a Nonuniform Magnetic Field, *JSME International Journal, Series B*, Vol. 38, No. 3, pp. 382 - 387.

Ishizawa, S., and Hori, E., 1966, The Flow of a Viscous Fluid through a Porous Wall into a Narrow Gap, *Bulletin of JSME*, Vol. 9, No.36, pp. 719 - 730.

Jischke, M. C., and Farshchi, M., 1980, Boundary Layer Regime for Laminar Free Convection between Horizontal Circular Cylinders, *Journal of Heat Transfer*, Vol. 102, pp. 228 - 235.

Joseph, D. D., and Tao, L. N., 1966, Lubrication of a Porous Bearing - Stokes' Solution, *Journal of Applied Mechanics*, Vol. 33, No. 4, pp. 753 - 760.

Kaneko, S., 1989a, Application of Porous Materials to Annular Plain Seals: Part I - Static Characteristics, *Journal of Tribology*, Vol. 111, No. 4, pp. 655 - 660.

Kaneko, S., 1989b, Static and Dynamic Characteristics of Porous Journal Bearings with Anisotropic Permeability, *JSME International Journal*, Series 3: Vibration, Control Engineering, Vol. 32, No. 1, pp. 91 -99.

Kaneko, S., and Doi, Y., 1989, Static and Dynamic Characteristics of Porous Journal Bearings with Nonuniform Permeability, *JSME International Journal*, Series 3: Vibration, Control Engineering, Vol. 32, No. 2, pp. 294 -302.

Kaneko, S., and Hashimoto, Y., 1995, A Study of the Mechanism of Lubrication in Porous Journal Bearings: Effects of Dimensionless Oil-Feed Pressure on Frictional Characteristics, *Journal of Tribology*, Vol. 117, No. 2, pp. 291 - 296.

Kaneko, S., Hashimoto, Y., and Hiroki, I., 1997, Analysis of Oil-Film Pressure Distribution in Porous Journal Bearings under Hydrodynamic Lubrication Condition Using an Improved Boundary Condition, *Journal of Tribology*, Vol. 119, No. 1, pp. 171 - 178.

Kaneko, S., Inoue, H., and Ushio, K., 1994a, Experimental Study on Mechanism of Lubrication in Porous Journal Bearings. No Oil Film Formed in Bearing Clearance, *JSME International Journal*, Series C, Vol. 37, No. 1, pp. 185 - 192.

Kaneko, S., and Obara, S., 1990, Experimental Investigation of Mechanism of Lubrication in Porous Journal Bearings: Part 1 - Observation of Oil Flow in Porous Matrix, *Journal of Tribology*, Vol. 112, No. 4, pp. 618 - 630.

Kaneko, S., Ohkawa, Y., and Hashimoto, Y., 1994b, A Study of the Mechanism of Lubrication in Porous Journal Bearings: Effects of Dimensionless Oil-Feed Pressure on Static Characteristics under Hydrodynamic Lubrication Conditions, *Journal of Lubrication Technology*, Vol. 116, No. 3, pp. 606 - 611.

Kaneko, S., Takabatake, H., and Ito, K., 1999, Numerical Analysis of Static Characteristics at Start of Operation in Porous Journal Bearings with Sealed Ends, *Journal of Tribology*, Vol. 121, No. 1, pp. 62 - 68.

Kataoka, K., and Takigawa, T., 1981, *Intermixing over Cell Boundary between Taylor Vortices*, AIChE Journal, Vol. 27, No. 3, pp. 504 - 508.

Khonsari, M. M., and Booser, E. R., 2001, *Applied Tribology: Bearing Design and Lubrication*, John Wiley & Sons, Inc., New York.

Koster, J. N., 1983, Interferometric Investigation of Convection in Plexiglas Boxes, *Experiments in Fluids*, Vol. 1, pp. 121 - 128.

Koster, J. N., and Müller, U., 1980, Free Convection in Vertical Slots, *Natural Convection in Enclosures*, ed. I. Catton and K. E. Torrance, ASME-HTD, Vol. 8, pp. 27 - 30.

Koster, J. N., and Müller, U., 1981, Time-Dependent Free Convection in Vertical Slots, *Physical Reviews Letters*, Vol. 47, pp. 1599 - 1601.

Koster, J. N., and Müller, U., 1982, Free Convection in Vertical Gaps, *Journal of Fluid Mechanics*, Vol. 125, pp. 429 - 451.

Koster, J. N., and Müller, U., 1983, Visualization of Free Convective Flow in Hele-Shaw Cells, *Flow Visualization III: Proceedings of the Third International Symposium of Flow*, September 6 - 9, University of Michigan, Ann Harbor, Michigan, USA.

Koster, J. N., and Müller, U., 1984, Oscillatory Convection in Vertical Slots, *Journal of Fluid Mechanics*, Vol. 139, pp. 363 - 390.

Kuehn, T. H., and Goldstein, R. J., 1976, An Experimental and Theoretical Study of Natural Convection in the Annulus between Horizontal Concentric Cylinders, *Journal of Fluid Mechanics*, Vol. 74, pp. 695 - 719.

Kuehn, T. H., and Goldstein, R. J., 1980, An Parametric Study of Prandtl Number and Diameter Ratio Effects on Natural Convection Heat Transfer in Horizontal Cylindrical Annuli, *Journal of Heat Transfer*, Vol. 102, pp. 768 - 770.

Kulkarni, S. V., and Kumar, V., 1975, Lubrication Equation for Non-Isotropic Porous Bearings Considering Slip Velocity, *Journal of the Institute of Engineers (India)*, Vol. 56, Part ME, pp. 110 - 112.

Kumar, A., 1998, Conical Whirl Instability of Turbulent Flow Hybrid Porous Journal Bearings, *Tribology International*, Vol. 31, No. 5, pp. 235 - 243.

Kumar, A., and Kumar, P., 1996, An Application of Short Bearing Theory to Analyse the Effect of Variable Permeability on Steady State Performance of Turbulent Hydrodynamic Porous Journal Bearings, *Indian Journal of Engineering and Materials Sciences*, Vol. 3, No. 2, pp. 57 - 62.

Kumar, A., and Rao, N. S., 1992, Turbulent Hybrid Journal Bearings with Porous Bush: A Steady State Performance, *Wear*, Vol. 154, No. 1, pp. 23 - 35.

Kumar, A., and Rao, N. S., 1993, Steady State Performance of Finite Hydrodynamic Porous Journal Bearings in Turbulent Regimes, *Wear*, Vol. 167, pp. 121 - 126.

Kumar, A., and Rao, N. S., 1994, Stability of a Rigid Rotor in Turbulent Hybrid Porous Journal Bearings, *Tribology International*, Vol. 27, No. 5, pp. 299 - 305.

Kumar, V., 1973, Characteristics of Partial Porous Journal Bearings of Finite Length Considering Curvature and Slip Velocity, *Wear*, Vol. 26, No. 3, pp. 355 - 367.

Kumar, V., 1976, Elastic and Damping Properties of Partial Porous Journal Bearings of Finite Length and Arbitrary Wall Thickness Taking Film Curvature and Slip Flow into Account, *Wear*, Vol. 40, No. 3, pp. 293 - 308.

Kumar, V., 1978, A Lubrication Equation Including Slip Velocity for Hydrodynamic Porous Bearings in the Lower Turbulent Regime - A Perturbation Approach, *Wear*, Vol. 51, No. 1, pp. 25 - 37.

Kumar, V., 1979, Linearized Turbulent Lubrication Equation for Finite Self-Acting Porous Bearings Considering Slip Velocity over a Hydrodynamically Rough Permeable Boundary, *Wear*, Vol. 53, pp. 263 - 277.

Kumar, V., 1980a, Porous Metal Bearings - A Critical Review, *Wear*, Vol. 63, pp. 271 - 287.

Kumar, V., 1980b, Estimation of the Performance of a Narrow Porous Journal Bearing with Hydrodynamic Turbulent Lubrication Considering Slip Velocity and Arbitrary Wall Thickness, *Wear*, Vol. 64, No. 2, pp. 355 - 365.

Kumar, V., 1981a, Theoretical Hydrodynamic Load Capacity of an Axially Undefined Full Porous Journal Bearing in the Turbulent Regime Considering Slip Velocity and Curvature, *Wear*, Vol. 65, No. 3, pp. 277 - 284.

Kumar, V., 1981b, Hydrodynamic Load Capacity of a Full Porous Journal Bearing of Finite Length in the Turbulent Regime Considering Slip Flow and Curvature, *Wear*, Vol. 67, No. 2, pp. 167 - 176.

Kumar, V., 1983, Exact Mathematical Analysis for the Determination of Performance Characteristics of Thin Partial Porous Metal Bearings of Infinite Length, *Wear*, Vol. 86, No. 1, pp. 11 - 20.



Kumar, V., 1987, Analysis of Self Acting Sintered Partial Porous Journal Bearing of Finite Length in the Turbulent Regime with Slip and Curvature Considerations, *Journal of the Institute of Engineers (India)*, Vol. 68, Part 1-2, pp. 41 - 47.

Kumar, V., and Wadhwa, A. D., 1984, Performance Characteristics of Narrow Partial Porous Metal Journal Bearings, *Mechanical Engineering Bulletin*, Vol. 15, No. 3, pp. 77 - 80.

Lauder, B. E., and Ying, W. M., 1972, Numerical Solutions of Flow between Rotating Cylinders, *Journal of Mechanical Engineering Science*, Vol. 14, No. 6, pp. 400 - 403.

Lauder, B. E., and Ying, W. M., 1974, Laminar Heat Transfer in Rotating Eccentric Annuli, *Journal of Mechanical Engineering Science*, Vol. 16, No. 5, pp. 306 - 309.

Leong, J. C., and Lai, F. C., 2001, Effective Permeability of a Layered Porous Cavity, *Journal of Heat Transfer*, Vol. 123, pp. 512 - 519.

Lin, J. R., 1995, Dynamic Behavior of Pure Squeeze Films in Short Porous Journal Bearings Using the Brinkman Model, *Journal of Physics D: Applied Physics*, Vol. 28, No. 10, pp. 2188 - 2196.

Lin, J. R., and Hwang, C. C., 1993, Lubrication of Short Porous Journal Bearings -- Use of the Brinkman-Extended Darcy Model, *Wear*, Vol. 161, No.1-2, pp. 93 - 104.

Lin, J. R., and Hwang, C. C., 1994a, Hydrodynamic Lubrication of Finite Porous Journal Bearings: Use of the Brinkman-Extended Darcy Model, *International Journal of Mechanical Sciences*, Vol. 36, No. 7, pp. 631 - 644.

Lin, J. R., and Hwang, C. C., 1994b, Static and Dynamic Characteristics of Long Porous Journal Bearings: Use of the Brinkman-Extended Darcy Model, *Journal of Physics D: Applied Physics*, Vol. 27, No. 3, pp. 635 - 643.

Lin, J. R., and Hwang, C. C., 1994c, Linear Stability Analysis of Short Porous Journal Bearings: Use of the Brinkman-Extended Darcy Model, *Journal of Tribology*, Vol. 117, No. 1, pp. 199 - 202.

Lin, J. R., and Hwang, C. C., 1994d, Linear Stability Analysis of Finite Porous Journal Bearings: Use of the Brinkman-Extended Darcy Model, *International Journal of Mechanical Sciences*, Vol. 36, No. 7, pp. 645 - 658.

Lin, J. R., and Hwang, C. C., 1995, On the Lubrication of Short Porous Journal Bearings: Use of the Brinkman Model, *Journal of Tribology*, Vol. 117, No. 1, pp. 196 - 199.

Lin, J. R., Hwang, C. C., and Yang, R. F., 1996, Hydrodynamic Lubrication of Long, Flexible, Porous Journal Bearings Using the Brinkman Model, *Wear*, Vol. 198, No.1-2, pp. 156 - 164.

Linn, F. C., 1969, Lubrication of Animal Joints, *Journal of Lubrication Technology*, Vol. 91, No. 2, pp. 329 - 341.

Mack, L. R., and Bishop, E. H., 1968, Natural Convection between Horizontal Concentric Cylinders for Low Rayleigh Numbers, *Quarterly Journal of Mechanics and Applied Mathematics*, Vol. 21, pp. 223 - 241.

Majumdar, B. C., and Rao, N. S., 1979, On the Analysis Solution of Hydrodynamic Oil Porous Journal Bearings, *Proceedings of the National Conference On Indian Tribology*, Vol. 1, pp. 70 - 80.

Mak, W. C., and Conway, H. D., 1977a, Analysis of a Short, Porous, Flexible Journal Bearing, *International Journal of Mechanical Sciences*, Vol. 19, No. 5, pp. 295 - 300.

Mak, W. C., and Conway, H. D., 1977b, The Lubrication of a Long, Porous, Flexible Journal Bearing, *Journal of Lubrication Technology*, Vol. 99, No. 4, pp. 449 - 454.

Mak, W. C., and Conway, H. D., 1978, Effects of Velocity Slip on the Elastohydrodynamic Lubrication of Short, Porous Journal Bearings, *International Journal of Mechanical Sciences*, Vol. 20, No. 11, pp. 767 - 775.

Malashetty, M. S., Umavathi, J. C., and Prathap Kumar, J., 2001, Convective Flow and Heat Transfer in an Inclined Composite Porous Medium, *Journal of Porous Media*, Vol. 4, No. 1, pp. 15 - 22.

Malik, M., Chandra, M., and Sinhasan, R., 1981a, Analysis of a Centrally Loaded 120 Degree Partial Porous Journal Bearing Taking Tangential Velocity Slip Into Account, *Journal of Mechanical Engineering Science*, Vol. 23, No. 4, pp. 171 - 178.

Malik, M., Sinhasan, R., and Chandra, M., 1981b, On the Performance Characteristics of Three-Lobe Porous Hydrodynamic Journal Bearings, *ASLE Transaction*, Vol. 24, No. 3, pp. 354 - 361.

Måløy, K. J., and Goldburg, W., 1993, Spatial Anisotropy of Velocity Fluctuations on Small Length Scales in a Taylor-Couette Cell, *Physical Review E*, Vol. 48, No. 1, pp. 322 - 327.

McCloud, K. V., and Maher, J. V., 1996, Growth-Direction Dependent of Steady-State Saffman-Taylor Flow in an Anisotropic Hele-Shaw Cell, *Physical Review E*, Vol. 54, No. 2, pp. 1625 - 1629.

Meena, S., and Kandaswamy, P., 2001. Effect of Slip on the Flow between Eccentric Cylinders, *Journal of Porous Media*, Vol. 4, No. 1, pp. 79 - 88.

Meurisse, M., and Giudicelli, B., 1999, A 3D Conservative Model for Self-Lubricated Porous Journal Bearings in a Hydrodynamic Steady State, *Journal of Tribology*, Vol. 121, No. 3, pp. 529 - 537.

Mitani, H., and Yokota, M., 1973. Bearing Performance of Oil Impregnated Aluminum Bronze Sintered Bearings, *Journal of the Japanese Society of Powder and Powder Metallurgy*, Vol. 20, No. 4, pp. 113 - 120.

Mokhtar, M. O. A., Rafaat, M., and Shawki, G. S. A., 1984, Experimental Investigations into the Performance of Porous Journal Bearings, SAE Technical Paper No. 840097.

Moon, P., and Spencer, D. E., 1971, *Field Theory Handbook*, Springer-Verlag, New York.

Morgan, V. T., 1957. Study of Design Criteria of Porous Metal Bearings, *Proceedings of the 1957 Conference on Lubrication and Wear*, Institute of Mechanical Engineers, London, Paper 88, pp. 405 - 408.

Morgan, V. T., 1963, The Effect of Porosity on Some of the Physical Properties of Powder Metallurgy Components, *Powder Metallurgy*, Vol. 12, pp. 72 - 86.

Morgan, V. T., 1964, Hydrodynamic Porous Metal Bearings, *Lubrication Engineering*, Vol. 20, No. 11, pp. 448 - 455.

Morgan, V. T., 1965, Closure to Discussion on Porous Metal Bearings, *Lubrication Engineering*, Vol. 21, No. 1, pp. 33.

Morgan, V. T., 1966, Porous Metal Bearings, Chapter 24, *Principles of Lubrication*, ed. A. Cameron, Longmans, London, pp. 542 - 559.

Morgan, V. T., 1969a, Porous Metal Bearings, *Powder Metallurgy*, Vol. 12, No. 24, pp. 426 - 451.

Morgan, V. T., 1969b, Porous Metal Bearings, *Tribology*, Vol. 2, pp. 107 - 115.

Morgan, V. T., 1970, Tribology in Powder Metallurgy, *Tribology*, Vol. 3, pp. 111 - 112.

Morgan, V. T., and Cameron, A., 1957, Mechanism of Lubrication in Porous Metal Bearings, *Proceedings of the 1957 Conference on Lubrication and Wear*, Institution of Mechanical Engineers, London, Paper 89, pp. 151 - 157.

Murti, P. R. K., 1971a, Pressure Distribution in Narrow Porous Bearings, *Journal of Lubrication Technology*, Vol. 93, No. 4, pp. 512 - 513.

Murti, P. R. K., 1971b, Hydrodynamic Lubrication of Long Porous Bearings, *Wear*, Vol. 18, No. 6, pp. 449 - 460.

Murti, P. R. K., 1972a, Hydrodynamic Lubrication of Short Porous Bearings, *Wear*, Vol. 19, No. 1, pp. 17 - 25.

Murti, P. R. K., 1972b, Hydrodynamic Lubrication of Finite Porous Bearings, *Wear*, Vol. 19, No. 1, pp. 113 - 115.

Murti, P. R. K., 1972c, Some Aspects of Slip-Flow in Porous Bearings, *Wear*, Vol. 19, No. 2, pp. 123 - 129.

Murti, P. R. K., 1973a, Discussion on "Lubrication of Porous Journal Bearings, *Journal of Lubrication Technology*, Vol. 95, No. 2, pp. 259 - 260.

Murti, P. R. K., 1973b, Lubrication of Narrow Porous Bearings with Arbitrary Wall Thickness, *Journal of Lubrication Technology*, Vol. 95, No. 4, pp. 511- 517.

Murti, P. R. K., 1973c, Lubrication of Finite Porous Journal Bearings, *Wear*, Vol. 26, No. 1, pp. 95 - 104.

Murti, P. R. K., 1973d, Effect of Slip-Flow on Pressure Distribution in Narrow Porous Bearings, *Wear*, Vol. 25, pp. 365 - 372.

Murti, P. R. K., 1973e, Effect of Slip-Flow in Narrow Porous Bearings, *Journal of Lubrication Technology*, Vol. 95, No. 4, pp. 518 - 523.

Murti, P. R. K., 1975, Effect of Slip Flow in Narrow Porous Bearings with Arbitrary Wall Thickness, *Journal of Applied Mechanics*, Vol. 42, No. 2, pp. 305 - 310.

Murti, P. R. K., 1976, Author Closure on "Effect of Slip Flow in Narrow Porous Bearings with Arbitrary Wall Thickness", *Journal of Applied Mechanics*, Vol. 43, No. 2, pp. 373.

Nakoryakov, V. E., Zhak, V. D., and Safonov, S. A., 1991, Flow in a Hele-Shaw Cell at Large Velocities, *Russian Journal of Engineering Thermophysics*, Vol. 1, pp. 1 - 23.

Neale, G., and Nader, W., 1974, Practical Significance of Brinkman's Extension of Darcy's Law: Coupled Parallel Flows within a Channel and a Bounding Porous Medium, *Journal of Chemical Engineering*, Vol. 52, pp. 475 - 478.

Nield, D. A., and Bejan, A., 1999, *Convective in Porous Media*, 2<sup>nd</sup> ed., Springer, New York.

Ocvirk, F. W., 1952, Short-Bearing Approximation for Full Journal Bearings, National Advisory Committee of Aeronautics NACA, Technical Note 2808.

Ohmura, N., Kataoka, K., Mizumoto, T., Nakata, M. and Matsumoto, K., 1995, Effect of Vortex Cell Structure on Bifurcation Properties in a Taylor Vortex Flow System, *Journal of Chemical Engineering of Japan*, Vol. 28, No. 6, pp. 758 - 764.

Ohmura, N., Kataoka, K., Shibata, Y., and Makino, T., 1997, Effective Mass Diffusion over Boundaries in a Taylor-Couette Flow System, *Chemical Engineering Science*, Vol. 52, No. 11, pp. 1757 - 1765.

Ozisik, M. N., 1968, *Boundary Value Problems of Heat Conduction*, International Textbook Company, Pennsylvania.

Pan, C. P., and Lai, F. C., 1995, Natural convection in horizontal-layered porous annuli, *Journal of Thermophysics and Heat Transfer*, Vol. 9, No. 4, pp. 792 - 795.

Patankar, S. V., 1980, *Numerical Heat Transfer and Fluid Flow*, Hemisphere Publishing Corporation, New York.

Perumal, P. I., and Raman, R., 1985, Experimental Study on the Effect of Bearing Wall Thickness and Bearing Length on the Frictional Characteristics of Sintered Bearings, *Wear*, Vol. 104, pp. 287 - 296.

Powe, R. E., Carley, C. T., and Bishop, E. H., 1969, Free Convective Flow Patterns in Cylindrical Annuli, *Journal of Heat Transfer*, Vol. 91, No. 3, pp. 310 - 314.

Powe, R. E., Carley, C. T., and Carruth, S. L., 1971, A Numerical Solution for Natural Convection in Cylindrical Annuli, *Journal of Heat Transfer*, Vol. 93, No. 2, pp. 210 - 220.

Prakash, J., and Vij, S. K., 1972, Axially Undefined Porous Journal Bearing Considering Cavitation, *Wear*, Vol. 22, No. 1, pp. 1 - 14.

Prakash, J., and Vij, S. K., 1974, Analysis of Narrow Porous Bearings Using the Beavers-Joseph Criterion of Slip Velocity, *Journal of Applied Mechanics*, Vol. 41, No. 2, pp. 348 - 354.

Prakash, J., and Vij, S. K., 1976, Effect of Velocity Slip in Axially Undefined Porous Bearings, *Wear*, Vol. 38, No. 2, pp. 245 - 263.

Pratt, G. C., 1969, A Review of Sintered Metal Bearing Their Production, Properties, and Performance, *Powder Metallurgy*, Vol. 12, No.24, pp. 356 - 385.

Quan, Y., and Wang, P., 1985, Theoretical Analysis and Experimental Investigation of a Porous Metal Bearing, *Tribology International*, Vol. 18, No. 2, pp. 67 - 73.

Quan, Y., Ma, J., Tian, Y., Zhou, G., Shi, G., and Wang, G., 1985, Investigation of Sintered Bronze Bearings under High-Speed Conditions, *Tribology International*, Vol. 18, No. 2, pp. 75 - 80.

Raman, R., and Chennabasavan, T. S., 1998, Experimental Investigations of Porous Bearings under Vertical Sinusoidally Fluctuating Loads, *Tribology International*, Vol. 31, No. 6, pp. 325 - 330.

Raman, R., and Vinod Babu, L., 1984, Tests on Sintered Bearings with Reduced Oil Contents, *Wear*, Vol. 95, pp. 263 - 269.

Rana, R., 1977, *Numerical Simulation of Free Convection in a Multi-layer Geothermal Reservoir*, M. S. Thesis, Department of Mechanical Engineering, University of Hawaii, Hawaii.

Rana, R., Horne, R. N., and Cheng, P., 1979, Natural Convection in a Multi-layered Geothermal Reservoir, *Journal of Heat Transfer*, Vol. 101, pp. 411 - 416.



Reason, B. R., and Dyer, D., 1973, A Numerical Solution for the Hydrodynamic Lubrication of Finite Porous Journal Bearings, *Proceedings of the Institution of Mechanical Engineers*, Vol. 187, No. 7, pp. 71 - 78.

Reason, B. R., and Siew, A. H., 1985, A Refined Numerical Solution for the Hydrodynamic Lubrication of Finite Porous Journal Bearings, *Proceedings of the Institute Mechanical Engineering*, Part C: Mechanical Engineering Science, Vol. 199, No. 2, pp. 85 - 93.

Reddy, J. N., and Rasmussen, M. L., 1990, *Advanced Engineering Analysis*, Robert E. Krieger Publishing Company, Malabar, Florida.

Reynolds, O., 1886, On the Theory of Lubrication and Application to Mr. BEAUCHAMP TOWER's Experiments. Including an Experimental Determination of the Viscosity of Olive Oil, *Philosophical Transactions of the Royal Society of London*, Vol. 177, Part 1, pp. 157 - 234.

Rhodes, C. A., and Rouleau, W. T., 1965, Hydrodynamic Lubrication of Narrow Porous Metal Bearings with Seal Ends, *Wear*, Vol. 8, pp. 474 - 486.

Rhodes, C. A., and Rouleau, W. T., 1966, Hydrodynamics of Partial Porous Metal Bearings, *Journal of Basic Engineering*, Vol. 88, No. 1, pp. 53 - 60.

Rohde, S. M., 1973, Bounds for the Solution of Reynolds Equation, *Journal of Lubrication Technology*, Vol. 95, pp. 102 - 104.

Rouleau, W. T., 1962, A Note on the Lubrication of Porous Bearings, *Journal of Basic Engineering*, Vol. 84, No. 1, pp. 205 - 206.

Rouleau, W. T., 1963, Hydrodynamic Lubrication of Narrow Press-Fitted Porous Metal Bearings, *Journal of Basic Engineering*, Vol. 85, No. 1, pp. 123 - 128.

Rouleau, W. T., 1967, Discussion on "Lubrication of a Porous Bearing - Reynolds Solution", *Journal of Applied Mechanics*, Vol. 34, No. 2, pp. 525 - 526.

Rouleau, W. T., 1975, Discussion on "Effect of Slip Flow in Narrow Porous Bearings With Arbitrary Wall Thickness", *Journal of Applied Mechanics*, Vol. 42, No. 4, pp. 909.

Rouleau, W. T., and Steiner, L. I., 1974, Hydrodynamic Porous Journal Bearings. Part I - Finite Full Bearings, *Journal of Lubrication Technology*, Vol. 96, No. 3, pp. 346 - 353.

Saffman, P. G., and Taylor, Sir. G., 1958, *Proceedings of Royal Society, Series A*, Vol. 245, pp. 312 - 329.

Scott, J. J., 1963, Selecting the Right Lubricant for Self Lubricating Bearings and Parts, *Progress in Powder Metallurgy*, Vol. 19, pp. 127 - 134.

Shawki, G. S. A., Mokhtar, M. O. A., and Rafaat, M., 1984, Analysis of Porous Journal Bearings- Performance and Optimization, SAE Technical Paper No. 840098.

Shir, C. C., 1965, *The Lubrication of Porous Bearings*, M.S. Thesis, University of Minnesota, MN.

Shir, C. C., and Joseph, D. D., 1966, Lubrication of Porous Bearings - Reynolds' Solution, *Journal of Applied Mechanics*, Vol. 33, No. 4, pp. 761 - 767.

Singh, D. V., and Sinhasan, R., 1974, Stability and Relative Stability of Porous Journal Bearing System with Axes Skewed, *Journal of Lubrication Technology*, Vol. 96, No. 4, pp. 621 - 630.

Sinhasan, R., Malik, M., and Chandra, M., 1980, Analysis of Two-Lobe Porous Hydrodynamic Journal Bearings, *Wear*, Vol. 64, No. 2, pp. 339 - 353.

Sneck, H. J., 1967, A Mathematical Analog for Determination of Porous Metal Bearing Performance Characteristics, *Journal of Lubrication Technology*, Vol. 89, No. 2, pp. 222 - 226.

Sommerfeld, A., 1904, Zur Hydrodynamisch Theorie der Schmiermittelreibung, *Zeitschrift für Mathematische Physik*, Vol. 50, pp. 97 - 155.

Sowmyan, T., and Raman, R., 1977, Theoretical Performance Characteristics of Spherical Sintered Bearings, *Wear*, Vol. 43, No. 3, pp. 293 - 300.

Srinivasan, U., 1977, Load Capacity and Time-Height Relations for Squeeze Films between Double-Layered Porous Plates, *Wear*, Vol. 43, No. 2, pp. 157 - 168.

Steiner, L. I., 1970, *A Numerical Solution for the Hydrodynamic Porous Journal Bearing*, Ph.D. Dissertation, Carnegie-Mellon University, Pittsburgh, PA.

Storchheim, S., and Witt, R., 1962, Porous Aluminum Bearings, *Product Engineer*, Vol. 33, No. 7, pp. 53 - 55.

Szeri, A. Z., 1998, *Fluid Film Lubrication: Theory and Design*, Cambridge University Press, New York.

Tandon, P. N., Gupta, R. S., Dwivedi, A. P., Banerjee, M. B., and Dube, S. N., 1983, Effect of Rotation in the Lubrication of a Short Porous Journal Bearing: A Simple Model for Hip Joints, *Wear*, Vol. 87, No. 2, pp. 123 - 131.

Taylor, G. I., 1923, Stability of Viscous Liquid Contained between Two Rotating Cylinders, *Philosophical Transactions of the Royal Society of London. Series A*, Vol. 223, pp. 289 - 343.

Tian, Y., 1998, Static Study of the Porous Bearings by the Simplified Finite Element Analysis, *Wear*, Vol. 218, No. 2, pp. 203 - 209.

Van Dyke, M., 1982, *An Album of Fluid Motion*, Parabolic Press, Stanford, California.

Verma, P. D. S., 1983, Double Layer Porous Journal Bearing Analysis, *Mechanics of Materials*, Vol. 2, No. 3, pp. 233 - 238.

Wada, S., and Kawakami, Y., 1986, Hydrodynamic Lubrication of Porous Journal Bearings with Grease, *Bulletin of JSME*, Vol. 29, No. 249, pp. 943 - 949.

Wada, S., Nishiyama, N., and Nishida, S., 1985, Modified Darcy's Law for Non-Newtonian Fluids, *Bulletin of JSME*, Vol. 28, No. 246, pp. 3031 - 3037.

Williams, D. L., Von Herzen, R. P., Sclater, J. G., and Anderson, R. N., 1974, The Galapagos Spreading Centre: Lithospheric Cooling and Hydrothermal Circulation, *Geophysical Journal of Royal Astronomical Society*, Vol. 38, pp. 587 - 608.

Williams, J. A., 1994, *Engineering Tribology*, Oxford University Press, Oxford.

Wood, W. W., 1957, The Asymptotic Expansion at Large Reynolds Numbers for Steady Motion between Non-coaxial Rotating Cylinders, *Journal of Fluid Mechanics*, Vol. 3, Part 2, pp. 159 - 175.

Wooding, R. A., 1960, Instability of a Viscous Liquid of Variable Density in a Vertical Hele-Shaw Cell, *Journal of Fluid Mechanics*, Vol. 7, pp. 501 - 515.

Yang, L., and Farouk, B., 1992, Three-dimensional Mixed Convection Flows in a Horizontal Annulus with a Heated Rotating Inner Circular Cylinder, *International Journal of Heat and Mass Transfer*, Vol. 35, No. 8, pp. 1947 - 1956.

Yang, W., 1989, *Handbook of Flow Visualization*, Hemisphere Publishing Corporation, New York.

- Yang, W., 1994, *Computer-Assisted Flow Visualization Second Generation Technology*, CRC Press, Boca Raton, Florida.
- Yankovich, M. R., and Stevanovich, M., 1996a, Coefficients of Sliding Friction of Porous Bearings When  $PV = \text{Constant}$ , *Chemical and Petroleum Engineering*, Vol. 32, No. 1, pp. 9 - 11.
- Yankovich, M. R., and Stevanovich, M., 1996b, Calculation of a Structural Parameter for Porous Tin-Bronze Bearings, *Chemical and Petroleum Engineering*, Vol. 32, No. 1, pp. 12 - 15.
- Yao, L. S., 1980, Analysis of Heat Transfer in Slightly Eccentric Annuli, *Journal of Heat Transfer*, Vol. 102, pp. 279 - 284.
- Youssef, H., and Eudier, M., 1966, Production and Properties of a New Porous Bearings, *Modern Developments in Powder Metallurgy*, Vol. 3, pp. 129 - 137.
- Yung, K. M., and Cameron, A., 1979, Optical Analysis of Porous Metal Bearings, *Journal of Lubrication Technology*, Vol. 101, No. 1, pp. 99 - 104.
- Zaheeruddin, Kh., 1980, One-Dimensional Porous Journal Bearing Lubricated with Micropolar Fluid, *Wear*, Vol. 63, No. 2, pp. 257 - 270.
- Zhang, S. P., Yan, L., and Li, Q., 1992, Development of Porous Squeeze Film Damper Bearings for Improving the Blade Loss Dynamics of Rotor-Support Systems, *Journal of Vibration and Acoustics*, Vol. 114, No. 3, pp. 347 - 353.
- Zhilinskii, V. A., and Zozulya, V. D., 1977, Performance of Porous Bearings in Electric Motors, *Soviet Powder Metallurgy and Metal Ceramics*, Vol. 16, No. 1, PP. 70 - 73.

## APPENDIX A

### DERIVATION OF PERTURBED BOUNDARY CONDITION

Taylor's series expansion is given by

$$\phi|_{x+\Delta x} = \phi|_x + \frac{\partial \phi}{\partial x} \bigg|_x (\Delta x) + \dots \quad (\text{A.1})$$

Using above expansion, the velocity at  $R = (a/b) + \varepsilon \cos \theta$  can be expressed in the following fashion.

$$V|_{(a/b) + \varepsilon \cos \theta} = V|_{a/b} + \frac{\partial V}{\partial R} \bigg|_{a/b} (\varepsilon \cos \theta) + \dots \quad (\text{A.2})$$

Recall that the solution is assumed to have the following form

$$V = V_0 + \varepsilon \cos \theta V_1 + \dots \quad (\text{A.3})$$

Substitute equation (A.3) into equation (A.2) and apply the boundary condition,  $V = 1$  at  $R = (a/b) + \varepsilon \cos \theta$ , one obtains.

$$1 = [V_0|_{a/b} + \varepsilon \cos \theta V_1|_{a/b} + \dots] + \varepsilon \cos \theta [V_0'|_{a/b} + \varepsilon \cos \theta V_1'|_{a/b} + \dots] + \dots \quad (\text{A.4})$$

Here, the prime represents the partial derivative with respect to  $R$ . Equation (A.4) can be arranged to give,

$$1 = V_0 + \varepsilon \cos \theta (V_1 + V_0') + \dots \quad (\text{A.5})$$

Alternatively, the same expression can be obtained as follows. Substitute the boundary condition into equation (A.3) to obtain

$$1 = V_0|_{(a/b) + \varepsilon \cos \theta} + \varepsilon \cos \theta V_1|_{(a/b) + \varepsilon \cos \theta} + \dots \quad (\text{A.6})$$

Now, expanding the velocity terms using Taylor's series expansion, one obtains

$$1 = \left( V_0|_{a,b} + V_0'|_{a,b} \varepsilon \cos \theta + \dots \right) + \varepsilon \cos \theta \left( V_1|_{a,b} + V_1'|_{a,b} \varepsilon \cos \theta + \dots \right) + \dots \quad (\text{A.7})$$

Collect the terms of the same order of  $\varepsilon$  and rearrange the terms, one yields

$$1 = V_0' + \varepsilon \cos \theta (V_0' + V_1') + \dots \quad (\text{A.8})$$

Apparently, equations (A.5) and (A.8) are identical. This serves as a double check for the correct expansion of  $V'$  at  $R = a/b$ .

## APPENDIX B

### MATHCAD CALCULATION FOR FORCED CONVECTION

This appendix presents a sample of worksheet that performs the calculations for flow and temperature fields in Chapter Two using Mathcad 2000 Professional, ©1986-1999 MathSoft, Inc.

#### Couette Flow in Cylindrical Coordinate System

##### Notes:

layer 1: fluid layer  
layer 2: porous layer (Brinkman's model)

##### Governing Parameters:

Inner radius	$a \equiv 1$	Darcy number	$Da \equiv 10^{-2}$
Interface radius	$b \equiv 1.5$	Brinkman number	$Br \equiv 1$
Outer radius	$c \equiv 2$	Thermal conductivity ratio $k_1/k_2$	$k \equiv 1$
eccentricity ratio	$\varepsilon \equiv 0.1$		

##### Plotting Parameters:

$$\theta \equiv 90 \cdot \text{deg} \quad d := 0.05 \left( 1 - \frac{a}{b} \right)$$

$$i := \frac{a}{b}, \frac{a}{b} \cdot (1 + d) \dots 1 \quad j := 1, 1 + d \dots \frac{c}{b}$$

#### (a) Calculation for the velocity field

##### Declaration of Constants and Functions:

$$\gamma := \sqrt{\frac{1}{Da}}$$

$$f_1 := K0(\gamma) \cdot I0\left(\gamma \cdot \frac{c}{b}\right) - K0\left(\gamma \cdot \frac{c}{b}\right) \cdot I0(\gamma)$$

$$f_2 := \gamma \cdot \left( K0\left(\gamma \cdot \frac{c}{b}\right) \cdot I1(\gamma) + K1(\gamma) \cdot I0\left(\gamma \cdot \frac{c}{b}\right) \right)$$



$$f_3 := (a^2 + b^2) \cdot f_1 - (a^2 - b^2) \cdot f_2$$

$$f_4 := \frac{a \cdot b^2}{f_3^2} \left[ (a - b) \cdot f_1 - (a + b) \cdot f_2 \right]$$

$$f_8 := \frac{\left[ (a^2 - b^2) \cdot f_3 \cdot f_4 - b^4 \right] \cdot f_1 - \left[ (a^2 + b^2) \cdot f_3 \cdot f_4 + b^4 \right] \cdot f_2}{a \cdot f_3^2}$$

#### **First Leading Terms in the Velocity Field**

$$v_{10}(r) := \frac{a \cdot b}{f_3} \left[ (f_1 - f_2) \cdot r + \frac{f_1 + f_2}{r} \right]$$

$$v_{20}(r) := \frac{-2 \cdot a \cdot b}{f_3} \left( K_0\left(\gamma \cdot \frac{c}{b}\right) \cdot I_0(\gamma \cdot r) - I_0\left(\gamma \cdot \frac{c}{b}\right) \cdot K_0(\gamma \cdot r) \right)$$

#### **Checking**

$$z := 1$$

$$v_{10}(1) = 0.183$$

$$\frac{d}{dz} v_{10}(z) = -1.924$$

$$v_{20}(1) = 0.183$$

$$\frac{d}{dz} v_{20}(z) = -1.924$$

#### **Second Leading Terms in the Velocity Field**

$$v_{11}(r) := -f_4 \left[ (f_1 - f_2) \cdot r + \frac{f_1 + f_2}{r} \right]$$

$$v_{21}(r) := 2 \cdot f_4 \left( K_0\left(\gamma \cdot \frac{c}{b}\right) \cdot I_0(\gamma \cdot r) - I_0\left(\gamma \cdot \frac{c}{b}\right) \cdot K_0(\gamma \cdot r) \right)$$

#### **Checking**

$$z := 1$$

$$v_{11}(1) = 0.449$$

$$\frac{d}{dz} v_{11}(z) = -4.716$$

$$v_{21}(1) = 0.449$$

$$\frac{d}{dz} v_{21}(z) = -4.716$$

#### **Third Leading Terms in the Velocity Field**

$$v_{12}(r) := f_8 \left[ (f_1 - f_2) \cdot r + \frac{f_1 + f_2}{r} \right]$$

$$v_{22}(r) := -2 \cdot f_8 \left( K_0\left(\gamma \cdot \frac{c}{b}\right) \cdot I_0(\gamma \cdot r) - I_0\left(\gamma \cdot \frac{c}{b}\right) \cdot K_0(\gamma \cdot r) \right)$$

**Checking**

$$z := 1$$

$$v12(1) = 0.535$$

$$v22(1) = 0.535$$

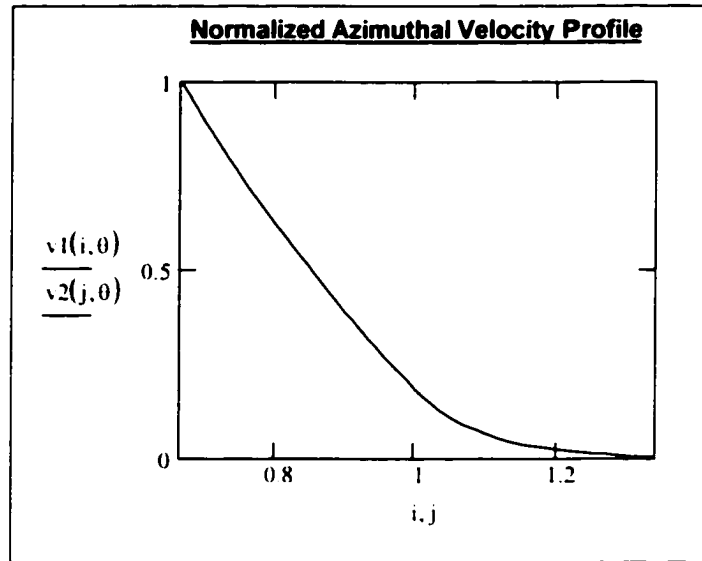
$$\frac{d}{dz} v12(z) = -5.629$$

$$\frac{d}{dz} v22(z) = -5.629$$

**General solution for velocity field**

$$v1(r, \theta) := v10(r) + \varepsilon \cdot \cos(\theta) \cdot v11(r) + (\varepsilon \cdot \cos(\theta))^2 \cdot v12(r)$$

$$v2(r, \theta) := v20(r) + \varepsilon \cdot \cos(\theta) \cdot v21(r) + (\varepsilon \cdot \cos(\theta))^2 \cdot v22(r)$$

**(b) Calculation for the temperature field****Declaration of Constants and Functions:**

$$I01 := I0(\gamma)$$

$$I0c := I0\left(\gamma \cdot \frac{c}{b}\right)$$

$$I20c := (I0c)^2$$

$$I11 := I1(\gamma)$$

$$I211 := (I11)^2$$

$$K01 := K0(\gamma)$$

$$K0c := K0\left(\gamma \cdot \frac{c}{b}\right)$$

$$K20c := (K0c)^2$$

$$K11 := K1(\gamma)$$

$$K211 := (K11)^2$$

$$\mathfrak{f}_6 := a^2 \cdot b^2 \cdot \frac{(\mathfrak{f}_1 + \mathfrak{f}_2)^2}{\mathfrak{f}_3^2}$$

$$\mathfrak{f}_7 := -2 \cdot a \cdot b \cdot \frac{\mathfrak{f}_4 \cdot (\mathfrak{f}_1 + \mathfrak{f}_2)^2}{\mathfrak{f}_3}$$

$$\mathfrak{f}_9 := \left( 2 \cdot a \cdot b \cdot \frac{\mathfrak{f}_8}{\mathfrak{f}_3} + \mathfrak{f}_4^2 \right) \cdot (\mathfrak{f}_1 + \mathfrak{f}_2)^2$$

$$\begin{aligned} F(R) := & (I0c \cdot K0I - K0c \cdot I0I)^2 \cdot \ln(R) \dots \\ & + -\gamma^2 \cdot \int_1^R R \cdot \ln(R) \cdot \left[ K20c \cdot (I1(\gamma \cdot R))^2 + I20c \cdot (K1(\gamma \cdot R))^2 \right] dR \dots \\ & + (\ln(R) - I) \cdot \int_1^R \frac{1}{R} \cdot (K0c \cdot I0(\gamma \cdot R) - I0c \cdot K0(\gamma \cdot R))^2 dR \dots \\ & + \gamma^2 \cdot \ln(R) \cdot \int_1^R R \cdot \left[ K20c \cdot (I1(\gamma \cdot R))^2 + I20c \cdot (K1(\gamma \cdot R))^2 \right] dR \dots \\ & + - \int_1^R \frac{\ln(R)}{R} \cdot (K0c \cdot I0(\gamma \cdot R) - I0c \cdot K0(\gamma \cdot R))^2 dR \dots \\ & + 2 \cdot \gamma^2 \cdot I0c \cdot K0c \cdot \left( \ln(R) \cdot \int_1^R R \cdot I1(\gamma \cdot R) \cdot K1(\gamma \cdot R) dR - \int_1^R R \cdot \ln(R) \cdot I1(\gamma \cdot R) \cdot K1(\gamma \cdot R) dR \right) \end{aligned}$$

$$F_1 := \frac{1 + Br \cdot \mathfrak{f}_6 \cdot \left[ 2 \cdot k \cdot \ln\left(\frac{c}{b}\right) + \left(\frac{b}{a}\right)^2 - 1 \right] - 4 \cdot Br \cdot k \cdot \frac{a^2 \cdot b^2}{\mathfrak{f}_3^2} \cdot F\left(\frac{c}{b}\right)}{-\left(k \cdot \ln\left(\frac{c}{b}\right) - \ln\left(\frac{a}{b}\right)\right)}$$

$$F_2 := \frac{Br \cdot \left[ -2 \cdot \mathfrak{f}_6 \cdot \left(\frac{b}{a}\right)^3 + \mathfrak{f}_7 \cdot \left[ 2k \cdot \ln\left(\frac{c}{b}\right) + \left(\frac{b}{a}\right)^2 - 1 \right] \right] - F_1 \cdot \left(\frac{b}{a}\right) + 8 \cdot Br \cdot k \cdot \frac{a \cdot b \cdot \mathfrak{f}_4}{\mathfrak{f}_3} \cdot F\left(\frac{c}{b}\right)}{-\left(k \cdot \ln\left(\frac{c}{b}\right) - \ln\left(\frac{a}{b}\right)\right)}$$

$$F_3 := Br \cdot \left[ -2 \cdot \mathfrak{f}_6 \cdot \left(\frac{b}{a}\right)^3 + \mathfrak{f}_7 \cdot \left(\frac{b}{a}\right)^2 \right] - F_1 \cdot \left(\frac{b}{a}\right) - F_2 \cdot \ln\left(\frac{a}{b}\right)$$

$$F_4 := 1 + Br \cdot \mathfrak{f}_6 \cdot \left(\frac{b}{a}\right)^2 - F_1 \cdot \ln\left(\frac{a}{b}\right)$$

$$F_5 := \frac{\text{Br} \left[ 3 \cdot \zeta_6 \cdot \left( \frac{b}{a} \right)^4 - 2 \cdot \zeta_7 \cdot \left( \frac{b}{a} \right)^3 + \zeta_9 \left[ 2 \cdot k \cdot \ln \left( \frac{c}{b} \right) + \left( \frac{b}{a} \right)^2 - 1 \right] \right] \dots}{- \left( k \ln \left( \frac{c}{b} \right) - \ln \left( \frac{a}{b} \right) \right)}$$

$$F_6 := \text{Br} \left[ 3 \cdot \zeta_6 \cdot \left( \frac{b}{a} \right)^4 - 2 \cdot \zeta_7 \cdot \left( \frac{b}{a} \right)^3 + \zeta_9 \cdot \left( \frac{b}{a} \right)^2 \right] + \frac{1}{2} \cdot F_1 \cdot \left( \frac{b}{a} \right)^2 - F_2 \cdot \left( \frac{b}{a} \right) - F_5 \cdot \ln \left( \frac{a}{b} \right)$$

#### **First Leading Terms in the Temperature Field**

$$\Theta_{10}(R) := -\text{Br} \cdot \zeta_6 \cdot R^{-2} + F_1 \cdot \ln(R) + F_4$$

$$\Theta_{20}(R) := 1 + \text{Br} \cdot \zeta_6 \left[ 2 \cdot k \cdot \ln(R) + \left( \frac{a}{b} \right)^{-2} - 1 \right] + F_1 \left( k \ln(R) - \ln \left( \frac{a}{b} \right) \right) - 4 \cdot \text{Br} \cdot k \cdot \frac{a^2 \cdot b^2}{\zeta_3^2} \cdot F(R)$$

#### **Checking**

$$z := 1$$

$$\Theta_{10}(1) = 0.648$$

$$\frac{d}{dz} \Theta_{10}(z) = -2.069$$

$$\Theta_{20}(1) = 0.648$$

$$\frac{d}{dz} \Theta_{20}(z) = -2.069$$

#### **Second Leading Terms in the Temperature Field**

$$\Theta_{11}(R) := -\text{Br} \cdot \zeta_7 \cdot R^{-2} + F_2 \cdot \ln(R) + F_3$$

$$\Theta_{21}(R) := \text{Br} \left[ -2 \cdot \zeta_6 \cdot \left( \frac{b}{a} \right)^3 + \zeta_7 \left[ 2 \cdot k \cdot \ln(R) + \left( \frac{a}{b} \right)^{-2} - 1 \right] \right] - F_1 \cdot \left( \frac{b}{a} \right) \dots$$

$$+ F_2 \cdot \left( k \ln(R) - \ln \left( \frac{a}{b} \right) \right) + 8 \cdot \text{Br} \cdot k \cdot \frac{a \cdot b \cdot \zeta_4}{\zeta_3} \cdot F(R)$$

#### **Checking**

$$z := 1$$

$$\Theta_{11}(1) = 0.704$$

$$\frac{d}{dz} \Theta_{11}(z) = -1.544$$

$$\Theta_{21}(1) = 0.704$$

$$\frac{d}{dz} \Theta_{21}(z) = -1.544$$

### Third Leading Terms in the Temperature Field

$$\Theta_{12}(R) := -Br \cdot \tilde{\kappa} \cdot R^{-2} + F_5 \cdot \ln(R) + F_6$$

$$\begin{aligned} \Theta_{22}(R) := & Br \left[ 3 \cdot \tilde{\kappa}_6 \left( \frac{b}{a} \right)^4 - 2 \cdot \tilde{\kappa}_7 \left( \frac{b}{a} \right)^3 + \tilde{\kappa}_9 \left[ 2 \cdot k \cdot \ln(R) + \left( \frac{b}{a} \right)^2 - 1 \right] \right] \dots \\ & + \frac{1}{2} \cdot F_1 \cdot \left( \frac{b}{a} \right)^2 - F_2 \cdot \left( \frac{b}{a} \right) \dots \\ & + F_5 \cdot \left( k \cdot \ln(R) - \ln \left( \frac{a}{b} \right) \right) - 4 \cdot Br \cdot k \cdot \left( 2 \cdot a \cdot b \cdot \frac{\tilde{\kappa}_8}{\tilde{\kappa}_3} + \tilde{\kappa}_4^2 \right) \cdot F(R) \end{aligned}$$

#### Checking

$$z := 1$$

$$\Theta_{12}(1) = 0.253$$

$$\frac{d}{dz} \Theta_{12}(z) = 1.308$$

$$\Theta_{22}(1) = 0.253$$

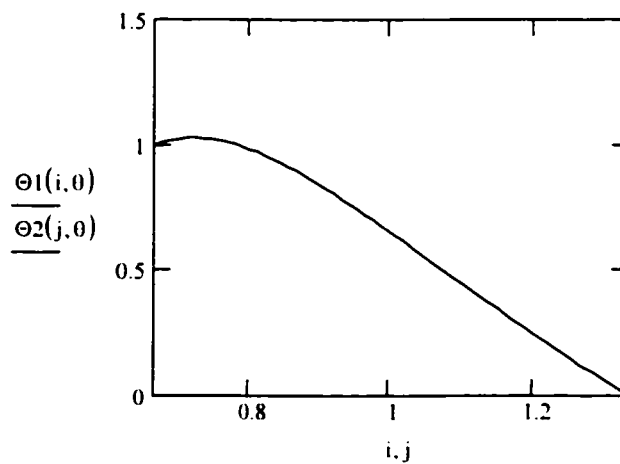
$$\frac{d}{dz} \Theta_{22}(z) = 1.308$$

### General solution for temperature field

$$\Theta_1(r, \theta) := \Theta_{10}(r) + \varepsilon \cdot \cos(\theta) \cdot \Theta_{11}(r) + (\varepsilon \cdot \cos(\theta))^2 \cdot \Theta_{12}(r)$$

$$\Theta_2(r, \theta) := \Theta_{20}(r) + \varepsilon \cdot \cos(\theta) \cdot \Theta_{21}(r) + (\varepsilon \cdot \cos(\theta))^2 \cdot \Theta_{22}(r)$$

#### Normalized Temperature Profile



## APPENDIX C

### DERIVATION OF INTERFACE CONDITIONS

The interface conditions between the fluid layer and the porous sleeve must satisfy several fundamental physical laws. Across the interface, the mass, the tangential velocity, the stress, and the pressure must be conserved for the flow. For the temperature field, the local temperature and its flux must balance from both sides of the interface. Rana (1977) and Rana et al. (1979) have introduced and successfully employed these conditions.

#### (a) Conservation of Mass across the Interface

Under the steady-state formulation, the conservation of mass for an incompressible fluid requires that the radial velocity components must be equal across the interface. Mathematically, this means

$$u_{r,i} = u_{r,p} \quad (C.1)$$

In terms of the dimensionless stream function, Eq. (C.1) can be expressed as

$$-\frac{1}{R} \frac{\partial \Psi}{\partial \theta} \Big|_i = -\frac{1}{R} \frac{\partial \Psi}{\partial \theta} \Big|_p \quad (C.2)$$

Eq. (C.2) can be further simplified to

$$\frac{\partial \Psi}{\partial \theta} \Big|_i = \frac{\partial \Psi}{\partial \theta} \Big|_p \quad \text{or} \quad \Psi_i = \Psi_p \quad (C.3a, b)$$

For simplicity, the constant of integration in Eq. (C.3b) has been chosen to be zero without the loss of generality.

(b) Continuity of Tangential Velocity Components across the Interface

Physically, the tangential velocity components from both the fluid film and the porous sleeve are expected to be the same. This condition leads to the continuity of azimuthal velocity components given as

$$u_{\theta,f} = u_{\theta,p}. \quad (C.4)$$

In terms of the dimensionless stream function, Eq. (C.4) can be expressed as

$$\left. \frac{\partial \Psi}{\partial R} \right|_f = \left. \frac{\partial \Psi}{\partial R} \right|_p. \quad (C.5)$$

(c) Continuity of Shear Stress across the Interface

The continuity of shear stress across the interface is given as  $\tau_f = \tau_p$ . In terms of velocity components, this interface condition can be expressed as

$$-\mu \left. \frac{\partial u_{\theta}}{\partial r} \right|_f = -\mu \left. \frac{\partial u_{\theta}}{\partial r} \right|_p. \quad (C.6)$$

In the normalized form, Eq. (C.6) becomes

$$\left. \frac{\partial V_{\theta}}{\partial R} \right|_f = \left. \frac{\partial V_{\theta}}{\partial R} \right|_p. \quad (C.7)$$

Recognize that the dimensional vorticity for both the fluid and porous layers is given by

$$\omega_z = \frac{u_{\theta}}{r} + \frac{\partial u_{\theta}}{\partial r} - \frac{1}{r} \frac{\partial u_r}{\partial \theta}. \quad (C.8)$$

The corresponding dimensionless form of Eq. (C.8) is expressed as

$$\Omega = \frac{V_\theta}{R} + \frac{\partial V_\theta}{\partial R} - \frac{1}{R} \frac{\partial V_R}{\partial \theta}. \quad (\text{C.9})$$

Eq. (C.9) can be specifically expressed for the fluid and porous layers, respectively, to read

$$\Omega_f = \frac{V_\theta}{R} \Big|_f + \frac{\partial V_\theta}{\partial R} \Big|_f - \frac{1}{R} \frac{\partial V_R}{\partial \theta} \Big|_f, \text{ and} \quad (\text{C.10})$$

$$\Omega_p = \frac{V_\theta}{R} \Big|_p + \frac{\partial V_\theta}{\partial R} \Big|_p - \frac{1}{R} \frac{\partial V_R}{\partial \theta} \Big|_p. \quad (\text{C.11})$$

Subtract Eq. (C.11) from Eq. (C.10) to yield

$$\Omega_f - \Omega_p = \frac{V_\theta}{R} \Big|_f - \frac{V_\theta}{R} \Big|_p + \frac{\partial V_\theta}{\partial R} \Big|_f - \frac{\partial V_\theta}{\partial R} \Big|_p - \frac{1}{R} \frac{\partial V_R}{\partial \theta} \Big|_f + \frac{1}{R} \frac{\partial V_R}{\partial \theta} \Big|_p. \quad (\text{C.12})$$

Along the interface,  $R = l$  and Eq. (C.12) is then simplified to read

$$\Omega_f - \Omega_p = V_{\theta f} - V_{\theta p} + \frac{\partial V_\theta}{\partial R} \Big|_f - \frac{\partial V_\theta}{\partial R} \Big|_p - \frac{\partial V_R}{\partial \theta} \Big|_f + \frac{\partial V_R}{\partial \theta} \Big|_p. \quad (\text{C.13})$$

According to the interface conditions (a), (b), and (c), the terms in the right hand side of Eq. (C.13) cancel each other and lead to

$$\Omega_f - \Omega_p = 0, \quad \text{or} \quad \Omega_f = \Omega_p. \quad (\text{C.14a, b})$$

#### (d) Balance of Pressure across the Interface

The continuity of pressure is given as

$$P_f = P_p. \quad (\text{C.15})$$

To make use of this piece of information, it is helpful to introduce the concept of total pressure.



$$P^0 = \frac{P}{\rho_i} + \frac{1}{2}(u_r^2 + u_\theta^2). \quad (\text{C.16})$$

Combining Eqs. (C.1), (C.4), and (C.15), it can be deduced that

$$P_i^0 = P_r^0. \quad (\text{C.17})$$

Recall that the general forms of  $r$ - and  $\theta$  momentum equations for both the fluid layer and porous sleeve are given by

$$u_r \frac{\partial u_r}{\partial r} + \frac{u_\theta}{r} \frac{\partial u_r}{\partial \theta} - \frac{u_\theta^2}{r} = -\frac{1}{\rho_i} \frac{\partial P}{\partial r} + \frac{\rho}{\rho_i} g_r - \frac{\nu}{r} \frac{\partial \omega_z}{\partial \theta} \left[ -\frac{\nu}{K} u_r \right], \text{ and} \quad (\text{C.18})$$

$$u_r \frac{\partial u_\theta}{\partial r} + \frac{u_\theta}{r} \frac{\partial u_\theta}{\partial \theta} + \frac{u_r u_\theta}{r} = -\frac{1}{\rho_i r} \frac{\partial P}{\partial \theta} + \frac{\rho}{\rho_i} g_\theta + \nu \frac{\partial \omega_z}{\partial r} \left[ -\frac{\nu}{K} u_\theta \right]. \quad (\text{C.19})$$

For the fluid layer, the terms in the square brackets in equations (C.18) and (C.19) are excluded. These terms in the square brackets are only included in the momentum equations for the porous sleeve. Since

$$u_\theta \omega_z = \frac{u_\theta^2}{r} + u_\theta \frac{\partial u_\theta}{\partial r} - \frac{u_\theta}{r} \frac{\partial u_r}{\partial \theta}, \text{ and} \quad (\text{C.20})$$

$$u_r \omega_z = \frac{u_r u_\theta}{r} + u_r \frac{\partial u_\theta}{\partial r} - \frac{u_r}{r} \frac{\partial u_r}{\partial \theta}. \quad (\text{C.21})$$

the general  $r$ - and  $\theta$  momentum equations can now be expressed as

$$r\text{-momentum: } \frac{\partial}{\partial r} \left( \frac{P}{\rho_i} \right) + u_r \frac{\partial u_r}{\partial r} + u_\theta \frac{\partial u_\theta}{\partial r} - u_\theta \omega_z = \frac{\rho}{\rho_i} g_r - \frac{\nu}{r} \frac{\partial \omega_z}{\partial \theta} \left[ -\frac{\nu}{K} u_r \right], \quad (\text{C.22})$$

$$\frac{\partial}{\partial r} \left( \frac{P}{\rho_i} \right) + \frac{1}{2} \frac{\partial u_r^2}{\partial r} + \frac{1}{2} \frac{\partial u_\theta^2}{\partial r} - u_\theta \omega_z = \frac{\rho}{\rho_i} g_r - \frac{\nu}{r} \frac{\partial \omega_z}{\partial \theta} \left[ -\frac{\nu}{K} u_r \right], \quad (\text{C.23})$$

$$\frac{\partial}{\partial r} \left[ \frac{P}{\rho_i} + \frac{1}{2}(u_r^2 + u_\theta^2) \right] - u_\theta \omega_z = \frac{\rho}{\rho_i} g_r - \frac{\nu}{r} \frac{\partial \omega_z}{\partial \theta} \left[ -\frac{\nu}{K} u_r \right], \quad (\text{C.24})$$

$$\frac{\partial P^0}{\partial r} - u_\theta \omega_z = \frac{\rho}{\rho_c} g_r - \frac{\nu}{r} \frac{\partial \omega_z}{\partial \theta} \left[ -\frac{\nu}{K} u_r \right], \text{ and} \quad (\text{C.25})$$

$$\theta\text{-momentum: } \frac{1}{r} \frac{\partial}{\partial \theta} \left( \frac{P}{\rho_c} \right) + \frac{u_r}{r} \frac{\partial u_r}{\partial \theta} + \frac{u_\theta}{r} \frac{\partial u_\theta}{\partial \theta} + u_r \omega_z = \frac{\rho}{\rho_c} g_\theta + \nu \frac{\partial \omega_z}{\partial r} \left[ -\frac{\nu}{K} u_\theta \right], \quad (\text{C.26})$$

$$\frac{1}{r} \frac{\partial}{\partial \theta} \left( \frac{P}{\rho_c} \right) + \frac{1}{2r} \frac{\partial u_r^2}{\partial \theta} + \frac{1}{2r} \frac{\partial u_\theta^2}{\partial \theta} + u_r \omega_z = \frac{\rho}{\rho_c} g_\theta + \nu \frac{\partial \omega_z}{\partial r} \left[ -\frac{\nu}{K} u_\theta \right], \quad (\text{C.27})$$

$$\frac{1}{r} \frac{\partial}{\partial \theta} \left[ \frac{P}{\rho_c} + \frac{1}{2r} (u_r^2 + u_\theta^2) \right] + u_r \omega_z = \frac{\rho}{\rho_c} g_\theta + \nu \frac{\partial \omega_z}{\partial r} \left[ -\frac{\nu}{K} u_\theta \right]. \quad (\text{C.28})$$

$$\frac{1}{r} \frac{\partial P^0}{\partial \theta} + u_r \omega_z = \frac{\rho}{\rho_c} g_\theta + \nu \frac{\partial \omega_z}{\partial r} \left[ -\frac{\nu}{K} u_\theta \right]. \quad (\text{C.29})$$

The derivative of the total pressure is given as

$$dP^0 = \frac{\partial P^0}{\partial r} dr + \frac{\partial P^0}{r \partial \theta} r d\theta. \quad (\text{C.30})$$

Integrating (C.30) from point  $(l, 0)$  to  $(l, 2\pi)$  along the interface, one obtains

$$P^0 = \int_{r=l}^{r=1} \frac{\partial P^0}{\partial r} dr + \int_{\theta=0}^{\theta=2\pi} \frac{\partial P^0}{\partial \theta} d\theta. \quad (\text{C.31})$$

Now, integrate Eqs. (C.25) and (C.29) and substitute into Eq. (C.31) to obtain

$$P^0 = \int_0^{2\pi} \left( \frac{\rho}{\rho_c} g_\theta + \nu \frac{\partial \omega_z}{\partial r} - u_r \omega_z \left[ -\frac{\nu}{K} u_\theta \right] \right) r d\theta. \quad (\text{C.32})$$

Since  $P'_l = P^0_r$ , one obtains

$$\int_0^{2\pi} \left( \frac{\rho}{\rho_c} g_\theta + \nu \frac{\partial \omega_z}{\partial r} - u_r \omega_z \right)_l r d\theta = \int_0^{2\pi} \left( \frac{\rho}{\rho_c} g_\theta + \nu \frac{\partial \omega_z}{\partial r} - u_r \omega_z - \frac{\nu}{K} u_\theta \right)_r r d\theta. \quad (\text{C.33})$$

Since  $g_r$  and  $g_\theta$  are independent of the layer structures, it is acceptable to write the followings,

$$\left. \frac{\rho}{\rho_c} g_r \right|_I = \left. \frac{\rho}{\rho_c} g_r \right|_P \quad \text{and} \quad \left. \frac{\rho}{\rho_c} g_\theta \right|_I = \left. \frac{\rho}{\rho_c} g_\theta \right|_P. \quad (\text{C.34})$$

Substitute Eq. (C.34) into Eq. (C.33) and simplify, one obtains

$$\int_0^{2\pi} \left[ \left( v \frac{\partial \omega_z}{\partial r} - u_r \omega_z \right)_I - \left( v \frac{\partial \omega_z}{\partial r} - u_r \omega_z - \frac{v}{K} u_\theta \right)_P \right] r d\theta = 0. \quad (\text{C.35})$$

According to the interface conditions (a) and (b), Eq. (C.35) becomes

$$\int_0^{2\pi} \left[ v \left( \frac{\partial \omega_z}{\partial r} \right)_I - \frac{\partial \omega_z}{\partial r} \right]_P - u_r (\omega_{z,I} - \omega_{z,P}) + \frac{v}{K} u_{\theta,P} \right] r d\theta = 0. \quad (\text{C.36})$$

Introducing dimensionless parameters,

$$R = \frac{r}{b}, \quad V_R = \frac{u_r}{\alpha/b}, \quad V_\theta = \frac{u_\theta}{\alpha/b}, \quad \text{and} \quad \Omega = \frac{\omega}{\alpha/b^2}.$$

Eq. (C.36) becomes

$$\int_0^{2\pi} \left[ Pr \left( \frac{\partial \Omega_I}{\partial R} - \frac{\partial \Omega_P}{\partial R} \right) - V_R (\Omega_I - \Omega_P) + \frac{Pr}{Da} V_{\theta,P} \right] R d\theta = 0. \quad (\text{C.37})$$

Recall from (C.14b), Eq. (C.37) is now further simplified to become

$$\int_0^{2\pi} \left( \frac{\partial \Omega_I}{\partial R} - \frac{\partial \Omega_P}{\partial R} + \frac{V_{\theta,P}}{Da} \right) R d\theta = 0. \quad (\text{C.38})$$

For the integration in Eq. (C.38) to be true for all values, the integral must be zero.

As a result, it can be concluded that

$$\frac{\partial \Omega_I}{\partial R} - \frac{\partial \Omega_P}{\partial R} + \frac{V_{\theta,P}}{Da} = 0, \quad \text{or} \quad \frac{\partial \Omega_I}{\partial R} = \frac{\partial \Omega_P}{\partial R} - \frac{V_{\theta,P}}{Da}. \quad (\text{C.39a, b})$$

#### (e) Continuity of Local Temperature across the Interface

Across the interface, the continuity of local temperature is given as  $T_i = T_p$ . In terms of the normalized temperature, this interface condition can be expressed as

$$\Theta_i = \Theta_p. \quad (\text{C.40})$$

(f) Continuity of Heat Flux across the Interface

The continuity of heat flux is given as  $q_i = q_p$ . This is then expressed as

$$-k_i \left. \frac{\partial T}{\partial r} \right|_i = -k_p \left. \frac{\partial T}{\partial r} \right|_p. \quad (\text{C.41})$$

In terms of the normalized temperature, Eq. (C.41) can be expressed as

$$\left. \frac{\partial \Theta}{\partial R} \right|_i = \frac{k_p}{k_i} \left. \frac{\partial \Theta}{\partial R} \right|_p. \quad (\text{C.42})$$

Based on the above derivation, the interface conditions and their equivalent expressions in terms of the dimensionless stream function and temperature are summarized as follows

(a) Conservation of Mass across the Interface

$$\Psi_i = \Psi_p. \quad (\text{C.3b})$$

(b) Continuity of Tangential Velocity Components across the Interface

$$\left. \frac{\partial \Psi}{\partial R} \right|_i = \left. \frac{\partial \Psi}{\partial R} \right|_p. \quad (\text{C.5})$$

(c) Continuity of Shear Stress across the Interface

$$\Omega_i = \Omega_p. \quad (\text{C.14b})$$

(d) Balance of Pressure across the Interface

$$\frac{\partial \Omega_l}{\partial R} = \frac{\partial \Omega_p}{\partial R} - \frac{V_{\theta,p}}{Da}, \quad (\text{C.39b})$$

(e) Continuity of Local Temperature across the Interface

$$\Theta_l = \Theta_p, \text{ and} \quad (\text{C.40})$$

(f) Continuity of Heat Flux across the Interface

$$\left. \frac{\partial \Theta}{\partial R} \right|_l = \frac{k_p}{k_l} \left. \frac{\partial \Theta}{\partial R} \right|_p. \quad (\text{C.42})$$

## APPENDIX D

### FINITE FOURIER COSINE TRANSFORM FROM 0 TO $2\pi$

The table below is a brief collection of the transformed functions used in this study. In general, the integration in Eq. (D.1) gives the transformation of other functions. No tabulated result is presented for the inverse transform because the calculation involving Eq. (D.2) is straightforward.

Integral Transform:

$$\bar{F}\{\Phi(r, \sigma)\}_l = \bar{\Phi}(r, n, \tilde{\sigma}) = \int_0^{2\pi} \cos n(\tilde{\sigma} - \sigma) \cdot \Phi(r, \sigma) d\sigma, \quad (\text{D.1})$$

where  $n$  is an integer.

$\Phi(r, \sigma)$	$n$	$\bar{\Phi}(r, n, \tilde{\sigma})$
$1$	$0$	$2\pi$
	otherwise	$0$
$g(r)$	$0$	$2\pi g(r)$
	otherwise	$0$
$\cos(\sigma)$	$1$	$\pi \cos(\tilde{\sigma})$
	otherwise	$0$
$\sin(\sigma)$	$1$	$\pi \sin(\tilde{\sigma})$
	otherwise	$0$
$\cos(\sigma) \sin(\sigma)$	$2$	$\pi \cos(\tilde{\sigma}) \sin(\tilde{\sigma})$
	otherwise	$0$
$\cos^2(\sigma)$	$0$	$\pi$
	$2$	$\pi \cos^2(\tilde{\sigma}) - \frac{\pi}{2}$
	otherwise	$0$
$\sin^2(\sigma)$	$0$	$\pi$
	$2$	$-\pi \cos^2(\tilde{\sigma}) + \frac{\pi}{2}$
	otherwise	$0$

Inverse Transform:

$$\Phi(r, \sigma) = \frac{1}{2\pi} \bar{\Phi}(r, 0, \sigma) + \frac{1}{\pi} \sum_{n=1}^{\infty} \bar{\Phi}(r, n, \sigma) \quad (\text{D.2})$$

## APPENDIX E

### MATHCAD CALCULATION FOR NATURAL CONVECTION

This appendix presents a sample of worksheet that performs the calculations for natural convection in Chapter Three using Mathcad 2000 Professional. ©1986-1999 MathSoft, Inc.

#### Natural Convection in Partially Porous Concentric Annulus

##### Notes:

layer 1: fluid layer  
layer 2: porous layer (Brinkman's model)

##### Governing Parameters:

Inner radius	$a := 1$	Darcy number	$Da := 10^{-2}$
Interface radius	$b := 1.5$	Rayleigh number	$Ra := 0.5$
Outer radius	$c := 2$	Thermal cond. ratio	$k := 1$
Permeability	$K := Da \cdot b^2$	Prandtl Number	$Pr := 20000$

##### Plotting Parameters:

$$\theta := 30 \text{ deg} \qquad d := 0.05 \left( 1 - \frac{a}{b} \right)$$

$$i := \frac{a}{b}, \frac{a}{b} + d, 1 \qquad j := 1, 1 + d, \frac{c}{b}$$

##### Declarations of Constants and Functions

For simplicity, we write  $k = k_1/k_2$ ,  $ab = a/b$ ,  $cb = c/b$ ,  $\ln ab = \ln(a/b)$ ,  $\ln cb = \ln(c/b)$ ,  
 $I_{01} = I_0(\gamma)$ ,  $K_{01} = K_0(\gamma)$ ,  $I_{11} = I_1(\gamma)$ ,  $K_{11} = K_1(\gamma)$ ,  
 $I_{0cb} = I_0(\gamma \cdot c/b)$ ,  $K_{0cb} = K_0(\gamma \cdot c/b)$ ,  $I_{1cb} = I_1(\gamma \cdot c/b)$ ,  $K_{1cb} = K_1(\gamma \cdot c/b)$ .

$$ab := \frac{a}{b} \qquad \ln ab := \ln(ab)$$

$$cb := \frac{c}{b} \qquad \ln cb := \ln(cb)$$

$$q := (k \cdot \ln cb - \ln ab)^{-1} \qquad \gamma := \frac{1}{\sqrt{Da}}$$



$$I01 := I0(\gamma)$$

$$K01 := K0(\gamma)$$

$$I0cb := I0(\gamma \cdot cb)$$

$$K0cb := K0(\gamma \cdot cb)$$

$$I11 := I1(\gamma)$$

$$K11 := K1(\gamma)$$

$$I1cb := I1(\gamma \cdot cb)$$

$$K1cb := K1(\gamma \cdot cb)$$

$$I2(x) := I0(x) - \frac{2}{x} \cdot I1(x)$$

$$K2(x) := K0(x) + \frac{2}{x} \cdot K1(x)$$

$$I21 := I01 - \frac{2}{\gamma} \cdot I11$$

$$K21 := K01 + \frac{2}{\gamma} \cdot K11$$

$$I2'1 := \gamma \cdot I11 - 2 \cdot I21$$

$$K2'1 := -\gamma \cdot K11 - 2 \cdot K21$$

$$I0cb := I0(\gamma \cdot cb)$$

$$I1cb := I1(\gamma \cdot cb)$$

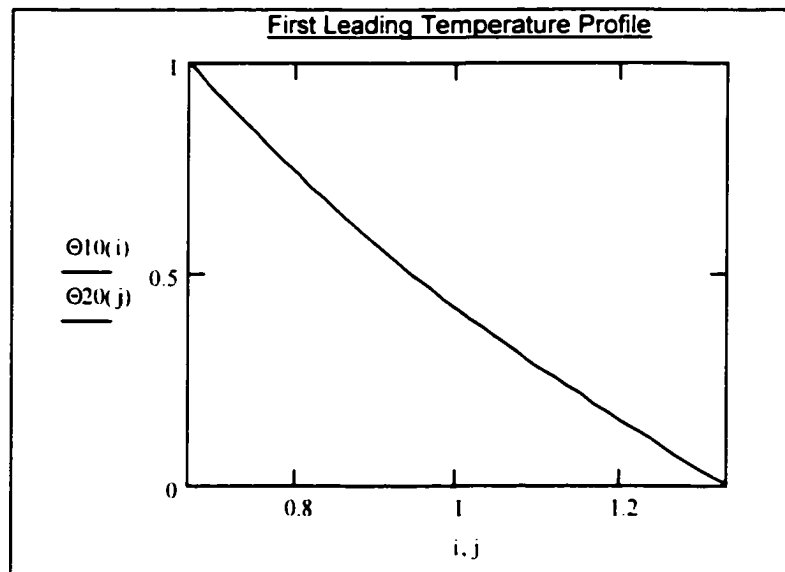
$$K0cb := K0(\gamma \cdot cb)$$

$$K1cb := K1(\gamma \cdot cb)$$

### First Leading Terms in Temperature Field

$$\Theta10(R) := q \cdot (k \cdot \ln cb - \ln(R))$$

$$\Theta20(R) := q \cdot (k \cdot \ln cb - k \cdot \ln(R))$$



### Checking

inner := ab

$$\Theta10(\text{inner}) = 1$$

outer := cb

$$\Theta20(\text{outer}) = 0$$

interface := 1

$$\Theta10(\text{interface}) - \Theta20(\text{interface}) = 0$$

$$k \cdot \left( \frac{d}{d_{\text{interface}}} \Theta10(\text{interface}) \right) - \frac{d}{d_{\text{interface}}} \Theta20(\text{interface}) = 0$$

$$\Gamma_{11} := \frac{\sin(\theta)}{2} \cdot q \quad \Gamma_{21} := k \cdot Da \cdot \sin(\theta) \cdot q$$

$$a_{\theta 11} := \frac{1}{1} \cdot \frac{2}{1} \cdot \left( \ln ab + \frac{1}{2} \right) - \frac{4}{ab^2} - \left( \frac{8}{3} \cdot \frac{4}{ab^2} - \frac{4}{ab^2} \right)$$

$$a_{\Delta 21} := \left( \frac{8}{3} \cdot \frac{4}{ab^2} - \frac{4}{ab^4} \right) \cdot \left( \gamma \cdot 101 - \gamma^2 - 111 \right) + \frac{8}{ab^2} \cdot 10cb + \left( \frac{cb^2}{2} \cdot \gamma - 1 \cdot 10cb - cb \cdot \gamma^2 \cdot 11cb \right)$$

$$a_{\theta 21} := \left( \frac{8}{3} \cdot \frac{4}{ab^2} - \frac{4}{ab^4} \right) \cdot \left( \gamma \cdot K01 + K11 \right) - \frac{2}{ab^2} \cdot K0cb + \left( \frac{cb^2}{2} \cdot \gamma - 1 \cdot K0cb + cb \cdot \gamma^2 \cdot K1cb \right)$$

$$a_{\Gamma 1} := \left( - \left( \ln ab - \frac{1}{2} \right) \cdot \frac{4}{ab^2} - \left( \ln ab - \frac{4}{ab^4} \right) \cdot \left( \frac{4}{3} \cdot \frac{8}{ab^4} - \frac{8}{ab^2} \right) + \left( \frac{8}{3} \cdot \frac{4}{ab^2} - \frac{4}{ab^4} \right) \cdot \left( \ln cb + \frac{1}{2} \right) + \left( \frac{2}{1} \right) \cdot \left( \frac{4}{cb^2} - \frac{2}{1} \right) \right) \cdot \Gamma_{21}$$

$$b_{\theta 11} := \frac{-1}{2} \cdot \left( \ln ab + \frac{1}{2} \right) + \frac{4}{ab^2} - \left( \frac{8}{1} \cdot \frac{4}{ab^2} - \frac{4}{ab^4} \right)$$

$$b_{\Delta 21} := \left( \frac{8}{1} \cdot \frac{4}{ab^2} + \frac{4}{ab^4} \right) \cdot \left( 111 - 111 \cdot \gamma^2 - \frac{2}{\gamma} \cdot 10cb - \frac{2}{cb^2} \cdot \gamma - 1 \cdot 10cb - cb \cdot \gamma^2 \cdot 11cb \right)$$

$$b_{\theta 21} := \left( \frac{8}{1} \cdot \frac{4}{ab^2} + \frac{4}{ab^4} \right) \cdot \left( K11 - K11 \cdot \gamma^2 - \frac{2}{\gamma} \cdot K0cb + \left( \frac{cb^2}{2} \cdot \gamma - 1 \cdot K0cb + cb \cdot \gamma^2 \cdot K1cb \right) \right)$$

$$b_{\Gamma 1} := \left( - \frac{ab^2}{2} \cdot \left( \ln ab - \frac{4}{ab^4} \right) + \left( \frac{8}{1} \cdot \frac{4}{ab^2} - \frac{4}{ab^4} \right) \cdot \left( \ln cb + \frac{1}{2} \right) + \left( \frac{2}{1} \right) \cdot \left( \frac{4}{cb^2} - \frac{2}{1} \right) \right) \cdot \Gamma_{21}$$

$$c_{\theta 11} := -1 - 1$$

$$c_{\Delta 21} := 111 - 111 \cdot \left( \gamma \cdot 101 - 111 \right) + \frac{Da}{\gamma} \cdot \left( \gamma \cdot 101 - 111 \right) + \left( \frac{Da}{1} \cdot \frac{1}{\gamma} \cdot 10cb - \frac{2}{cb^2} \cdot \gamma - 1 \cdot 10cb - cb \cdot \gamma^2 \cdot 11cb \right)$$

$$c_{\theta 21} := K11 + \left( \gamma \cdot K01 + K11 \right) \cdot \frac{Da}{\gamma} - \frac{2}{\gamma} \cdot \left( \frac{Da}{1} \cdot \frac{1}{\gamma} \cdot K0cb + \left( \frac{cb^2}{2} \cdot \gamma - 1 \cdot K0cb + cb \cdot \gamma^2 \cdot K1cb \right) \right)$$

$$c_{\Gamma 1} := \Gamma_{11} + \left[ 1 + 1 + \frac{1}{2} \cdot \left( - \frac{Da}{2} \cdot \left( \ln cb + \frac{1}{2} \right) - \frac{Da}{1} \cdot \frac{4}{cb^2} + \frac{1}{2} \cdot \frac{Da}{1} \right) \right] \cdot \Gamma_{21}$$

$$d_1 := \left[ a_{\theta 11} \cdot \left( b_{\theta 21} \cdot c_{\Delta 21} - b_{\Delta 21} \cdot c_{\theta 21} \right) + a_{\Delta 21} \cdot \left( b_{\theta 11} \cdot c_{\theta 21} - b_{\theta 21} \cdot c_{\theta 11} \right) + a_{\theta 21} \cdot \left( b_{\Delta 21} \cdot c_{\theta 11} - b_{\theta 11} \cdot c_{\Delta 21} \right) \right] \cdot \Gamma_{21}$$

$$B_{11} := d_1 \cdot \left[ a_{\Gamma 1} \cdot \left( b_{\Delta 21} \cdot c_{\theta 21} - b_{\theta 21} \cdot c_{\Delta 21} \right) + b_{\Gamma 1} \cdot \left( a_{\theta 21} \cdot c_{\Delta 21} - a_{\Delta 21} \cdot c_{\theta 21} \right) + c_{\Gamma 1} \cdot \left( a_{\theta 21} \cdot b_{\theta 21} - a_{\theta 21} \cdot b_{\Delta 21} \right) \right] \cdot \Gamma_{21}$$

$$\Delta_{21} := d_1 \cdot \left[ a_{\Gamma 1} \cdot \left( b_{\theta 21} \cdot c_{\theta 11} - b_{\theta 11} \cdot c_{\theta 21} \right) + b_{\Gamma 1} \cdot \left( a_{\theta 21} \cdot c_{\theta 11} - a_{\theta 21} \cdot c_{\theta 21} \right) + c_{\Gamma 1} \cdot \left( a_{\theta 21} \cdot b_{\theta 11} - a_{\theta 21} \cdot b_{\theta 21} \right) \right] \cdot \Gamma_{21}$$

$$B21 := d1 \cdot \left[ a_{\Gamma 1} \cdot (b_{B11} \cdot c_{A21} - b_{A21} \cdot c_{B11}) + b_{\Gamma 1} \cdot (a_{A21} \cdot c_{B11} - a_{B11} \cdot c_{A21}) \dots \right. \\ \left. + c_{\Gamma 1} \cdot (a_{B11} \cdot b_{A21} - a_{A21} \cdot b_{B11}) \right]$$

$$A11 := -B11 + 111 \cdot A21 + K11 \cdot B21 + \Gamma 21$$

$$C11 := \frac{-ab^2}{4} \cdot A11 - \frac{1}{2} \cdot \left( \ln ab + \frac{1}{2} \right) \cdot B11 - \frac{ab^2}{4} \cdot \left( \ln ab - \frac{1}{2} \right) \cdot \Gamma 11$$

$$D11 := \frac{ab^4}{8} \cdot A11 + \frac{ab^2}{4} \cdot B11 + \frac{ab^4}{8} \cdot \left( \ln ab - \frac{1}{4} \right) \cdot \Gamma 11$$

$$C21 := \frac{-\gamma^{-1}}{2} \cdot I0cb \cdot A21 + \frac{\gamma^{-1}}{2} \cdot K0cb \cdot B21 - \frac{1}{2} \cdot \left( \ln cb + \frac{1}{2} \right) \cdot \Gamma 21$$

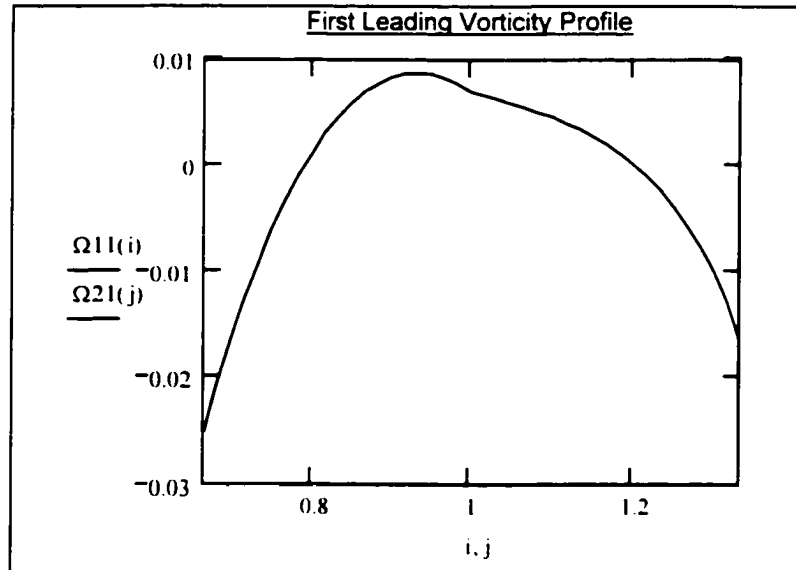
$$D21 := \left( \frac{cb^2}{2} \cdot \gamma^{-1} \cdot I0cb - cb \cdot \gamma^{-2} \cdot I1cb \right) \cdot A21 - \left( \frac{cb^2}{2} \cdot \gamma^{-1} \cdot K0cb + cb \cdot \gamma^{-2} \cdot K1cb \right) \cdot B21 + \frac{cb^2}{4} \cdot \Gamma 21$$

$$\Omega 11(R) := A11 \cdot R + B11 \cdot R^{-1} + \Gamma 11 \cdot R \cdot \ln(R)$$

$$\Omega 21(R) := A21 \cdot I1(\gamma \cdot R) + B21 \cdot K1(\gamma \cdot R) + \frac{\Gamma 21}{R}$$

$$\Psi 11(R) := C11 \cdot R + D11 \cdot R^{-1} + \left( \frac{A11}{8} - \frac{3\Gamma 11}{32} + \frac{\Gamma 11}{8} \ln(R) \right) \cdot R^3 + \frac{B11}{2} \cdot R \cdot \ln(R)$$

$$\Psi 21(R) := C21 \cdot R + \frac{D21}{R} + A21 \cdot \gamma^{-2} \cdot I1(\gamma \cdot R) + B21 \cdot \gamma^{-2} \cdot K1(\gamma \cdot R) + \frac{\Gamma 21}{2} \cdot R \cdot \ln(R)$$



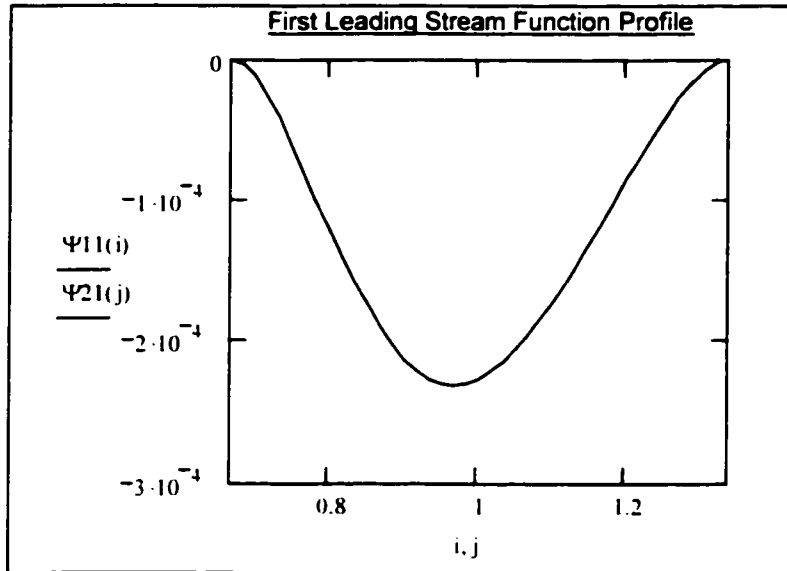
### Checking

interface := 1

$$\Omega 1 l(\text{interface}) - \Omega 2 l(\text{interface}) = 0$$

$$\frac{d}{d\text{interface}} \Omega 1 l(\text{interface}) - \frac{d}{d\text{interface}} \Omega 2 l(\text{interface}) \dots = 2.217 \times 10^{-15}$$

$$+ \frac{1}{Da} \frac{d}{d\text{interface}} \Psi 2 l(\text{interface})$$



### Checking

inner := ab

$$\Psi 1 l(\text{inner}) = 0$$

$$\frac{d}{d\text{inner}} \Psi 1 l(\text{inner}) = 0$$

outer := cb

$$\Psi 2 l(\text{outer}) = 0$$

$$\frac{d}{d\text{outer}} \Psi 2 l(\text{outer}) = 0$$

interface := 1

$$\Psi 1 l(\text{interface}) - \Psi 2 l(\text{interface}) = 0$$

$$\frac{d}{d\text{interface}} \Psi 2 l(\text{interface}) - \frac{d}{d\text{interface}} \Psi 2 l(\text{interface}) = 0$$

## Second Leading Terms in Temperature Field

$$\Gamma_{11}' := \frac{\cos(\theta)}{2} \cdot q$$

$$\Gamma_{21}' := k \cdot Da \cdot \cos(\theta) \cdot q$$

$$a'_{\Gamma 1} := \left[ -\left( \ln ab - \frac{1}{2} \right) \cdot \frac{ab^2}{4} - \left( \ln ab - \frac{1}{4} \right) \cdot \frac{ab^4}{8} - \frac{5}{32} \right] \cdot \Gamma_{11}' + \left[ \left( \frac{3}{8} - \frac{ab^2}{4} - \frac{ab^4}{8} \right) + \frac{1}{2} \cdot \left( \ln cb + \frac{1}{2} \right) + \frac{cb^2}{4} - \frac{1}{2} \right] \cdot \Gamma_{21}'$$

$$b'_{\Gamma 1} := \left[ \frac{-ab^2}{4} \cdot \left( \ln ab - \frac{1}{2} \right) + \frac{ab^4}{8} \cdot \left( \ln ab - \frac{1}{4} \right) - \frac{3}{32} \right] \cdot \Gamma_{11}' + \left[ \left( \frac{1}{8} - \frac{ab^2}{4} + \frac{ab^4}{8} \right) + \frac{1}{2} \cdot \left( \ln cb + \frac{1}{2} \right) - \frac{cb^2}{4} \right] \cdot \Gamma_{21}'$$

$$c'_{\Gamma 1} := \Gamma_{11}' + \left[ 1 + 1 + \frac{1}{Da} \cdot \left[ \frac{-1}{2} \cdot \left( \ln cb + \frac{1}{2} \right) \right] - \frac{1}{Da} \cdot \frac{cb^2}{4} + \frac{1}{2} \cdot \frac{1}{Da} \right] \cdot \Gamma_{21}'$$

$$B_{11}' := d_1 \cdot \left[ a'_{\Gamma 1} \cdot (b_{A21} \cdot c_{B21} - b_{B21} \cdot c_{A21}) + b'_{\Gamma 1} \cdot (a_{B21} \cdot c_{A21} - a_{A21} \cdot c_{B21}) \dots \right. \\ \left. + c'_{\Gamma 1} \cdot (a_{A21} \cdot b_{B21} - a_{B21} \cdot b_{A21}) \right]$$

$$A_{21}' := d_1 \cdot \left[ a'_{\Gamma 1} \cdot (b_{B21} \cdot c_{B11} - b_{B11} \cdot c_{B21}) + b'_{\Gamma 1} \cdot (a_{B11} \cdot c_{B21} - a_{B21} \cdot c_{B11}) \dots \right. \\ \left. + c'_{\Gamma 1} \cdot (a_{B21} \cdot b_{B11} - a_{B11} \cdot b_{B21}) \right]$$

$$B_{21}' := d_1 \cdot \left[ a'_{\Gamma 1} \cdot (b_{B11} \cdot c_{A21} - b_{A21} \cdot c_{B11}) + b'_{\Gamma 1} \cdot (a_{A21} \cdot c_{B11} - a_{B11} \cdot c_{A21}) \dots \right. \\ \left. + c'_{\Gamma 1} \cdot (a_{B11} \cdot b_{A21} - a_{A21} \cdot b_{B11}) \right]$$

$$A_{11}' := -B_{11}' + I_{11} \cdot A_{21}' + K_{11} \cdot B_{21}' + \Gamma_{21}'$$

$$C_{11}' := \frac{-ab^2}{4} \cdot A_{11}' - \frac{1}{2} \cdot \left( \ln ab + \frac{1}{2} \right) \cdot B_{11}' - \frac{ab^2}{4} \cdot \left( \ln ab - \frac{1}{2} \right) \cdot \Gamma_{11}'$$

$$D_{11}' := \frac{ab^4}{8} \cdot A_{11}' + \frac{ab^2}{4} \cdot B_{11}' + \frac{ab^4}{8} \cdot \left( \ln ab - \frac{1}{4} \right) \cdot \Gamma_{11}'$$

$$C_{21}' := \frac{-\gamma^{-1}}{2} \cdot I_{0cb} \cdot A_{21}' + \frac{\gamma^{-1}}{2} \cdot K_{0cb} \cdot B_{21}' - \frac{1}{2} \cdot \left( \ln cb + \frac{1}{2} \right) \cdot \Gamma_{21}'$$

$$D_{21}' := \left( \frac{cb^2}{2} \cdot \gamma^{-1} \cdot I_{0cb} - cb \cdot \gamma^{-2} \cdot I_{1cb} \right) \cdot A_{21}' - \left( \frac{cb^2}{2} \cdot \gamma^{-1} \cdot K_{0cb} + cb \cdot \gamma^{-2} \cdot K_{1cb} \right) \cdot B_{21}' + \frac{cb^2}{4} \cdot \Gamma_{21}'$$

$$a_{F11} := -ab + \frac{1}{ab}$$

$$a_{F21} := k^2 \cdot ab$$

$$a_{F21} := k^2 \cdot ab$$

$$a_{\Gamma 2} := \frac{ab^3}{64} \cdot A_{11}' + ab \cdot \left( \frac{\ln ab^2 - \ln ab}{8} \right) \cdot B_{11}' + \frac{ab}{2} \cdot \ln ab \cdot C_{11}' - \frac{\ln ab}{2 \cdot ab} \cdot D_{11}' + \frac{3}{128} \cdot ab \cdot \Gamma_{11}' - \frac{ab}{64} \cdot A_{11}' \dots \\ + ab^3 \cdot \left( \frac{\ln ab}{64} - \frac{3}{128} \right) \cdot \Gamma_{11}'$$

$$b_{F11} := 0$$

$$b_{E21} := cb$$

$$b_{F21} := \frac{1}{cb}$$

$$b_{\Gamma 2} := cb \cdot \gamma^{-3} \cdot \int_1^{cb} z^{-3} \cdot I0(\gamma \cdot z) \, dz \cdot A21' - cb \cdot \gamma^{-3} \cdot \int_1^{cb} z^{-3} \cdot K0(\gamma \cdot z) \, dz \cdot B21' + \frac{cb}{2} \cdot \ln cb \cdot C21' - \frac{\ln cb}{2 \cdot cb} \cdot D21' \dots \\ + cb \cdot \frac{\ln cb^2 - \ln cb}{8} \cdot \Gamma 21'$$

$$c_{F11} := -1 - 1$$

$$c_{E21} := k^2 - 1$$

$$c_{F21} := k^2 + 1$$

$$c_{\Gamma 2} := \frac{3}{64} \cdot A11' - \frac{1}{8} \cdot B11' + \frac{1}{2} \cdot C11' - \frac{1}{2} \cdot D11' + \frac{3}{128} \cdot \Gamma 11' - \frac{1}{64} \cdot A11' - \frac{7}{128} \cdot \Gamma 11' - \gamma^{-3} \cdot I01 \cdot A21' \dots \\ + \gamma^{-3} \cdot K01 \cdot B21' - \frac{1}{2} \cdot C21' + \frac{1}{2} \cdot D21' + \frac{1}{8} \cdot \Gamma 21'$$

$$d2 := \left[ a_{F11} \cdot (b_{F21} \cdot c_{E21} - b_{E21} \cdot c_{F21}) + a_{E21} \cdot (b_{F11} \cdot c_{F21} - b_{F21} \cdot c_{F11}) \dots \right]^{-1} \\ + a_{F21} \cdot (b_{E21} \cdot c_{F11} - b_{F11} \cdot c_{E21})$$

$$F11 := d2 \left[ a_{\Gamma 2} \cdot (b_{E21} \cdot c_{F21} - b_{F21} \cdot c_{E21}) + b_{\Gamma 2} \cdot (a_{F21} \cdot c_{E21} - a_{E21} \cdot c_{F21}) \dots \right] \\ + c_{\Gamma 2} \cdot (a_{E21} \cdot b_{F21} - a_{F21} \cdot b_{E21})$$

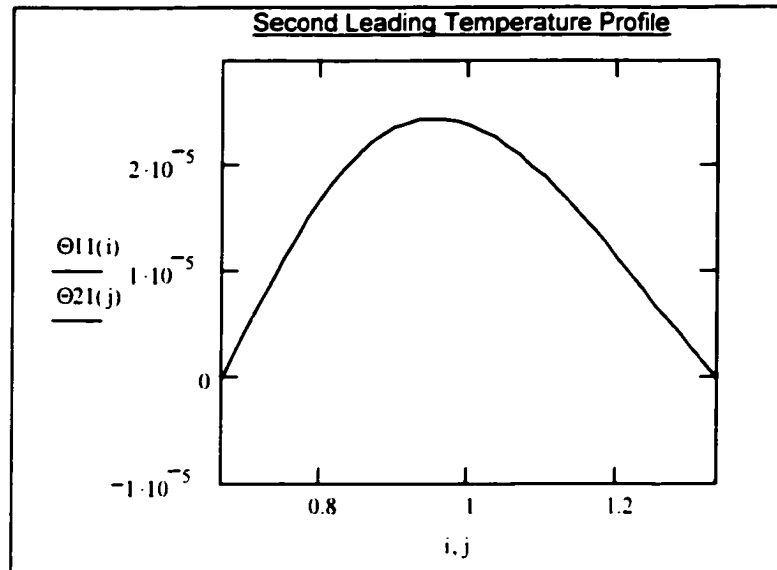
$$E21 := d2 \left[ a_{\Gamma 2} \cdot (b_{F21} \cdot c_{F11} - b_{F11} \cdot c_{F21}) + b_{\Gamma 2} \cdot (a_{F11} \cdot c_{F21} - a_{F21} \cdot c_{F11}) \dots \right] \\ + c_{\Gamma 2} \cdot (a_{F21} \cdot b_{F11} - a_{F11} \cdot b_{F21})$$

$$F21 := d2 \left[ a_{\Gamma 2} \cdot (b_{F11} \cdot c_{E21} - b_{E21} \cdot c_{F11}) + b_{\Gamma 2} \cdot (a_{E21} \cdot c_{F11} - a_{F11} \cdot c_{E21}) \dots \right] \\ + c_{\Gamma 2} \cdot (a_{F11} \cdot b_{E21} - a_{E21} \cdot b_{F11})$$

$$E11 := -F11 + k^2 \cdot E21 + k^2 \cdot F21 + \frac{3}{128} \cdot \Gamma 11' - \frac{1}{64} \cdot A11'$$

$$\Theta 11(R) := q \cdot \left[ \frac{A11'}{64} \cdot R^3 + \frac{\ln(R)^2 - \ln(R)}{8} \cdot B11' \cdot R + \frac{C11'}{2} \cdot R \cdot \ln(R) - \frac{D11'}{2} \cdot \frac{\ln(R)}{R} \dots \right] \\ + E11 \cdot R + \frac{F11}{R} + \left( \frac{\ln(R)}{64} - \frac{3}{128} \right) \cdot \Gamma 11' \cdot R^3$$

$$\Theta 21(R) := q \cdot k^2 \cdot \left( \frac{A21'}{\gamma^3} \cdot R \cdot \int_1^R \frac{I0(\gamma \cdot R)}{R^3} \, dR - \frac{B21'}{\gamma^3} \cdot R \cdot \int_1^R \frac{K0(\gamma \cdot R)}{R^3} \, dR + \frac{C21'}{2} \cdot R \cdot \ln(R) - \frac{D21'}{2} \cdot \frac{\ln(R)}{R} \dots \right) \\ + E21 \cdot R + \frac{F21}{R} + \frac{\ln(R)^2 - \ln(R)}{8} \cdot \Gamma 21' \cdot R$$



#### Checking

inner := ab

$$\Theta_{1l}(\text{inner}) = 0$$

outer := cb

$$\Theta_{2l}(\text{outer}) = 0$$

interface := l

$$\Theta_{1l}(\text{interface}) - \Theta_{2l}(\text{interface}) = 0$$

$$k \left( \frac{d}{d\text{interface}} \Theta_{1l}(\text{interface}) \right) - \frac{d}{d\text{interface}} \Theta_{2l}(\text{interface}) = 0$$

#### Second Leading Terms in Velocity Field

$$\begin{aligned} a'_{l2} := & -\frac{ab^3}{64} \cdot A_{11} - ab \cdot \left( \frac{\ln ab^2 - \ln ab}{8} \right) \cdot B_{11} - \frac{ab}{2} \cdot \ln ab \cdot C_{11} + \frac{\ln ab}{2 \cdot ab} \cdot D_{11} - \frac{3}{128} \cdot ab \cdot \Gamma_{11} \dots \\ & + \frac{ab}{64} \cdot A_{11} - ab^3 \cdot \left( \frac{\ln ab}{64} - \frac{3}{128} \right) \cdot \Gamma_{11} \end{aligned}$$

$$\begin{aligned} b'_{l2} := & -cb \cdot \gamma^{-3} \cdot \int_1^{cb} z^{-3} \cdot I_0(\gamma \cdot z) \, dz \cdot A_{21} + cb \cdot \gamma^{-3} \cdot \int_1^{cb} z^{-3} \cdot K_0(\gamma \cdot z) \, dz \cdot B_{21} - \frac{cb}{2} \cdot \ln cb \cdot C_{21} \dots \\ & + \frac{\ln cb}{2 \cdot cb} \cdot D_{21} - cb \cdot \frac{\ln cb^2 - \ln cb}{8} \cdot \Gamma_{21} \end{aligned}$$

$$\begin{aligned} c'_{l2} := & -\frac{3}{64} \cdot A_{11} + \frac{1}{8} \cdot B_{11} - \frac{1}{2} \cdot C_{11} + \frac{1}{2} \cdot D_{11} - \frac{3}{128} \cdot \Gamma_{11} + \frac{1}{64} \cdot A_{11} + \frac{7}{128} \cdot \Gamma_{11} + \gamma^{-3} \cdot I_0(\gamma \cdot A_{21}) \dots \\ & + \left( \gamma^{-3} \cdot K_0(\gamma \cdot B_{21}) \right) + \frac{1}{2} \cdot C_{21} - \frac{1}{2} \cdot D_{21} - \frac{1}{8} \cdot \Gamma_{21} \end{aligned}$$

$$F11' := d2 \cdot \left[ a'_{\Gamma 2} \cdot (b_{E21} \cdot c_{F21} - b_{F21} \cdot c_{E21}) + b'_{\Gamma 2} \cdot (a_{F21} \cdot c_{E21} - a_{E21} \cdot c_{F21}) \dots \right. \\ \left. + c'_{\Gamma 2} \cdot (a_{E21} \cdot b_{F21} - a_{F21} \cdot b_{E21}) \right]$$

$$E21' := d2 \cdot \left[ a'_{\Gamma 2} \cdot (b_{F21} \cdot c_{F11} - b_{F11} \cdot c_{F21}) + b'_{\Gamma 2} \cdot (a_{F11} \cdot c_{F21} - a_{F21} \cdot c_{F11}) \dots \right. \\ \left. + c'_{\Gamma 2} \cdot (a_{F21} \cdot b_{F11} - a_{F11} \cdot b_{F21}) \right]$$

$$F21' := d2 \cdot \left[ a'_{\Gamma 2} \cdot (b_{F11} \cdot c_{E21} - b_{E21} \cdot c_{F11}) + b'_{\Gamma 2} \cdot (a_{E21} \cdot c_{F11} - a_{F11} \cdot c_{E21}) \dots \right. \\ \left. + c'_{\Gamma 2} \cdot (a_{F11} \cdot b_{E21} - a_{E21} \cdot b_{F11}) \right]$$

$$E11' := -F11' + k \cdot E21' + k \cdot F21' - \frac{3}{128} \cdot \Gamma 11 + \frac{1}{64} \cdot A11$$

$$\mathbf{x}_1 := \frac{\Gamma 11 \cdot \Gamma 11'}{4 \cdot Pr}$$

$$\mathbf{x}_2 := \frac{1}{Pr} \cdot \left( \frac{A11 \cdot \Gamma 11' + A11' \cdot \Gamma 11}{4} - \frac{3 \Gamma 11 \cdot \Gamma 11'}{16} \right) - q \cdot \left( \frac{3}{64} \cdot \sin(\theta) \cdot \Gamma 11' - \frac{1}{64} \cdot \cos(\theta) \cdot \Gamma 11 \right)$$

$$\mathbf{x}_3 := \frac{1}{Pr} \cdot \left[ \frac{A11 \cdot A11'}{4} + \frac{3}{32} \cdot (A11 \cdot \Gamma 11' - 3 \cdot A11' \cdot \Gamma 11 + \Gamma 11 \cdot \Gamma 11') \dots \right. \\ \left. + q \cdot \left[ \sin(\theta) \cdot \left( \frac{-3}{64} \cdot A11' + \frac{1}{8} \cdot B11' + \frac{7}{128} \cdot \Gamma 11' \right) + \cos(\theta) \cdot \left( \frac{1}{64} \cdot A11 - \frac{3}{128} \cdot \Gamma 11 \right) \right] \right]$$

$$\mathbf{x}_4 := \frac{B11 \cdot \Gamma 11' - B11' \cdot \Gamma 11}{2 \cdot Pr} - \frac{q}{8} \cdot (\sin(\theta) \cdot B11' - \cos(\theta) \cdot B11)$$

$$\mathbf{x}_5 := \frac{1}{Pr} \cdot \left( \frac{-A11 \cdot B11' + A11' \cdot B11}{2} + \frac{5 \cdot B11 \cdot \Gamma 11' - B11' \cdot \Gamma 11}{8} + C11 \cdot \Gamma 11' - C11' \cdot \Gamma 11 \right) \dots \\ + -q \cdot \left[ \sin(\theta) \cdot \left( \frac{B11'}{8} + \frac{C11'}{2} \right) + \cos(\theta) \cdot \left( \frac{B11}{8} - \frac{C11}{2} \right) \right]$$

$$\mathbf{x}_6 := \frac{1}{Pr} \cdot \left( \frac{3 \cdot A11 \cdot B11' + 5 \cdot A11' \cdot B11}{8} - A11 \cdot C11' + A11' \cdot C11 - \frac{3 \cdot B11 \cdot \Gamma 11' + 5 \cdot B11' \cdot \Gamma 11}{32} - C11' \cdot \Gamma 11 \right) \dots \\ + -q \cdot \left[ \sin(\theta) \cdot \left( \frac{C11'}{2} + E11 \right) + \cos(\theta) \cdot E11' \right]$$

$$\mathbf{x}_7 := \frac{B11 \cdot B11' - D11 \cdot \Gamma 11' - D11' \cdot \Gamma 11}{Pr} - \frac{q}{2} \cdot (\sin(\theta) \cdot D11' + \cos(\theta) \cdot D11)$$

$$\mathbf{x}_8 := \frac{1}{Pr} \cdot \left( -A11 \cdot D11' - A11' \cdot D11 + \frac{B11 \cdot B11'}{2} \dots \right) + q \cdot \left[ \sin(\theta) \cdot \left( \frac{D11'}{2} + F11 \right) - \cos(\theta) \cdot F11' \right] \\ + B11 \cdot C11' + B11' \cdot C11 - D11' \cdot \Gamma 11$$

$$\mathbf{x}_9 := \frac{B11 \cdot D11' - B11' \cdot D11}{Pr}$$

$$y_1 := q \cdot k \cdot \gamma^{-3} \cdot (-\sin(\theta) \cdot A21' + \cos(\theta) \cdot A21)$$

$$y_2 := q \cdot k \cdot \gamma^{-3} \cdot (\sin(\theta) \cdot B21' - \cos(\theta) \cdot B21)$$

$$y_3 := q \cdot k \cdot \frac{-\sin(\theta) \cdot \Gamma 21' + \cos(\theta) \cdot \Gamma 21}{8}$$

$$y_{4a} := \frac{-\gamma}{2} \cdot A21 \cdot \Gamma 21'$$

$$y_{4b} := \frac{-\gamma}{2} \cdot B21 \cdot \Gamma 21'$$

$$y_{4c} := -q \cdot k \cdot \left[ \sin(\theta) \cdot \left( \frac{C21'}{2} + \frac{\Gamma 21'}{8} \right) + \cos(\theta) \cdot \left( \frac{-C21}{2} + \frac{\Gamma 21}{8} \right) \right]$$



$$\begin{aligned}
y_{5a} &:= -\gamma \cdot A21 \cdot C21' & y_{5b} &:= \gamma \cdot B21 \cdot C21' \\
y_{5c} &:= -q \cdot k \cdot \left[ \sin(\theta) \cdot \left( \frac{C21'}{2} + E21 - \frac{\Gamma21'}{8} \right) + \cos(\theta) \cdot E21' \right] \\
y_{6a} &:= \frac{1}{2} \cdot (A21 \cdot \Gamma21' + A21' \cdot \Gamma21) & y_{6b} &:= \frac{1}{2} \cdot (B21 \cdot \Gamma21' + B21' \cdot \Gamma21) \\
y_{7a} &:= A21 \cdot C21' + A21' \cdot \left( C21 + \frac{\Gamma21}{2} \right) & y_{7b} &:= B21 \cdot C21' + B21' \cdot \left( C21 + \frac{\Gamma21}{2} \right) \\
y_8 &:= \Gamma21 \cdot \Gamma21' - q \cdot k \cdot \frac{\sin(\theta) \cdot D21' + \cos(\theta) \cdot D21}{2} \\
y_{9a} &:= A21 \cdot (\gamma^{-1} \cdot \Gamma21' - \gamma \cdot D21') - q \cdot k \cdot \gamma^{-3} \cdot \sin(\theta) \cdot A21' \\
y_{9b} &:= -B21 \cdot (\gamma^{-1} \cdot \Gamma21' - \gamma \cdot D21') + q \cdot k \cdot \gamma^{-3} \cdot \sin(\theta) \cdot B21' \\
y_{9c} &:= q \cdot k \cdot \left[ \sin(\theta) \cdot \left( \frac{D21'}{2} + F21 \right) - \cos(\theta) \cdot F21' \right] \\
y_{10a} &:= A21 \cdot (D21' - \gamma^{-2} \cdot \Gamma21') - A21' \cdot (D21 - \gamma^{-2} \cdot \Gamma21) \\
y_{10b} &:= B21 \cdot (D21' - \gamma^{-2} \cdot \Gamma21') - B21' \cdot (D21 - \gamma^{-2} \cdot \Gamma21) \\
y_{11} &:= -D21 \cdot \Gamma21' + D21' \cdot \Gamma21
\end{aligned}$$

$$\begin{aligned}
Z(R) &:= y_1 \cdot \int_1^R z^{-3} \cdot I0(\gamma \cdot z) \, dz + y_2 \cdot \int_1^R z^{-3} \cdot K0(\gamma \cdot z) \, dz + y_3 \cdot \ln(R)^2 + y_{4a} \cdot I0(\gamma \cdot R) \cdot \ln(R) + y_{4b} \cdot K0(\gamma \cdot R) \cdot \ln(R) \dots \\
&\quad + y_{4c} \cdot \ln(R) + y_{5a} \cdot I0(\gamma \cdot R) + y_{5b} \cdot K0(\gamma \cdot R) + y_{5c} + y_{6a} \cdot I1(\gamma \cdot R) \cdot R^{-1} \cdot \ln(R) + y_{6b} \cdot K1(\gamma \cdot R) \cdot R^{-1} \cdot \ln(R) \dots \\
&\quad + y_{7a} \cdot I1(\gamma \cdot R) \cdot R^{-1} + y_{7b} \cdot K1(\gamma \cdot R) \cdot R^{-1} + y_8 \cdot R^{-2} \cdot \ln(R) + y_{9a} \cdot I0(\gamma \cdot R) \cdot R^{-2} + y_{9b} \cdot K0(\gamma \cdot R) \cdot R^{-2} \dots \\
&\quad + y_{9c} \cdot R^{-2} + y_{10a} \cdot I1(\gamma \cdot R) \cdot R^{-3} + y_{10b} \cdot K1(\gamma \cdot R) \cdot R^{-3} + y_{11} \cdot R^{-4}
\end{aligned}$$

$$\begin{aligned}
k1 &:= \left[ \frac{x_1}{384} \cdot \ln ab^2 + \left( \frac{-25 \cdot x_1}{4608} + \frac{x_2}{384} \right) \cdot \ln ab + \left( \frac{415 \cdot x_1}{110592} - \frac{25 \cdot x_2}{9216} + \frac{x_3}{384} \right) \right] \cdot ab^6 \dots \\
&\quad + \left[ \frac{x_4}{144} \cdot \ln ab^3 + \left( \frac{-11 \cdot x_4}{576} + \frac{x_5}{96} \right) \cdot \ln ab^2 \dots \right] \cdot ab^4 \dots \\
&\quad + \left[ \left( \frac{85 \cdot x_4}{3456} - \frac{11 \cdot x_5}{576} + \frac{x_6}{48} \right) \cdot \ln ab - \frac{137 \cdot x_4}{10368} + \frac{19 \cdot x_5}{1728} - \frac{x_6}{72} \right] \\
&\quad + \left[ \frac{-x_7}{32} \cdot \ln ab^2 + \left( \frac{x_7}{64} - \frac{x_8}{16} \right) \cdot \ln ab \right] \cdot ab^2 + \frac{x_9}{16} \cdot \ln ab
\end{aligned}$$

$$\begin{aligned}
k2 &:= \left[ \frac{x_1}{64} \cdot \ln ab^2 + \left( \frac{-7 \cdot x_1}{256} + \frac{x_2}{64} \right) \cdot \ln ab + \frac{35 \cdot x_1}{2048} - \frac{7 \cdot x_2}{512} + \frac{x_3}{64} \right] \cdot ab^5 \dots \\
&\quad + \left[ \frac{x_4}{36} \cdot \ln ab^3 + \left( \frac{-x_4}{18} + \frac{x_5}{24} \right) \cdot \ln ab^2 + \left( \frac{13 \cdot x_4}{216} - \frac{x_5}{18} + \frac{x_6}{12} \right) \cdot \ln ab + \left( \frac{-293 \cdot x_4}{10368} + \frac{43 \cdot x_5}{1728} - \frac{5 \cdot x_6}{144} \right) \right] \cdot ab^3 \dots \\
&\quad + \left[ \frac{-x_7}{16} \cdot \ln ab^2 - \left( \frac{x_7}{32} + \frac{x_8}{8} \right) \cdot \ln ab + \frac{x_7}{64} - \frac{x_8}{16} \right] \cdot ab + \frac{x_9}{16 \cdot ab}
\end{aligned}$$

$$k_{AC} := \frac{-1}{4} \cdot \int_1^{cb} z^{-1} \cdot I2(\gamma \cdot z) \, dz$$

$$k_{BC} := \frac{-1}{4} \cdot \int_1^{cb} z^{-1} \cdot K2(\gamma \cdot z) \, dz$$

$$k_{cC} := \frac{1}{4} \cdot \left[ \int_1^{cb} z^{-1} \cdot I2(\gamma \cdot z) \cdot \left( \int_1^z y \cdot Z(y) \cdot K2(\gamma \cdot y) \, dy \right) dz - \int_1^{cb} z^{-1} \cdot K2(\gamma \cdot z) \cdot \left( \int_1^z y \cdot Z(y) \cdot I2(\gamma \cdot y) \, dy \right) dz \right]$$

$$k_{AD} := \frac{1}{4} \cdot \int_1^{cb} z^3 \cdot I2(\gamma \cdot z) \, dz$$

$$k_{BD} := \frac{1}{4} \cdot \int_1^{cb} z^3 \cdot K2(\gamma \cdot z) \, dz$$

$$k_{cD} := \frac{1}{4} \cdot \left[ - \int_1^{cb} z^3 \cdot I2(\gamma \cdot z) \cdot \left( \int_1^z y \cdot Z(y) \cdot K2(\gamma \cdot y) \, dy \right) dz + \int_1^{cb} z^3 \cdot K2(\gamma \cdot z) \cdot \left( \int_1^z y \cdot Z(y) \cdot I2(\gamma \cdot y) \, dy \right) dz \right]$$

$$a_{B12} := \left( \frac{1}{12} - \frac{ab^2}{8} + \frac{ab^6}{24} \right) + \frac{1}{8 \cdot ab^2} - \frac{1}{4} + \frac{ab^2}{8}$$

$$a_{A22} := \left( \frac{1}{12} - \frac{ab^2}{8} + \frac{ab^6}{24} \right) \cdot I2(\gamma) - k_{AC} - k_{AD}$$

$$a_{B22} := \left( \frac{1}{12} - \frac{ab^2}{8} + \frac{ab^6}{24} \right) \cdot K2(\gamma) - k_{BC} - k_{BD}$$

$$a_{k3} := \frac{415x_1}{110592} - \frac{25x_2}{9216} + \frac{x_3}{384} - \frac{137x_4}{10368} + \frac{19x_5}{1728} - \frac{x_6}{72} + \left( \frac{1}{12} - \frac{ab^2}{8} + \frac{ab^6}{24} \right) \cdot \left( \frac{-13x_1}{216} + \frac{x_2}{18} - \frac{x_3}{12} + \frac{x_8}{4} \right) \dots$$

$$+ \frac{1}{8 \cdot ab^2} \cdot (-2k_2 \cdot ab - 4k_1) + \frac{1}{4} \cdot k_2 \cdot ab^3 - \frac{1}{2} \cdot k_1 \cdot ab^2 - k_{cC} - k_{cD}$$

$$b_{B12} := \frac{-1}{3} + \frac{ab^2}{4} + \frac{ab^6}{12} + \frac{1}{4ab^2} - \frac{ab^2}{4}$$

$$b_{A22} := \left( \frac{1}{3} - \frac{ab^2}{4} - \frac{ab^6}{12} \right) \cdot I21 - 2k_{AC} + 2k_{AD}$$

$$b_{B22} := \left( \frac{1}{3} - \frac{ab^2}{4} - \frac{ab^6}{12} \right) \cdot K21 - 2k_{BC} + 2k_{BD}$$

$$b_{k3} := \frac{35x_1}{2048} - \frac{7x_2}{512} + \frac{x_3}{64} - \frac{293x_4}{10368} + \frac{43x_5}{1728} - \frac{5x_6}{144} + \frac{x_7}{64} - \frac{x_8}{16} + \frac{x_9}{16} - 2k_{cC} + 2k_{cD} \dots$$

$$+ \left( \frac{1}{3} - \frac{ab^2}{4} - \frac{ab^6}{12} \right) \cdot \left( \frac{-13x_1}{216} + \frac{x_2}{18} - \frac{x_3}{12} + \frac{x_8}{4} \right) + \frac{1}{4 \cdot ab^2} \cdot (-2k_2 \cdot ab - 4k_1) - \frac{1}{2} \cdot k_2 \cdot ab^3 + k_1 \cdot ab^2$$

$$c_{B12} := -2 - 2$$

$$c_{A22} := 2I21 - (\gamma \cdot I11 - 2 \cdot I21) + \frac{2}{Da} \cdot kAC - \frac{2}{Da} \cdot kAD$$

$$c_{B22} := 2K21 - (-\gamma \cdot K11 - 2 \cdot K21) + \frac{2}{Da} \cdot kBC - \frac{2}{Da} \cdot kBD$$

$$c_{k3} := \frac{7 \cdot x_1}{54} - \frac{5 \cdot x_2}{36} + \frac{x_3}{3} + \frac{x_4}{32} - \frac{x_5}{16} + \frac{x_6}{4} - \frac{x_7}{4} - \frac{x_9}{4} + 2 \cdot \left( \frac{-13 \cdot x_1}{216} + \frac{x_2}{18} - \frac{x_3}{12} + \frac{x_8}{4} \right) + \frac{2}{Da} \cdot kcC - \frac{2}{Da} \cdot kcD$$

$$d3 := \left[ \begin{array}{l} a_{B12} \cdot (b_{B22} \cdot c_{A22} - b_{A22} \cdot c_{B22}) + a_{A22} \cdot (b_{B12} \cdot c_{B22} - b_{B22} \cdot c_{B12}) \dots \\ + a_{B22} \cdot (b_{A22} \cdot c_{B12} - b_{B12} \cdot c_{A22}) \end{array} \right]^{-1}$$

$$B12 := d3 \cdot \left[ \begin{array}{l} a_{k3} \cdot (b_{A22} \cdot c_{B22} - b_{B22} \cdot c_{A22}) + b_{k3} \cdot (a_{B22} \cdot c_{A22} - a_{A22} \cdot c_{B22}) \dots \\ + c_{k3} \cdot (a_{A22} \cdot b_{B22} - a_{B22} \cdot b_{A22}) \end{array} \right]$$

$$A22 := d3 \cdot \left[ \begin{array}{l} a_{k3} \cdot (b_{B22} \cdot c_{B12} - b_{B12} \cdot c_{B22}) + b_{k3} \cdot (a_{B12} \cdot c_{B22} - a_{B22} \cdot c_{B12}) \dots \\ + c_{k3} \cdot (a_{B22} \cdot b_{B12} - a_{B12} \cdot b_{B22}) \end{array} \right]$$

$$B22 := d3 \cdot \left[ \begin{array}{l} a_{k3} \cdot (b_{B12} \cdot c_{A22} - b_{A22} \cdot c_{B12}) + b_{k3} \cdot (a_{A22} \cdot c_{B12} - a_{B12} \cdot c_{A22}) \dots \\ + c_{k3} \cdot (a_{B12} \cdot b_{A22} - a_{A22} \cdot b_{B12}) \end{array} \right]$$

$$A12 := - \left( 13 \cdot \frac{x_1}{216} - \frac{x_2}{18} + \frac{x_3}{12} - \frac{x_8}{4} + B12 \right) + (A22 \cdot I21 + B22 \cdot K21)$$

$$C12 := \frac{-ab^2}{8} \cdot A12 + \frac{1}{8ab^2} \cdot (B12 - 2k2 \cdot ab - 4k1)$$

$$D12 := \frac{ab^6}{24} \cdot A12 + \frac{ab^2}{8} \cdot B12 + \frac{ab^3}{4} \cdot k2 - \frac{1}{2} \cdot k1 \cdot ab^2$$

$$C22 := kAC \cdot A22 + kBC \cdot B22 + kcC$$

$$D22 := kAD \cdot A22 + kBD \cdot B22 + kcD$$

$$\begin{aligned} \Omega 12(R) := & \left[ \frac{x_1}{12} \cdot \ln(R)^2 + \left( \frac{-x_1}{9} + \frac{x_2}{12} \right) \cdot \ln(R) + \left( \frac{13 \cdot x_1}{216} - \frac{x_2}{18} + \frac{x_3}{12} \right) \right] \cdot R^4 \dots \\ & + \left[ \frac{x_4}{12} \cdot \ln(R)^3 + \left( \frac{-x_4}{16} + \frac{x_5}{8} \right) \cdot \ln(R)^2 + \left( \frac{x_4}{32} - \frac{x_5}{16} + \frac{x_6}{4} \right) \cdot \ln(R) + A12 \right] \cdot R^2 \dots \\ & + \left( \frac{x_7}{4} \cdot \ln(R) + \frac{x_8}{4} \right) + \left( \frac{-x_9}{4} \cdot \ln(R) + B12 \right) \cdot R^{-2} \end{aligned}$$

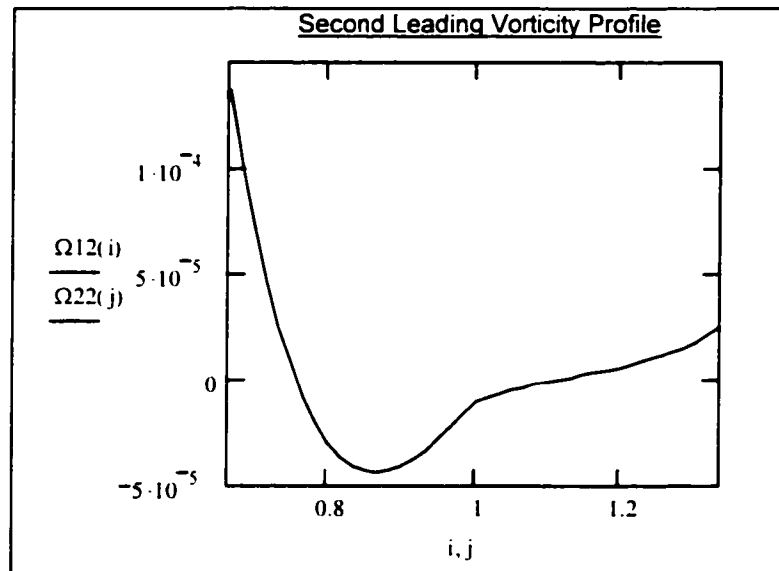
$$\Omega 22(R) := \left[ B22 + \int_1^R (x \cdot Z(z) \cdot I2(\gamma \cdot z)) \, dz \right] \cdot K2(\gamma \cdot R) + \left[ A22 - \int_1^R (x \cdot Z(z) \cdot K2(\gamma \cdot z)) \, dz \right] \cdot I2(\gamma \cdot R)$$

$$\begin{aligned} \Psi 12(R) := & \left[ \frac{x_1}{384} \cdot \ln(R)^2 + \left( \frac{-25 \cdot x_1}{4608} + \frac{x_2}{384} \right) \cdot \ln(R) + \left( \frac{415 \cdot x_1}{110592} - \frac{25 \cdot x_2}{9216} + \frac{x_3}{384} \right) \right] \cdot R^6 \dots \\ & + \left[ \frac{x_4}{144} \cdot \ln(R)^3 + \left( \frac{-11 \cdot x_4}{576} + \frac{x_5}{96} \right) \cdot \ln(R)^2 \dots \right. \\ & \quad \left. + \left( \frac{85 \cdot x_4}{3456} - \frac{11 \cdot x_5}{576} + \frac{x_6}{48} \right) \cdot \ln(R) - \frac{137 \cdot x_4}{10368} + \frac{19 \cdot x_5}{1728} - \frac{x_6}{72} + \frac{A12}{12} \right] \cdot R^4 \dots \\ & + \left[ \frac{-x_7}{32} \cdot \ln(R)^2 + \left( \frac{x_7}{64} - \frac{x_8}{16} \right) \cdot \ln(R) + C12 \right] \cdot R^2 + \frac{x_9}{16} \cdot \ln(R) - \frac{B12}{4} + D12 \cdot R^{-2} \end{aligned}$$

$$\Psi_{22}(R) := (C_{22}R^2 + D_{22}R^{-2}) \dots$$

$$+ \frac{-1}{4R^2} \int_1^R z^3 \left[ \left[ B_{22} + \int_1^z (y \cdot Z(y) \cdot I_2(\gamma \cdot y)) dy \right] \cdot K_2(\gamma \cdot z) \dots \right. \\ \left. + \left[ A_{22} - \int_1^z (y \cdot Z(y) \cdot K_2(\gamma \cdot y)) dy \right] \cdot I_2(\gamma \cdot z) \right] dz \dots$$

$$+ \frac{R^2}{4} \int_1^R \left[ \left[ B_{22} + \int_1^z (y \cdot Z(y) \cdot I_2(\gamma \cdot y)) dy \right] \cdot K_2(\gamma \cdot z) \dots \right. \\ \left. + \left[ A_{22} - \int_1^z (y \cdot Z(y) \cdot K_2(\gamma \cdot y)) dy \right] \cdot I_2(\gamma \cdot z) \right] dz$$



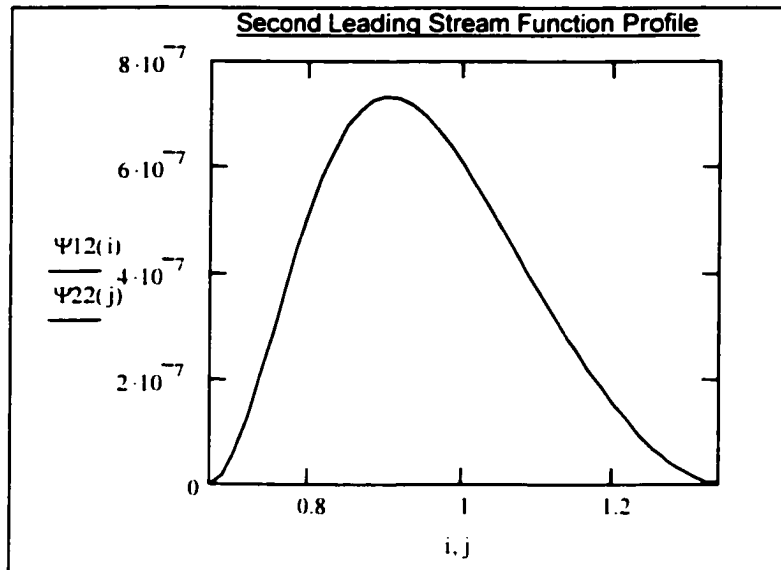
#### Checking

interface := 1

$$\Omega_{12}(\text{interface}) - \Omega_{22}(\text{interface}) = 0$$

$$\frac{d}{d\text{interface}} \Omega_{12}(\text{interface}) - \frac{d}{d\text{interface}} \Omega_{22}(\text{interface}) \dots = -6.014 \cdot 10^{-14}$$

$$+ \frac{1}{Da} \frac{d}{d\text{interface}} \Psi_{22}(\text{interface})$$



**Checking**

inner := ab

$$\Psi_{12}(\text{inner}) = 0$$

$$\frac{d}{d\text{inner}} \Psi_{12}(\text{inner}) = 0$$

outer := cb

$$\Psi_{22}(\text{outer}) = 0$$

$$\frac{d}{d\text{outer}} \Psi_{22}(\text{outer}) = 0$$

interface := 1

$$\Psi_{12}(\text{interface}) - \Psi_{22}(\text{interface}) = 0$$

$$\frac{d}{d\text{interface}} \Psi_{12}(\text{interface}) - \frac{d}{d\text{interface}} \Psi_{22}(\text{interface}) = 0$$

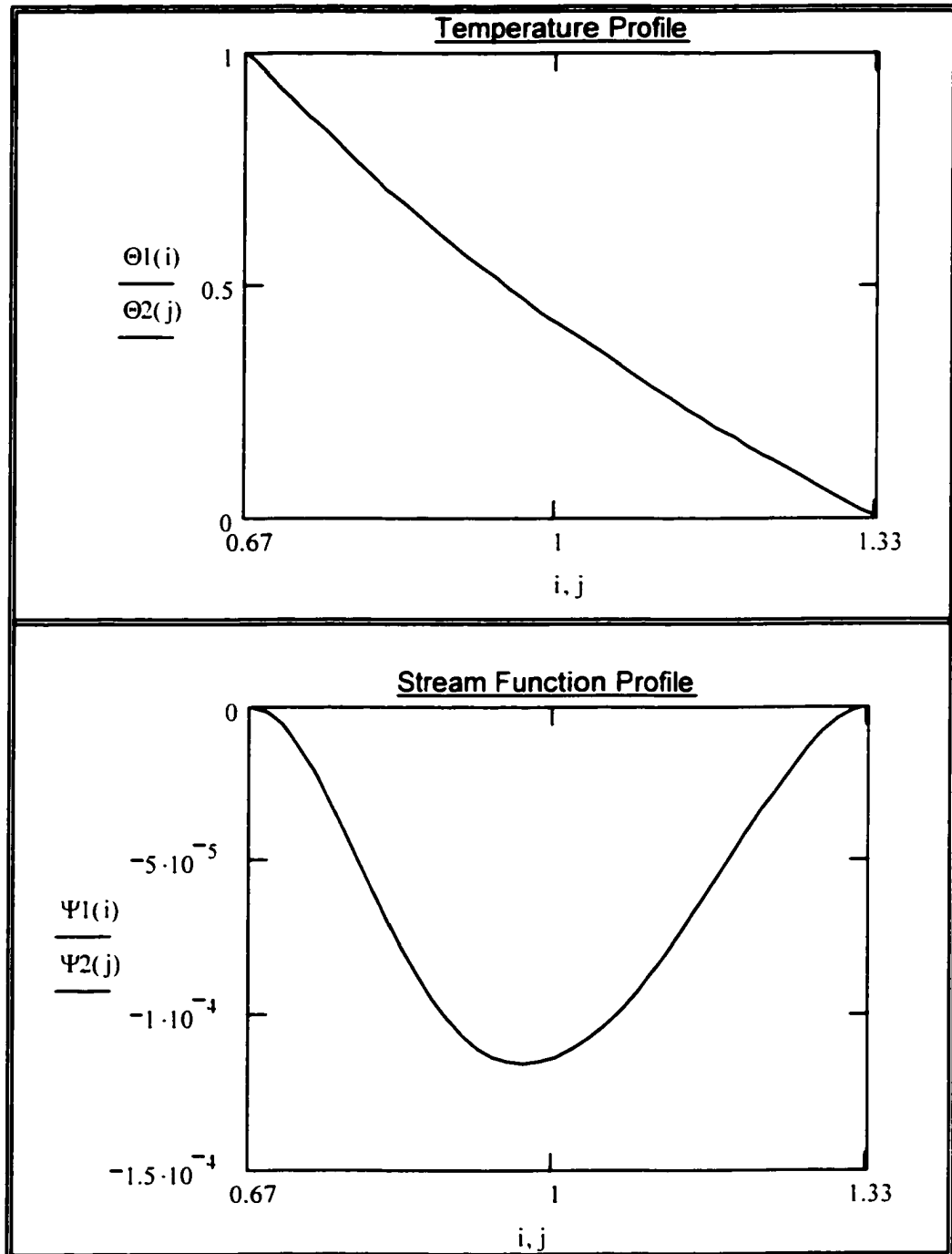
### Composite Velocity and Temperature Fields

$$\Psi_1(R) := Ra \cdot \Psi_{11}(R) + Ra^2 \cdot 0$$

$$\Theta_1(R) := \Theta_{10}(R) + Ra \cdot \Theta_{11}(R)$$

$$\Psi_2(R) := Ra \cdot \Psi_{21}(R) + Ra^2 \cdot 0$$

$$\Theta_2(R) := \Theta_{20}(R) + Ra \cdot \Theta_{21}(R)$$



**APPENDIX F**  
**ADDITIONAL PLOTS OF FLOW AND TEMPERATURE FIELDS**  
**FOR MIXED CONVECTION**

This appendix shows plots of some additional runs for Chapter Four. These plots are not included and discussed in the chapter because the effects of these cases are not of primary interest.

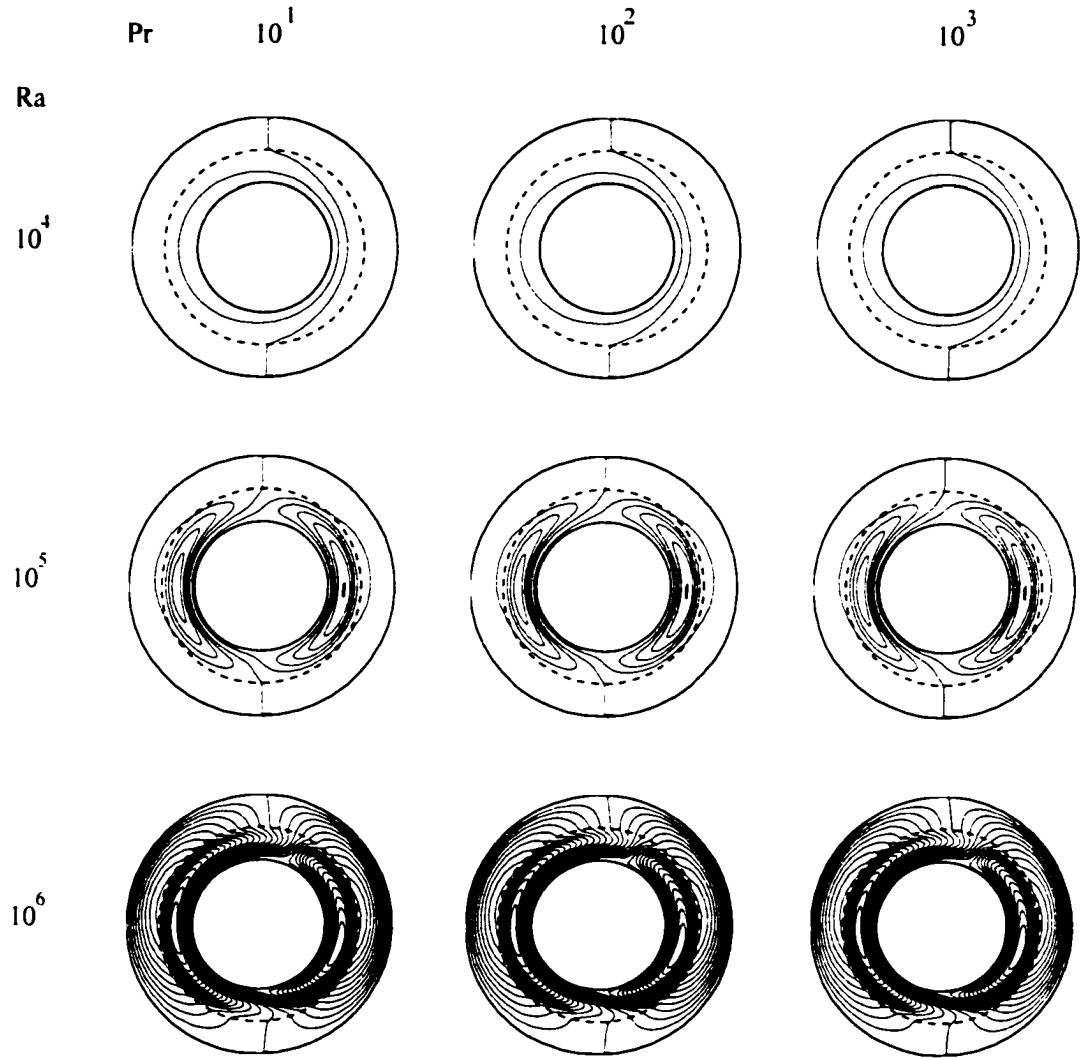
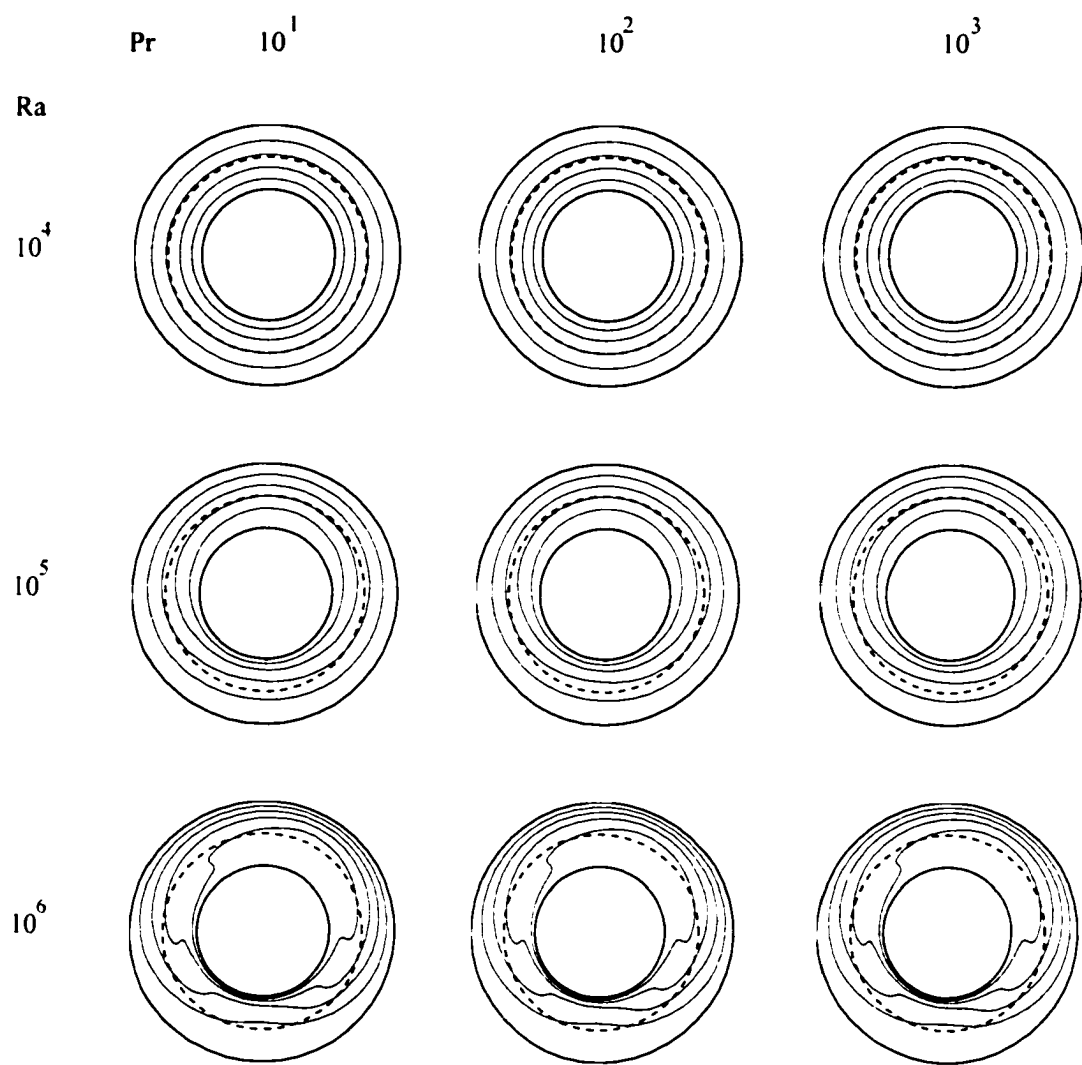


Figure F1 Flow fields of a concentric partially porous annulus space for  $b = 1.50$ ,  $Da = 10^{-4}$ ,  $k_1/k_2 = 1.0$ , and  $Pe = 10$  ( $\Delta\Psi = 1.0$ ).





**Figure F2** Temperature fields of a concentric partially porous annulus space for  $b = 1.50$ ,  $Da = 10^{-4}$ ,  $k_1/k_2 = 1.0$ , and  $Pe = 10$  ( $\Delta\Theta = 0.2$ ).

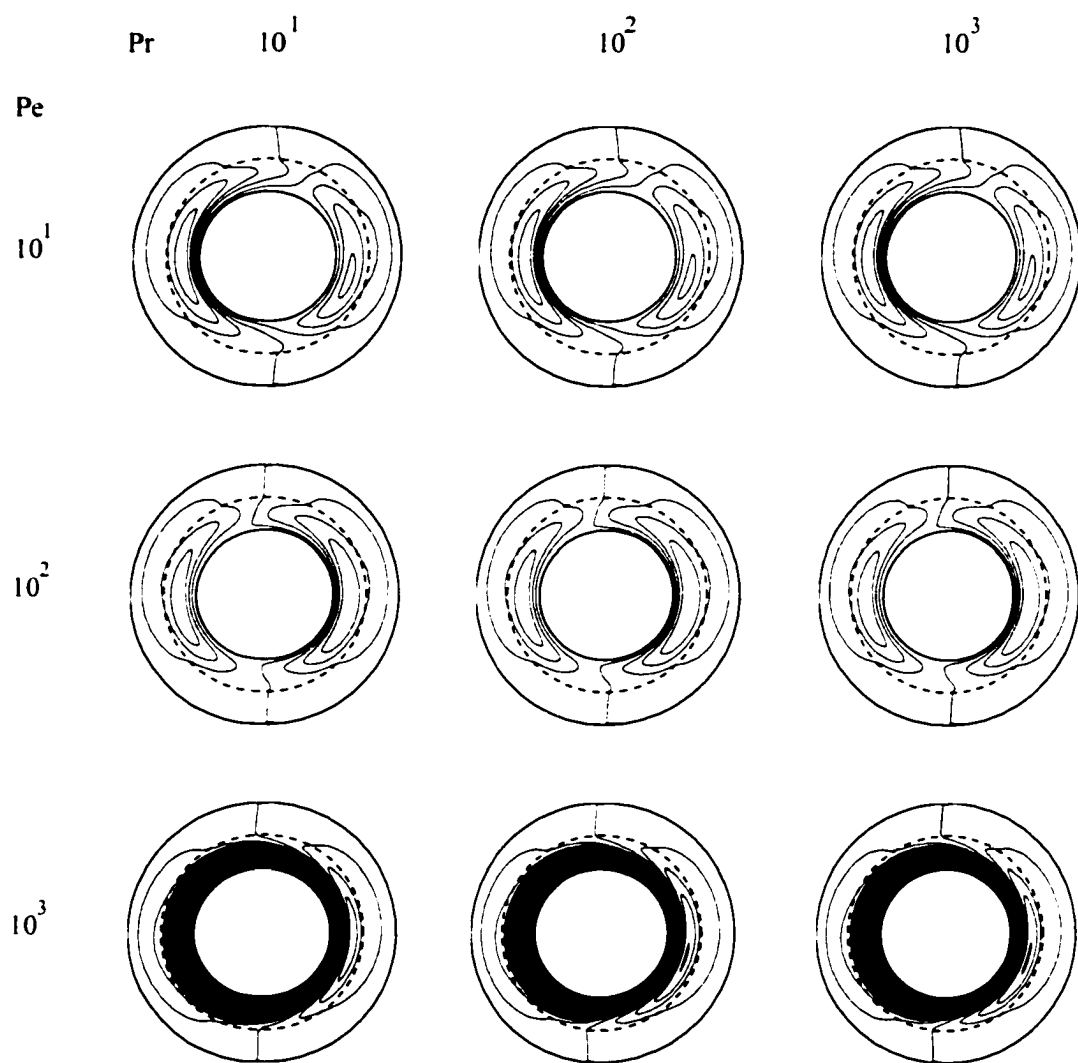
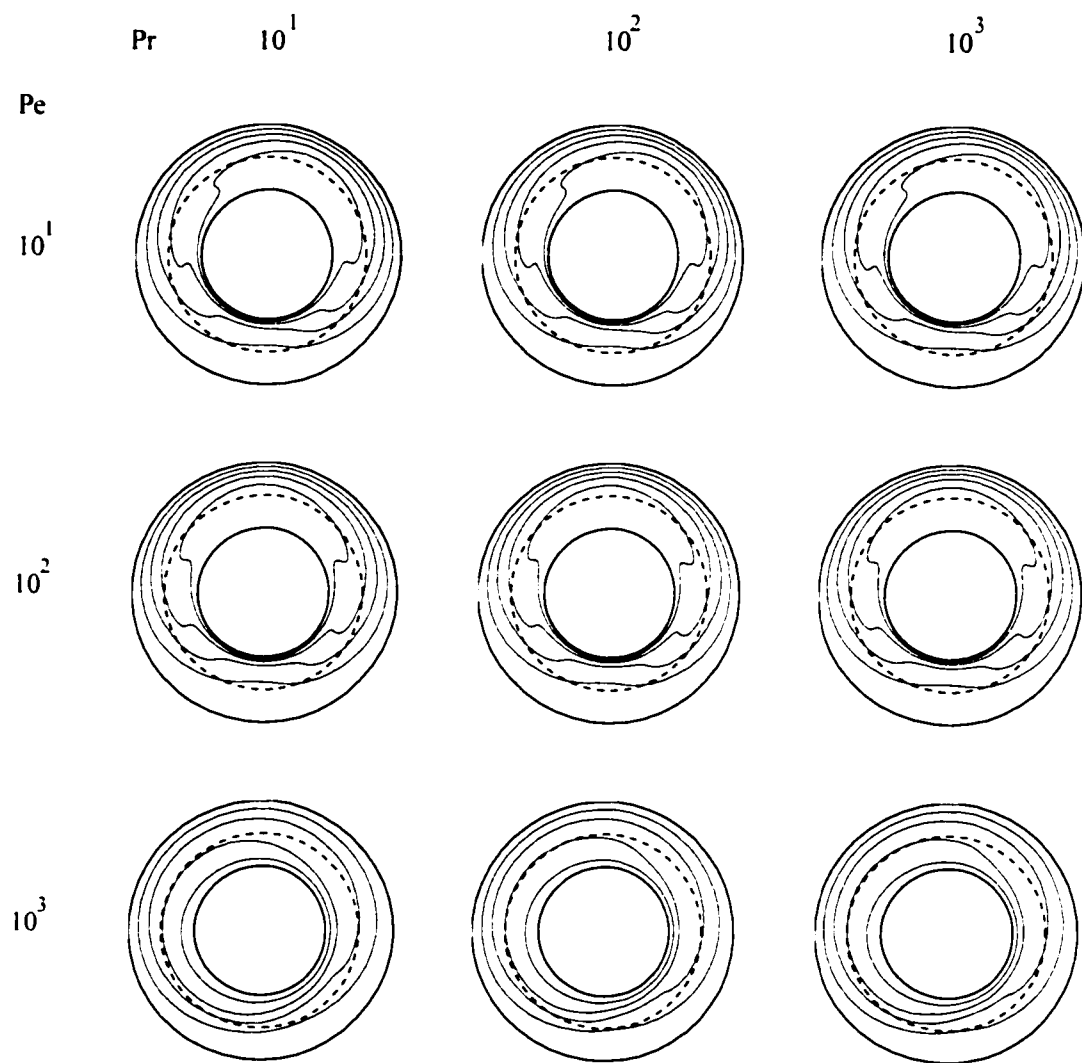


Figure F3 Flow fields of a concentric partially porous annulus space for  $h = 1.50$ ,  $Da = 10^{-4}$ ,  $k_1/k_2 = 1.0$ , and  $Ra = 10^6$  ( $\Delta\Psi = 0.5$ ).



**Figure F4** Temperature fields of a concentric partially porous annulus space for  $b = 1.50$ ,  $Da = 10^{-4}$ ,  $k_1/k_2 = 1.0$ , and  $Ra = 10^6$  ( $\Delta\Theta = 0.2$ ).

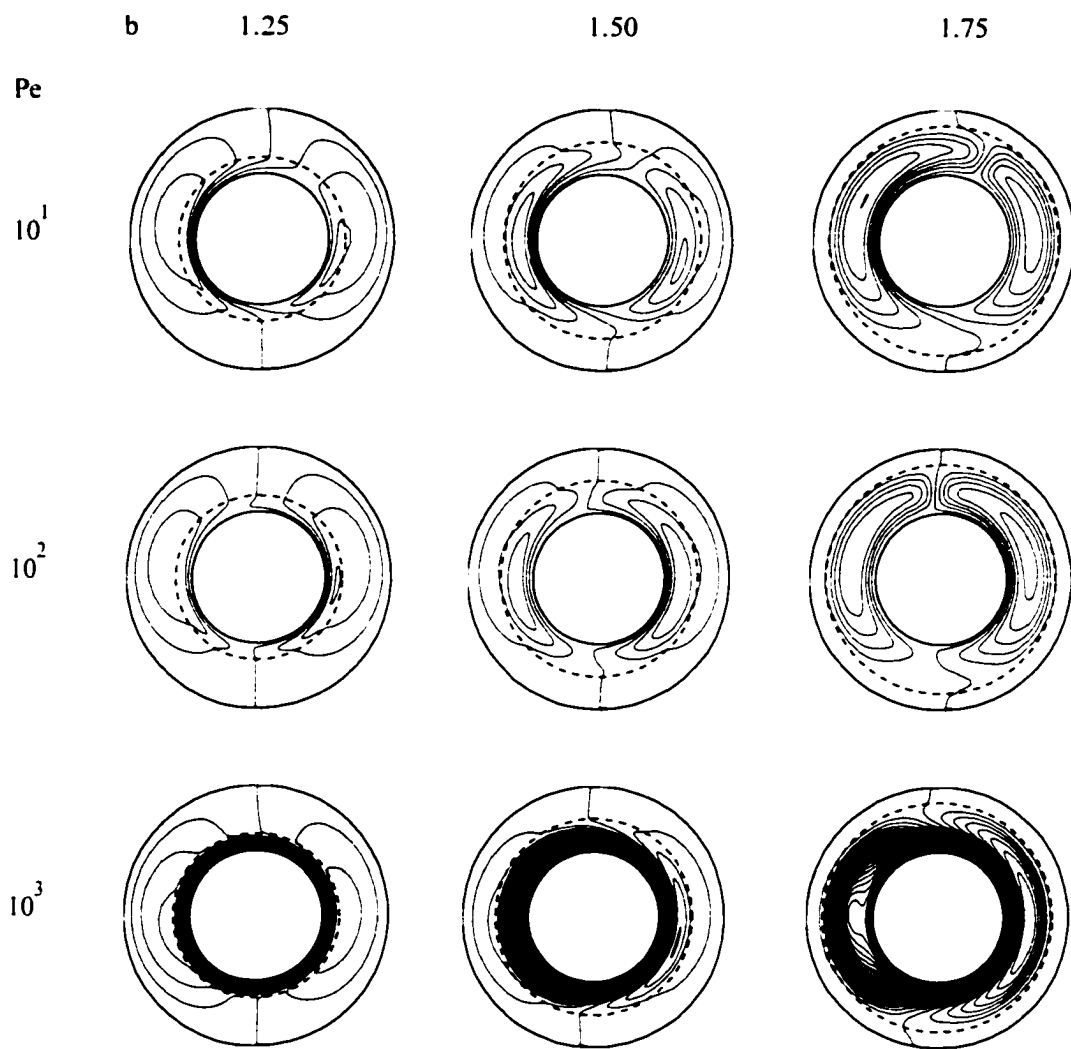
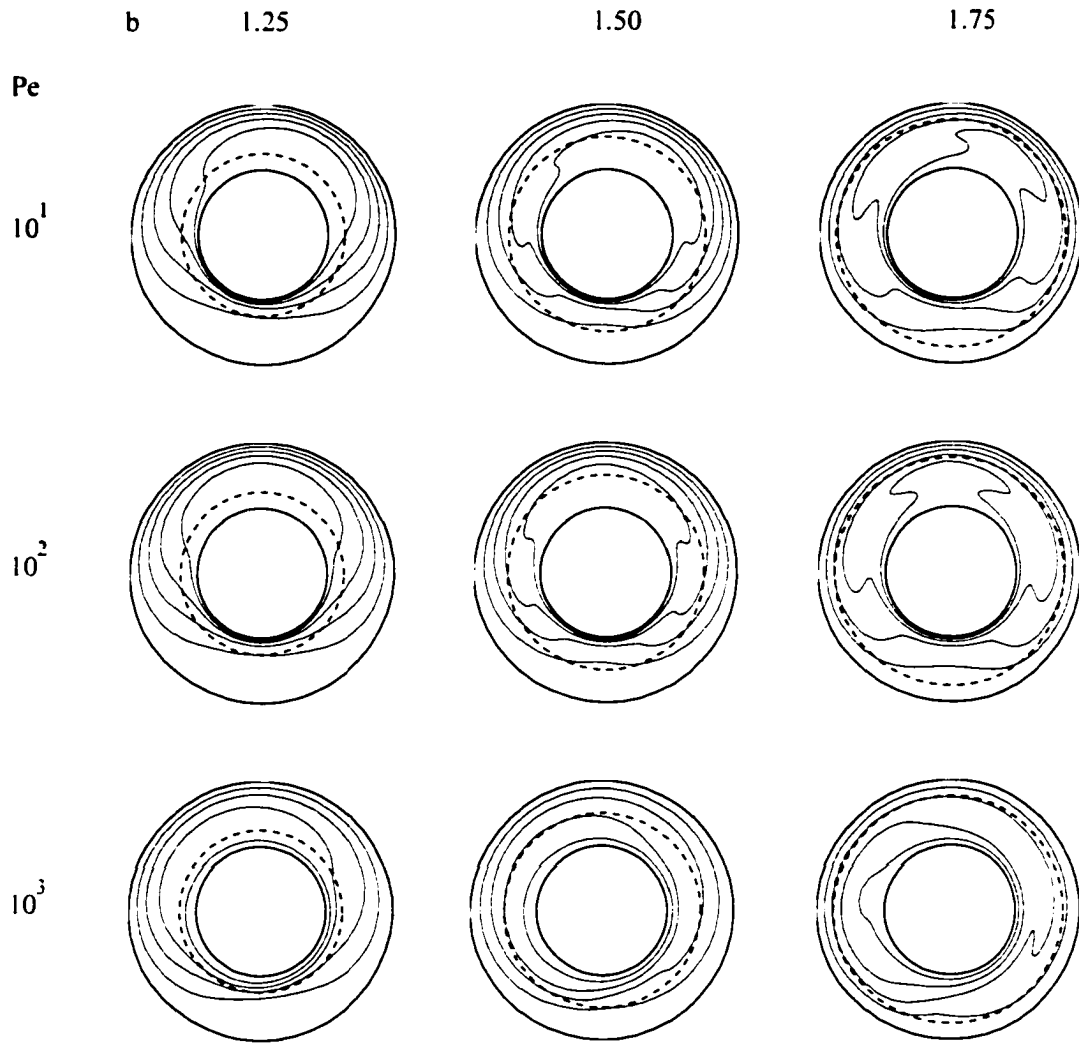


Figure F5 Flow fields of a concentric partially porous annulus space for  $Da = 10^{-4}$ ,  $k_1/k_2 = 1.0$ ,  $Pr = 20,000$ , and  $Ra = 10^6$  ( $\Delta\Psi = 5.0$ ).



**Figure F6** Temperature fields of a concentric partially porous annulus space for  $Du = 10^{-4}$ ,  $k_1/k_2 = 1.0$ ,  $Pr = 20,000$ , and  $Ra = 10^6$  ( $\Delta\Theta = 0.2$ ).

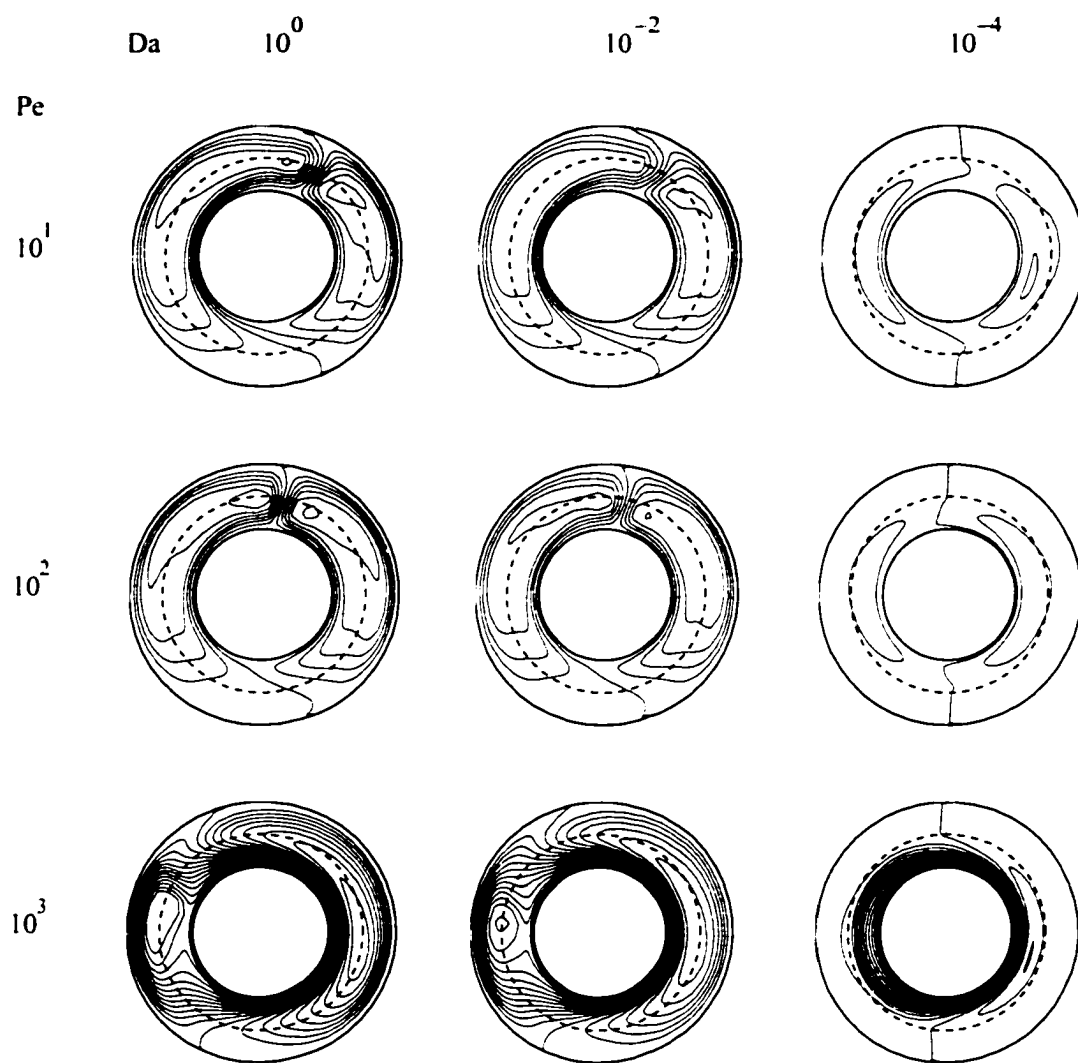


Figure F7 Flow fields of a concentric partially porous annulus space for  $b = 1.50$ ,  $k_1/k_2 = 1.0$ ,  $Pr = 20,000$ , and  $Ra = 10^6$  ( $\Delta\Psi = 10.0$ ).

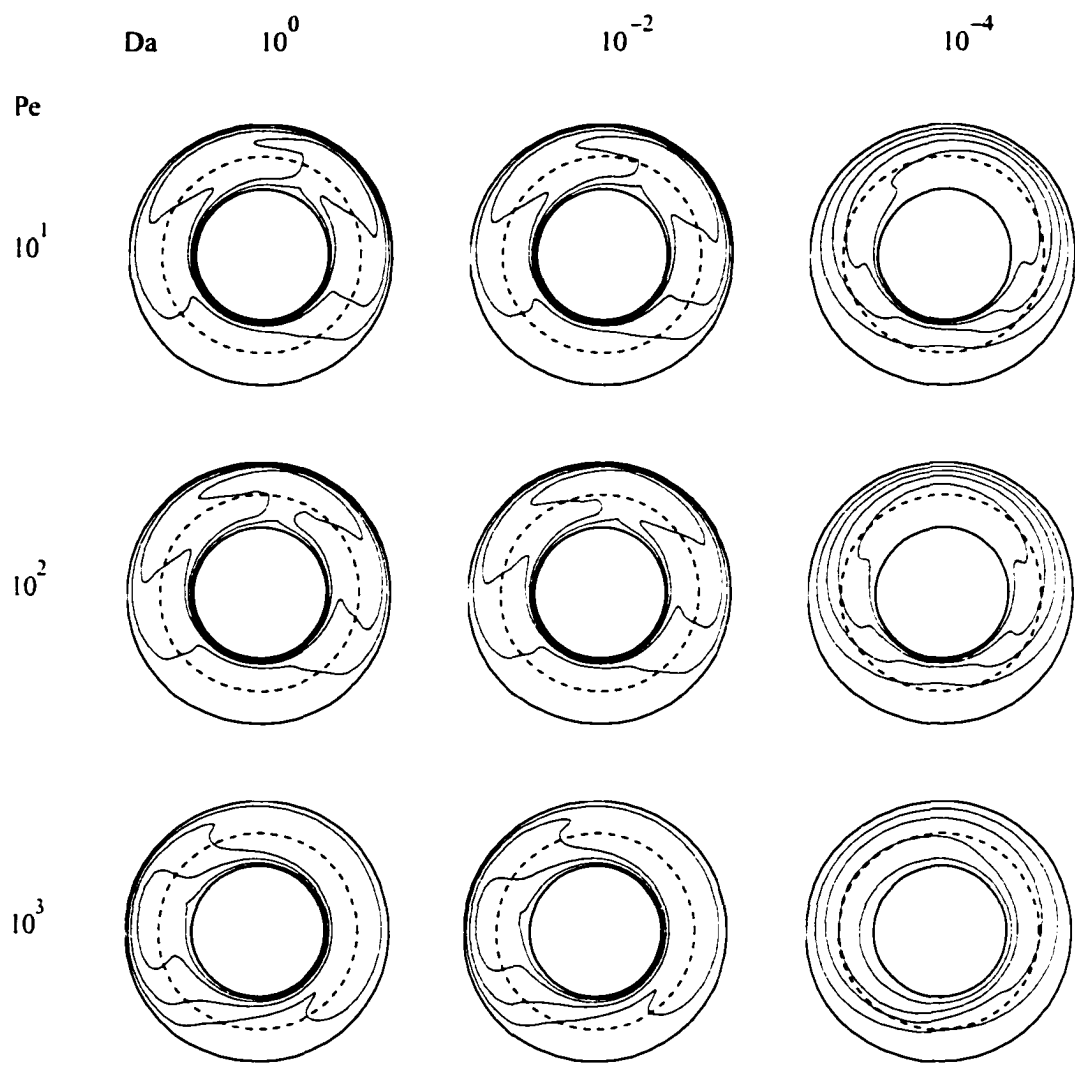
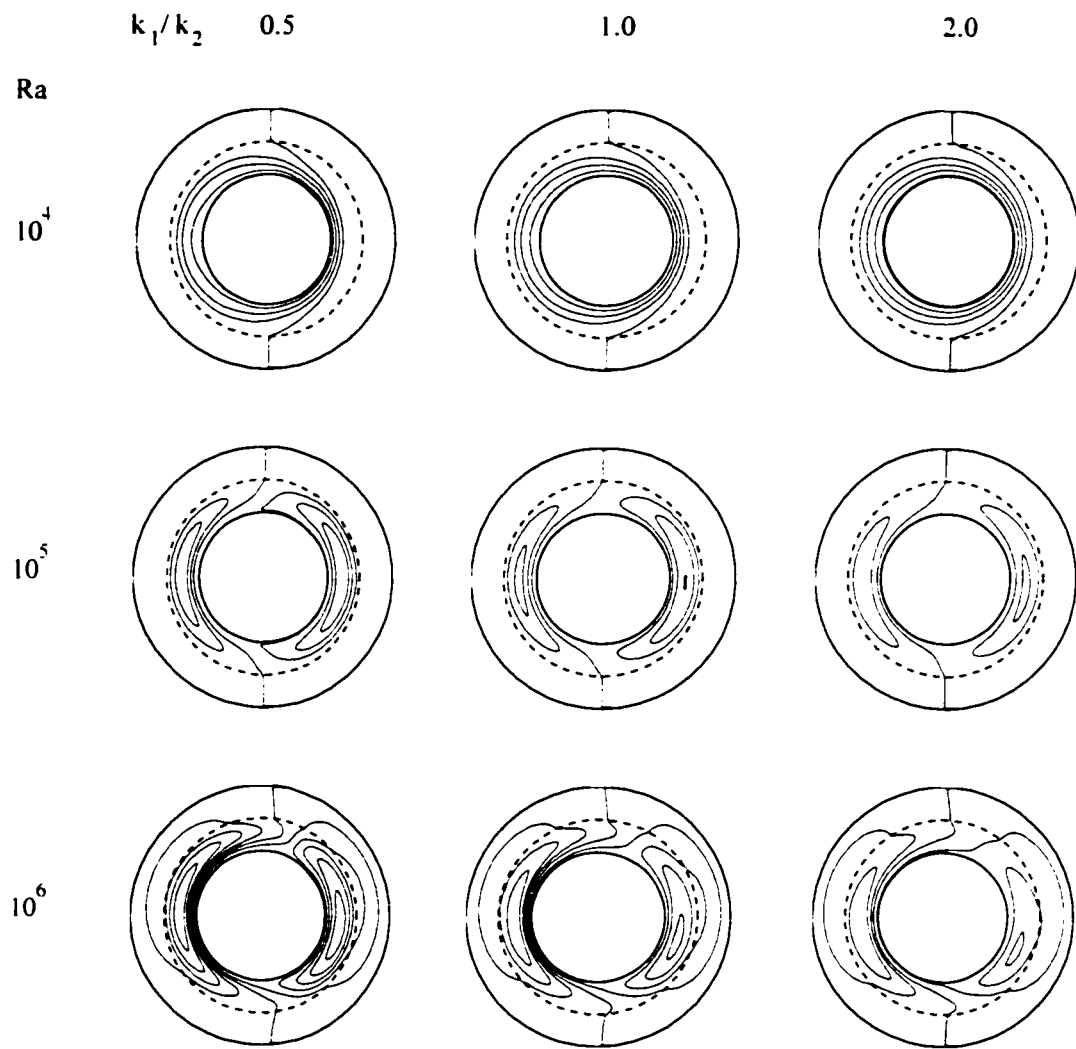


Figure F8 Temperature fields of a concentric partially porous annulus space for  $b = 1.50$ ,  $k_1/k_2 = 1.0$ ,  $Pr = 20,000$ , and  $Ra = 10^6$  ( $\Delta\Theta = 0.2$ ).



**Figure F9** Flow fields of a concentric partially porous annulus space for  $b = 1.50$ ,  $Da = 10^{-6}$ ,  $Pe = 10$ , and  $Pr = 20,000$  ( $\Delta\Psi = 0.5$  for  $Ra = 10^4$ ,  $\Delta\Psi = 2.0$  for  $Ra = 10^5$ , and  $\Delta\Psi = 5.0$  for  $Ra = 10^6$ ).



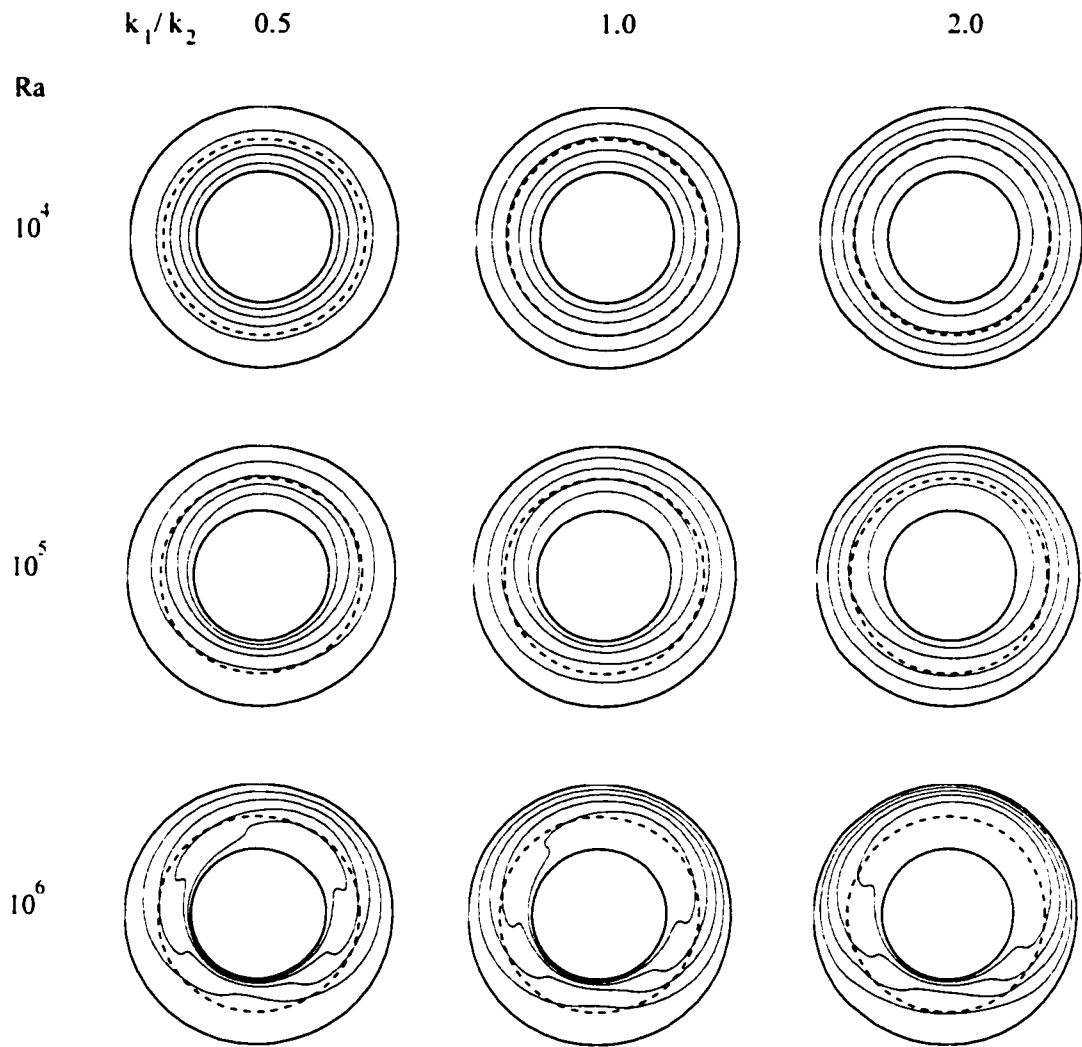


Figure F10 Temperature fields of a concentric partially porous annulus space for  $h = 1.50$ ,  $Da = 10^{-6}$ ,  $Pe = 10$ , and  $Pr = 20,000$  ( $\Delta\Theta = 0.2$ ).

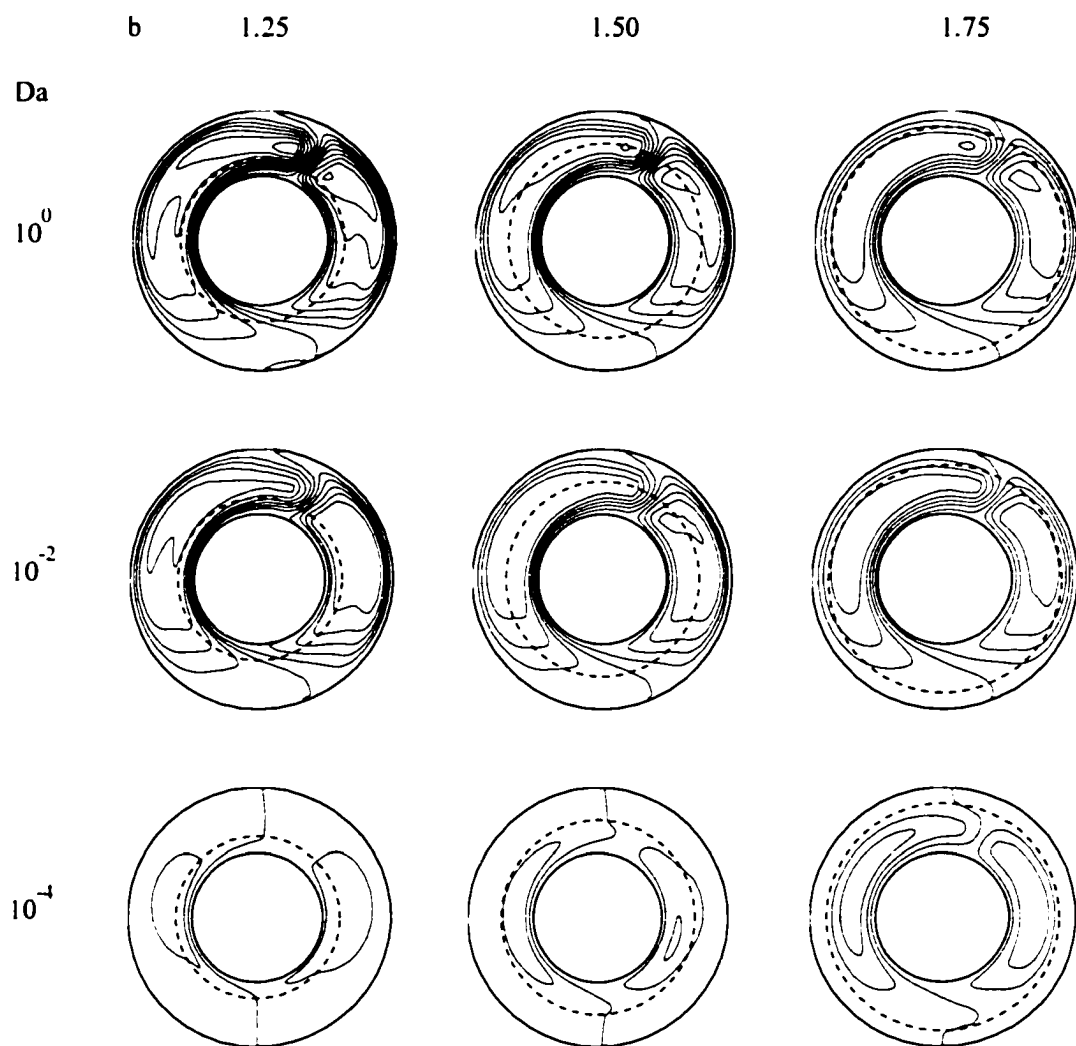


Figure F11 Flow fields of a concentric partially porous annulus space for  $k_1, k_2 = 1.0$ ,  $Pe = 10$ ,  $Pr = 20,000$ , and  $Ra = 10^6$  ( $\Delta\Psi = 10.0$ ).

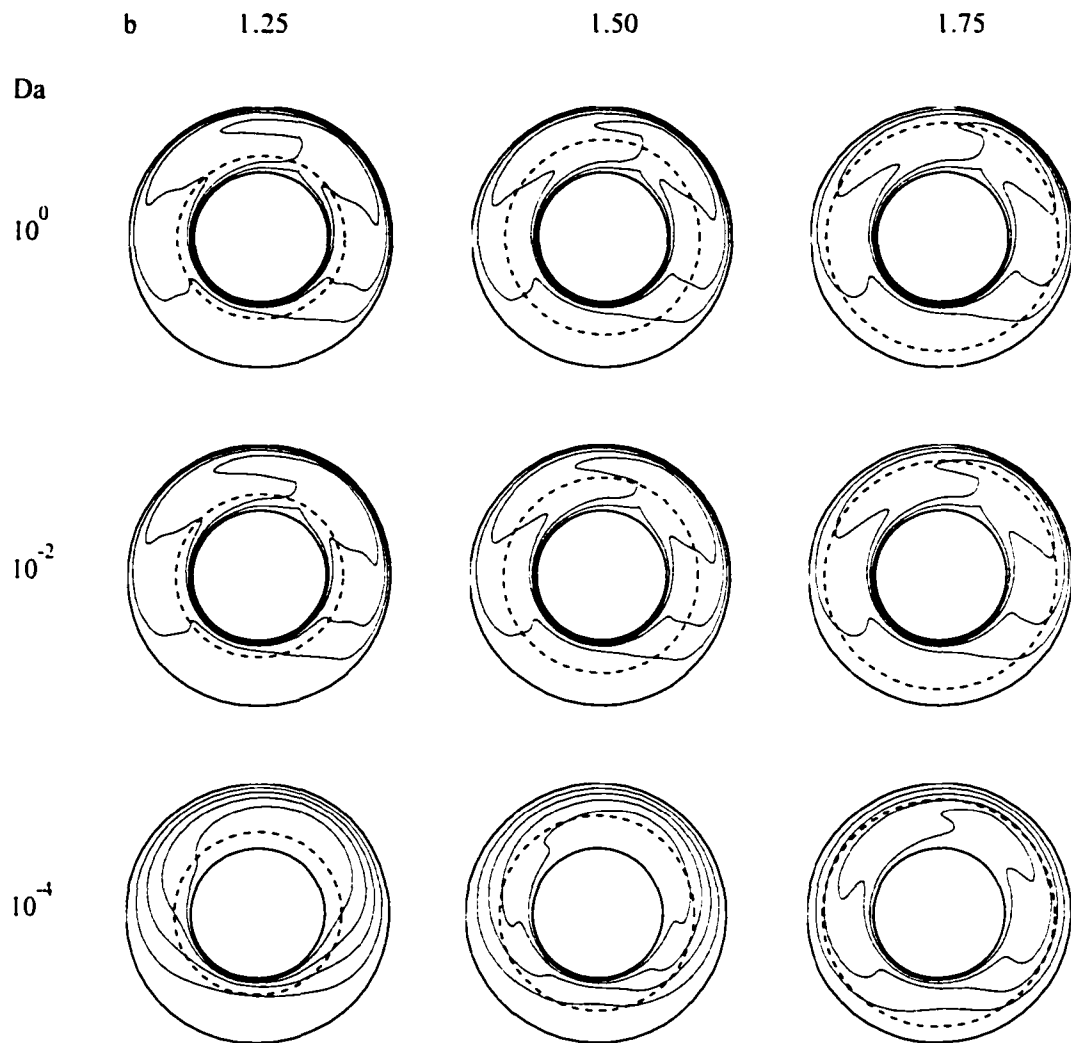


Figure F12 Temperature fields of a concentric partially porous annulus space for  $k_1/k_2 = 1.0$ ,  $Pe = 10$ ,  $Pr = 20,000$ , and  $Ra = 10^6$  ( $\Delta\Theta = 0.2$ ).

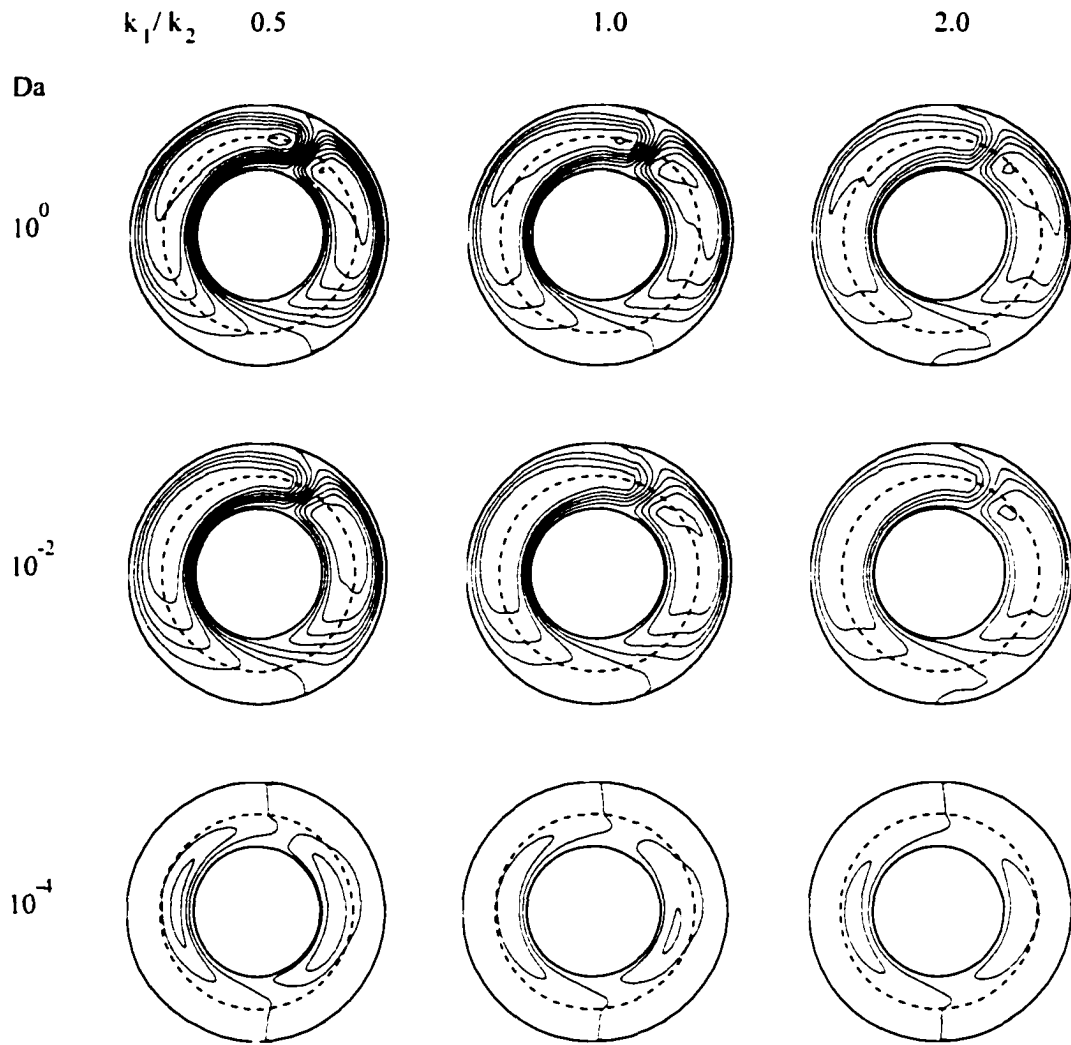


Figure F13 Flow fields of a concentric partially porous annulus space for  $b = 1.50$ ,  $Pe = 10$ ,  $Pr = 20,000$ , and  $Ra = 10^6$  ( $\Delta\Psi = 10.0$ ).

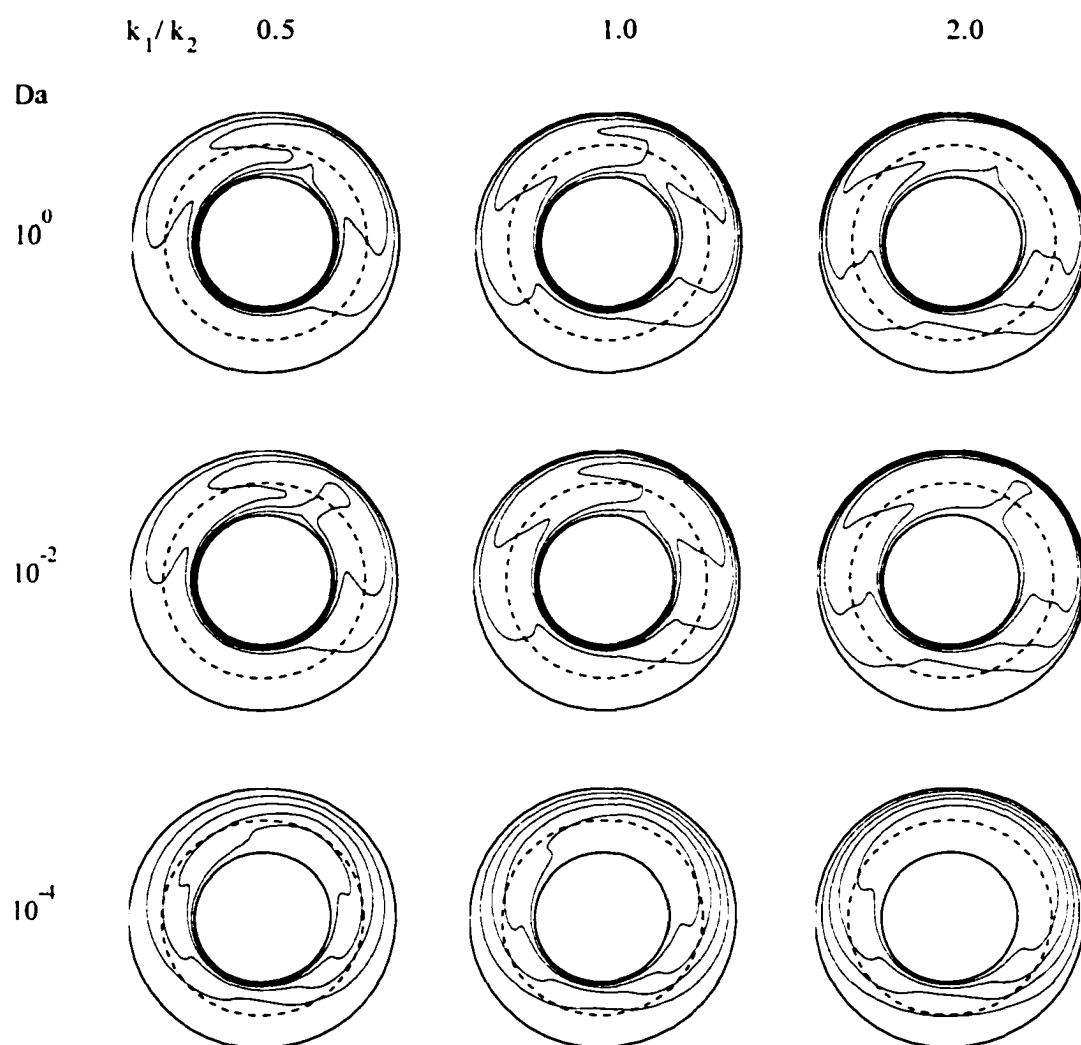
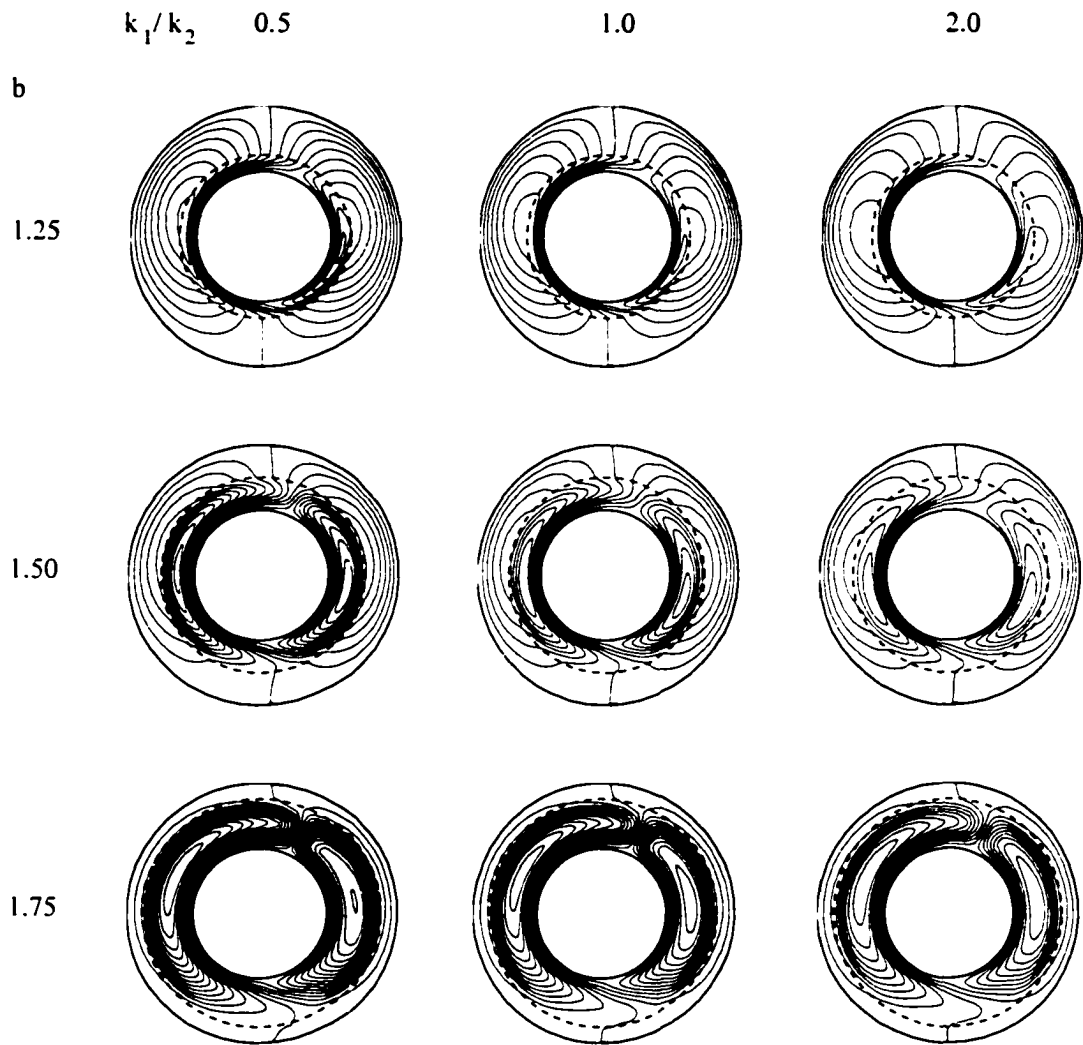
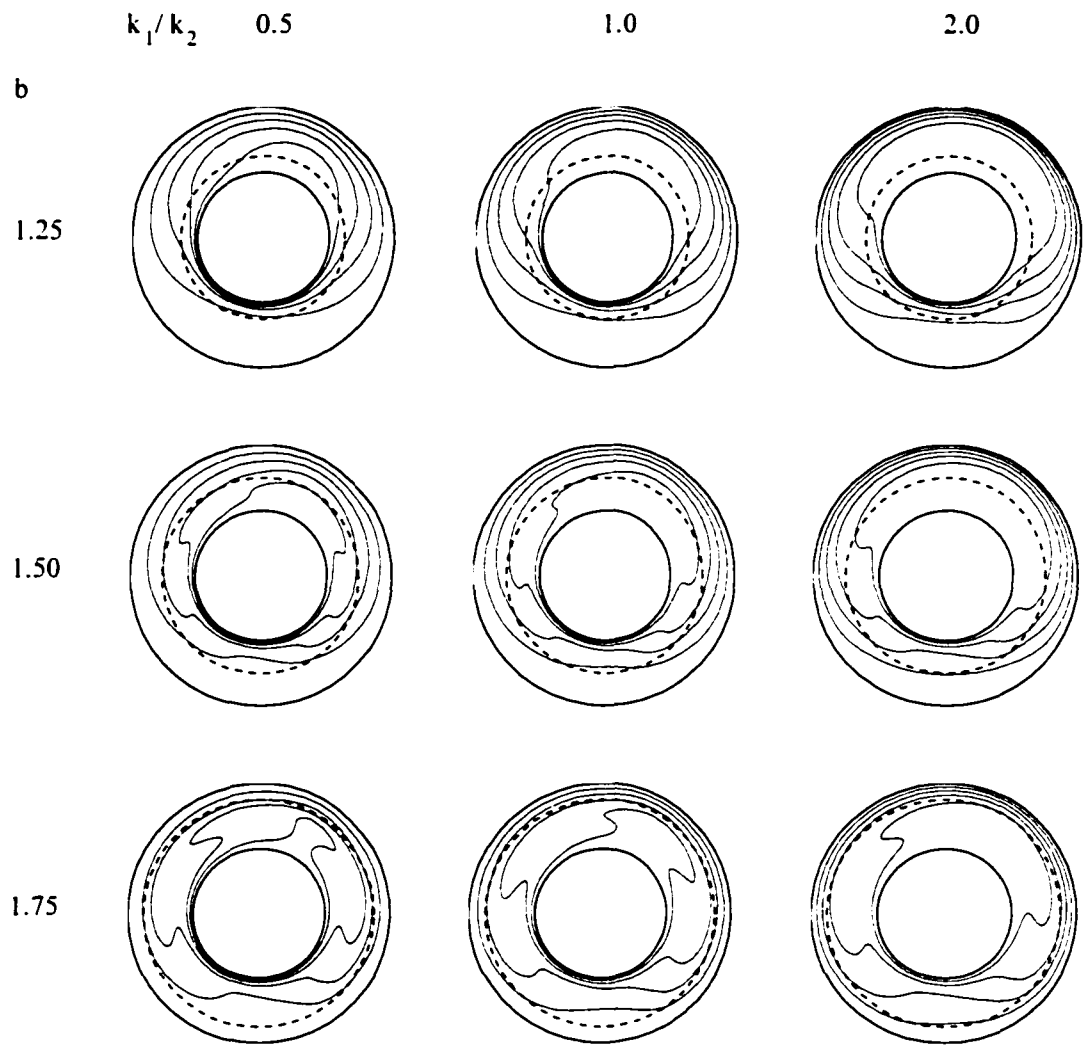


Figure F14 Temperature fields of a concentric partially porous annulus space for  $b = 1.50$ ,  $Pe = 10$ ,  $Pr = 20,000$ , and  $Ra = 10^6$  ( $\Delta\Theta = 0.2$ ).



**Figure F15**      Flow fields of a concentric partially porous annulus space for  $Da = 10^{-4}$ ,  $Pe = 10$ ,  $Pr = 20,000$ , and  $Ra = 10^6$  ( $\Delta\Psi = 10.0$ ).



**Figure F16**      Temperature fields of a concentric partially porous annulus space for  $Da = 10^{-4}$ ,  $Pe = 10$ ,  $Pr = 20,000$ , and  $Ra = 10^6$  ( $\Delta\Theta = 0.2$ ).